
Cassini-Huygens and Beyond – Tools for Dust Astronomy

Habilitationsschrift

zur Erlangung der Venia Legendi
der Fakultät für Luft- und Raumfahrttechnik und Geodäsie
der Universität Stuttgart

vorgelegt von
Dr.-Ing. Ralf Srama

Nov. 2009

Science, like life, feeds on its own decay. New facts burst old rules;
then newly developed concepts bind old and new together
into a reconciling law.

William James, 1842-1910

A Dictionary of Scientific Quotations, A. L. Mackay

Contents

1	Dust in the Solar System and Beyond	3
1.1	Interstellar Dust	3
1.2	Interplanetary Dust	10
1.3	Planetary Dust	13
2	Cassini's Cosmic Dust Analyser	19
2.1	Field of View and Pointing	21
2.2	General Description	23
2.3	Software	26
2.4	Sensitivity	28
3	Cosmic Dust Analyser Performance	33
3.1	Amplifier Switching and Signal Deconvolution	33
3.2	Time Variations and Classification Scheme	40
3.3	Calibration Overview	42
3.4	Impact Ionisation Detector Calibration	52
3.5	Chemical Analyser Target Calibration	66
3.6	Laser Yield Measurements	74
3.7	High Rate Detector	79
3.8	Dead Time Correction	80
3.9	Calibration Outlook	87
4	CDA Measurements and Selected Results	91
4.1	Dust Analyser Operations	91
4.2	The HRD and CDA Noise Rate	96
4.3	Comparative Impact Signals	103
4.4	Rate and Density Measurements in Saturn's E Ring	111
4.5	Dust Measurements in the Equinox Mission	136
4.6	Outreach	136
5	New Dust Instrumentation	139
5.1	Introduction	139
5.2	Dust Telescope Technology	140
5.3	Types of Dust Telescopes	147
6	Future Dust Missions	153
6.1	Cosmic DUNE	153

Contents

6.2	DuneXpress	157
6.3	SARIM – Sample Return of Interstellar Matter	161
Bibliography		169
About the Author		179
A	Appendix	183
A.1	Cassini-Huygens Mission Facts	183
A.2	Cosmic Dust Analyser Functional Diagram	186
A.3	The Dust Accelerator Facility	187
A.4	Dust Analyser Calibration Tables	189
A.5	Hyperplane Fitting of Impact Charges	193
A.6	CDA Bench Checkout Equipment Software	195
A.7	Hight Rate Detector Sensitivity	196
A.8	High Rate Detector Noise	197
A.9	Measurements of Interstellar Dust	198
A.10	Acronyms	203

Preamble

When I started this work a few years ago, the question was: What shall be the focus of the work? My main project is the Cassini Cosmic Dust Analyser project and there are certainly enough data and exiting results in our hands to fill many PhD works or Habilitations.

Nevertheless, it was already clear at this time, that big new developments with outstanding new challenges and possibilities were coming up: The definition, design, manufacturing and test of our *Dust Telescope* with its components *Trajectory Sensor* and *LAMA*. This new work was so promising, that I wanted to include this by describing its underlying technology, its performance and applications for future missions. Fortunately, ESA issued a call for mission proposals in the framework *Cosmic Vision 2015-2025* in 2007. This opportunity was coming at the right time, since we were just ready to specify the requirements and performance of a Dust Observatory based on our new developments [Srama et al., 2005a].

Two dust missions were proposed, the DuneXpress mission [Grün et al., 2009], a low-cost mission for the measurement of interplanetary and interstellar dust at Earth distance, and a more advanced mission called SARIM [Srama et al., 2009a]. Whereas DuneXpress is using in-situ dust detection techniques exclusively, SARIM combined both, in-situ sensors like the *Dust Telescope* and dust collection methods for sample return.

So what is new, that we want to fly now dedicated dust missions costing 100 M€ or more? Why is this more interesting than 10 years ago? The answer is given by the results of the former in-situ dust missions Ulysses, Galileo and, especially, Cassini.

Ulysses discovered the interstellar dust in our Solar System, streaming like the interstellar gas into our heliosphere and reaching distances as close as 0.6 AU from the Sun. All three missions detected and characterised nanometre-sized grains – originating from the jovian and saturnian system, swirled around by the planetary magnetospheres, and catapulted into interplanetary space with speeds similar to the solar wind. Those dust streams follow unbound orbits and can be detected 500 Mkm away from their source, but still carrying the intrinsic signatures of their parent bodies, the moons Io (jovian system) and Enceladus (saturnian system).

But the main trigger came from the results of the Cassini dust detector. First, the electrical primary charges of individual interplanetary dust grains were measured. This showed, that the measurement principle of charge induction is a well suited method for the study of particle trajectories and led to the development of the *Trajectory Sensor*.

The second achievement of Cassini's Dust Analyser is the outstanding performance of its integrated time-of-flight mass spectrometer. Thousands of icy dust grains of different populations were measured in their compositional properties, including interplanetary dust grains, jovian and saturnian dust streams, Saturn's ring particles and dust particles in the Hill spheres of moons. One main result of the compositional analysis of icy dust grains in Saturn's E ring was

Contents

even the proof for a liquid ocean of salt water below the icy surface of Enceladus [Postberg et al., 2009b]. Consequently, astrobiologists ranked the moon Enceladus as the most habitable world in our Solar System.

Can you now imagine, what we are able to learn from future dust instrumentation which is ten times more capable than the already advanced dust detector onboard Cassini? Cassini was a major step forward and motivated us, to do even better in the future by using *Dust Telescope* technology.

Dust is transporting information over space and time – by its characterisation we learn about distant worlds, which are either in our neighborhood, like moon surfaces, or which are far away like our galactic environment. This research area is named *Dust Astronomy* and its tools are *Dust Telescopes* and *Dust Cameras*. The compositional analysis of dust grains from distant objects allows us to look into stars (interstellar dust) and into moons (ice geysers on Enceladus, volcanoes on Io), without the need of close encounters. *Dust Astronomy* opens a new window to investigate astrophysical and planetological questions. This is the main message of this work.

The chapters lead from the scientific background of dust science, over the experience with the Cassini dust detector, to the definition of new dust instrumentation and their application on future dust missions.

A broader chapter was dedicated to the advanced dust detector onboard Cassini, starting with the description of the sensor, followed by its calibration and performance, its limits and results. Here, also some details are given you will not find in previously published papers.

The Cassini dust measurements will remain the fundament for dust science for many more years, justifying day by day the necessity of a *Dust Astronomy* mission.

1 Dust in the Solar System and Beyond

1.1 Interstellar Dust

The investigation of the roots of our Solar System and mankind is one of the main scientific questions in astrophysics. How do Planetary Systems form? What are the ingredients and conditions? How does the system evolve with time, and finally, how does it end? Is humankind special and unique in the universe? How can we describe the periodic cycle of formation, evolution and destruction of a Solar System? Nowadays, no scientist is able to answer the questions asked, but a major role plays cosmic dust.

Interstellar dust is recycled in the universe over its lifetime and it is a major component to form stars and planetary systems. Our Earth and even humankind is made out of dust in this regard and is therefore we are interested to understand this cycle of formation, evolution and destruction. Furthermore, the properties of interstellar dust play an important role in the understanding of astronomical observations. The dominant source of electromagnetic energy in the universe is starlight (UV, optical, near-infrared), but the quantification of the amount of starlight produced is difficult: interstellar dust grains attenuate an unknown fraction of the light before it exits the galaxy into the intergalactic medium. Only 11% of $0.1 \mu\text{m}$ and 87% of the $2.1 \mu\text{m}$ photons escape their host galaxies and can be observed [Driver et al., 2008]. Surveys during the past decade at larger wavelengths revealed massive galaxies radiating at high redshifts in the submillimetre range. Half of the starlight from these dusty starburst galaxies is absorbed and thermally re-radiated by clouds of dust with temperatures around 30 K [Devlin et al., 2009]. The spectral energy distribution peaks at $100 \mu\text{m}$ in the rest frame leading to redshifted wavelengths between 200 and $500 \mu\text{m}$.

For the study of cosmological models the determination of the energy emitted by galaxies is extremely important and interstellar dust plays a major role in those investigations. Galaxies contain billions of stars bound together by gravitation and our own Sun is only one of 200 billion stars in our Milky Way. In order to determine the energy emission of our universe, the radiation of the galaxies has to be investigated. Besides stars, galaxies contain a lot of gas and dust (Fig. 1.1). The dust is responsible to block and absorb the star light such that only half of the light is reaching our telescopes on our Earth: The universe is twice as bright as previously thought, or with other words, dust blocks approximately half of the light that the universe generates. The absorbed energy is not lost and it increases the temperature of the interstellar dust grains until their emitted heat is in equilibrium with the environment. The amount of heat radiated by the dust seemed to be higher than the energy of the stars until Driver and

his colleagues explained the discrepancy [Driver et al., 2008]. After carefully measuring the brightness of thousands of disc-shaped galaxies with different orientations, they matched their observations to computer models of dusty galaxies. From this they were able to calibrate the models and, for the first time, determine how much light is obscured when a galaxy has a face-on orientation. Now they were able to determine the absolute fraction of light that escapes in each direction from a galaxy. Applying now these new models, the energy balance of the universe is achieved and the impact of this model is, that massive centres of galaxies might emit five times more energy than observed. Although new and modern telescopes allow us to see further into space, the obscuring effect from tiny interstellar dust grains has to be eliminated.

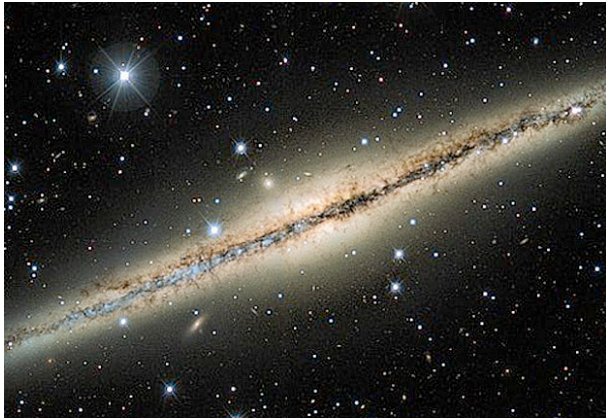


Figure 1.1: Edge-on view of the spiral galaxy NGC 891. Dust blocks the star light and appears as a dark band. Courtesy C. Howk (JHU), B. Savage (U. Wisconsin), N. A. Sharp (NOAO)/WIYN/NOAO/NSF

1.1.1 Origin and Composition

Dust is often an underestimated part of our universe. It plays a major role during the cool-down of the interstellar medium and during the formation and development of stars in galaxies. But where does the dust come from? In our Milky Way the dust originates mainly from old stars. In contrast, less known is the origin of the dust in the early universe. Supernovae were assumed to be the main production regions in the early universe. This picture might have to be revised after Sloan and his colleagues detected dust around a primitive carbon star [Sloan et al., 2009/1/16]. Carbon stars are red giants showing spectral lines of carbon and carbon rich compounds like CN and CH (Fig. 1.2). In our Milky Way, primarily those stars generate carbon rich dust in their atmospheres which is transported to the interstellar medium by stellar winds. Furthermore, it was unclear to which extent such processes were relevant in the early universe, where the overall abundance of heavy elements¹ was much lower than today. However, the spectroscopic study of individual young objects (or to be more specific, individual stars) at large distances is extremely difficult.

But there is another way to learn about the properties of young objects and their dust production mechanisms: The study of objects in our neighborhood with a low metallicity. The carbon star MAG 29 of a nearby galaxy called Sculptor Dwarf is 280.000 light years away and

¹Elements heavier than hydrogen and helium are named *metals*.

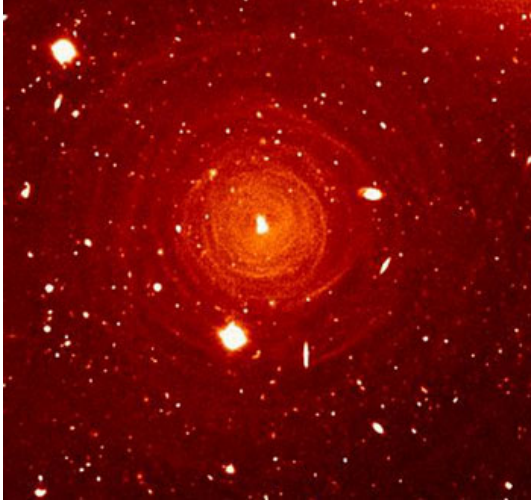


Figure 1.2: Shells of dust and gas around the carbon star CW Leonis in our milky way, 650 light years away from our Solar System (courtesy Izan Leao et al.)

shows a metallicity of only 4% of the solar abundance. This low value makes the chemical composition of the star similar to the primitive environment in galaxies of the early universe. Nevertheless, typical absorption bands of dust were found in the spectra by Sloan and his colleagues using the space telescope Spitzer. The data are interpreted as a significant mass loss and a substantial dust production. This shows, that a low abundance of heavy elements is no hurdle for the production of dust in the vicinity of a carbon star.

The observational evidence for large amounts of dust in distant Quasi-Stellar Objects (QSOs²) was reported by e.g. Bertoldi et al. [2003]. Signatures of thermal emission from hot dust, heated directly by the central active nucleus of high-redshift QSOs were also reported by Hines et al. [2006].

Recently, in-depth studies of spectral features in the mid-infrared using the Spitzer Space Telescope allowed even the determination of the mineralogical composition of dust for the quasar PG 2112+059 [Markwick-Kemper et al., 2007]. Spectral fitting revealed evidence for Mg-rich amorphous silicates with olivine stoichiometry, as well as the first detection of Al₂O₃ (corundum) and MgO (periclase). Markwick-Kemper and co-authors concluded, that such a mixed composition supports the model of a clumpy density structure of the grain-forming region. The silicates encompass 57% of the identified dust mass, while corundum takes approximately 38 wt.%. Furthermore, an identified feature at 11.2 μm was interpreted as crystalline silicate forsterite with minor contributions from polycyclic aromatic hydrocarbons. Crystalline silicates require high temperatures in order to counteract a rapid alteration and destruction from cosmic rays.

In carbon-rich environments, a variety of carbon compounds can form which may act as seed particles for the nucleation of some sorts of amorphous carbon. The presence of carbon grains in the envelopes of carbon-rich stars is well accepted. An emission band at 7.7 μm has been attributed to aromatic C-C stretching vibrations in soot-grains, and IUE spectra of RCrB

²QSOs appear as normal stars, but have very large redshifts.

stars³ showed a wide absorption band at 240-250 nm attributed to carbon grains. Polycyclic aromatic hydrocarbons (PAHs) have attracted particular attention in recent years. Although still controversial, the unidentified infrared spectral bands in the 3 to 13 μm region are generally attributed to PAHs.

The major sources of interstellar dust are evolved stars and envelopes of novae and supernovae explosions [Jones, 2005]. About 90% of the stellar mass loss is provided by cool, high-luminosity stars, in particular by asymptotic giant branch (AGB) and post-AGB stars. As the ejected gas cools in expanding stellar winds, solid particles condense out of the gas phase. Additionally, a significant amount of dust is generated in the envelopes of novae and supernovae explosions.

Stars that are in their late evolutionary stages (on the asymptotic giant branch of the Hertzsprung-Russell diagram) lose up to 10^{-4} solar masses per year, and, thereby, provide by far the largest mass contribution to the interstellar medium. The cooling, expanding gas flows from these stars give rise to physical conditions that allow solid dust particles to condense. The carbon-to-oxygen ratio in the stellar atmospheres determines whether carbon particles or silicates and metal oxides form. Clusters of typically 10 to 100 atoms form out of the gas phase as seed nuclei, at which point other chemical species can condense onto the surface to form solid macroscopic particles [Sedlmayr and Krüger, 1997]. The chemical and mineralogical composition of these particles depends strongly on the abundances of elements in the circumstellar envelope.

Dust is emitted not only from evolved stars, but also from supernovae, Wolf-Rayet (WC) stars and novae [Amari and Lodders, 2006]. In addition to chemical and mineralogical composition, isotopic abundances can give valuable information about the particles origin. For example, excesses of ^{44}Ca , the decay product of ^{44}Ti , and ^{28}Si found in some primitive meteorites, provides strong evidence that some grains incorporated into the meteoritic material formed in a supernova explosion [Amari et al., 2001].

Silicate spectral bands at 10 and 18 μm present evidence of stardust in circumstellar envelopes [Dorschner, 2001]. The IRAS LRS catalogue contains more than 2000 objects with either the 10 or 18 μm features in emission, or with the 10 μm feature in absorption. More recent observations with ISO yielded a mineralogical diversity of crystalline silicates in circumstellar environments. For example, the strongest of the mid-infrared (MIR) bands in the 20 to 50 μm wavelength region can be attributed to Mg-rich (Fe-poor) olivine and pyroxene particles. Emission bands in MIR spectra of the post-AGB star AFGL4106 are assigned to crystalline silicate grains and its features can be reproduced in laboratory spectra of forsterite (Mg_2SiO_4) and enstatite (MgSiO_3).

³R Coronae Borealis is a yellow supergiant star with variable brightness (magnitude 6 to 14 in intervals of several months) in the constellation of Corona Borealis. The accepted interpretation is that the sudden drop in brightness is caused by a rapid condensation of carbon dust in the star's atmosphere blocking the light.

Apart from silicates, metal oxides can be expected in O-rich stars. However, the only direct evidence of a metal oxide in stardust so far comes from a distinct band at $13\mu\text{m}$, tentatively linked with aluminium oxide. This identification is supported by the detection of pre-solar corundum ($\alpha\text{-Al}_2\text{O}_3$) in primitive meteorites, although the spectra can also be explained with Al-O vibrations of spinel (MgAl_2O_4) which is also identified in primitive meteorites.

Other stardust components include silicon carbide and other oxygen-free solids. Many carbon-rich stars show a strong emission feature at $11.3\mu\text{m}$, the strength of which is strongly correlated with the star's mass loss rate. This feature has been assigned to Si-C vibrations of silicon carbide condensed in the stellar wind, and SiC grains with sizes up to $20\mu\text{m}$ were found in primitive meteorites. Isotopic studies showed the existence of different SiC sources: AGB and post-AGB stars as main sources, as well as supernovae, novae and WC stars.

Observations of circumstellar envelopes, combined with theoretical modelling implies particle size distributions strongly increasing towards smaller particles (described by an exponential or power law). Maximum sizes derived for young dust particles formed in envelopes of single stars are thought to be only $0.1\mu\text{m}$ [Jura, 1996, Whittet, 2002], although there are indications that dust particles can grow to significantly larger sizes ($\approx 100\mu\text{m}$) under certain circumstances like in discs around binary stars.

The investigation of the composition and size distribution of interstellar dust in our Solar System addresses the scientific key questions:

- Can we identify original stardust in the interstellar medium?
- What is the elemental composition of grains and its variability?
- What is the nature of carbonaceous dust?
- What is the composition of silicate grains?
- Can we identify SiC in ISD particles?
- Where is the iron?
- What are the sizes of compositionally different grains?

The Interstellar Medium

Dust grains are born in star environments and they are ejected to the interstellar medium. Their lifetime is estimated to be $4 \cdot 10^8$ years and the grains are subject to the influences of the interstellar space which alters and processes the particles. Grains cycle several times between the diffuse interstellar medium and other more dense regions. They can be destroyed in a newly forming star, or they can become part of a planetary system - interstellar dust are repeatedly recycled by the galactic evolution process [Dorschner and Henning, 1995].

In general, dust spatial densities range from 0.1 to 100 cm^{-3} in the diffuse medium and inter-cloud regions, from 100 to 1000 cm^{-3} in HII regions and up to approximately 10^5 cm^{-3} in dark clouds and molecular clouds. The environmental temperatures processing the grains range from 10 to 10^4 K . Dust is not only processed during its residence in these dense regions, but also plays a major role in the evolution of the cloud structures themselves. Without

dust, molecular clouds would not exist in the form we observe them and the grain surfaces are an efficient source for H₂. Furthermore, dust plays a major role in the redistribution of energy within the radiation environment, and shields the inner part of dense clouds from the interstellar UV radiation.

The shape, composition and size of interstellar grains is altered in dense clouds, where dust particles are altered by condensation of gas species or collisions (aggregation leads to a particle growth, [Ossenkopf and Henning, 1994]). A mantle with a thickness of about 20 nm can condense on the surface in molecular clouds and aggregation leads to larger grains with fluffy structures and varying grain densities.

Grains might also lose their volatile constituents in diffuse interstellar clouds due to ultraviolet irradiation [Greenberg et al., 1995] and thermal sputtering in supernova shock fronts. Such shock waves provide an effective destruction mechanism for ISD grains where small grains are caught in the shock and collide with bigger grains that don't follow the shock's motion due to their larger inertia [Jones et al., 1996].

What are the ice mantles of the grains are made of? The analysis of IR spectra observed by the telescopes ISO and Spitzer revealed the composition of ice mantles in cold clouds. The constituents found include water, CO₂, CO and CH₃OH, with smaller admixtures of CH₄, NH₃, H₂CO and HCOOH [Boogert and Ehrenfreund, 2004]. Ice coatings might form within relative short time scales of 10⁵ years and an example of an IR spectrum is shown in Fig. 1.3. After the formation of an icy coating, chemical reactions and processes caused by UV irradiation or ion bombardment can produce complex organic molecules leading to an organic refractory material on the surface.

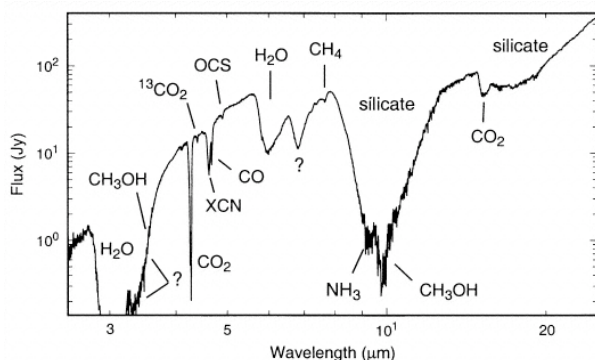


Figure 1.3: IR spectrum of W33A observed by ISO in 1996 as an example of a condensed ice mantle on silicate grains. The principal identified and unidentified spectral features of interstellar ices are labelled. [Gibb et al., 2000]

Dwek [1998] concluded that dust contains about 40% of the total mass of heavy elements in the Galaxy and that the mass of interstellar dust in the ISM is linearly proportional to the interstellar metallicity. Interstellar dust grains carry most of the mass of the refractory elements in the interstellar medium like Fe, Mg, Si as well as C and O [Tielens, 1998]. For example, Fe, which is ejected into the interstellar space during supernova explosions, is generally taken as a marker for overall metallicity. However, in the interstellar medium, typically more than 90% of the iron is inside interstellar dust grains. The lifetime of iron in dust grains indicates that iron is present in a robust grain core that is not destroyed by interstellar shocks. Although constituents of interstellar dust grains are partially known, there are no direct measurements

of the full grain composition, nor is the intrinsic metallicity of the interstellar medium well understood.

The current tools available for astronomers are remote sensing observations of the interstellar dust and the interstellar medium [Dorschner and Henning, 1995]. Spectroscopic measurements of the absorption and emission bands are the common standard technique. UV measurements determined the characteristics of the extinction bump at around 217 nm to be an absorption by electronic transitions of graphite. But due to the limited access to interstellar grains, many questions are still open. Until today, compositional information is only derived from remote sensing observations and results of the Stardust mission are still outstanding. Can destruction and formation processes like coagulation and condensation be identified in the composition and size-distribution of interstellar grains? Are there multi-component grains and are silicates mixed-in with carbonaceous material? What is the overall metallicity of the local interstellar medium?

Local Interstellar Dust

Our Solar System is currently moving through the nearby ISM which is dominated by shells of gas with low density ($n(\text{H}) \approx 0.3 \text{ cm}^{-3}$) (LIC, Local Interstellar Cloud). This local bubble was caused by supernova explosions and belongs to a cluster of clouds originating from the direction of the associations of Scorpius-Centaurus and Orion, star-forming regions in our neighborhood. It was shown by [Grün and Landgraf, 2000] that dust particles with different sizes behave differently in the LIC: Whereas small particles couple via electromagnetic interactions to the ISM on length scales < 3 light years, bigger grains ($> 10 \mu\text{m}$) couple to the gas over much longer scales (30 to 300 light years) and remain unaffected over larger distances: they might come directly from their source region.

For the first time, 15 years ago, interstellar dust was identified inside our planetary system by the dust detector onboard the Ulysses spacecraft [Grün et al., 1994]. A flow of μm -sized interstellar grains has been identified at a distance of about five AU from the Sun. The observed flux was $1.5 \cdot 10^{-4} \text{ m}^{-2} \text{ s}^{-1}$ of particles with a mean mass of $3 \cdot 10^{-13} \text{ g}$ giving a mass flux of $5 \cdot 10^{-17} \text{ g m}^{-2} \text{ s}^{-1}$. The interstellar dust enters the Solar System with 24 km s^{-1} and its direction of 259° longitude and $+8^\circ$ latitude was found to be compatible with the direction of the interstellar gas [Landgraf, 2000].

In-situ measurement methods allowed the determination of dust masses for individual dust impacts and the detected grain sizes differed with distance to the Sun revealing a lack of small grains ($< 3 \mu\text{m}$) inside a heliocentric distance of 3 AU [Landgraf et al., 2000]. At distances between 0.7 and 3 AU the Cassini and Galileo dust instruments detected only particles bigger than $0.5 \mu\text{m}$ [Altobelli et al., 2005b]. Most recently, a re-analysis of the Helios data set, measured at 0.3 AU heliocentric distance, revealed grains even bigger than $1 \mu\text{m}$. [Landgraf et al., 1999] explained bigger grain sizes in the vicinity of the Sun by a filtering effect by electromagnetic and radiation pressure forces.

In addition to in-situ methods, ground based radar technology allows the detection of big interstellar meteors with hyperbolic speeds and grain sizes $> 40 \mu\text{m}$ [Baggaley, 2000]. A gen-

eral background influx of extra-solar system particles from southern ecliptic latitudes with enhanced fluxes from discrete sources was identified (upstream direction of β Pictoris). This direction is different from the flow of small interstellar grains and no explanation exist about this discrepancy.

New missions and instrumentation are necessary to investigate the nature of interstellar dust in our vicinity. Galactic dust is abundant in the Earth's environment and therefore the size distribution, directionality and time variation of interstellar grains at one AU distance shall be studied in the future.

1.2 Interplanetary Dust

Dust plays a key role when a molecular cloud collapses and forms a protostar surrounded by a flat disc-like structure consisting of gas and dust. About 1 to 2% of the total mass of the accretion disc is provided by dust. The formation of a Planetary System can be described by three phases [Weidenschilling, 2000]. The first stage is the formation stage, lasting about 10^5 years, where the protoplanetary disc is built up by infalling material from the collapsing cloud. The viscous stage lasts approximately $10^5 \dots 10^6$ years, the disc has been formed and the mixture of gas and dust is transported inwards. Here, the formation of planetary bodies is already possible. The third stage is named clearing stage and lasts longer for about 10^7 years. The gaseous component of the disc is dispersed and the new and young star becomes optically visible (T Tauri star).

Micron-sized dust particles grow by collisional processes into kilometre-sized objects (planetesimals) during the second evolution stage. If the planetesimals become large enough to decouple from the nebula gas motion, they move on Keplerian orbits around the young star. The growth process triggers the planet formation and is of high interest for astronomers. The initial dust size distribution is an important parameter in order to model this process and the characterisation of interplanetary dust mass distribution helps to improve our understanding.

Another possibility to study the formation process of the protoplanetary disc is the investigation of interplanetary dust compositions. Dust grains are altered by the heat of the collapsing cloud and by accretion shocks. The volatile components of the dust particles are vaporised according to the environmental temperatures, and grains closer to the protostar are subject to higher temperatures. The later recondensation of material represents the temperature profile of the pre-solar nebula and grains such that dust grains in the outer part of the disc carry larger amounts of volatile materials with slightly different isotopic compositions. Dust in the outer regions remains almost unprocessed and reflects the characteristics of interstellar dust. Today, we find pre-solar grains in meteorites, in comets and in interplanetary dust particles (Fig. 1.4).

It is widely accepted that comets transport fresh and unaltered material from the outer part of the system into the inner Solar System. However, recent results of the Stardust mission changed our view in this regard. Brownlee and Stardust Mission Team [2006] found, that most of the solid particles bigger than $5 \mu\text{m}$, which were collected by the mission, are mineral

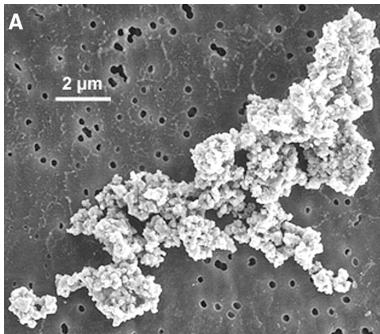


Figure 1.4: Secondary electron image of a chondritic Interplanetary Dust Particle (RB-12A). The 10 μm particle embeds interstellar grains, which contain organic carbonaceous matter and silicates [Bradley et al., 2005].

grains or assemblages of high temperature minerals that condense at 1400K or above. This is interpreted as direct evidence for a radial transport of large solid grains from the center of the solar nebula to the outer system, the Kuiper belt.

Zolensky et al. [2006] reported about a very wide range of olivine and low-Ca pyroxene compositions in the grains collected at comet Wild 2 and he concluded, that the compositions found require a wide range of formation conditions reflecting very different formation locations in the protoplanetary disk. An abundance of high temperature minerals like silicate grains form primarily in the inner region of the solar nebula and their occurrence in a comet indicates a significant radial mixing in the early Solar System.

The outer Solar System preserved volatile ices which survived the formation process. Comets originate from the outer Solar System – they preserve ices and material of the pre-solar cloud and are the least altered objects. Thus grains originating from comets are of specific interest, and in recent years the interplanetary probes Giotto, VeGa 1, VeGa 2, ICE, Deep Space 1, Stardust, and Deep Impact investigated the target comets Halley, Giacobini-Zinner, Grigg-Skjellerup, Borelly, Wild 2 and Tempel 1. A significant refractory component of cometary material are silicates and Stardust results showed, that they are a mix of crystalline grains (enstatite and forsterite) and glassy amorphous grains. A few Wild 2 grains were identified to contain calcium/aluminium-rich inclusions (CAIs) similar to those found in meteorites known as chondrites. Thought to be the oldest objects in the Solar System, chondrites have always been a puzzle because they contain minerals that formed at low temperatures as well as minerals, like CAIs, that must have formed at high temperatures. Higher temperatures are typical for the inner solar nebula meaning that they have to be subsequently transported to the comet formation zone - or they may be real stardust, produced in the atmosphere of another star many million years ago.

Although the cometary Wild 2 samples returned by Stardust provide currently the most important data set, evidence for relatively unaltered interstellar material was found already in fluffy interplanetary dust particles (IDP) collected in the stratosphere. Some grains contain a special silicate phase named GEMS (Glass with Embedded Metal and Sulfides) which is indeed similar to those found throughout interstellar and circumstellar space. Isotopic anomalies of H, N, O in IDPs indicate a pre-solar or interstellar origin of the constituents of IDPs. In some IDPs Messenger and Walker [1997] discovered hotspots of extreme isotopic anomalies of up to a factor of 50. These anomalies likely represent the partial preservation of materials that experienced extreme chemical mass fractionation in the cold, dense molecular cloud predating

our Solar System. The largest D/H ratios observed so far in extraterrestrial materials occur in IDPs, reaching the values of some molecules in interstellar molecular clouds.

Cometary material is a major link between the early Solar System and its formation process, and the current conditions with its mixtures of altered and unaltered materials which are distributed in small bodies like meteoroids, comets, asteroids and planets. An analysis of the physical and chemical properties of cometary dust improves our understanding about the origin of the solar system, the early evolution of the protoplanetary disc, and even the life bearing chemistry which was delivered to Earth over 4 billion years ago.

Although comets are the most obvious source of interplanetary dust in the inner Solar System, there exist a variety of dusty phenomena and dust sources in our system. An recent summary about interplanetary dust was given by Grün et al. [2001]. Our current knowledge is based on remote sensing observations (light scattering, thermal emissions), in-situ dust experiments (Pioneer, Giotto, Helios, Heos, Nozomi, Golid, Galileo, Cassini, Ulysses, Stardust, New Horizon), crater studies of moon rocks or of planetary moon surfaces, meteor radar studies and laboratory sample analysis (dust extracted from polar ices, dust collected in the stratosphere, dust returned by Stardust, dust and space debris impact residues of returned satellite parts).

IDPs are born in cometary comae, by asteroid collisions, by meteoroid impacts onto surfaces of small bodies (asteroids, small planetary moons) and in planetary environments (Jupiter and Saturn dust streams). Today, the most efficient source for IDPs are cometary tails: icy and silicate grains released by the cometary nucleus during the sublimation of volatile ices in the vicinity of the Sun. Larger dust particles preserve the orbital parameters of the comet and form the known cometary trail. This trail can be studied directly when the Earth passes through the trail, leading to the known yearly meteor showers. However, our knowledge is primarily based on spacecraft data as the results of the Giotto mission and its target comet Halley. In-situ dust experiments measured the size distribution from sub-micron to millimetre sized grains of the inner coma during the flyby in 1986 [McDonnell et al., 1991]. The results showed that large grains (mass $> 10^{-6}$ g) were more numerous than was previously expected, such that these large grains dominated the mass output of the comet. Hörz et al. [2006] confirmed this finding of a relatively shallow mass distribution at large grain masses by analysing the Stardust data of the comet Wild 2.

The asteroid belt with its numerous small bodies are another important source of IDPs. Collisions within the belt and micrometeoroid impacts on their surfaces generate fragments with a wide size distribution. These fragments form a tiny dust ring in the asteroid belt region, which was identified by IR observations using the satellite IRAS [Sykes and Greenberg, 1986]. Asteroidal dust carries the compositional signature of their parent bodies which are primarily silicates and metal-rich materials.

Which forces do influence interplanetary dust grains? A nice overview is given in various chapters of the book by Grün et al. [2001]. Generally, gravity (Sun and planets and moons), Lorentz forces (interplanetary magnetic field, planetary magnetospheres), radiation and solar

wind pressure, plasma drag and Poynting-Robertson drag are the relevant forces. Depending on the local parameters of the dust environment, the forces have varying influences on the dust grains. In the environment with higher gas densities (comets, gas plumes of Enceladus), gas drag forces are relevant, too. Collisions between micrometeoroids do not play a role in the low-density interplanetary space.

The Poynting-Robertson force is a force which leads to a transport of dust from the asteroid belt and the outer Solar System to the inner system. The grains become concentrated in the zodiacal dust cloud with a concentration along the ecliptic plane. The dust particles absorb light energy from one direction (the Sun) and re-emit the energy equally in all directions. Because the dust is moving perpendicular to the radiation, the radiation is coming at a slight angle towards the particle leading to a loss of kinetic energy. The particles slow down and spiral towards the Sun limiting their life time.

The zodiacal cloud contains both, fresh dust from cometary trails, and old cometary dust dispersed over time which cannot be associated to a particular comet any more. Today, the relative contributions by asteroidal and cometary dust to the zodiacal cloud are still unknown, and the last 40 years of space exploration by dust detectors onboard interplanetary spacecrafts as well as optical observations lead only to a coarse insight into the cloud dynamics.

What is the ratio of cometary versus asteroidal particles at 1 AU, and what are the orbital characteristics of different types of cometary and asteroidal particles at 1 AU? How much is dust from comets chemically different to dust from asteroids? Are there large organic molecules in cometary and asteroidal dust that can be precursors of life?

For a better understanding of the influence of the asteroidal and cometary dust sources, in-situ studies of the dust populations by advanced dust detectors is necessary, which are able to simultaneously measure dust trajectories as well as their composition [Grün et al., 2003].

1.3 Planetary Dust

Planetary dust describes the population of dust grains which is bound by gravity to a central planet or its moons. It is well known by the formation of dust rings like in the Jupiter or Saturn system. The two spacecrafts which studied these systems are Galileo in the jovian system [Krüger et al., 2005] and Cassini in the saturnian system [Srama et al., 2006, Kempf, 2007]. Besides Jupiter and Saturn, dusty rings are also known from Uranus and Neptune, but their study by in-situ methods was not possible until today. The rings from the gas giants are well known, but it is not very well known, that a terrestrial planet like Mars is supposed to have a dusty ring. However, this ring would be very faint and its discovery is still outstanding by both, remote sensing methods and in-situ methods, respectively [Sasaki, 1999, Krivov and Hamilton, 1997].

Dust in planetary systems is present in manyfold ways: The visible and non-visible ring systems of the outer planets are the most popular phenomena. But three other mechanisms are not so well known, namely the dust clouds around small bodies, the high-velocity dust streams of the jovian and saturnian system, and the active ice geysers on the surface of plan-

etary moons like Enceladus (Fig. 1.5). Dust clouds around planetary moons were discovered by the dust detector onboard Galileo [Krüger et al., 1999, Krivov et al., 2003]. The continuous bombardment of the moon surfaces by the dust ring background particles, interplanetary micrometeoroids and interstellar dust grains generate a faint shell above the surface, filled with ejecta particles produced on the moons surface upon the primary dust impacts. This process is ongoing on all surfaces in the planetary system which are not protected by an atmosphere. This includes asteroids, comets, the Earth's moon and all planetary moons (except Titan). This process was extensively studied in the jovian system [Krivov et al., 2002, Sremčević et al., 2005, Krüger, 2003] and offer unique possibilities for dust environmental studies.

First, the impact generated cloud represents the flux and mass distribution of the primary impactors and the study of the dust cloud provides insights into the interplanetary dust population (or any other primary impactor population). Of special interest is the mass infall and contamination of the saturnian main dust rings by the interplanetary dust population.

Second, the dust cloud grains consist mainly of the surface material. Compositional measurements allow for remote studies of the surface composition with a spatial resolution, which is of the order of the dust grain altitude. This method would allow in-situ studies of moon or planetary surfaces by orbiters without the need of a lander. However, until today a clear dust cloud identification around Saturn's moons is outstanding due to the strong E-ring particle background and Cassinis operational constraints.



Figure 1.5: Left: Saturn's outer blueish E ring along the orbit of the moon Enceladus. Cassini acquired this global view during a Sun occultation of the planet. Right: Image of the dust plumes at the south pole of Enceladus. (NASA/JPL/SCI PIA08329 PIA08386)

Another phenomena are the nanometer-sized dust streams from the jovian and saturnian system. Very small dust grains originating from the Jupiter system were detected by the spacecrafts Ulysses and Galileo up to 500 million kilometer away [Grün et al., 1993]. The particles have sizes usually between 5 and 50 nm and speeds above 100 km s^{-1} and their strong charge-to-mass ratios lead to a strong coupling to the electromagnetic environment, leading to trajectory modulations of the grains on their way out through the planetary system⁴. Krüger et al. [2003] even showed a correlation between the dust stream flux detected by

⁴The dust grains are electrically charged due to the environmental plasma and the solar UV radiation. The co-rotating electric field component in Jupiter's magnetosphere accelerate the charged grains outwards.

Galileo and the volcanic activity on the surface of Jupiter's moon Io. Earlier it was shown, that Jupiter's fine volcanic ash particles are the main source for the dust stream phenomena in the jovian system (Fig. 1.6). Based on the experience in the jovian system, Horányi [2000] predicted similar dust streams originating from the saturnian system, which were discovered by Cassini in 2004 approximately 70 million kilometers away from Saturn [Kempf et al., 2005a]. A detailed analysis lead to the conclusion, that such stream particles originate from the inner ring of Saturn. And even with such tiny grains - consisting of less than one million atoms - a compositional analysis was possible [Kempf et al., 2005b]!

The third dusty phenomena is the already mentioned volcanic activity. Volcanoes or ice geysers eject huge amounts of gas and dust grains to high altitudes. Some dust grains gain enough kinetic energy to escape from its source and they become a ring particle in orbit around the central planet (Fig. 1.6). As usual, the dust grain properties represent their sources. The dust densities and fluxes correlate with the source activity (volcano or geyser activity), the dust size distribution indicates and constrains the dust production mechanism, and the dust grain composition is a sample ejected directly from the interior of a planetary body.

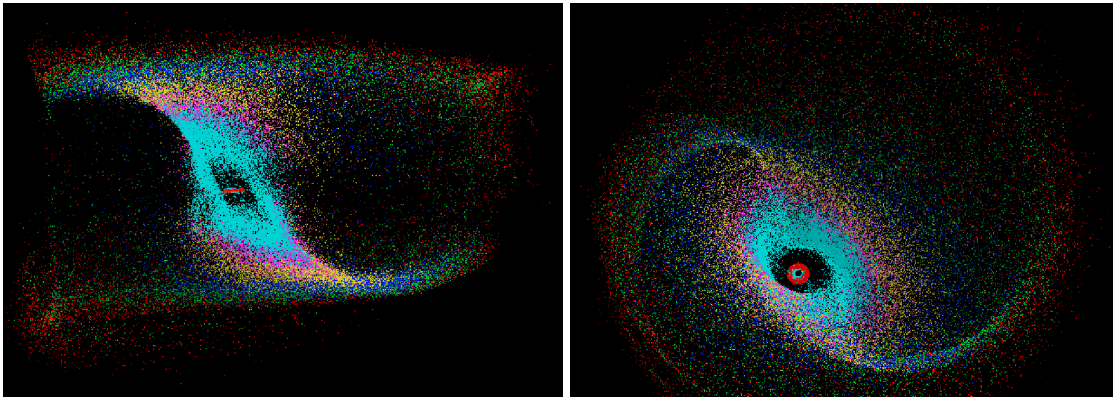


Figure 1.6: Escape of charged dust grains from the jovian magnetosphere (left: side view, right: top view). Each coloured point represents the position of a dust grain after 15 hours of traveling, launched at the orbit of Jupiter's moon Io. The colour represents the dust grain radius (red:5-7 nm, green 7-9 nm, dark blue 9-12 nm, orange 12-16 nm, purple 16-20 nm, light blue >20 nm). Bigger grains remain on bound orbits close to Jupiter in the centre (red ellipse). The 5 nm sized grains reach distances of 10 Mkm and speeds of 300 km s^{-1} . This simulation of 120 000 dust grains by A. Graps illustrates, that dust grains transport information over space and time. They originate from Io's volcanic ash and they can be measured outside Jupiter's magnetosphere at distances as far as 3 AU (courtesy A. Graps).

The enormous potential of this method of in-situ compositional measurements was revealed recently by Cassini observations of the Cosmic Dust Analyser (CDA). The CDA instrument determined the composition of Saturn's E-ring particles which originate primarily from the plumes of Enceladus' ice geysers (Fig. 1.5). Saturn's moon Enceladus emits plumes of water vapour and ice particles from fractures near its south pole, raising the possibility of a subsurface ocean. CDA recorded thousands of mass spectra in-situ with sizes between $0.1 \mu\text{m}$ and

1 μm [Postberg et al., 2008]. A previous in-situ analysis of those particles concluded that the minor organic or siliceous components, identified in the ice grains through mass spectrometry, could be evidence for an interaction between the rocky Enceladus core and liquid water. However, it was not clear if the liquid is still present today, or, if it has frozen. Now, Postberg et al. [2009b] reported the identification of a population of E ring grains that are rich in sodium salts, which can arise only if the plumes emanate from liquid water that is, or was, in contact with rocky material. The proof of liquid water in the outer Solar System is of high value for the field of astrobiology and the origin and formation of life.

This result clearly underlines the power of the remote, but in-situ method, of dust detection by interplanetary spacecrafts. Grün et al. [2003] applied this scheme especially to the measurement of interstellar dust and defined the research field of *Dust Astronomy*. Dust grains are born at one location in space and transport their identity over space and time. All phenomena mentioned make use of this scheme. For example dust stream particles are born in the inner jovian or saturnian system, but they are detected outside of the magnetosphere of the planets, millions, or even hundreds of millions kilometer away from there source, but still carrying their information. Right in this moment, dust grains emitted by Jupiter's moon Io might enter the Earth' atmosphere and could be detected by sensitive and appropriate dust instrumentation. Dust grains from the interior of Enceladus carry their information out to the spatially extended E-ring, from four Saturn radii distance to eight saturnian radii or even further (Fig. 1.7). More locally constrained, dust grains in the clouds around small bodies preserve the compositional information of the surface.

On a global scale, interstellar grains are produced in far stellar environments, travel many light years until they enter our Solar System, waiting to be detected and analysed by dust instrumentation. But let's go back to the dust born in our Solar System. Once the dust source is identified, the modeling of the dust dynamics and evolution from its source (e.g. Enceladus) to the spacecraft position at the detection time is possible. Kempf et al. [2009] launched dust grains at the surface of Enceladus taking into account the speed and size distribution of the ice grains in the plume, and the authors were able to model and reproduce the shape of the observed E ring.

The model results constrain on the other hand parameters of the magnetosphere, dust charging processes and plasma properties. Charged dust grains are excellent probes for the magnetosphere provided that the dust source region is known. In contrast, the source region might be constrained if the magnetosphere properties are known well enough.

The paragraphs above already indicated the excellence of the dust instrument onboard Cassini. The Cosmic Dust Analyser is the most advanced dust detector in interplanetary space today [Srama et al., 2004a]. Its achievements are manifold and a break-through in dust science. This generation of dust detector has significantly improved the already established Galileo- and Ulysses-type detectors. It combines its sensitivity with reliability and dust grain compositional measurements. The sensitivity to measure the primary charges carried by individual dust grains was improved by a factor of ten. A well defined decontamination procedure before and after spacecraft launch provides mass spectra with only minor constituents

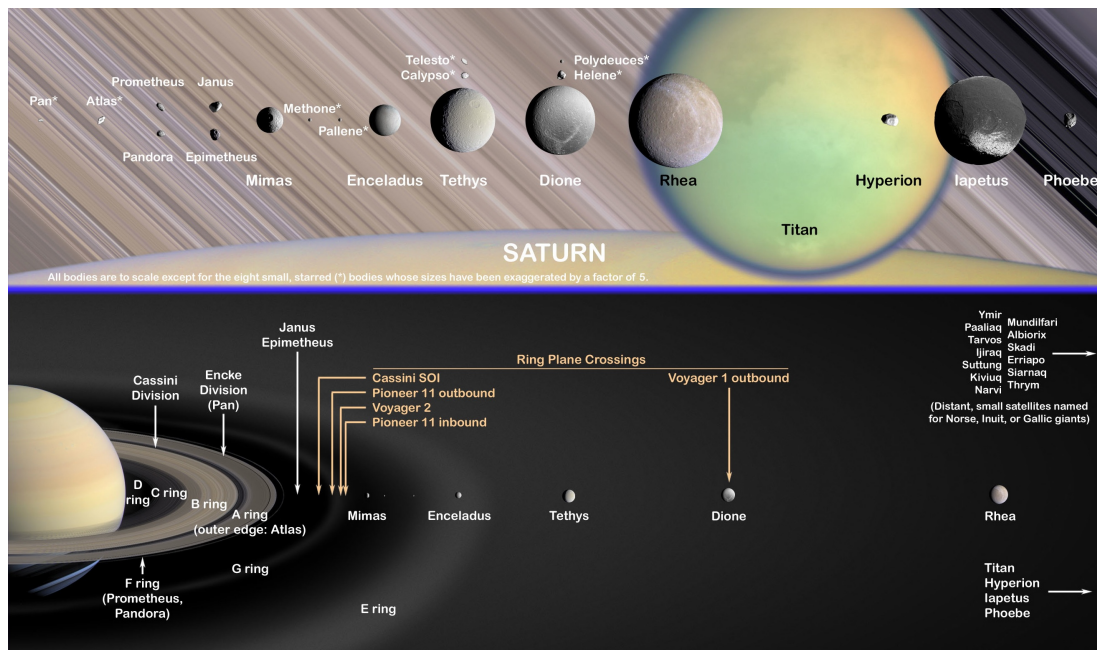


Figure 1.7: Saturn System with its moons and rings. The E ring describes a band along the orbit of the moon Enceladus. (D. Seal)

from contaminants in contrast to former flown spectrometers aboard Stardust or Giotto [Postberg et al., 2009a]. Therefore it was no surprise, that CDA already made major discoveries on its way out to Saturn in the years 1999 to 2004.

In 1999 CDA discovered and determined the interstellar dust flux at one AU distance from the Sun [Altobelli et al., 2003], followed by the first direct detection of primary charges of interplanetary dust grains [Kempf et al., 2004]. The integrated mass spectrometer recorded, for the first time, the composition of interplanetary dust grains between Earth and Jupiter [Hillier et al., 2007a]. The sensitive spectrometer was also able to determine the composition of Jupiter's dust streams [Postberg et al., 2006], and later, CDA discovered similar dust streams originating from the inner saturnian system [Kempf et al., 2005a]. The compositional analysis of Saturn's dust streams were achieved by Kempf et al. [2005b] and extensive studies of icy ring particle compositions were performed [Postberg et al., 2008, Hillier et al., 2007b]. The modeling of Saturn's dust stream dynamics, their coupling to the magnetosphere of and the interplanetary magnetic field and the influence of CMEs and CIRs is in the investigation and publishing phase today. Furthermore, CDA measured a much larger E ring than expected [Srama et al., 2006], determined ring density profiles [Kempf et al., 2008] and dust grain potentials which revised the known magnetospheric properties [Kempf et al., 2006]. CDA detected the outer edge of the G ring [Kempf, 2007] and discovered, together with the magnetometer and the INMS instrument aboard Cassini, the plumes of the moon Enceladus [Spahn et al., 2006].

1 *Dust in the Solar System and Beyond*

Further current work is related to the measurement and modelling of the dust dynamics of the E ring and their time-variability, the existence of retrograde particles in Saturn's system (either caught by Saturn's gravity or originating from the retrograde moon Phoebe) and the infall of interplanetary and interstellar grains into the system. Especially the measurement of the composition of interstellar and interplanetary particles at Saturn's distance would provide unique results for the understanding of the birth and evolution of our planetary system.

After describing the scientific background, more details about the most advanced dust detector *Cosmic Dust Analyser* are given in the following chapters 2. How does it work, what are the main issues and where are the limits in dust grain characterisation today? Presented are a new calibration scheme, a noise analysis (chapter 3), and selected results of the dust measurements with Cassini in the saturnian system (chapter 4). The experience and overwhelming performance of CDA over so many years provided the data necessary to design and develop new dust instrumentation (chapter 5): Dust grain charge detection in space is possible, and, TOF mass spectrometry of in-situ dust impacts is a reliable and sensitive method for particle detection and characterisation. This work describes two new dust sensor technologies as components of a *Dust Telescope*, and finishes by the proposal of future dust missions (chapter 6), which opens a new window for the exploration of astrophysical and planetological questions.

2 Cassini's Cosmic Dust Analyser

The Cassini-Huygens Mission provides the opportunity for a thorough investigation of the interplanetary dust complex and the saturnian dust environment. The scientific objectives were stated in the proposal dated 1989 as: "The overall objective of the proposed investigation is the exploration of the physical, chemical and dynamical properties of small dust particles in interplanetary space and in the saturnian environment. The parameters to be studied include mass, composition, electric charge, speed and flight direction of individual particles. The impact rate, mass distribution, average composition, angular distribution, and charge will be determined with respect to heliocentric and saturnian distances, to the distance from rings and satellites and to magnetospheric coordinates."

Cassini-Huygens is the first spacecraft which orbits Saturn. The former experimental results are based on former Voyager and Pioneer flyby measurements and give only snapshots of the complex dust environment of Saturn. Simulations of dusty rings in the saturnian system were based on the results of the former Voyager missions. Now, the dust experiment on Cassini-Huygens provides much better results in quantity and quality. The long measurement time of over 5 years around Saturn allows extensive studies of the ring details. Especially the results of the Galileo dust detector in the jovian system lead to ideas and predictions of dusty phenomena like dust atmospheres around small moons [Krüger et al., 2000, Thiessenhusen et al., 2000], dust streams [Horányi, 2000] and halo orbits [Howard et al., 2000] in the saturnian system. Tab. 2.1 shows a summary of the former dust detectors on interplanetary spacecrafts.

The scientific goals of the Cassini dust instrument were defined as:

Cruise Science Extend studies of interplanetary dust to the orbit of Saturn. Sample the chemical composition of dust in interplanetary space and across the asteroid belt. Determine the flux of interstellar particles during solar maximum conditions. Search for dust streams originating from Saturn.

Jupiter flyby Investigate the dynamics of the Io dust streams as discovered by Ulysses and Galileo. Characterise their direction, size-mass-distribution and correlation with the jovian and interplanetary magnetic field. Investigate the dust stream fluxes caused by the jovian system with respect to the Jupiter distance. Analyse dust stream particles at a different epoch from Galileo. Characterise the elemental composition of dust stream particles.

Rings Map size distribution of ring material, search for ring particles beyond the known E ring. Analyse the chemical composition of ring particles. Study dynamical processes (erosional and electromagnetic) responsible for the E ring structure, study interactions between the E ring and Saturn's magnetosphere, search for electromagnetic resonances.

Table 2.1: Comparison of former interplanetary missions including dust instrumentation. The probes Helios, Stardust and Cassini are able to determine the dust composition via TOF spectrometry. The mass threshold is given for an impact speed of 20 km s^{-1} . The detectors onboard Heos, Helios, Ulysses, Nozomi, Galileo, Cassini and Stardust are based upon impact ionisation technologies. The detector onboard New Horizon is a PVDF type detector and Pioneer used simple threshold detectors. The ESA mission Rosetta carries various dust instrumentation suited only for the analysis of low-velocity impacts ($<500 \text{ ms}^{-1}$).

Spacecraft	Mass threshold [kg]	Dynamic range	Sensitive area [m ²]	References
Pioneer 8,9	2×10^{-16}	100	0.009	[Berg and Richardson, 1968]
Pioneer 10	2×10^{-12}	1	0.26	[Humes et al., 1974]
Pioneer 11	1×10^{-11}	1	0.26 (0.57)	[Humes, 1980]
HEOS 2	2×10^{-19}	10^4	0.010	[Hoffmann et al., 1975]
Helios 1,2	9×10^{-18}	10^4	0.012	[Dietzel et al., 1973]
Giotto PIA	3×10^{-19}	10^6	0.0005	[Kissel, 1986]
Giotto DIDSY	10^{-20}	10^{14}	0.1	[McDonnell et al., 1986]
VeGa 1,2 PUMA	10^{-20}	10^6	0.0005	[Kissel et al., 1986]
VeGa 1,2 DUCMA	10^{14}	10^3	0.0075	[Perkins et al., 1985]
VeGa 1,2 SP1	2×10^{-18}	10^5	0.0081	[Göller et al., 1987]
VeGa 1,2 SP2	1×10^{-14}	10^8	0.05	[Sagdeev et al., 1985]
Hiten	2×10^{-18}	10^4	0.01	[Igenbergs et al., 1991]
Ulysses	2×10^{-18}	10^6	0.10	[Grün et al., 1992a]
Galileo	2×10^{-18}	10^6	0.10	[Grün et al., 1992b]
Stardust CIDA	2×10^{-18}	10^4	0.01	[Kissel et al., 2004]
Stardust DFMI	10^{-15}	10^6	var.	[McDonnell et al., 2000]
Nozomi	2×10^{-18}	10^6	0.01	[Igenbergs et al., 1998]
Cassini DA	5×10^{-19}	10^6	0.1	[Srama et al., 2004a]
Cassini HRD	3×10^{-16}	10^4	0.006	[Srama et al., 2004a]
New Horizons	1×10^{-15}	10^5	0.1	[Horanyi et al., 2009]
Bepi Colombo	TBD	TBD	0.01	[Nogami et al., 2009]

Determine dust and meteoroid distribution both, in the vicinity of the rings and in interplanetary space.

Icy satellites Define the role of meteoroid impacts as mechanism of surface modifications. Obtain information on the chemical composition of satellites from the analysis of gravitationally bound ejecta particles in the vicinity of the satellites (within Hill spheres). Investigate interactions with the ring system and determine the importance of the various satellites as a source for ring particles.

Magnetosphere of Saturn Determine the role that dust plays as source and sink of charged particles in the magnetosphere. Search for electromagnetically dominated dust (small particles) and for dust streams.

2.1 Field of View and Pointing

The stated objectives of this investigation require a versatile instrument consisting of several components which are optimised individually for different tasks. Therefore the detection of dust particle impacts is accomplished by two different methods: (1) a High Rate Detector subsystem (HRD), using two separate polyvinylidene fluoride (PVDF) sensors, for the determination of high impact rates during saturnian ring plane crossings and (2) a Dust Analyser (DA) using impact ionisation. The DA measures the electric charge carried by dust particles, the velocity vector, the mass and the chemical composition, whereas the High Rate Detector is capable of determining particle mass for particles with a known speed. The DA itself consists of three subsystems, the charge detector (entrance grids), the IID and the Chemical Analyser [Srama et al., 2004a]. The Chemical Analyser was developed by the Univ. of Kent, Canterbury, U. K., under the leadership of J. A. M. McDonnell (now at Open Univ.).

The general purpose of this instrument is to map the whole hemisphere with its field-of-view. On Galileo, this was achieved with the wide aperture of $\pm 70^\circ$ degree and a mounting of the instrument by 55 degrees with respect to the Galileo spin axis. Originally the Cassini-Huygens design included a continuously rotating pointing platform for the fields and particles instruments which was canceled during a descoping process in order to limit the spacecraft costs. Although the CDA instrument was mounted nearly perpendicular to the Cassini spin axis (Fig. 2.1), wide coverage cannot be obtained with a mainly 3-axis stabilised spacecraft. Furthermore, the rotation rate of Cassini is restricted to the maximum value of $0.26^\circ \text{ s}^{-1}$ and, during high activity periods, other instruments determine the orientation of the spacecraft. All these constraints lead to a redesign of the instrument and a turntable was added at the interface to the spacecraft.

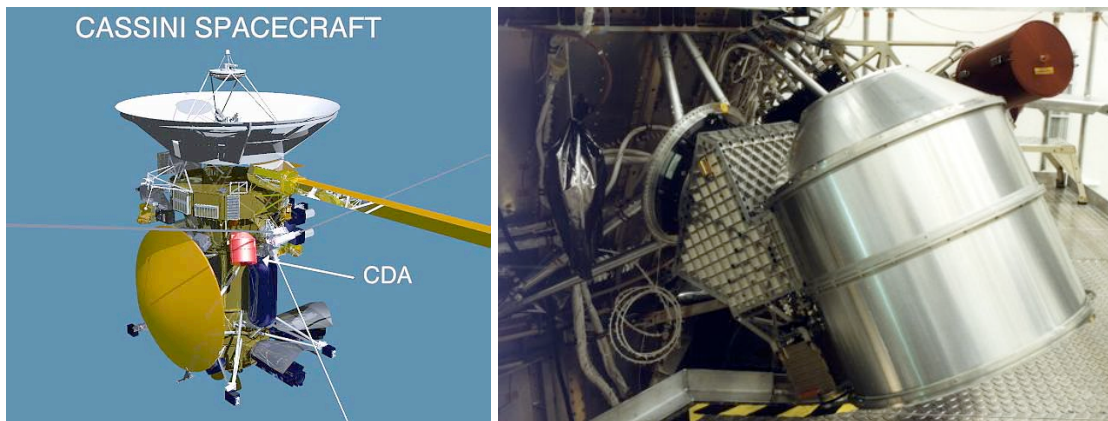


Figure 2.1: The Cassini/Huygens spacecraft (left, NASA/JPL) and the Cosmic Dust Analyser mounted at the spacecraft bus (right).

The mounting vector of the turntable points 15 degrees below the spacecraft x-y plane (Fig. 2.2). Furthermore, this vector points 30 degrees away from the +y-axis towards -x. The co-

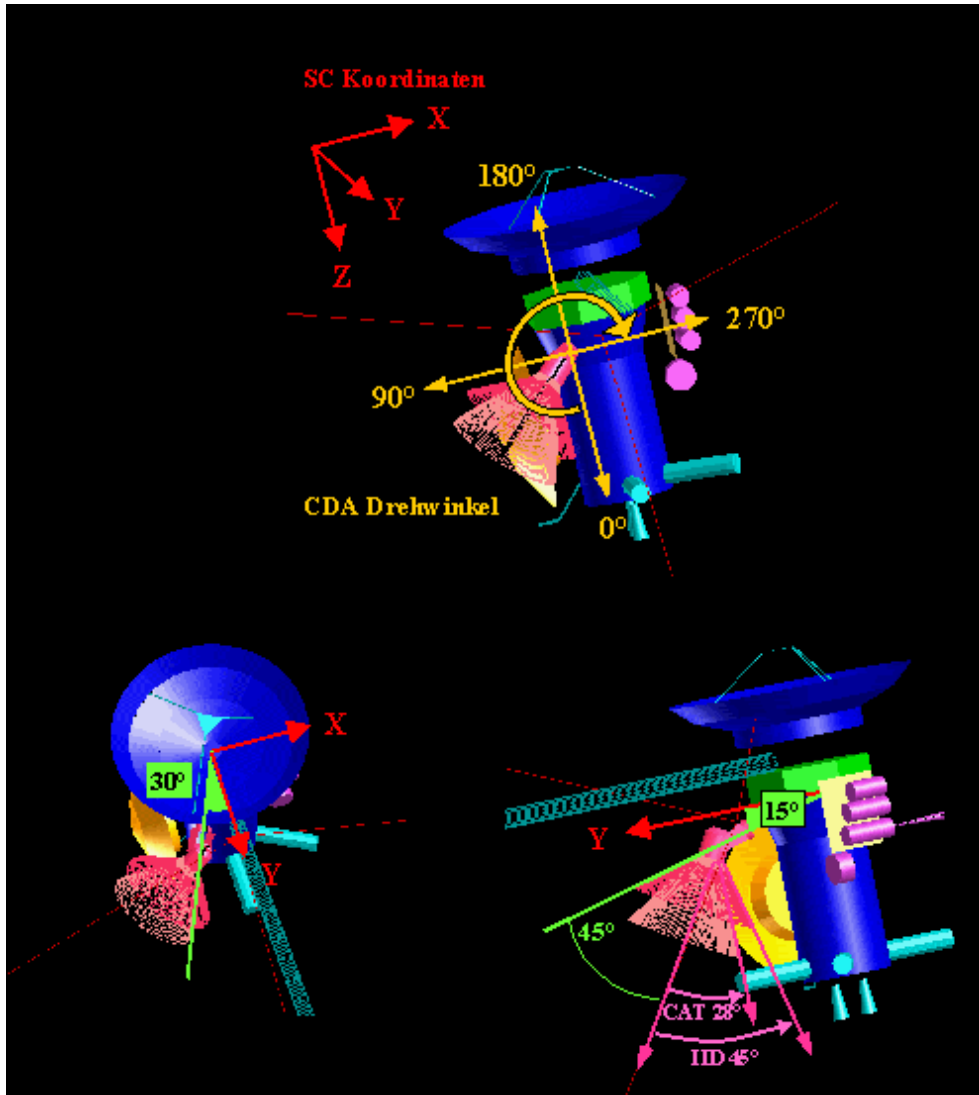


Figure 2.2: Coordinate system of Cassini and mounting of the CDA instrument. The articulation angle of CDA is defined as shown in the top image. The zero degree position of CDA corresponds to the main engine direction. An angle of 90° is compatible with the $-X$ direction which allows combined measurements with the INMS instrument.

ordinates of the articulation axis with respect to the spacecraft x-y-z coordinate system are $(-0.483; 0.837; 0.259)$. The Dust Analyser detectors (IID, CAT and HRD) are mounted at 45° with respect to the articulation axis. The boresight vector of the field-of-view has the coordinates $(-0.250; 0.433; 0.866)$ in the launch position (0° position, downwards to $+z$). The turntable enables the instrument to rotate by 270 degrees. The cable wrap drum inside the turntable does not allow a full revolution. The "lower right" quarter of the full circle cannot be reached by the instrument. The spacecraft coordinate system is such that the x-y plane is perpendicular to the spacecraft spin axis z. The $+z$ direction points to the main engine, whereas the Huygens probe points towards $-x$. Besides the high gain antenna (which points towards

-z), Cassini-Huygens has two low gain antennas (LGA). LGA 1 points towards the -z direction whereas LGA 2 points towards the Huygens probe (-x-axis). During the inner cruise, the 3-axis stabilised spacecraft has an orientation such that the high gain antenna points towards the Sun and the selected low gain antenna points towards the Earth as precisely as possible. Fig. 2.3 shows the field-of-view of the IIT for a variety of articulation angles in the spacecraft coordinate system.

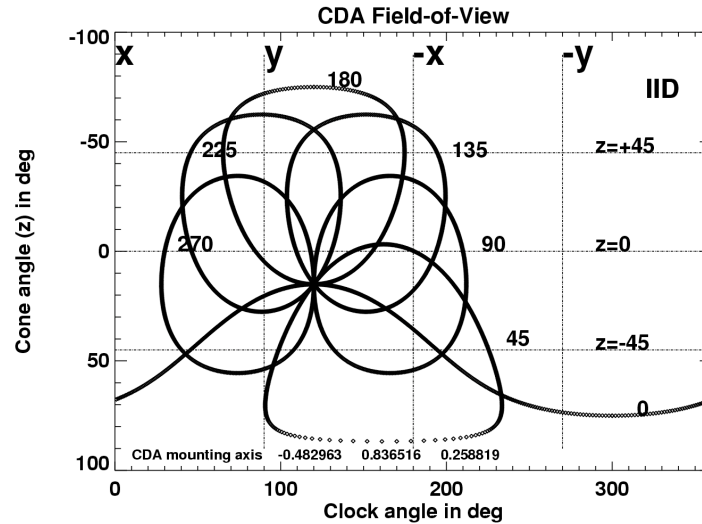


Figure 2.3: The field-of-view of the Impact Ionisation Target (IIT) for different articulation angles (0, 45, 90, 135, 180, 225 and 270) in the spacecraft coordinate system. The spacecraft axes are labeled at the top. The z-asymmetry is caused by the mounting of CDA 15° below the xy plane. The field-of-view of the CAT is $\pm 28^\circ$. The field-of-view of the IIT is $\pm 45^\circ$. The FOV of the CAT is published in Srama et al. [2004a].

2.2 General Description

The instrument consists of the sensor housing with its entrance grids, impact targets, the High Rate Detector [Srama et al., 2004a], the electronics box and the turntable (Fig. 2.4). The interior of the sensor housing was purged with dry nitrogen until launch in order to avoid any contamination of the sensitive multiplier and the rhodium target of the Chemical Analyser. A cover avoids contamination of the sensor targets until three weeks after launch. A redundant pyro device moves a lever which unlatches the cover, and preforced springs jettison the cover to a normal direction. All major parts were made of milled aluminum while a honeycomb structure provided the required stiffness for the cover and the cylindrical sensor housing. The preamplifier box is located directly above the main electronics and occupies a separate housing to keep the input cables as short as possible and to minimize any interference with the main electronics.

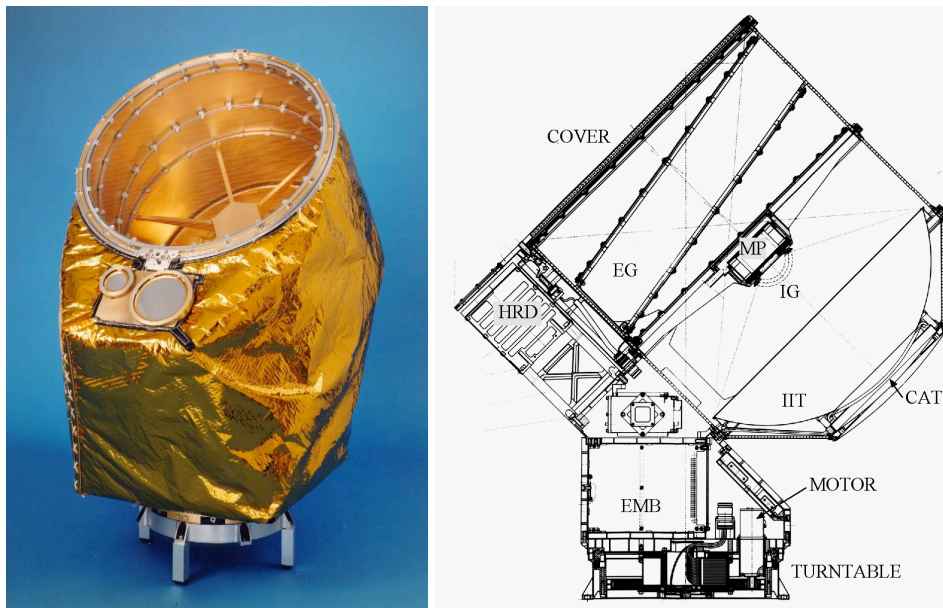


Figure 2.4: The Cosmic Dust Analyser (left: Lossen Foto GmbH).

The turntable of the instrument allows a rotation by 270° . The turn limit is given by the capability of the integrated cable wrap drum and the mechanical end stops. A design with two layers of plastic balls (PEEK) and a bearing diameter of 240 mm was selected and qualified. The torque necessary for the turn is provided by a Phytron ZSS32 stepper motor and a gear with a total gear ratio of approx. 1000:1. Special electronics were developed by Phytron to achieve very low power consumption and a maximum torque. The motor has a compensating pole configuration and a Mu-metal shielding to keep the stray magnetic fields as low as possible. The motor can be operated by four different motor currents between 150 and 300mA and consumes between 2 and 5 Watts. The turn speed of the platform can be set and is normally in the range of 7° per minute.

The grid system (EG) at the front end allows measurement of the dust charge and velocity [Auer et al., 2002]. This configuration is based on a method first described in Auer [1975]. The four grids are made of stainless steel and each of them has a transmission of 95%. The innermost and outermost of the four grids are grounded, the other two grids are connected to a charge sensitive amplifier. A charged dust particle entering the sensor will induce a signal which corresponds directly to the charge of the particle [Srama et al., 2004a, Kempf et al., 2004]. When the dust particle is far away from the sensor walls, all field lines are ending on the grids and the error in charge measurement is small. The output voltage of the amplifier will rise until the particle passes the second grid (Fig. 2.5). As long as the particle is located between the second and third grid the output voltage remains more or less constant. As soon as the dust particle has passed the third grid, the voltage begins to fall until the fourth grid is passed. The distance of the fourth grid from the first grid, divided by the duration of the charge signal is equal to the particle's velocity component normal to these grids. Due to the

inclination of 9° for the inner two grids, the path length between the grids depends on the angle of incidence, and allows a determination of the directionality of the incident particle in one plane. The choice of 9° is a compromise between angular resolution and tube length of the detector. The larger the angle the better the angular resolution, but the bigger and heavier the instrument. The detection of particle charges as low as 10^{-15} C has been achieved although the grid capacitance is high (≈ 200 pF). The speed obtained by the entrance grid system is used to verify and calibrate the indirect determination of particle speed based on the rise times of the impact ionisation signals.

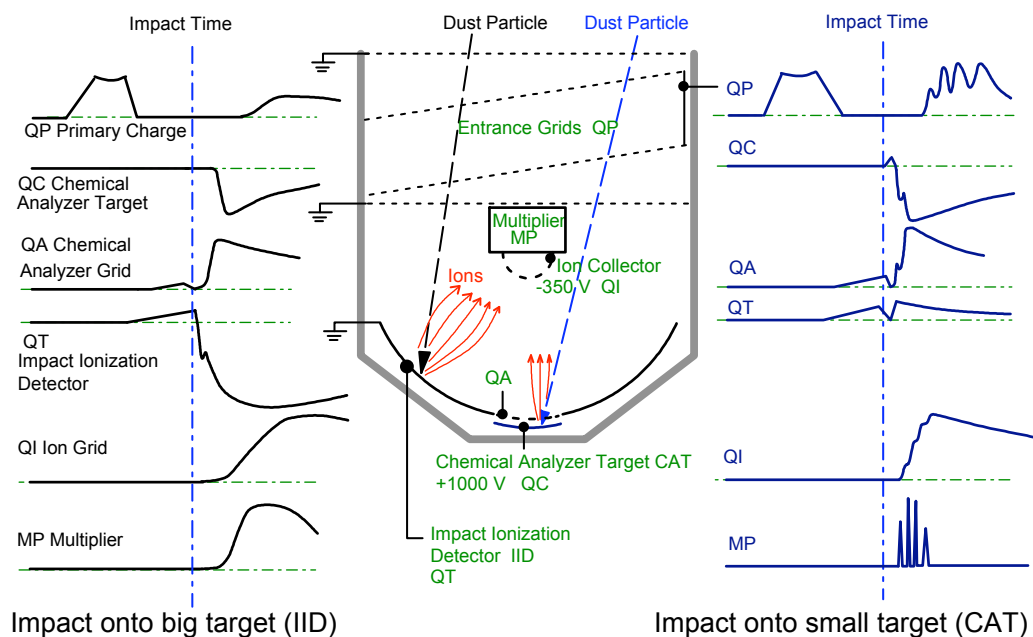


Figure 2.5: Cross section of the instrument and impact signals of the two target locations. Left: Signals of IID impacts. Right: Signals of CAT impacts with a time-of-flight mass spectrum at the multiplier channel.

A particle can impact either on the big gold plated Impact Ionisation Target (IIT, 40 cm diameter) or the small rhodium Chemical Analyzer Target (CAT, a 16 cm diameter plate with a thickness of 0.3 mm). In both cases the impact physics is the same: The impact produces particle and target fragments (ejecta), neutral atoms, ions and electrons (impact plasma). An electric field separates electrons (collected by the targets) and ions (collected by the ion grid). Charge sensitive amplifiers collect the charges at the various targets and grids. Amplifiers are connected at the Chemical Analyzer Target (QC), the Chemical Analyser Grid (QA), the Impact Ionisation Target (QT), the Ion Grid (QI), the Entrance Grids (QP), the Multiplier Anode (QMA) and the Multiplier Dynodes (DLA). In order to increase the dynamic range, the amplifiers for QC, QT and QI are working with two measurement ranges.

The signals at the output of the electron multiplier must cover an exceptionally large dynamic range for two reasons. A wide dynamic range is required for measurement of a large range of ion abundances for any one impact, but, more importantly, a wide dynamic range is needed to make chemical analysis measurements over the desired six orders of magnitude in range of particle masses impacting the system. Because of the random nature of the impact events and the short ion time-of-flight, it is clearly impossible to make real time gain changes for each event. Ordinary logarithmic amplifiers are not fast enough and do not have sufficient dynamic range for the time-of-flight measurements. An innovative solution to this problem has been created through the development of the Dynode Logarithmic Amplifier (DLA). This system sums the linear signals from six different dynodes of the Johnston MM-1 multiplier in such a way that for large impacts the amplifiers for highest gain dynodes produce fixed (saturated) outputs that sum with an unsaturated low gain dynode signal. Thus it is a fast, low-noise, piece-wise linear approximation to true logarithmic performance. This special electronics was developed by the Rutherford Appleton Laboratory, U.K. (RAL) and the Univ. Wuppertal (Prof. A. Glasmachers). The main electronics was developed by MPIK whereas the mechanical design was done by G. Pahl (Munich). The CDA mechanics manufacturing and space environmental tests were carried out by DLR Berlin (F. Lura). The Chemical Analyser was developed under the supervision of Open University, U.K. (J. A. M. McDonnell, S. Green, J. Hillier).

The integrated Chemical Analyser consists of the Chemical Analyzer Target, the Chemical Analyzer Grid (68% transmission) and the multiplier. The Chemical Analyser Grid is located 3 mm in front of the target and electrically grounded, whereas the target is set to a potential of +1000 V. The strong electric field between target and grid separates the impact charges very quickly and accelerates the ions towards the multiplier. The curved shape of the target and grid provides a better focusing of the ions onto the multiplier. This time-of-flight mass spectrometer has a flight path length of 230 mm and gives information about the elemental composition of the micrometeoroids [Hillier et al., 2006, Kempf et al., 2005b]. The functional block diagram of CDA can be found in section A.2

2.3 Software

All the outputs of the amplifiers are continuously compared with a channel-specific reference value (threshold). If one threshold is exceeded, an event trigger is released. Starting with the trigger time, the sampling frequencies for the QC, QT, QI channels and the DLA are increased and the signals are digitised and stored in memory. The data processing by the 6 MHz MA31750 microprocessor system includes the calculation of signal rise times, amplitudes and integrals. A wavelet algorithm allows signal smoothing and a lossy compression. A lossless RICE compression algorithm can reduce the raw data by a factor of three. Approximately 1500 bytes are necessary for the lossless storage of one data frame. The data processing time limits the dead time of the instrument to one second. The calculated signal parameters are used for onboard data classification. Each event increases the value of one of twenty counter values. About half of the instrument memory is needed for the execution of the onboard software. The remaining memory is used to store event data. The classification and prioritisation

of detected events is a very complex procedure and is still subject to changes. The onboard program was written in ADA using a TARTAN development system (KCS GmbH and Univ. Mannheim/Helfert Informatik). The TARTAN compiler runs under a VMS operating system which is emulated under Linux. Onboard data processing algorithms were developed by V. Tschernjowski (DLR Berlin, QP signal detection) and G. Schlotzhauer (DLR Berlin, wavelet compression).

The signals of the channels QP, QC, QT, QI and MP are digitized with 8 bit resolution and are stored in a raw data frame. Typical impact signals are shown in Fig. 2.5. The sampling frequency is different for the various channels and the sampling frequency alters even within one channel: The channels QC, QT and QI are digitised continuously with 0.375 MHz until an event is detected by exceeding the specified thresholds. After this trigger the sampling frequencies are increased to 6 MHz (QC and QI) and 3 MHz (QT), respectively. The last 16 samples preceding the trigger are stored together with the following sampling points. This preserves the signal shape before the impact is detected by the electronics and allows a later reconstruction of the entire slope. Signals with slow rise times benefit especially from this system since otherwise the first part of the signal would be missing and the determination of the rise time would be impossible. The sampling frequency of 375 kHz is a compromise between acceptable time resolution and low power consumption.

An event causes an instrument dead time of one second to allow for complex data processing. The major software processing steps are shown in Fig. 2.6 and are listed below:

1. Buffer read-out of channels QC, QP, QI, QT, DLA
2. Integer wavelet transformation of signal channels
 - Set small coefficients to zero (leads to a smooth curve after reverse transformation)
 - Reverse transformation with most significant coefficients
3. Determination of peaks, rise times, amplitudes and times at 50% of the full amplitude
4. Classification of the event and increment the appropriate counter by 1
5. Further compression of the already wavelet transformed data by a RICE compression algorithm.
6. Enable the event trigger and awaiting the next impact

The information from step 3 will be used to identify the impact location (big or small target) and to classify the event as good, poor or noise in order to increase the appropriate counter. Wall impacts occur as abundant as IIT impacts (Fig. 2.7) and the onboard signal classification eliminates about 90% of such signals by analysing the signals of the target, the ion grid and, especially the entrance grid signals.

The chosen integer reversible wavelet transformation provides an almost lossless tool to smooth and reduce the data without losing the original signal shape and height.

Twenty counters provide a characterisation in size, speed and impact location. Each counter has 16 bits and the counters are merged in four priority groups. The priorities will be used to give memory readout guidelines by command to the instrument. All these efforts have only the goal to compress the data. The highest compression level is given by the contents of the 20 counters¹; The next compression level are the extracted data of rise times and amplitudes;

¹the number of counters changed with the flight software version

The lowest compression level are the wavelet treated sampling curves of an event. In order to adjust the memory readout data rate to the spacecraft storage capabilities and telemetry modes, a special data frame was developed which allows a readout of selected information. Therefore it will be possible to readout e.g. only counter-data together with the multiplier raw data. It is clear that ancillary data such as impact time and spacecraft boresight information belong to each data frame. Further capabilities are to put science data in housekeeping data frames and vice versa. This gives the CDA instrument further flexibilities for spacecraft downlink capabilities of 40 bps and lower as they occurred between launch and summer 2000. However, such low data rates did not occur after the year 2000.

The standard software version 10.0 has a dead time of 1.0 seconds, which limits the number of compositional measurements during fast ring plane crossings or moon flybys. Therefore a special flight software was developed for high-rate mass spectra recordings like e.g. Enceladus plume crossings. Here the buffer readout and data processing was constrained to the multiplier channel only, saving hundreds of milliseconds of readout and processing time (Fig. 2.6). Furthermore, a self-developed simple peak detection algorithm analyses the multiplier raw data and only signals containing peaks (mass spectra) are saved in memory. The event recording dead time of this scheme is approximately 12 ms (no mass lines found) or 100 ms (mass spectrum), respectively. This recording scheme was applied during Enceladus plume crossings in 2008 and Fig. 2.8 shows the time difference between recorded events.

2.4 Sensitivity

A computer simulation program was used to calculate the geometric detection probability of the sensors. Under the condition of an isotropic flux of particles with an incidence angle θ the sensitive area of the Impact Ionisation Target and the Chemical Analyser Target were calculated. The result is shown in Fig. 2.9. The calculations clearly show the decrease of sensitivity for increasing incidence angles. The Chemical Analyser Target does not detect any impacts with incidence angles larger than 28° and the Impact Ionisation Target has a limit of 45° . These limits are due to the shielding by the side walls of the detector cone. The calculations have taken the obscuration of the multiplier housing and struts into account. Therefore, the sensitivity of the Chemical Analyser Target is not maximal for normal incidence ($\theta = 0^\circ$). The IID curve is based on a \cos^4 function, whereas the CAT sensitivity can be described by a \cos^3 function for angles larger than 15° . Caused by the axial symmetry, the solid angle interval is $d\Omega = 2\pi \sin(\theta) d\theta$. The relative sensitivity $I(\theta)$ is therefore given by Eq. 2.1.

$$I(\theta) = d\Omega = 2\pi \sin(\theta) d\theta \frac{A(\theta)}{A(\theta = 0)} \quad (2.1)$$

An integration of this function leads to the effective solid angle interval covered by the detector which is 0.473 sr for the Chemical Analyser and 0.591 sr for the Impact Ionisation Detector (Tab. 2.2).

Table 2.2: Solid angle of the CDA subsystems and the Galileo Dust Detector System.

Subsystem	Aperture in \pm degree	Solid angle in sr
IID	45	0.59
CAT	28	0.47
HRD	88	≈ 3
Galileo DSS	70	1.45

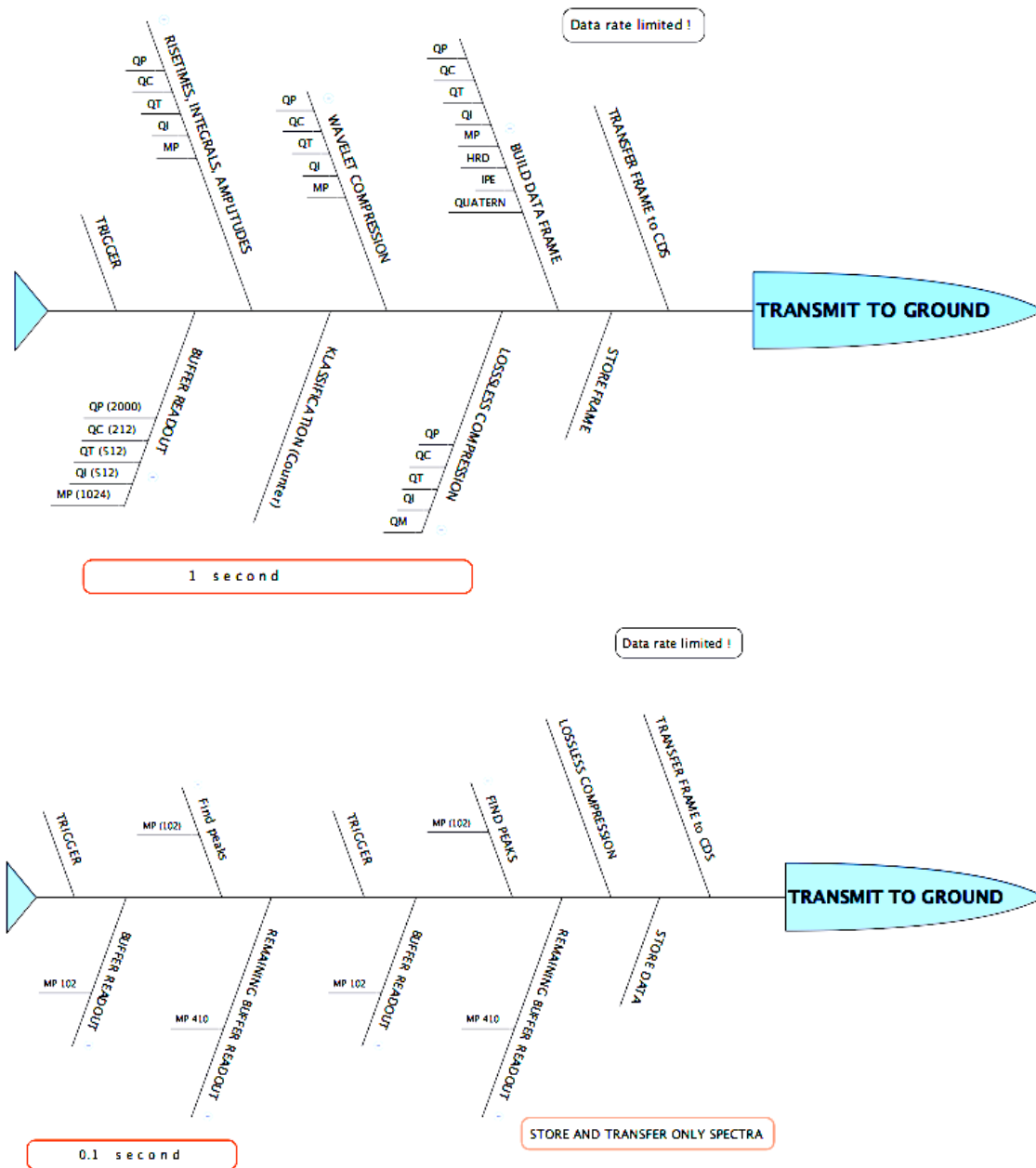


Figure 2.6: Flight Software processing scheme of flight software version 10.0 (top) and version 12.2 (bottom). The version 12.2 limits the signal recording to the multiplier channel for a fast mass spectra recording. By this limited processing, the dead time was reduced to less than 100 ms in contrast to the former dead time of one second.

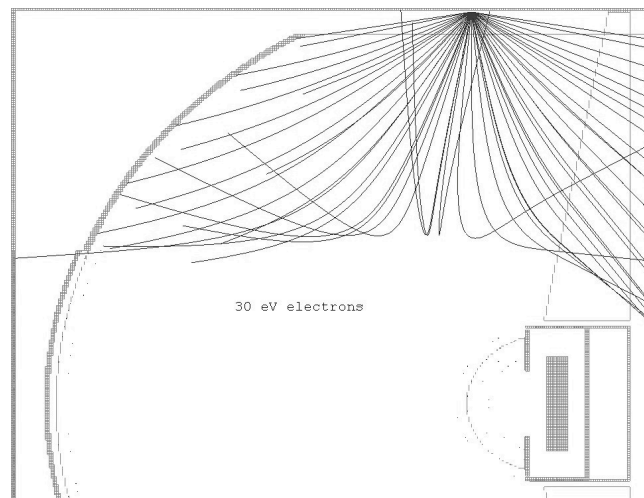


Figure 2.7: Simulated electron trajectories of charges generated by a wall impact (courtesy E. Grün).

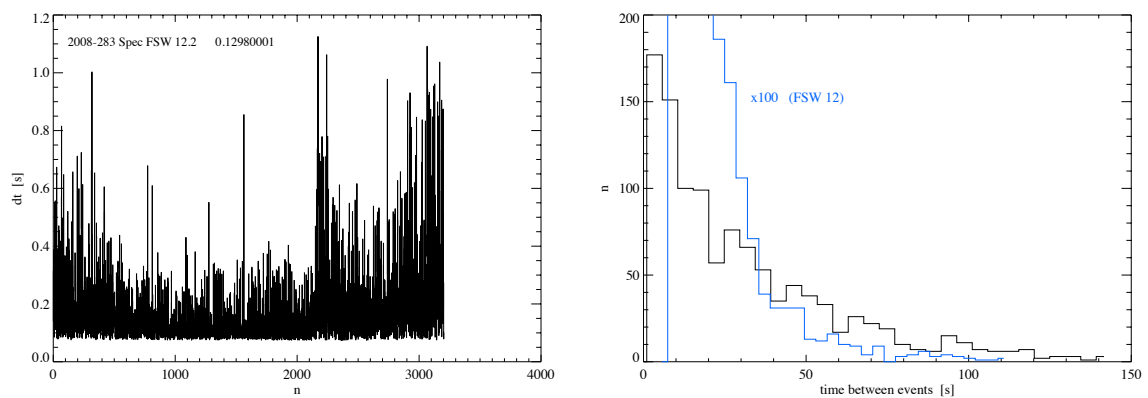


Figure 2.8: Time difference between event triggers using the new flight software version 12.2 (left). The time difference refers to impacts onto the CAT showing a mass spectrum. The minimum dead time is approximately 100 ms. The right histogram compares the two flight software versions 10.0 and 12.2. The dead time of the software version 12.2 is much smaller and the time axis was stretched by a factor of 100 (blue curve).

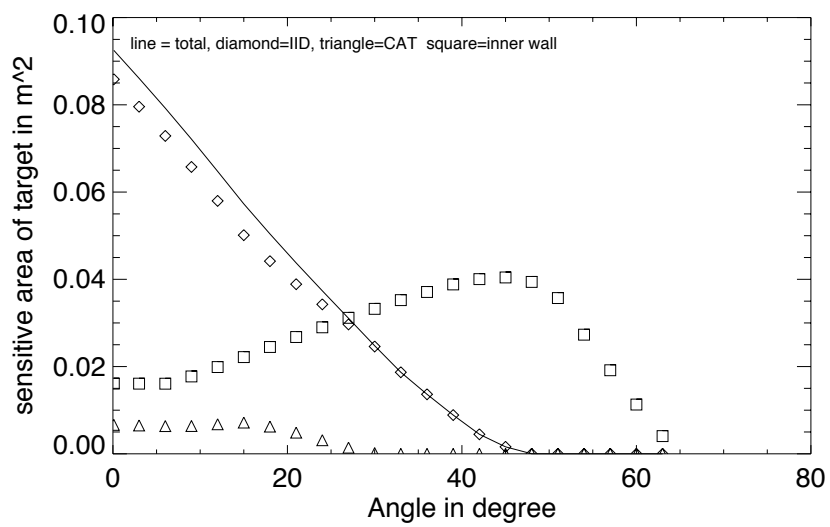


Figure 2.9: Sensitive area of the big IIT (\diamond), the CAT (\triangle) and the inner housing (\square).

3 Cosmic Dust Analyser Performance

3.1 Amplifier Switching and Signal Deconvolution

The preamplifiers of the three main signal channels QC, QT and QI were required to have a very wide dynamics. The impact charge generated by a dust impact varies from fC to nC, which represents a dynamic range of six orders of magnitude and the ADC converts the signal with a resolution of 8 bits. No common amplifier is capable to perform such a measurement and two measures were taken to fulfill the requirements: First, the amplifier switches its measurement range from a sensitive state to an insensitive state automatically if the signal exceeds a certain threshold. The second method is the means of a logarithmic amplifier which was described in Srama [2000b]. However, the shape of the raw data of a switched signal become rather discontinuous and the signal has to be reconstructed to evaluate the rise time and amplitude properly. The rise times are used to calibrate the particle impact and are therefore essential.

In order to calibrate the signal reconstruction, trapezoid shaped pulses were entered at the amplifier inputs using different rise times (between 5 and 70 μs) and different amplitudes (1 pC to 1 nC). For this purpose capacitors with 10 and 100 pF and voltage amplitudes between 0.1 and 10 V were used. The raw signal output is shown as the dashed blue line in Fig. 3.2. Two slow signals (left) and two fast signals (right) are shown. The upper signals have higher amplitudes than the lower two plots. Generally, the reconstruction is more critical for smaller signals, and a procedure was found to accomplish a rather smooth rising flank. However, the reconstruction has limits and the signal shape varies with impact charge and speed. Fast and/or large impacts show a strong pre-peak in the target electron signal [Stübig, 2002, Ratcliff et al., 1997] which cannot be reconstructed properly anymore. A signal with a leading peak in the target signal QT is shown in Fig. 3.1. The pre-peak is highly variable in its amplitude. Fig. 3.3 shows the impact signals of an E-ring particle impacting with $\approx 6 \text{ km s}^{-1}$. The target charge (QT) was so strong that the amplifier switched to the insensitive range and the reconstructed curve has a small slowly leading segment (curve recorded in the sensitive range) after the reconstruction.

The reconstructed signals show an exponential decay although the input signal was a trapezoid with a constant voltage after the rise. The decay (Fig. 3.2) is caused by the RC component of the charge sensitive amplifier. For an accurate signal reconstruction and interpretation, the signals would have to be deconvolved before rise times and amplitudes are determined. A deconvolution would lead to higher amplitudes and steeper rise times. The upper right plot shows a signal QI with an amplitude of $4.4 \cdot 10^{-10} \text{ C}$, although the input charge was almost $1 \cdot 10^{-9} \text{ C}$ (a rise time of 35 μs was used). Even very short rise times of 5 μs lead to amplitudes not higher than $6.1 \cdot 10^{-10} \text{ C}$. There is a second process decreasing the final measured

3 Cosmic Dust Analyser Performance

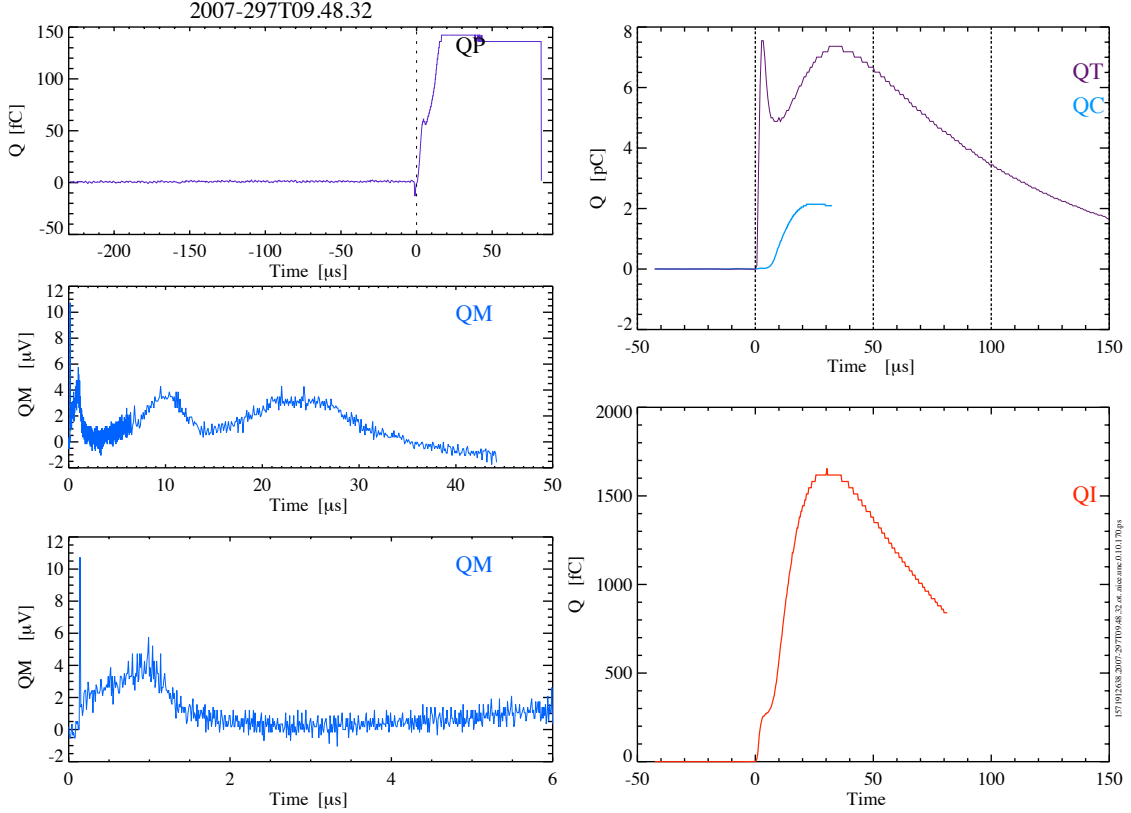


Figure 3.1: Common charge signals of an IID impact with a relative impact speed of approx. 5.6 km s^{-1} at a distance of $4 R_S$ and an altitude of -19000 km below the ring plane. The electron signal QT reveals the leading peak of the primary ionisation. The later broad maximum is caused by the impact of secondary ejecta.

amplitude: Due to the reload of the larger capacitance of the charge sensitive amplifier in the insensitive channel, charge is “lost” and a step in the reconstructed signal shape occurs. For the signal reconstruction and deconvolution we use the fact, that a convolution is a multiplication in Fourier-space. First, the convolution of the functions $f_1(t)$ and $f_2(t)$ is defined as:

$$(f_1 * f_2)(t) = \int_{-\infty}^{+\infty} f_1(u) f_2(t - u) du$$

with the time t , and the functions $f_1(t)$ and $f_2(t)$. In our case, $f_1(t)$ is the unknown original signal and $f_2(t)$ is the impulse response function of the form e^{-at} defined below (decay of signal with time constant). Then, we achieve the original signal by using the convolution rule

$$F[f_1 * f_2](t) = F[f_1(t)] \cdot F[f_2(t)] \quad (3.1)$$

3.1 Amplifier Switching and Signal Deconvolution

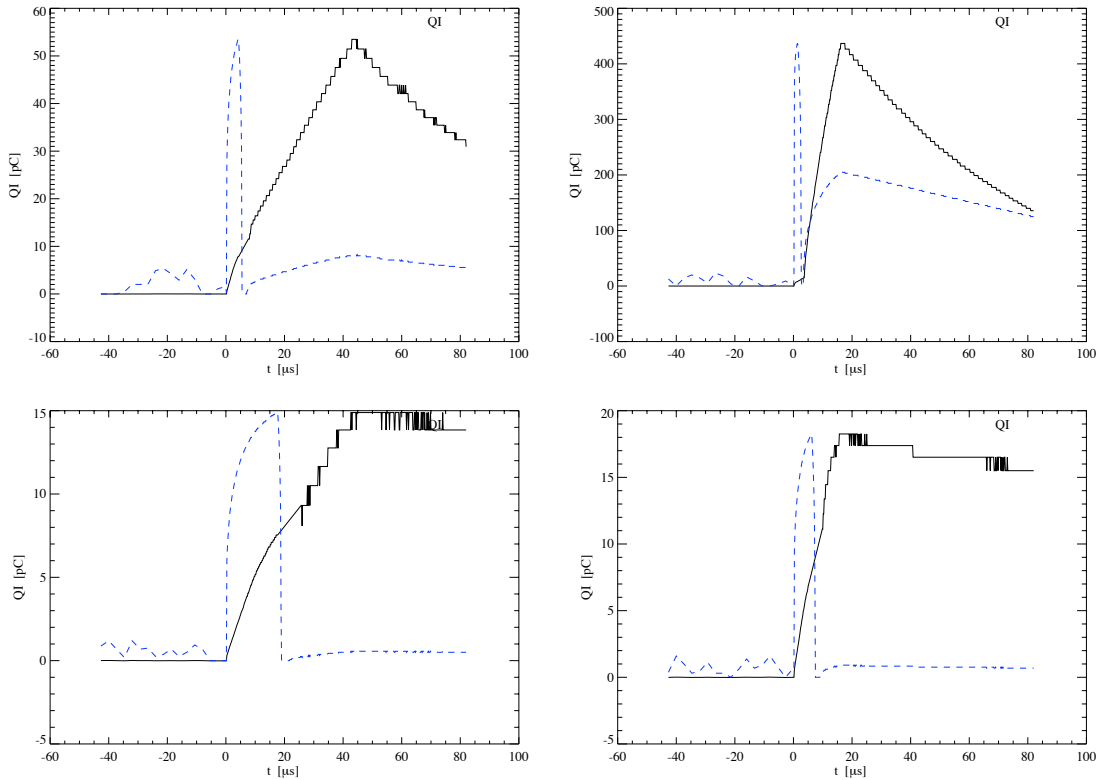


Figure 3.2: Amplifier switch correction of QI channel signals. The original signal used was a trapezoid shaped signal (blue dashed line). The reconstructed signals are shown by the black continuous line. The tests were performed on January 10, 2008. A trapezoidal shaped signal was used which is well reconstructed.

This allows us to achieve the reconstructed original signal curve $f_1(t)$ simply with

$$F[f_1(t)] = \frac{F[f_1 * f_2](t)}{F[f_2(t)]} \quad (3.2)$$

since $F[f_1 * f_2](t)$ is nothing else than our measured signal (`s_falt`). In the following IDL¹ code example, `signal_org` is the deconvolved signal and `filter` the function f_2 :

```

filter = a0 + a1*ea2*t
fft_sig = FFT(s_falt, /Double)
fft_fil = FFT(filter, /Double)
signal_org = FFT(fft_sig/fft_fil, /INVERSE, /double)
signal_org_r = DOUBLE(signal_org) ;take only real part
fourier_faktor = (MAX(s_falt))/(MAX(signal_org_r)) ;normalize
signal_org_r = signal_org_r > 0 ;take only positive values
signal_org = fourier_faktor * signal_org_r

```

¹Interactive Data Language

3 Cosmic Dust Analyser Performance

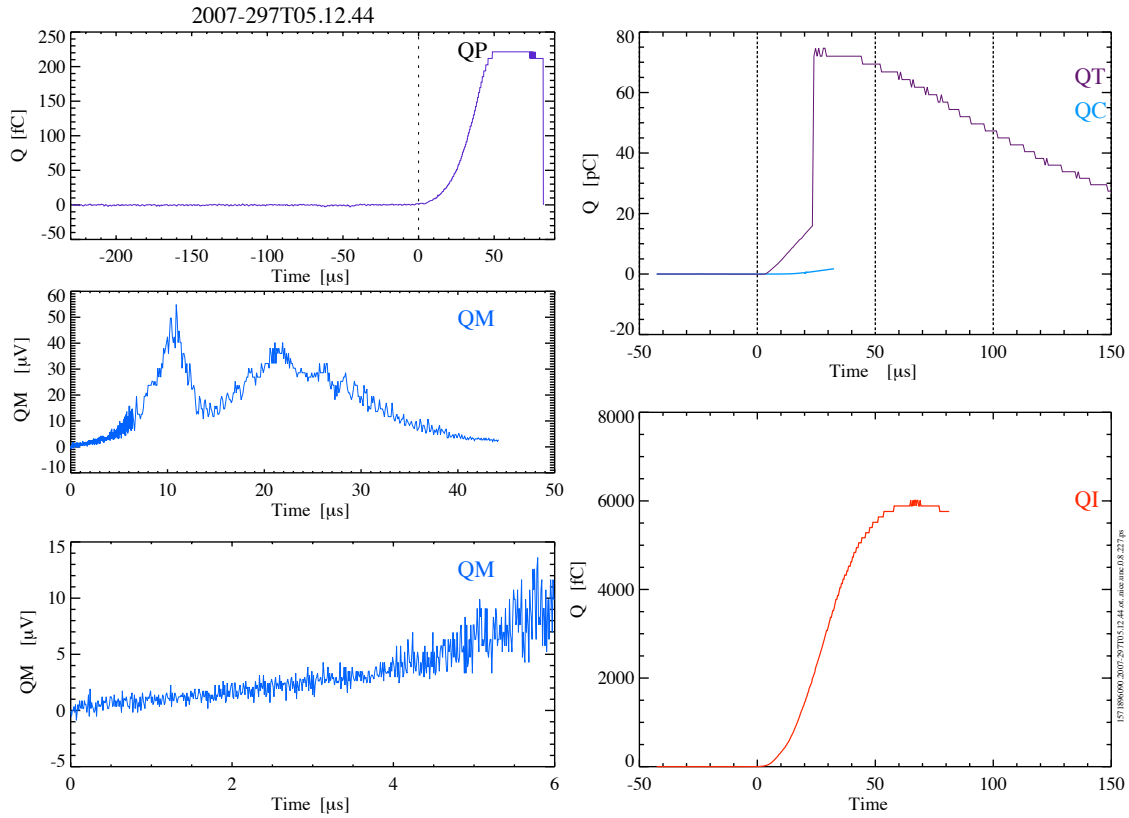


Figure 3.3: Impact signal of a dust grain at a saturnian distance of $4.3 R_S$ and a latitude of 0.3° (1290 km altitude). Although Cassini had a speed of 16.5 km s^{-1} , the relative keplerian impact speed was only 6.3 km s^{-1} . The impact occurred at the IID and the target signal QT switched to the insensitive range. The diagram shows the reconstructed QT signal.

Examples of deconvolved signals are shown in Fig. 3.4 and Fig. 3.5. At the first glance, deconvolved signals look similar to derived signals, but a direct comparison shows totally different curves. In general, the ion grid signal should show the different slopes related to the maxima of the multiplier signal. However, IID impacts show only seldom a fine structure in the rising flank of the QI signal.

The exponential decay was fitted using the general function $Q = Q_0 \cdot e^{-\frac{t}{RC}}$ representing the discharging of a capacitor C over a resistor R (flight spare instrument). The time t has the unit of seconds.

$$Q = A_0 + A_1 \cdot e^{A_2 t} \quad \text{with} \quad A_2 = \frac{t_{\frac{1}{2}}}{\ln(\frac{1}{2})} \quad \text{or} \quad t_{\frac{1}{2}} = \frac{-\ln(2)}{A_2} \quad (3.3)$$

$$F(q^{(QC)}) = 99.7 + 70.5 \cdot e^{-39216 \cdot t} \quad \text{and} \quad t_{\frac{1}{2}} = 1.77 \cdot 10^{-5} \quad (3.4)$$

$$F(q^{(QT)}) = -55.4 + 255.3 \cdot e^{-7281 \cdot t} \quad \text{and} \quad t_{\frac{1}{2}} = 9.5 \cdot 10^{-5} \quad (3.5)$$

$$F(q^{(QI)}) = -12.8 + 239.7 \cdot e^{-16438 \cdot t} \quad \text{and} \quad t_{\frac{1}{2}} = 4.2 \cdot 10^{-5} \quad (3.6)$$

For the evaluation of the data of the CDA **flight unit**, the signals have to be fitted as well and the values achieved for the flight model are slightly different:

$$F(q^{(QC)}) = 109 + 65.2 \cdot e^{-42254 \cdot t} \quad \text{and} \quad t_{\frac{1}{2}} = 16.4 \cdot 10^{-6} \quad (3.7)$$

$$F(q^{(QT)}) = -42.9 + 220.8 \cdot e^{-8670 \cdot t} \quad \text{and} \quad t_{\frac{1}{2}} = 80 \cdot 10^{-6} \quad (3.8)$$

$$F(q^{(QI)}) = 0.54 + 97.5 \cdot e^{-18072 \cdot t} \quad \text{and} \quad t_{\frac{1}{2}} = 38 \cdot 10^{-6} \quad (3.9)$$

The exponential decay of the impact charge Q and its time constant τ is defined as $\tau = R \cdot C$ and $t_{\frac{1}{2}} = R \cdot C \cdot \ln(\frac{1}{2})$ and is identical for the sensitive and unsensitive range of the amplifiers. The signal decreases by 50% during the decay time $t_{\frac{1}{2}}$.

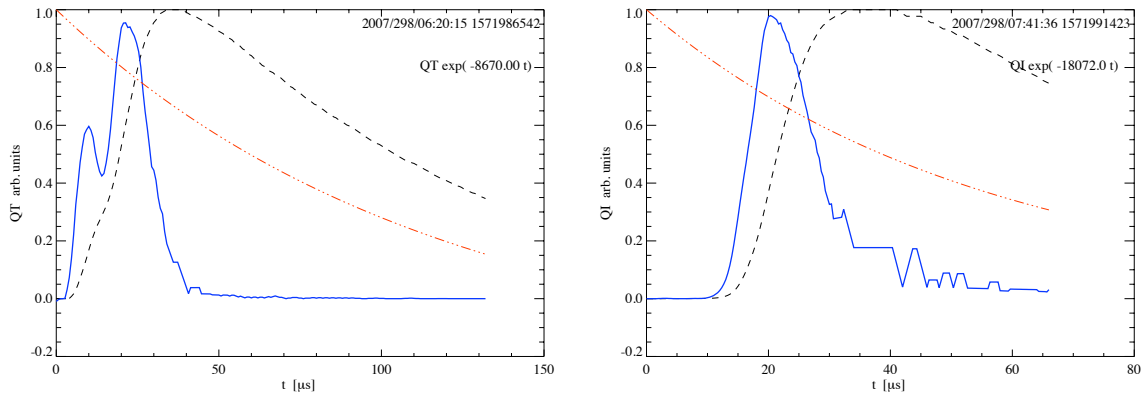


Figure 3.4: Left: The original QT signal (dashed black line) was deconvolved taking into account the time constant of the amplifier (thin red line). The real input signal (blue) shows a much stronger prepeak and a faster rise time. The deconvolved signal shows much more fine structure than the integrated raw signal. Here, the QT raw signal almost has no indication of a leading peak. The leading peak represents the electrons of the primary impact ionisation process whereas the later slow peak is caused by the secondary impact charges. Right: The deconvolved ion grid signal (blue) and the original QI charge signal as recorded by the amplifier. The original signals were already converted from digital numbers to Coulomb.

3 Cosmic Dust Analyser Performance

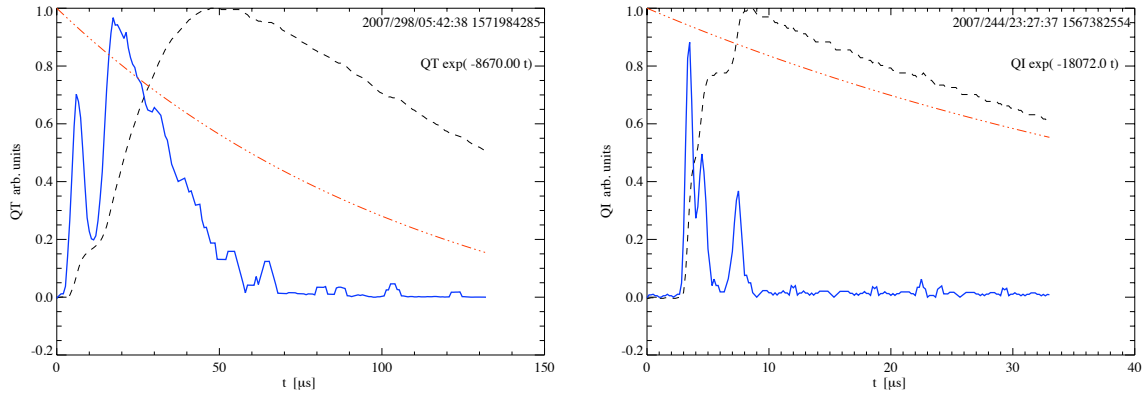


Figure 3.5: Left: Raw target signal QT of an IID impact (dashed) and its deconvolved signal (blue continuous line) with a strong prepeak. Right: Example of the deconvolved ion grid signal of a CAT impact. Mass spectra cause spikes on the ion grid channel which are related to the various ion species. The deconvolved signal reveals the peaks even clearer (right). The mass spectrum of this event is shown in 3.6.

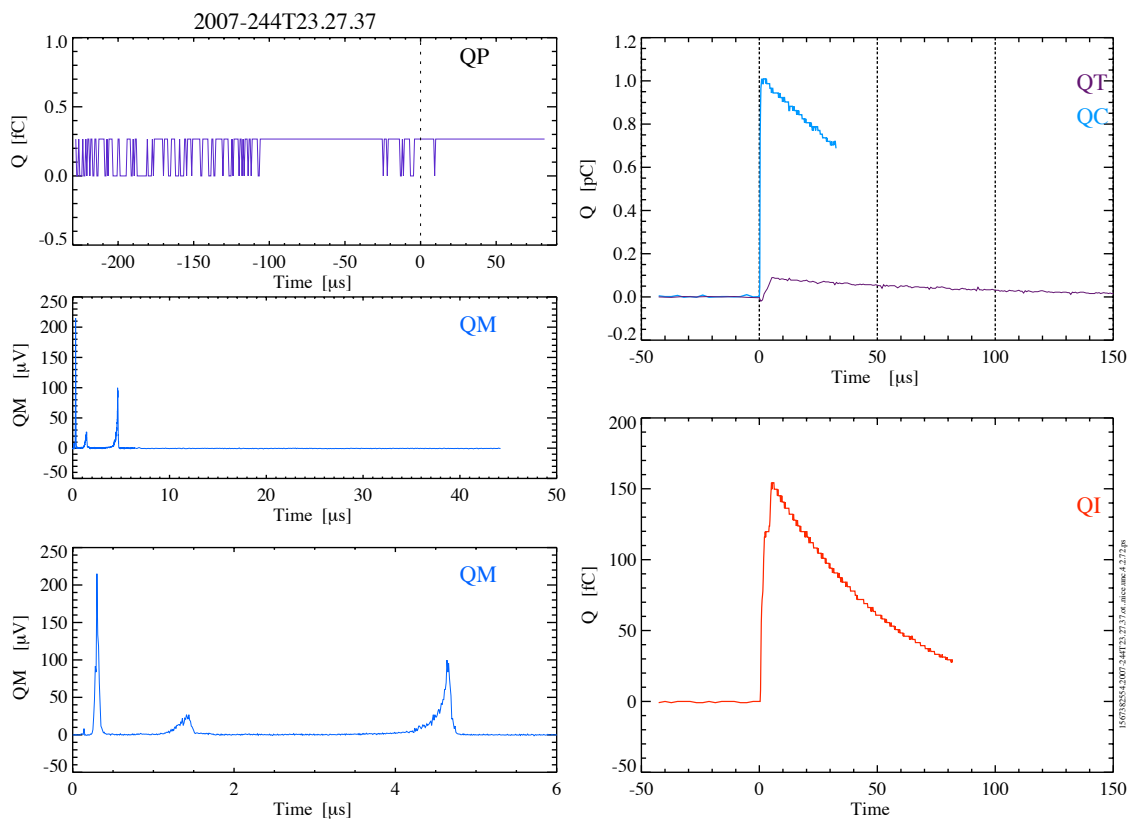


Figure 3.6: CAT impact with steps in the ion grid channel signal.

Unfortunately, the entire CDA calibration was based on raw data which were *not* deconvolved and we have to keep this in mind for future projects.

Another side effect of the amplifier switching is the introduction of noise into other channels (cross talk). The switching in channel QT generates spikes in the adjacent channels of QI and QC (the impact to channel QA was not investigated). The spike is positive in the case of QI (Fig. 3.7) and negative in the case of QC (not shown). The input of a 600 pC signal at QT produced a jump in the QI signal by 5 dn (corresponding to 3 fC). This behaviour is reproducible. Real flight data of the QC channel show a short breakdown (negative peak) during this phase which can have drops from 100 dn to 50 dn.

Generally, the signal reconstruction is difficult and a lossy process: Charge loss, unknown signal shapes and the signal decay are leading to uncertainties in the recovered wave forms. Fortunately, in flight large signals with switched amplitudes are seldom due to the high abundance of submicron grains in the entire saturnian system.

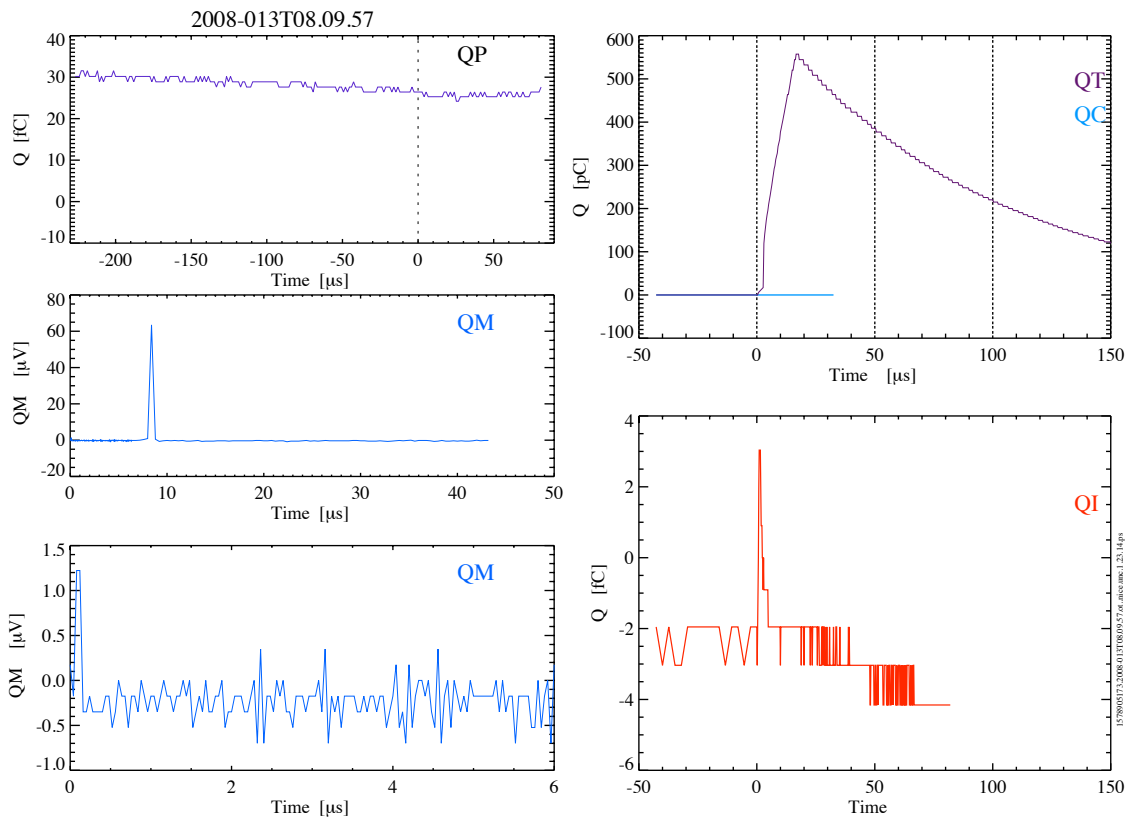


Figure 3.7: Electrical cross-talk from channel QT to channel QI during the switch of the QT amplifier. The QT amplifier switching generates a positive peak at the channel QI. The spikes in the channel QM are common and are related to other processes.

3.2 Time Variations and Classification Scheme

No calibration of an electronic system is stable in time. Time variations exist for all electronic components, even for simple devices like resistors, capacitors and transistors. Time variations are triggered by aging, thermal gradients and thermal variations, high-energy radiation, contamination or unique events which alter or degrade an existing system of mechanics and electronics. Such a system is the combination of the target electrodes of CDA (compare Fig. 2.5) and the consecutive electronics (an overview is shown in Fig. A.5).

By the evaluation of CDA counter data and the ratio between CAT and IIT impacts, discrepancies were found which triggered a deeper analysis of the automatically generated test pulses. The test pulses have basically five levels, each level relates to a certain charge value which is taken as an input for the charge sensitive preamplifiers of the target and grid channels. The absolute values of the charge levels are of no interest here, but the relative changes over time are significant. Fig. 3.8 shows the development of the charge levels (different colored symbols) for the both target channels QT and QC. For both channels two immediate changes (drop in amplification) were noticed: The channel QT test pulses changed in the time frames of between [2008-038T23:54:27 – 2008T039T19:52:23] and [2008-224T16:11:33 – 2008-239T09:23:44].

A more detailed analysis of the channel noise behaviour constrained the time windows further to [2008-039T14:13:55 – 2008-039T19:50:15] and [2008-224T18:30:00 – 2008-224T23:30:00] and the amplification drop factors are 195 and 22, respectively. This factor of 22 remained constant and is still applicable on day 2009-212. Although these values are rather high, they are only a small percentage of the overall dynamic range of 10^6 .

The second change around 2008-224² is a mitigation of the already occurred drop in amplification (healing), which is very unusual for already degraded components.

The second channel with an observed drop in amplification factor is the small target channel QC. This channel showed only one significant change (drop) by a factor of 140 in the time frame [2008-283T16:02:41 – 2008-283T21:31:02] and this factor remained stable until 2009-212³. Furthermore, a change of the acceleration grid channel QA was also noted (time range [2008-208 – 2008-261]). Since no raw data are available from this channel, the exact drop factor could not be determined. On the other hand, the ion grid channel QI and the multiplier channel QM are unaffected.

The suspected degraded electronic device was considered to be the FET at the front end of the charge sensitive amplifier. But healing effects of FET devices were unlikely under the flown environmental conditions. It is assumed that the high gas and dust densities with its high and frequent impact charges have directly or indirectly changed the amplification factors. The

²A ring plane crossing occurred at 2008-039T17:51 at 3.86 saturnian radii distance. On day 2008-224T21:06 Cassini encountered Enceladus (E4, orbit 80) at an altitude of 50 km and entered the plume with high gas and dust densities. CDA used the Flight Software version 12.2 and no raw data are available of the target channels during this phase.

³An Enceladus flyby occurred at 2008-283T19:06 (E5, orbit 88) with an altitude of 25 km and a plume crossing. CDA used the Flight Software version 12.2.

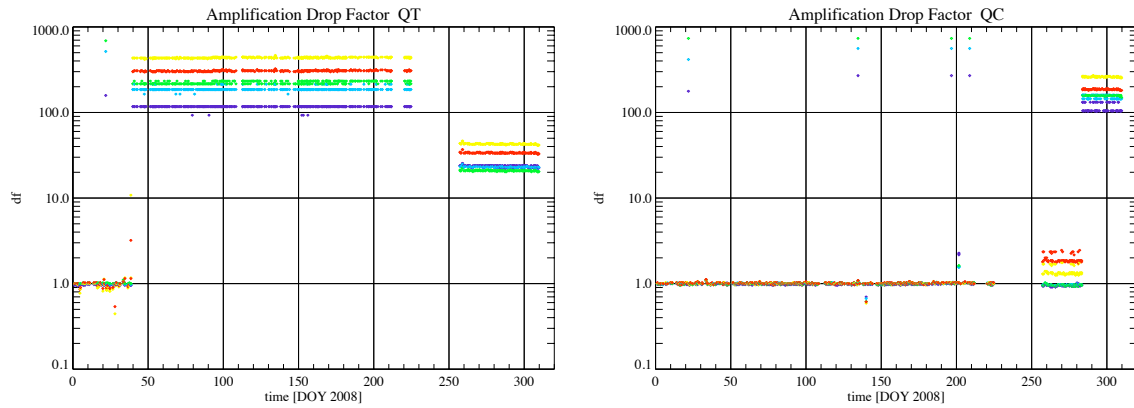


Figure 3.8: Time variations of the amplification factor at the target channels IIT (left) and CAT (right). This curve is based on the analysis of test pulses which are automatically sent every day. The test pulse contains five steps and the amplification drop factor was determined for each individual step (color). The five steps follow the rainbow color scheme from purple over blue and green to yellow and red. The purple symbols represent the lowest step of the test pulse.

flyby geometry of the Enceladus encounters is shown in Fig. A.4.

A consequence of the change in amplification at the target channels was a faulty classification of the events by the onboard software. This would have no significant effect as long as all events are downlinked by Cassini. However, the classification is used by the onboard flight software of CDA to prioritise the events for data readout, meaning that the number of transferred noise events is limited although it might dominate. The very low target amplitudes lead to the effect that all events, including CAT impacts showing mass spectra, were classified as noise event. The limited bandwidth of normally 524 bps (approximately one event every 20 seconds) can not guarantee any more the downlink of all strong target impacts.

The solution of this problem is a new classification scheme based mainly on the ion grid amplitude and the number of mass lines found in the multiplier channel. The latter criterion is used in order to separate Chemical Analyser Target impacts from Impact Ionisation Target impacts and the ion yield determines the counter number (representing the mass threshold). The new classification is shown in Tab. 3.1.

It is obvious that a new classification scheme has to be verified by an application to real data sets. Four data sets were selected as test cases: The ring plane crossings on day 2006-337, 2007-114, 2008-131 and 2008-321. It is of course important, to check both cases, the original amplifier state of the years 2006 and 2007 as well as the changed status in 2008. The comparison between the original (black curve) and the new classification scheme (red dashed curve) is shown in Fig. 3.9 and Fig. 3.10. The new classification even provides more realistic relations between CAT and IIT impacts. According to the ratio of their target areas, the amount of CAT classified impacts (A-counters) should not exceed approximately 15%. This constraint is fulfilled by the new classification scheme in all test cases. For example, on day 2007-114 the number of CAT classified events is 267 and the number of IIT events was calculated to 2138

3 Cosmic Dust Analyser Performance

Table 3.1: Revised counter definition taking into account the low amplitudes of the target channels. The new scheme will be applied starting early 2010.

counter #	name	description
0	A0	CAT impact, >3 mass lines, QI signal $>3.29 \cdot 10^{-12}$ C (200 dn)
1	A1	CAT impact, >3 mass lines, QI signal $>1.66 \cdot 10^{-12}$ C (170 dn)
2	A2	CAT impact, >2 mass lines, QI signal $>6.71 \cdot 10^{-13}$ C (130 dn)
3	A3	CAT impact, >2 mass lines, QI signal $>3.31 \cdot 10^{-13}$ C (100 dn)
4	A4	CAT impact, >2 mass lines, QI signal $>1.45 \cdot 10^{-13}$ C (70 dn)
5	A5	CAT impact, >2 mass lines, QI signal $>5.82 \cdot 10^{-14}$ C (45 dn)
6	A6	CAT impact, >2 mass lines, QI signal $>2.57 \cdot 10^{-14}$ C (30 dn)
7	A7	CAT impact, >2 mass lines, QI signal $>1.03 \cdot 10^{-14}$ C (20 dn)
8	I0	IIT impact, QI signal $>2.62 \cdot 10^{-12}$ C (190 dn)
9	I1	IIT impact, QI signal $>1.32 \cdot 10^{-12}$ C (160 dn)
10	I2	IIT impact, QI signal $>6.71 \cdot 10^{-13}$ C (130 dn)
11	I3	IIT impact, QI signal $>3.31 \cdot 10^{-13}$ C (100 dn)
12	I4	IIT impact, QI signal $>1.45 \cdot 10^{-13}$ C (70 dn)
13	B0	(Noise) - Strong signals on all targets
14	QT only	(Noise) - Strong and fast signal on QT channel only
15	S0	spare counter
16	A8	CAT impact, >2 mass lines, QI signal $>9.06 \cdot 10^{-16}$ C (12 dn)
17	I5	IIT impact, QI signal $>5.82 \cdot 10^{-14}$ C (45 dn)
18	I6	IIT impact, QI signal $>1.75 \cdot 10^{-14}$ C (25 dn)
19	I7	IIT impact, QI signal $>3.04 \cdot 10^{-15}$ C (14 dn)
20	W0	Wall impact (big), QI signal $>1.75 \cdot 10^{-14}$ C (25 dn)
21	W1	Wall impact (small), QI signal $>1.95 \cdot 10^{-15}$ C (13 dn)
22	N0	Noise - high baseline on channel QC
23	N2	Noise
24	T0	Test pulse o.k.
25	T1	Test pulse
26	XX	internal interrupt counter

giving a ratio of 8 which is realistic.

3.3 Calibration Overview

The proper calibration of space flight instruments is essential for the correct analysis and understanding once the data are on ground. Furthermore, it is normal that the methods and the understanding of an instrument develops with time and that the calibration changes based on new laboratory or in-flight data. The disadvantage of new calibration algorithms is, that the already calibrated data have to be reprocessed and already published information has to be revised. However, this process is painful but necessary, since the understanding of scientific processes grows with its accuracy. Many years from today, scientists will still work with the data and the latest calibration can be applied from the beginning. Here, the re-evaluation of

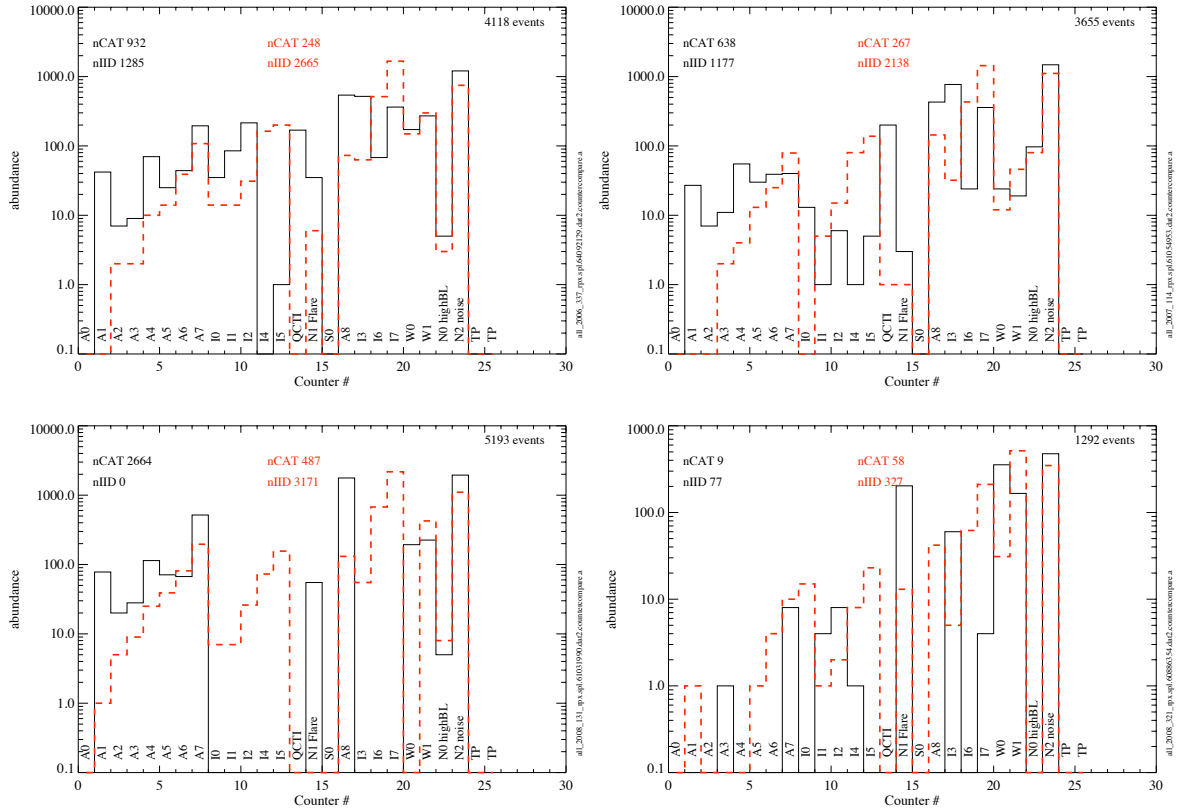


Figure 3.9: Comparison of the old counter classification scheme (black line) [Srama et al., 2006] and the new definition of Tab. 3.1. Data of four ring plane crossings were investigated: 2006-337 (upper left), 2007-114 (upper right), 2008-131 (lower left) and 2008-321 (lower right).

the old calibration data from the years 2000 or even earlier with new techniques changes the output parameters (dust speed and dust mass), but do not revolutionise the overall picture of former results and publications. It is a matter of fact, that for some investigations, a consistent calibration even with simpler methods is more important, than a very sophisticated processing using many different parameters.

One argument to proceed with calibration activities is, that new flight data will allow for additions of the current calibration (given by the fact, that an understanding of the particle speed, mass and composition in the saturnian system constraints the signal parameters). New knowledge leads to new calibration process, which in turn lead to a new understanding and again to new ideas for an improved calibration. This spiral can be done almost endlessly if the calibration process is self-calibrating. This means, that we know e.g. the impact speed and that we set the constraints to derive the dust speed with the lowest error possible [Srama, 2000b]. But this is based on the data set we have already. In this data set, the combination of dust speeds and dust masses are unfortunately linked together. This is the case in the laboratory (there are no fast dust grains with sizes above $1 \mu\text{m}$, Fig. 3.12), as well as in a planetary

3 Cosmic Dust Analyser Performance

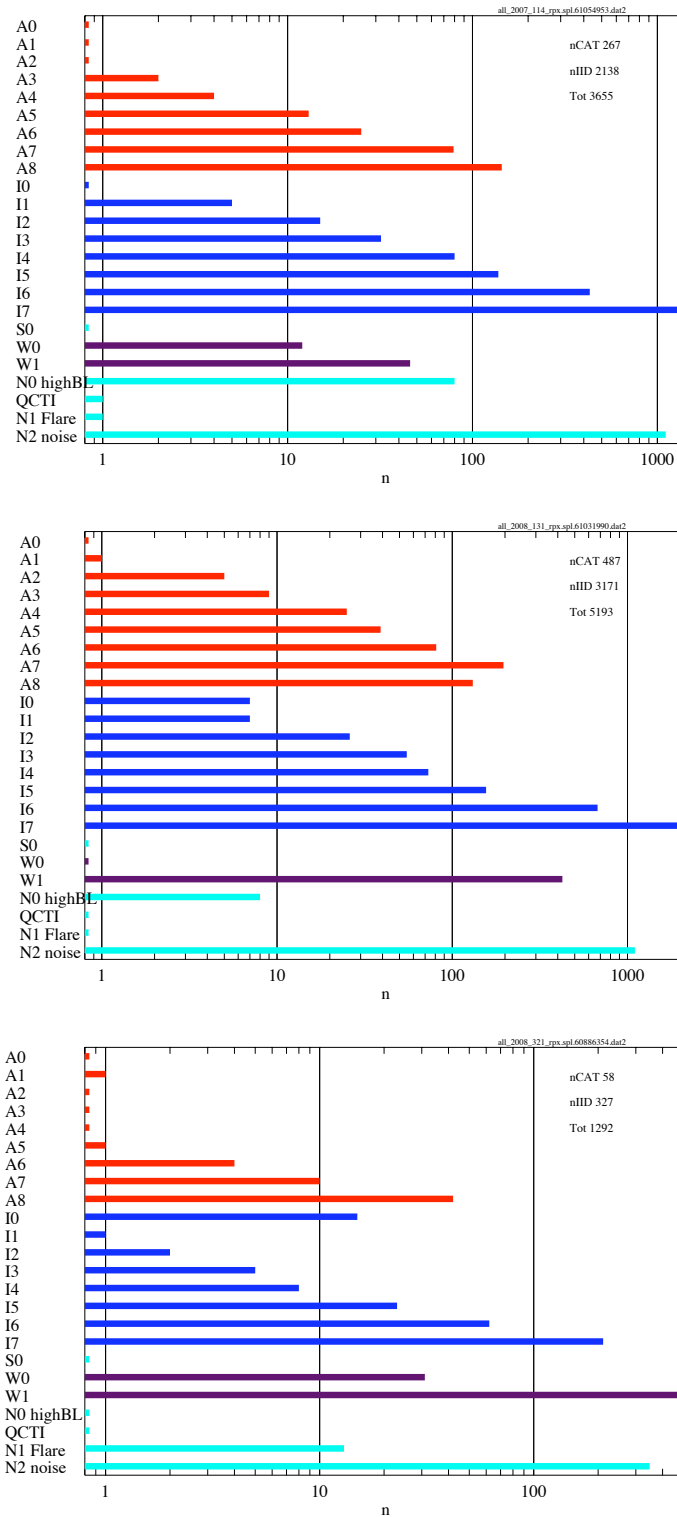


Figure 3.10: The new classification scheme of the ring plane crossing data shown in Fig. 3.9 (2007-114, 2008-131 and 2008-321) sorted by counter type (A: CAT, I:IIT, W: Wall, N: Noise, S: Spare). The mass thresholds for the individual counters are given in Tab. A.3 and A.4. The ring plane crossings occurred at $6.57 R_S$, $4.48 R_S$ and $4.34 R_S$.

environment: Large grains are found at different places than smaller grains. The planetary environment (magnetospheric parameters with its plasma and electromagnetic forces) separates the dust populations [Horányi et al., 2008] and dust is distributed to its physical parameters. If we could prove for example, that only water ice grains with a size of $0.3 \mu\text{m}$ occur at a saturnian distance between 15 and 16 R_S and latitudes between 10° and 20° , we would have an excellent calibration source! Unfortunately, the measurement of dust size and composition is exactly the output we expect from a calibrated instrument. The approach between laboratory calibration and in-flight data results needs time to learn and constrain the particle parameters. A good example is the abundance of water ice in the saturnian system. Now, we know that these are water ice particles, which helps in calibration. But we were not able to calibrate the instrument with accelerated micron sized water ice particles in the laboratory and we will never be.

In the laboratory, we learned how to generate higher charges in front of a target using lasers. The dust accelerator in Heidelberg is not able to accelerate 5 micron sized particles with speeds of 10 km s^{-1} which would be necessary to generate impact charges above $1 \cdot 10^{-12}$ Coulomb. The new cross-calibration of laser generated plasmas with hypervelocity impact plasmas is currently investigated and documented by A. Mocker in a PhD thesis. There are a number of further new approaches and capabilities in the laboratory and in general on ground (modelling) which will provide new constraints for a better calibration and they are listed in a separate subsection at the end of this chapter.

Another argument for re-evaluation of calibration processes is the progress in laboratory technologies. I have already mentioned the new approach using lasers for stimulating impact charges, but which is not part of this work. The main progress is the means of new dust source materials which can be accelerated in the accelerator laboratory [Burchell et al., 1999, Burchell, M.J. et al., 2002, Hillier et al., 2009, Goldsworthy et al., 2003, Lascelles et al., 1997].

Although some new data are available, the main reason for the re-calibration is simply the possibility to combine the available data sets of Stübig [2002] and Srama [2000b] for a new approach in data evaluation.

In summary, this chapter is by far not complete as explained. New ideas, methods and latest flight data will always provide the possibility to refine calibration curves. After having this said, I can start to show some general diagrams of the data used for calibration. It has to be mentioned that most of the diagrams and plots are not published until today.

The instrument calibration setup with the CDA in the vacuum chamber of the Heidelberg dust accelerator is shown in Fig. 3.11. The flight spare unit was mounted in the chamber on a turn table for angular variations and on a movable table to change the impact location on the target. The instrument was connected by a power line and a data line similar to the original spacecraft mounting. By this means the CDA operated autonomously and it was controlled by a special Ground Support Equipment (GSE) computer and software. The data format achieved was similar to the later flight data, although the CDA software used at this time was working differently from what is currently onboard Cassini. This software was very basic and used only a two-event queue buffer for readout. In contrast, the measurement software onboard to-

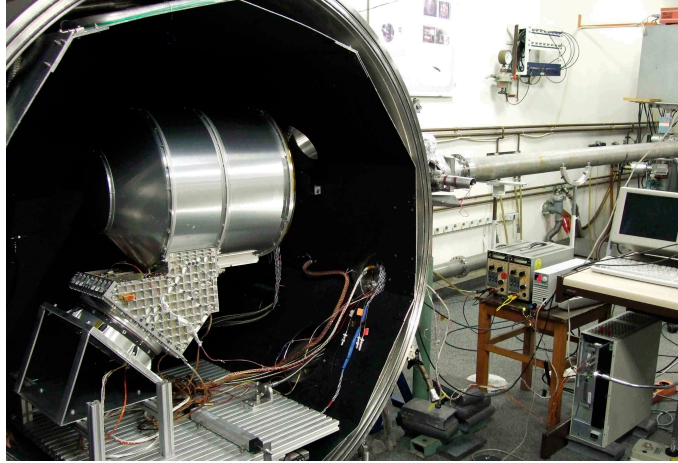


Figure 3.11: The CDA instrument is mounted in the vacuum chamber at the dust accelerator facility in Heidelberg at the MPI Nuclear Physics. Such a setup was used for the recording of the calibration data shown in this chapter. The instrument is mounted on top of a turn table (horizontal rotation axis) and a table which can be shifted horizontally. The moving platforms were controlled from outside using mechanical feedthroughs and high-precision potentiometers guaranteed a high position accuracy.

day can store roughly 48 events and has data compression and smart classification algorithms.

The data set from Stübiger [2002] and Srama [2000b] were combined and provide a new unique data set which allows for a more extensive investigation of speed and mass determination. Although the Stübiger data set contains many different materials, it was found that their individual speed and mass range is not sufficient to really enhance the current knowledge. But it contains also many iron dust impacts which are useful for this work. An overview of all dust particles is shown in Fig. 3.12. In total the impact signals of all measurement channels of CDA for 4706 dust impacts were recorded, analysed and archived in a special data structure for later detailed analysis. The diagram shows two plots: the charge over mass (left) and the mass over speed (right). Each symbol represents one individual dust impact. The direct measurements of the particle parameters are always speed (via time-of-flight using two induction tubes in the beam line) and dust surface charge (via direct charge induction employing a metal tube and a charge sensitive amplifier). The dust mass is simply calculated by the equivalence of particle kinetic energy $E_{kin} = \frac{1}{2}m \cdot v^2$ and the energy achieved in the acceleration field $E_{qU} = q \cdot U$ giving directly the mass m by measuring the particle speed v , the particle charge q and the acceleration voltage U

$$m = \frac{2 \cdot q \cdot U}{v^2} \quad (3.10)$$

The clustering of the events in a region constrained by dashed lines is obvious (Fig. 3.12). The boundaries are given by mass (size) distribution of the dust power in the dust source, the surface charge and the acceleration voltage. Although in principle very low speeds (below 1 km s^{-1}) are possible, the accelerator electronics does not support the selection of such low-charged dust grains. The higher speed limit is given by the maximum charge to mass ratio

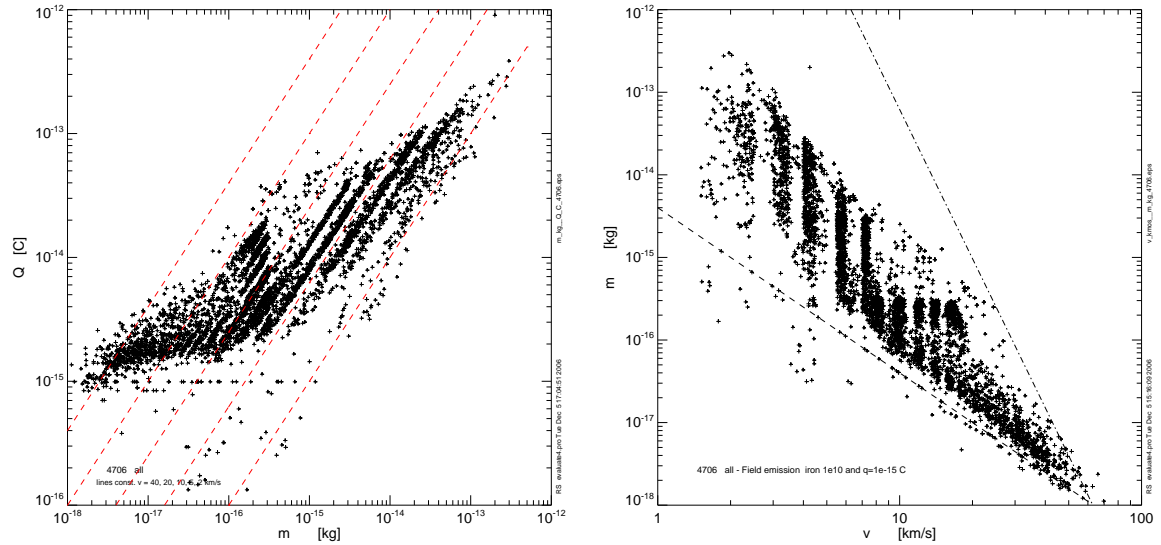


Figure 3.12: Overview of the speed and mass range of the dust grains used for calibration and provided by the dust accelerator. The data from M. Stübig and R. Srama were merged to total number of 4706 dust impact. Left: Dust charge and dust mass. Dashed lines indicate particles with a constant speed of 40 km s^{-1} , 20 km s^{-1} , 10 km s^{-1} , 6 km s^{-1} and 2 km s^{-1} ; Right: Dust mass and dust speed. Dashed lines indicate the physical limits of a minimum dust charge which is detected by the accelerator electronics of approximately 1 fC (bottom) and the maximum charge a grain can carry on its surface (field emission limit of $\approx 1 \cdot 10^{10} \text{ V/m}$).

of the grain which is higher for small particles. In principle, 10 nm sized grains would reach 100 km s^{-1} or higher speeds, but such tiny grains cannot be extract from the dust source due to clustering and their high adhesive forces. Only dust grains with a solid and hard surface which are not too small (the extract limit as roughly at 40 nm) can be extracted and accelerated [Stübig et al., 2001] (Fig. 3.13). It is also obvious from Eq. 3.10 that faster grains are generally smaller than slower ones if their surface charge is identical. The mass range of dust grains given at a constant speed is determined by the amount of surface charge which is limited to the bottom (by the sensitivity of the dust accelerator electronics) and to the top (grain charging is limited due to field emission).

Typical impact energies are only 10 nJ and rather low, but already sufficient to generate enough impact charges for impact ionisation instruments. It has to be stated, that each of the points in the diagrams of Fig. 3.12 and Fig. 3.13 do produce a self-triggering signal at the CDA instrument. But this means, that the dust mass range offered by the accelerator is wider, specifically to lower speeds. There are of course low-speed grains which did not produce a sufficiently high signal on the CDA channels. The flight unit of CDA onboard Cassini, however, operates with a lower detection threshold than the flight spare unit in the laboratory. This behaviour was surprising and it was caused by the electrical noise in the dust accelerator laboratory. The electrical and electromagnetic noise onboard Cassini is better than in our ac-

celerator laboratory!

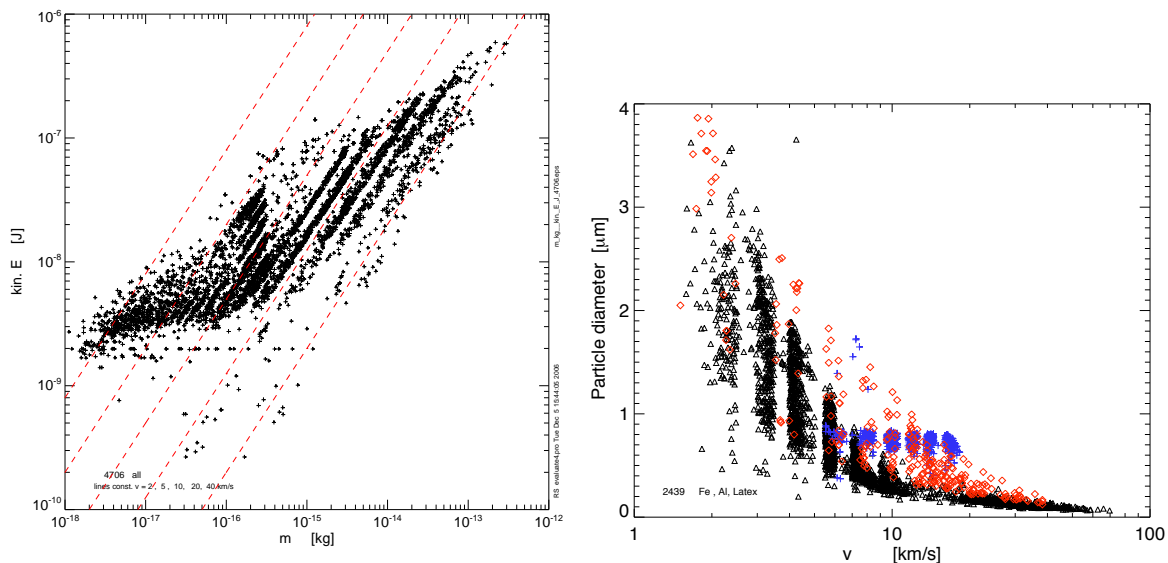


Figure 3.13: Kinetic energy, mass, speed and particle diameter of the 4706 dust grains used for calibration. The dashed lines indicate constant impact speeds of 40 km s^{-1} , 20 km s^{-1} , 10 km s^{-1} , 6 km s^{-1} and 2 km s^{-1} (left). The largest grains reached approximately $4 \mu\text{m}$ and were mainly out of aluminium (right). The symbol colors are black (iron), red (aluminium) and blue (latex). Only submicron grains were detected by CDA above 10 km s^{-1} .

For calibration the dust particle parameters speed, mass, charge, composition, impact angle and impact position on the target are important. These parameters are easily calculated or measured during tests in the accelerator laboratory. The aim in calibration is the determination of dust speed and mass, which depends of course on the impact location. Without the knowledge of the impact location on the target, no speed and mass determination is possible. As described above, the instrument contains a large target (IIT), a small target (CAT) and further mechanical structure like the inner housing, the multiplier mounting made out of aluminium and the entrance grids (4 grids with a transmission of 95% each). The determination of the impact location from the impact signals alone is by far not trivial and extensive studies were performed in Srama [2000b] to find conditions and constraints for a safe impact location determination, which is, in the first step, the separation of CAT impacts from IIT impacts (assuming already the recognition of wall and structure impacts). For a target impact both signals have to be present, the target signal (either QT or QC) and the ion grid signal (QI). For larger impacts a clear multiplier signal is also in coincidence (compare e.g. Fig. 4.11).

The best criterium found to determine the impact target was the ratio between the target signals QT and QC. An impact on the large target (QT) should cause only a small signal at the adjacent target (QC) and vice versa (Fig. 3.14). But even this simple consideration surprises with its physical nature: Even for an IIT impact, the signal of the adjacent target (QC) can be

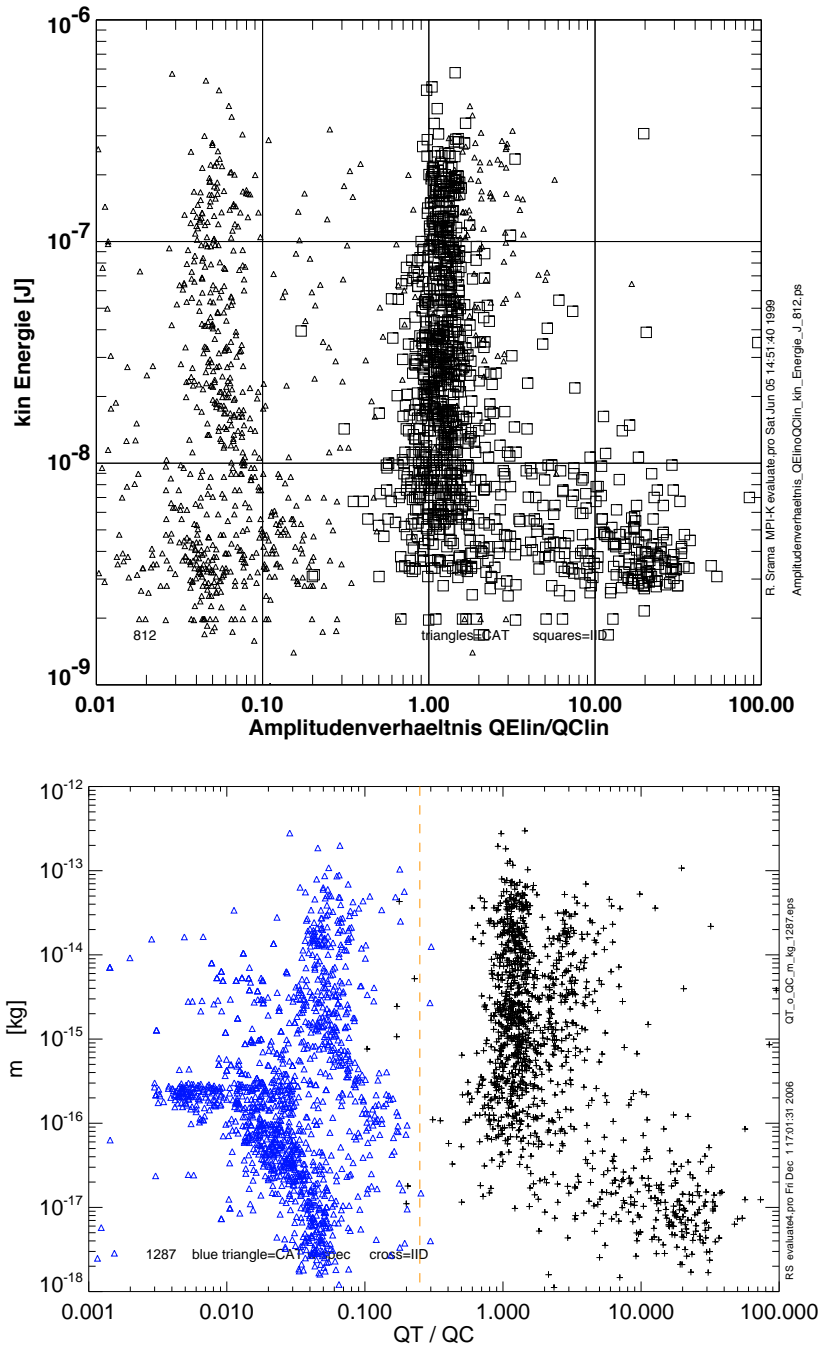


Figure 3.14: The ratio between the both target signals QT and QC is a good criterium to define the impact location (IIT or CAT). If the QC signal is at least 3 times stronger than the QT signal, the particle impact occurred at the small CAT. The separation is necessary before a speed and mass calibration can be applied to the signals.

stronger than the QT signal, and the ratio QT/QC becomes smaller than one! How can this be explained?

There is no or only a minor electrical crosstalk. Although it was not directly proved, the only explanation is, that this is caused by the generated fragments of the dust impact. The ejecta will impact on adjacent target areas due to the hemispherical shape of the target. Those secondary impacts generate again electrons and ions which are attracted by the target. The electric field in front of the small target is much stronger (333 V mm^{-1}) than the field in front of the large target ($<1.7 \text{ V mm}^{-1}$). Charges generated at the small target are therefore collected much more efficient and faster leading finally to stronger charge signals. Nevertheless, there is a clear boundary between the both point clusters in Fig. 3.14. The proposed boundary of 0.3 ± 0.05 is given in Eq. 3.11. Srama [2000b] found a ratio of 0.25 which is shown as a dashed line in the diagram.

$$\frac{QT}{QC} > 0.3 \quad \text{for IIT impacts and} \quad \frac{QT}{QC} < 0.3 \quad \text{for CAT impacts} \quad (3.11)$$

Ratios above 0.3 are related to IIT impacts, smaller ratios are caused by Chemical Analyser impacts. Nevertheless it has to be mentioned, that this boundary is defined by our calibration data set with a limited range of particle masses. We were unable to measure the ratio for grains above $5 \mu\text{m}$ in size in the laboratory.

A second good criterium for CAT impacts is of course the occurrence of a time-of-flight spectrum in the multiplier channel. A mass spectrum is always related to hits of the CAT. IIT impacts show only very broad features in the multiplier channel. However, wall and structure impacts have to be sorted out beforehand by an analysis of the QP channel and the occurrence of a valid QI signal. A more detailed analysis is given in Srama [2000b] and specifically in Stübig [2002]. Basically, a strong QP signal before the trigger time indicates a wall or structure impact (compare Fig. 4.12). For a valid target impact, the QI amplitude has to be within a certain range ($3 < \frac{Q_{\text{target}}}{QI} < 15$).

An established parameter in instrument calibration of the impact ionisation process is the charge to mass ratio of the impact plasma in dependence of the impact speed. The ratios for the target and ion grid signal of CAT and IIT impacts is presented in Fig. 3.15. The diagrams of iron impacts show the known rise with impact speed and a simple approach is defined by Eq. 3.12.

$$Q \sim m^\alpha \cdot v^\beta \quad (3.12)$$

Common values were defined by Krüger [2003] for the Galileo dust detector with $\alpha \approx 1$ and $\beta \approx 3.5$ although the value β can vary from 1.5 to 5.5 [Auer, 2001, Göller and Grün, 1989]. The CDA instrument has a slightly different geometry by the incorporated Chemical Analyser. Stübig [2002] performed extensive studies using this power law and concluded with similar values but highly dependent on the impact speed itself and the projectile material (Fig. 3.16). It is not the task of this work to verify the old results, but to take a *new approach* for the relation between impact speed, impact charge and the particle mass. Rather than defining various exponents for different speed regions for α and β , tabulated values, shown as blue symbols in Fig. 3.15, are proposed. It is clear that there is an error of a factor of approximately

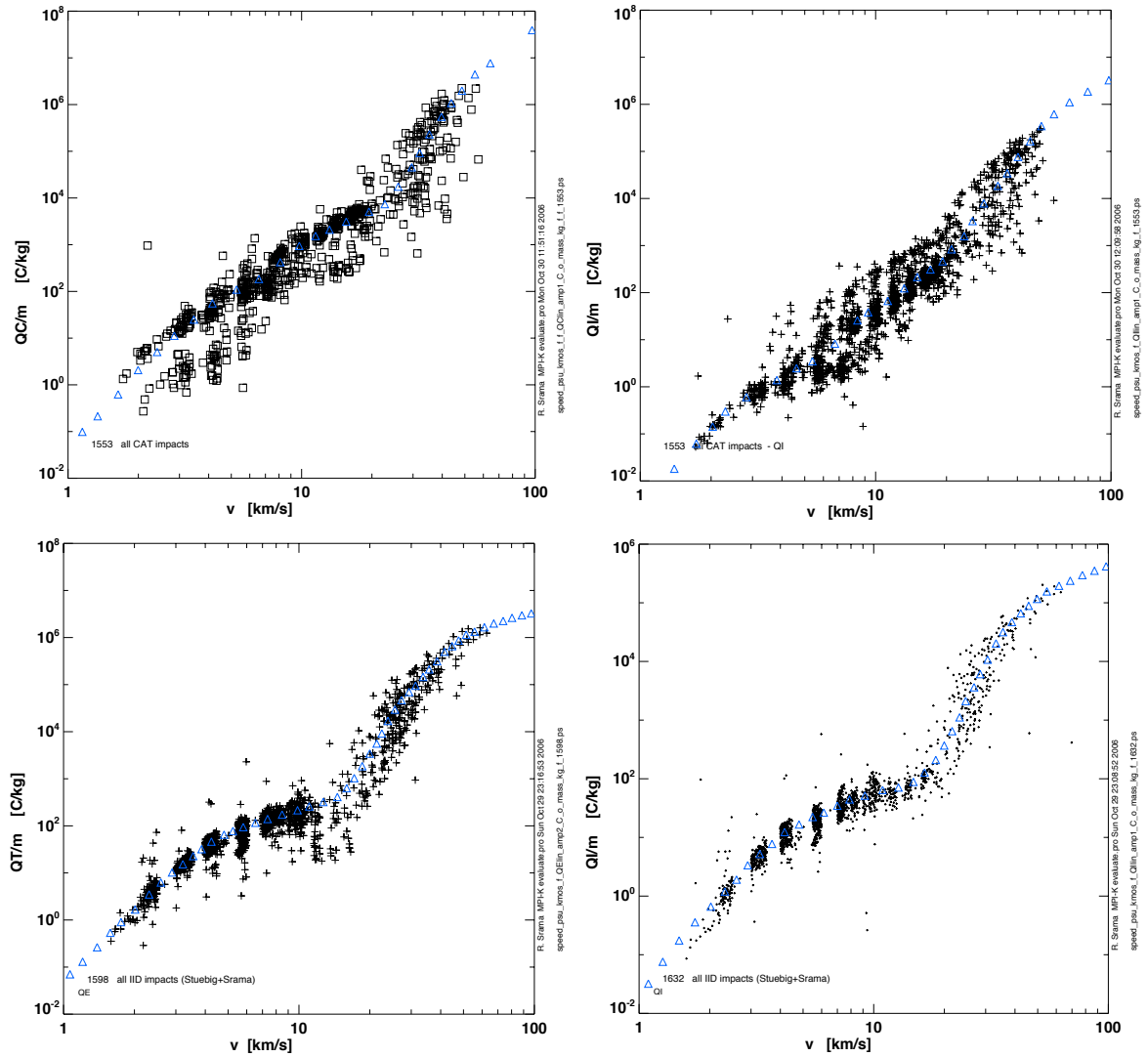


Figure 3.15: Charge over mass ratios for CAT impacts (top) and IIT impacts (bottom). The curve is biased by the selection rule of the dust accelerator and the used particle sizes in the dust source during the calibration tests. The fit by a linear function is not proposed, but individual tabulated values (blue). The dent in the middle of the lower two plots are attributed to a change of the impact ionisation process: Lower speeds produce impact ejecta, higher speeds do not generate impact ejecta. The blue symbols outside the clusters are speculative but are introduced to achieve monotony and continuity.

5 in the tabulated values. The values shown are valid for iron projectiles only and are listed in Tab. A.1 and Tab. A.2 in chapter A.4.

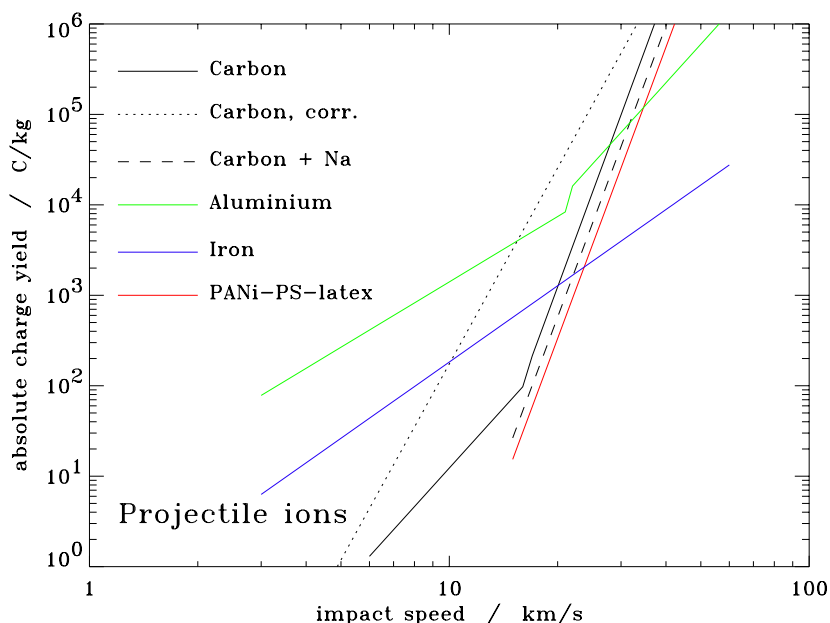


Figure 3.16: Absolute charge to mass yields of projectile ions depending on the impact speed after Stübig [2002]. The total ion yield is higher, since the target ions contribute the majority of the ions. The different line colors and styles indicate different projectile materials, explained in the legend. The dotted black line is a theoretically calculated charge yield that takes into account the formation of cluster ions.

3.4 Impact Ionisation Detector Calibration

The target geometries and field configurations are different for the two subsystems IID and CA. The large IID target has a very low electrical field strength of approximately 1 V/mm in front of the surface (350 V over 20 cm in a hemispherical configuration), whereas the Chemical Target attracts the electrons with 333 V/mm to its surface. The much stronger field configuration has advantages and disadvantages. An advantage is that the plasma charges are immediately separated in the electric field which causes a steep and high target amplitude. This finally means a high sensitivity to small dust impacts. The disadvantage of a fast rise time is the loss of rise time information for the derivation of the impact speed (see section 3.5.1).

The voltages were carefully set to the lowest values providing the best results. The -350 V of the IID were selected based on former results of the Galileo detector design. This voltage was set to the lowest value which is enough to collect the entire impact plasma charge of a micron sized dust particle impact in the common speed range ($\approx 10 \text{ km s}^{-1}$). However, very large grains or impact speeds of the stream particles of more than 100 km s^{-1} generate ions and electrons of higher energies ($>100 \text{ eV}$) which can escape from the electric field and are not collected at the target or the ion grid.

The situation for CAT impacts is a bit different. Here the very strong field ensures the collection of all electrons as long as the field is effective. A dense impact plasma as obtained by e.g.

10 μm sized grains causes Debye shielding and the clouds expands before the field between the grid and target can influence the charges. We have two different target systems which need a complete separate calibration, although we can apply the same methods since both systems represent impact ionisation detectors.

3.4.1 Dust Impact Speed

The determination of the dust impact speed is an established, but also still inaccurate process. The impact process generates an impact plasma which is separated in an electric field. The dust impact generates a primary charge (electrons and ion of the primary impact plasma) and a secondary charge. The secondary charge is produced by the secondary impacts of the fragments and ejecta generated during the hypervelocity impact. The ejecta have speeds of a few km s^{-1} and a broad emission angle. These fragments hit other target areas a few microseconds after the primary impact and generate again charges which are collected by the electrodes. The rising flank of the collected electrons at the target channel QT consists out of two components [Ratcliff et al., 1995, Stübig, 2002]. The faster the impact speed, the more primary charge is generated and the leading fast peak (also shown after deconvolution in Fig. 3.5) is stronger. This leads to a faster rise time - the major principle in speed calibration of impact ionisation detectors. Depending on the ratio between primary and secondary peak amplitude, the overall signal rise time is shaped and defined.

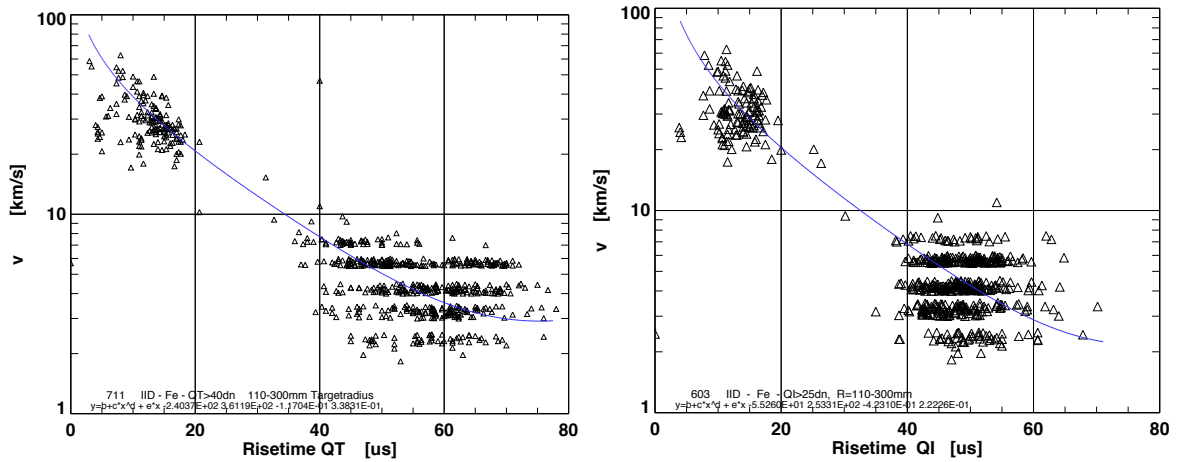


Figure 3.17: Dependence between the signal rise time and the dust impact speed for iron impactors onto the IIT. Left: Electron signal of the QT channel. Right: Ion signal of the ion grid channel. The blue lines are fitted functions given in Eq. 3.13 and 3.14. Both fits comply with the requirement of an asymptotic approximation towards the $v=0$ axis.

The **rise time** dependence from the impact speed is shown in Fig. 3.17. For a consistent result, only iron impacts were taken which enclose the largest data set. Impact signals of grains around 10 km s^{-1} were too small to trigger the instrument reliably, and a speed gap between

3 Cosmic Dust Analyser Performance

10 km s⁻¹ and 16 km s⁻¹ occurs simply due to the lack of sufficiently large dust grains at the dust accelerator facility. The two point clusters also reflect the two impact process regions: Low impact speeds with a minor component of the primary impact charges, and high impact speeds with a dominating primary charge peak. This causes a clear separation in the value of the rise time. A consideration of a point cluster alone gives not such a clear dependence on the impact speed. It is impossible to determine, if the impact speed was e.g. 3 km s⁻¹ or 6 km s⁻¹. A rather high uncertainty (error factor) in speed determination is the consequence, and an error factor of ≈2 is normal. The errors are discussed in one of the next paragraphs separately.

The rise time t_r is defined as the time between 10% and 90% of the signal amplitude. The impact speed v_{IID}^{QT} is then given by Eq. 3.13. For this fit only QT signals larger than $6.5 \cdot 10^{-14}$ C were considered to ensure an accurate determination of the rising flank.

$$v_{IID}^{QT}(t_r) = -240 + 361 \cdot t_r^{-0.117} + 0.338 \cdot t_r \quad \text{with } t_r \text{ in } \mu\text{s} \text{ and } v_{IID}^{QT} \text{ in km s}^{-1} \quad (3.13)$$

The impact speed derived by the ion grid signal is given by Eq. 3.14. The rise time range for an application of this fit lies between 1 μs and 75 μs and the QI amplitude shall be higher than 20 fC.

$$v_{IID}^{QI}(t_r) = -55.3 + 253 \cdot t_r^{-0.423} + 0.222 \cdot t_r \quad \text{with } t_r \text{ in } \mu\text{s} \text{ and } v_{IID}^{QI} \text{ in km s}^{-1} \quad (3.14)$$

In the discussion of the ion grid signal rise time it has to be added, that the signal shape has two further parameters in contrast to the target signal. The electrons are fast due to their low mass, but the ions need a significant time to reach the ion grid. Even the IID with its total voltage of 350 V forms a simple time-of-flight spectrometer. Hydrogen reaches the ion grid after about 3 μs , carbon already takes 11 μs , sodium 15 μs and gold up to 44 μs . This fine structure is normally not seen in the shape of the ion grid signal, but determines the duration of the rise time. In addition, we do have the large amount of secondary impact ejecta with its secondary signal, leading to very long rise times of up to 70 μs on both, the target and ion grid. Secondly, the ions of the impact plasma have a broad energy distribution of up to 100 eV (especially for high impact speeds). It is obvious that not all ions are collected at the ion grid and a significant amount of the ions are not focused onto the grid but they hit the structure or they leave the sensor (passing again the entrance grids). In short words: the ion grid signal is incomplete, a significant amount of the charge is simply lost. This biases also the signal shape and the rise time determination.

Unfortunately, there are more facts changing the ratio between primary and secondary ionisation, which have not been studied in detail until today. Those factors are the impact angle, the particle and target density, surface roughness and dust particle shape.

There are a couple of parameters of the QT and QI channel which have been tested on its relation to the impact speed. Those parameters were:

- Time difference of the QI and QT amplitude, where amplitude is defined by either 100% , 90% or 10% of the signal. No trend or dependence was identified.

- Time difference of QI and QT, defined by 50% of the amplitude. This shows basically no trend, but for impact speeds above 20 km s^{-1} the time difference between the QI and QT signal is more than $-3 \mu\text{s}$.

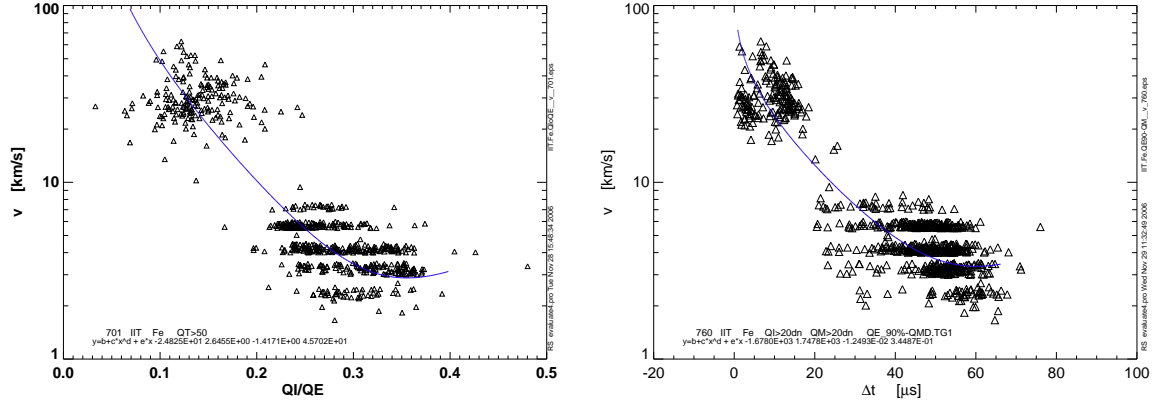


Figure 3.18: More methods for IIT speed calibration: amplitude ratio QI/QT (left), time difference of QT and QM signal (right).

One could think that high impact speeds generate more ions with higher energies in the impact plasma leading to a stronger decrease of the QI signal with impact speed. Plotting the ratio of QI and QT (R_{QIQT}) over the impact speed gives in fact a decrease with impact speed (Fig. 3.18), which was fitted by Eq. 3.15. In order to reliably determine this ratio, the QT signal has to be greater than $9.5 \cdot 10^{-14} \text{ C}$.

$$v [\text{km s}^{-1}] = -24.83 + 2.65 \cdot R_{QIQT}^{-1.42} + 45.7 \cdot R_{QIQT} \quad (3.15)$$

The time difference between the target and multiplier signal provides another method to derive the impact speed (Fig. 3.18). The time of the first maximum of the multiplier was subtracted from the time when the QT amplitude reaches 90%. This requires a clear signal at the multiplier which is normally provided if the QI amplitude exceeds values of 13 fC. Eq. 3.16 gives the achieved formula with the time difference T_{QT-QM} in μs .

$$v [\text{km s}^{-1}] = -1678 + 1748 \cdot T_{QT-QM}^{-0.0125} + 0.345 \cdot T_{QT-QM} \quad (3.16)$$

The error factors for the various methods to determine the dust speed is shown in Fig. 3.19. The x-axis shows the ratio of the calculated speed v_{fit} and the true impact speed v . An integration over the individual segments gives a cumulative distribution (dash-dotted line). The levels of 16% and 84% of the maximum define the standard deviation of $\pm 1 \sigma$. The logarithmic x-axis results in an error factor and not in an absolute value of deviation.

A further method to derive the dust speed is the analysis of the **induced charge** signal in the QP channel. This method was extensively described in Kempf et al. [2004], Kempf [2007] and Auer et al. [2002] and provides the most accurate procedure. However, this method can only

3 Cosmic Dust Analyser Performance

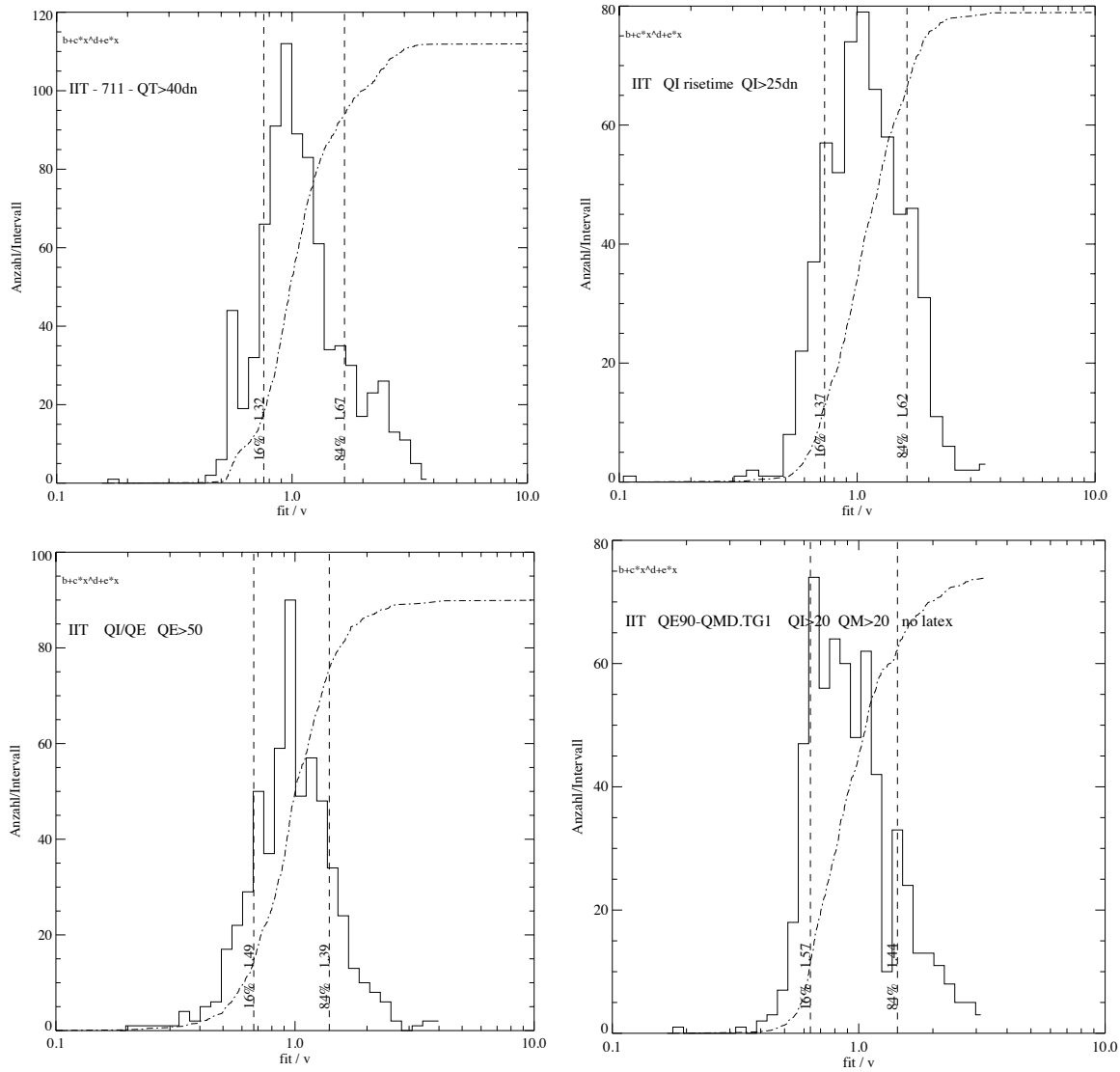


Figure 3.19: Error factors of the various speed calibration methods for IIT impacts. The error factors are 1.67 (QT rise time method, top left), 1.62 (QI rise time method, top right), 1.5 (QI/QT amplitude ratio, bottom left), and 1.57 (time difference T_{QT-QM} , bottom right).

be applied to particles carrying primary charges of at least 1 fC. Such high surface charges are related to particles larger than $4 \mu\text{m}$ if their surface potential is 5 V. In-situ measurements and models have shown, that such grain sizes are constrained to Saturn's ring plane and radial distances below $7 R_S$.

3.4.2 Dust Mass

The relationship between the impact charge Q , the dust speed v and the dust mass m is well established. The larger the dust grain the more impact charge is generated; and the faster the impact speed, the greater is the impact charge (Eq. 3.12). Normally, the charge rises directly with the dust mass, whereas the speed has a stronger dependency with exponents $\beta > 2$, which exceeds the gain in kinetic energy. Since the default speed exponent β of the equation $Q \sim m^\alpha \cdot v^\beta$ is 3.5, the plots in Fig. 3.20 show the ratio of $\frac{Q}{v^{3.5}}$ over the dust mass. This simple relation indicated by the clear trend of the points seems to be true. But it has to be noted that the speed window was highly constrained to achieve such a nice dependence. The speed considered in the diagrams were below 20 km s^{-1} . Higher impact speeds do not comply with the fits given by Eq. 3.17 and 3.18. Stübig [2002] therefore concluded with smaller speed exponents for higher impact speeds of only 2 instead of 4.4.

$$\frac{QT}{v^{3.5}} = 4751 \cdot m^{1.30} \implies m = \frac{QT^{0.769}}{672 \cdot v^{2.69}} \quad (3.17)$$

$$\frac{QT}{v^{3.5}} = 575 \cdot m^{1.28} \implies m = \frac{QT^{0.781}}{143 \cdot v^{2.73}} \quad (3.18)$$

For the dust mass calculation we need the impact speed v and the impact charge Q in order to apply Eq. 3.17 and 3.18. However, the formulas were derived under an *important constraint*: within a speed window of 1 km s^{-1} , the variation in particle mass was only a factor of 10 during the tests at the accelerator (compare Fig. 3.12). This is much too less to cover the speed and mass range required. For this reason a **new method is applied using 3-dimensional hyperplanes** in the phase space of Q , m and v .

Since this method is new, some details will be given how the data in the phase space $\{v, m, Q\}$ are fitted. First, the data are logarithmised, and the data range is defined in all dimensions followed by a segmentation in “tiles” (compare section A.5). Finally, the IDL routine *SFIT* is used to fit the 3-dimensional data set. The *SFIT* function determines a polynomial fit of degree n to a surface and returns a parameter array k_x . The hyperplane function is defined in Eq. 3.19:

$$f(x, y) = \sum_{i, j=0}^n k_{j, i} \cdot x^i \cdot y^j \quad (3.19)$$

In our case, fits with a maximum degree of two are sufficient to fit the data accurately and the simplified formula uses only six parameters (Eq. 3.20):

$$f(x, y) = k_0 + k_1 \cdot y + k_2 \cdot y^2 + k_3 \cdot x + k_4 \cdot x \cdot y + k_5 \cdot x^2 \quad (3.20)$$

The function $f(x, y)$ is nothing else than our dust mass m (in kg), whereas x is the impact speed v (in km s^{-1}) and y is the impact charge Q (in C). Before applying the fit formula, we have to take the logarithms of the values of v and m . Then, the impact charge QT of IIT

3 Cosmic Dust Analyser Performance

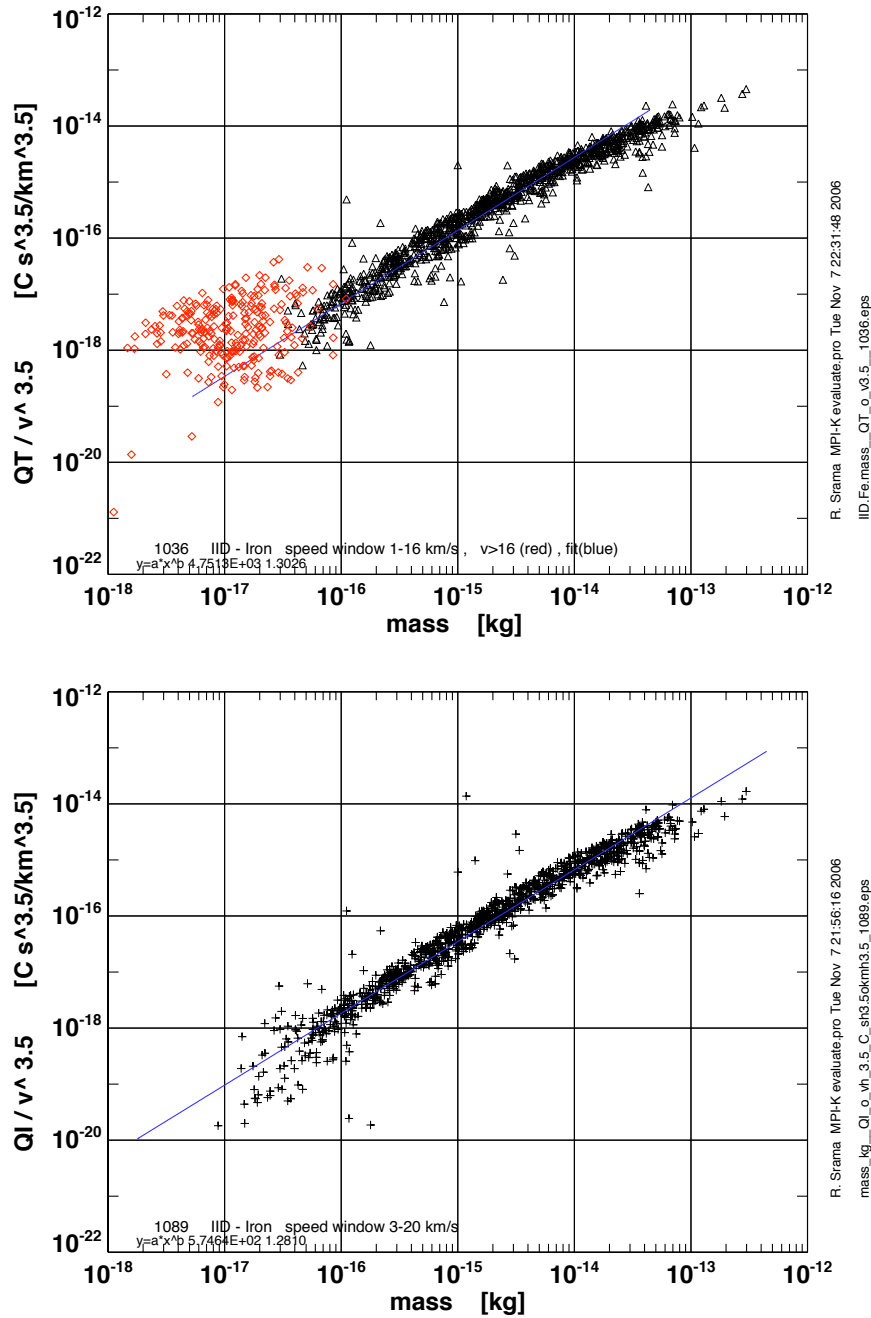


Figure 3.20: Ratio $Q/v^{3.5}$ over mass m for the QT signal (top) and QI signal (bottom). Only IIT impacts and iron projectiles were considered. A speed window of $1 \dots 16 \text{ km s}^{-1}$ (QT) and $3 \dots 20 \text{ km s}^{-1}$ (QI) was applied to the data. The red symbols in the upper plot represent impact speeds $> 16 \text{ km s}^{-1}$ and indicate another physical impact process.

impacts of iron dust grains can be described by Eq. 3.21.

$$\log(m_{QT}) = 10.02 + 2.943 \cdot \log(QT) + 0.0941 \cdot (\log(QT))^2 - 5.133 \cdot \log(v) - 0.135 \cdot \log(v) \cdot \log(QT) + 0.0614 \cdot (\log(v))^2 \quad (3.21)$$

The function is applied to both accelerator data sets, the results from Heidelberg and the results achieved during tests at the plasma accelerator in Munich using greater particle masses. The application range of the function is $v = 1.5 \dots 100 \text{ km s}^{-1}$, $Q = 10^{-20} \dots 10^{-10} \text{ C}$, and $m = 10^{-14} \dots 10^{-9} \text{ kg}$. The hyperplane of the fit is shown in Fig. 3.21 for two different 3D views. The axis are dust speed (x), dust charge QT (y) and dust mass (z). From modelling of dust stream impacts (S. Hsu), we know some constraints for the dust mass for impact speeds above 100 km s^{-1} . The figure shows a 3D box with the gridded and colored surface and symbols. The red symbols are the original data points, the blue symbols are projections to the fitted hyperplane connected by a thin bright blue line. The plane nicely combines the the low-speed impact events ($< 10 \text{ km s}^{-1}$) and the high-speed region. This was not possible by the simple approximation as shown in Fig. 3.20.

There is, of course, a larger error for the higher charge-to-mass ratios, since the calibration results at the plasma accelerator in Munich have greater uncertainties as well. There, the dust mass determination was uncertain caused by multiple impacts and the charge measurement was done with switched amplifiers introducing further errors as well ⁴. The hyperplane decreases for lower masses and lower speeds as predicted by Eq. 3.12. The approximation of the dust mass by the fit of a hyperplane in 3D space is new, and provides, for the first time, a method describing the relations between dust speed, mass and charge yield by using a *monotone and continuous function for the entire speed and mass range*.

The error of the fit function is given by the distances between the red and projected blue symbols in Fig. 3.21 which are connected by a thin line. A detailed error analysis is given by the evaluation of the ratio between the dust mass of the original data and the mass determined by the fit function (Eq. 3.21). The error factor is given by the limit of 16% and 84% marks using a logarithmic x-axis. The three dimensional fit provides error factors which are lower than the common former error factors of 10 and they have been calculated to 1.75 (Fig. 3.22). However, this assumes the knowledge of the dust speed and an accurate measurement of the dust charge. The dust charge measurement is accurate by 10% and is not the major error factor. The dust speed has uncertainties up to a factor of 1.7 and determines the overall accuracy. A multiplication of the two factors of 1.7 (speed) and 1.75 (mass) gives a total error factor of 3 which seems to be too low. A calculation using error propagation concludes again with error factors of half an order of magnitude assuming a speed of 10 km s^{-1} and an absolute speed error of 5 km s^{-1} . If we set $f(v, Q) = \log(m(v, Q))$ we derive Eq. 3.22 with the knowledge of $(\log(x))' = \frac{1}{x \cdot \ln(10)}$.

⁴At this facility a stream of dust grains with different sizes is accelerated at once, and the dust mass determination is achieved by the analysis of a hole in a 100 nm thin nitrocellulose foil.

$$\Delta f(v, Q) = \frac{\delta f(v, Q)}{\delta v} \Delta v + \frac{\delta f(v, Q)}{\delta Q} \Delta Q \quad (3.22)$$

$$= \left[\frac{-5.13}{v \cdot \ln(10)} - 0.135 \cdot \frac{\log(QT)}{v \cdot \ln(10)} + 0.122 \cdot \frac{\log(v)}{v \cdot \ln(10)} \right] \cdot \Delta v + \quad (3.23)$$

$$\left[\frac{2.94}{QT \cdot \ln(10)} + \frac{0.19 \cdot \log(QT)}{QT \cdot \ln(10)} - \frac{0.135}{QT \cdot \ln(10)} \right] \cdot \Delta QT$$

It has to be kept in mind, that Eq. 3.21 was derived with iron particles only. The fit method described here require a data set as large as possible to guarantee a wide application range in speed and mass space.

There exist, of course, the possibility to fit the three dimensional data with a hyperplane of a lower degree. The benefit is a constant slope of the charge-mass relation for a given velocity and this procedure is closer to the work of Stübig [2002] and Göller and Grün [1989]. The curvature of the hyperplane in Fig. 3.21 leads currently to a very strong rise at higher impact charges QT. We can avoid this by searching a hyperplane with the function $\log(m) = a_0 + a_1 \cdot \log(Q) + a_2 \cdot \log(v) + a_3 \cdot \log(v) \cdot \log(Q)$ and Eq. 3.24 is the direct result taking the QT calibration data. This equation does not consider calibration results with big grains from Munich, since those data scatter significantly and for the first step, the data approximation was searched.

$$\log(m_{QT}) = -6.30 + 0.453 \cdot \log(QT) - 6.71 \cdot \log(v) - 0.271 \cdot \log(v) \cdot \log(QT) \quad (3.24)$$

Similar to the minimum we get in the curve $v = \text{const.}$ and $v \geq 60 \text{ km s}^{-1}$ for the hyperplane with $n = 2$, we encounter a problem with the plane slope. The equation describes a plane which turns from a positive slope for low velocities to a negative slope at high velocities ($> 60 \text{ km s}^{-1}$). Such a calibration function might be applicable in the speed range $v = 1 \dots 60 \text{ km s}^{-1}$, but it is unacceptable for velocities outside of this range. Although we have no access to particles with higher speeds in the laboratory, we have proved the existence of stream particles with its high velocities in space and we have to find a calibration function which provides a better approximation in the high speed range. In order to do so, I include further data points at $v = 200 \text{ km s}^{-1}$ on the basis of the modelling results of S. Hsu to reach a positive slope of the hyperplane at higher speeds. The result is Eq. 3.25 and the corresponding plane is shown in Fig. 3.23.

$$\log(m_{QT}) = -9.64 + 0.214 \cdot \log(QT) - 3.82 \cdot \log(v) - 0.0628 \cdot \log(v) \cdot \log(QT) \quad (3.25)$$

How accurate is the fit using just a one dimensional relation? The error is slightly higher than for a two dimensional fit, and the cumulative distribution reveals an error factor of 2.42. In contrast, the error for the two dimensional fit with Eq. 3.22 was only 1.75. Nevertheless, the smooth surface provides a consistent way to determine the dust mass m of IIT impacts from the QT signal and a known speed v .

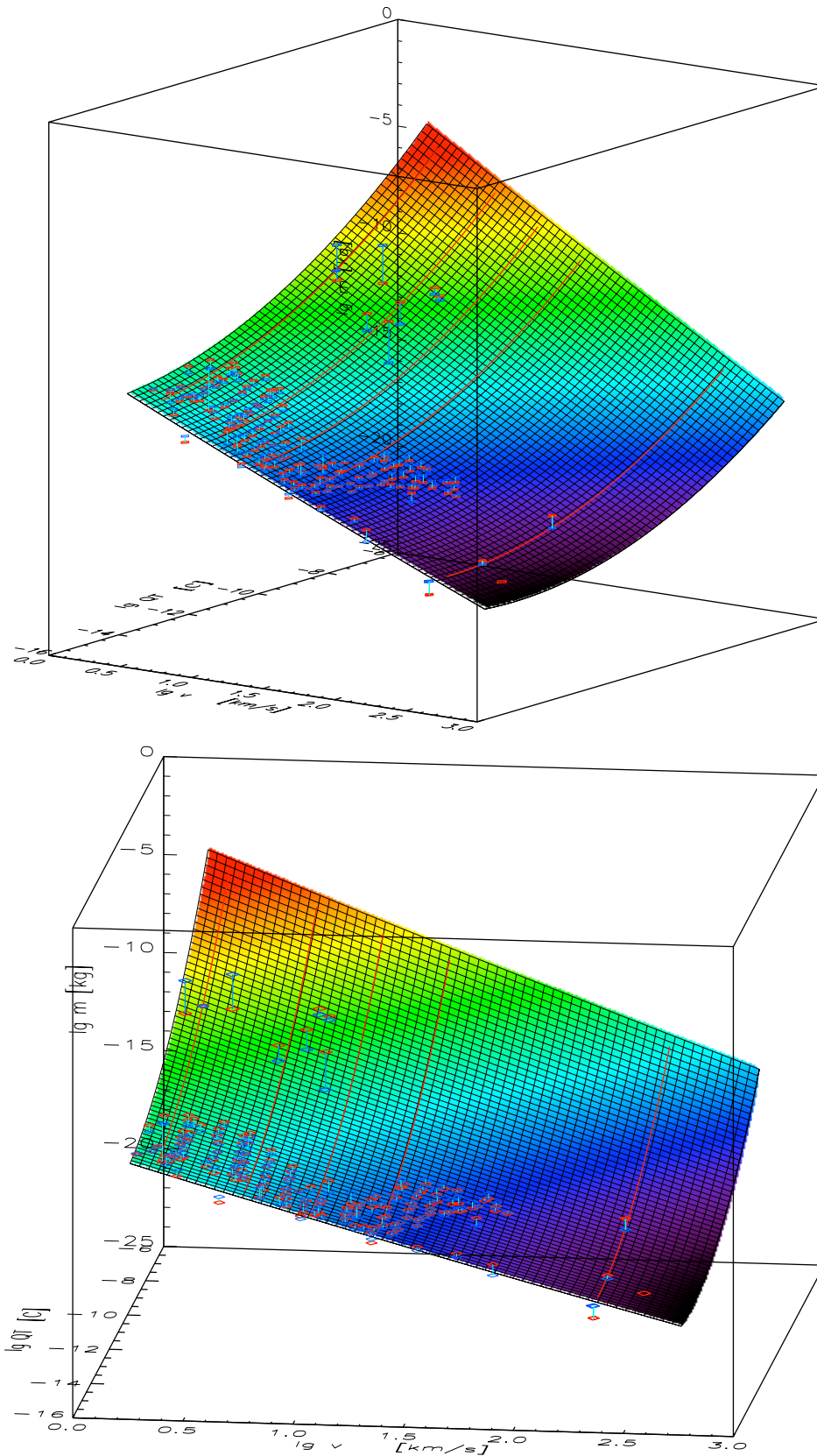


Figure 3.21: Two views of the fitted hyperplane of QT calibration data of IIT impacts (red symbols). The axis $[x,y,z]$ are $[v, QT, m]$ and only iron particles were considered. The blue symbols are the projected data points onto the hyperplane.

3 Cosmic Dust Analyser Performance

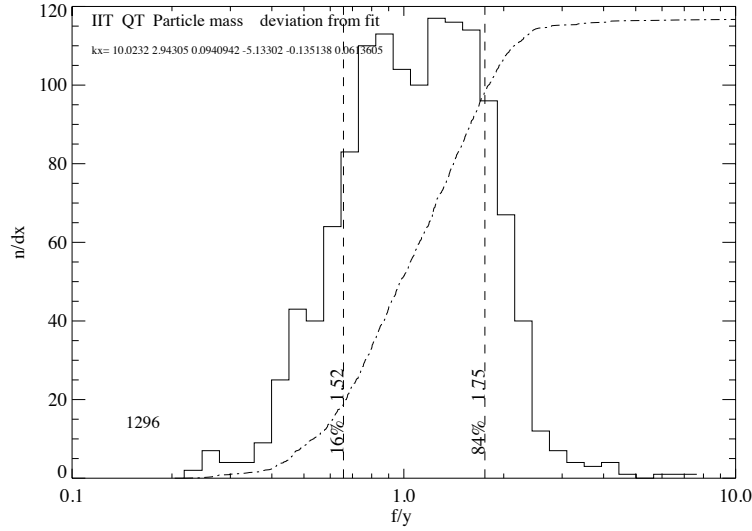


Figure 3.22: Histogram of the ratio f/y with f =calculated dust mass by fit-function and $y = m$. The derived error factor is 1.75 for iron impacts onto the IIT and the histogram belongs to the data shown in Fig. 3.21.

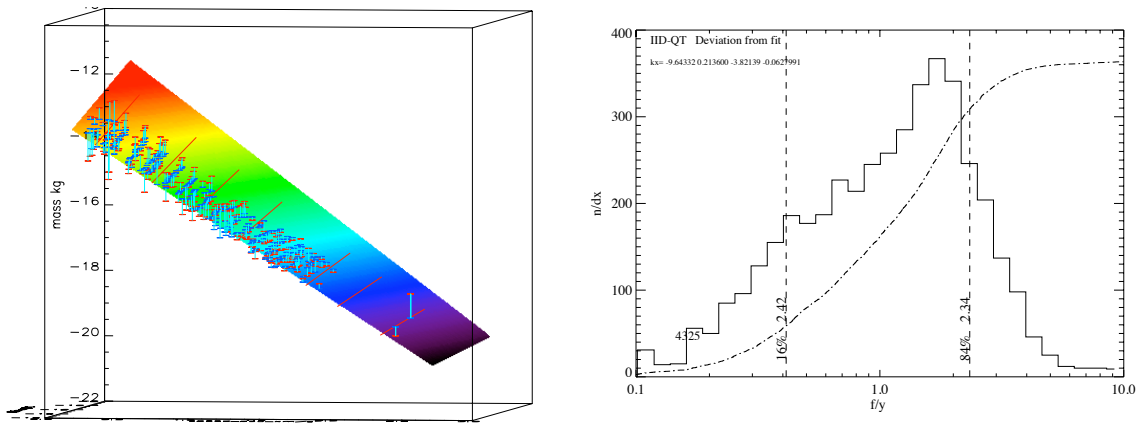


Figure 3.23: Low dimensional hyperplane approximation of the phase space $\{v, QT, m\}$. The plane slope for $v = \text{const.}$ is always positive as required. The error factor of this fit of 2.42 is given by the histogram (right).

The same fitting procedure was applied to the ion grid signal and the result is shown in Fig. 3.24. The applied fit range was set to $v = 1.6 \dots 64 \text{ km s}^{-1}$, $QI = 10^{-15} \dots 10^{-12} \text{ C}$ and $m = 10^{-18} \dots 10^{-12.5} \text{ kg}$. This fit results in a hyperplane with the maximum degree $n = 2$ for each dimension and the function is given by Eq. 3.26.

$$\begin{aligned} \log(m_{QI}) = & 8.15 + 2.10 \cdot \log(QI) + 0.0439 \cdot (\log(QI))^2 - 10.24 \cdot \log(v) \quad (3.26) \\ & - 0.497 \cdot \log(v) \cdot \log(QI) + 0.215 \cdot (\log(v))^2 \end{aligned}$$

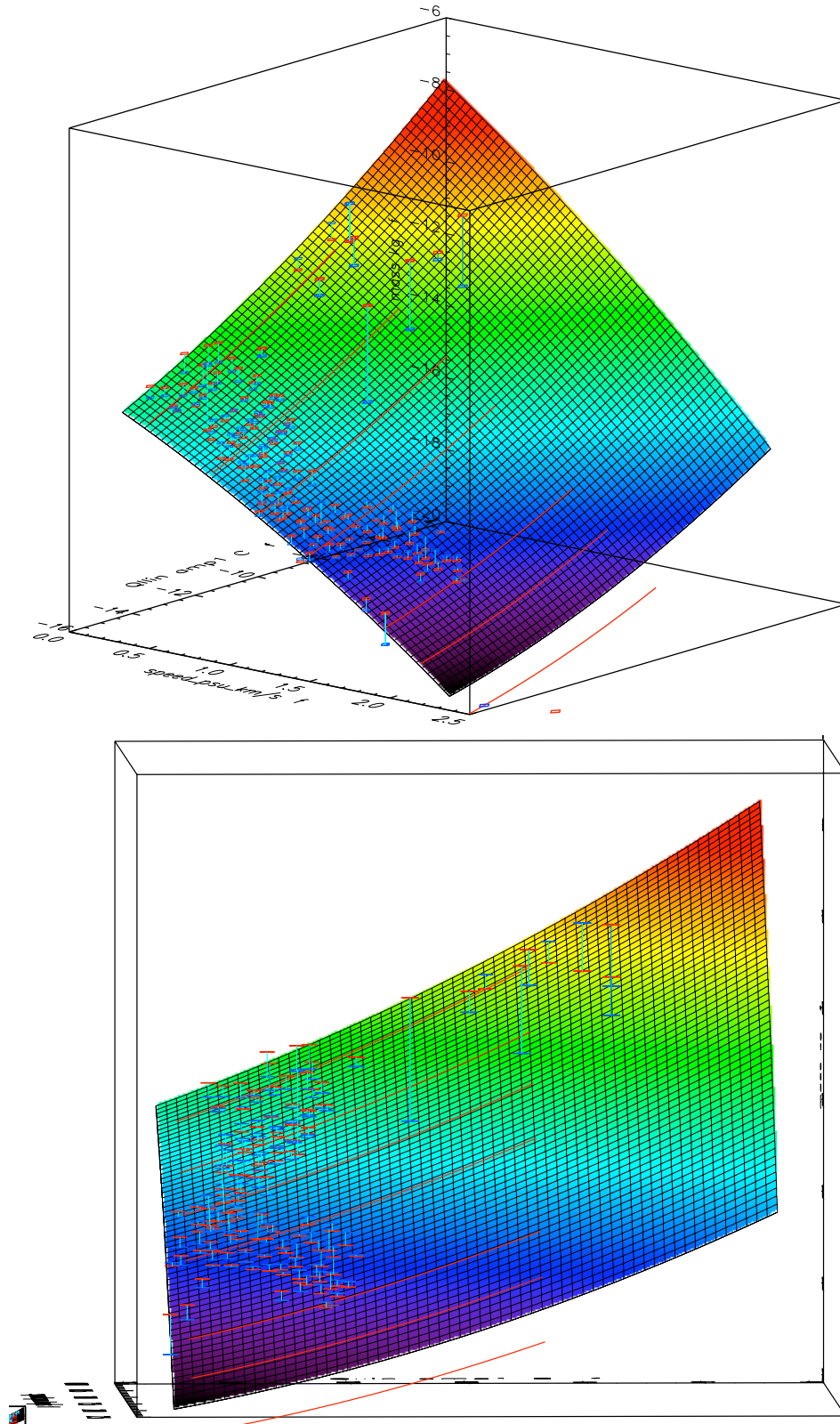


Figure 3.24: Hyperplane approximation of the particle mass m (z-axis) for IIT impacts using the charge signal QI and the particle speed v (xy-axis).

3 Cosmic Dust Analyser Performance

As in the previous surface plots, the red symbols are the real calibration data points and the blue symbols are the projected values. The bottom view along the speed axis (the QI charge increases from left to right and the z-axis is the mass) nicely shows the deviation between the two points indicated by the blue thin lines. The red lines are lines with equal speed. The hyperplane forms a curved surface which rises with increasing impact charge and decreasing impact speed. This shape is similar to the function derived for the channel QT which is no surprise.

The approximation given in Eq. 3.26 did not result in a hyperplane which makes sense in its physical behaviour, although the fit represents the given data with an error factor of 1.52. In this case, the Munich data points with its big masses were not taken into account. This data approximation leads to an unphysical surface shape: The surface was curved such that the dust mass decreases with increasing charge QI at constant impact velocities ($v > 100 \text{ km s}^{-1}$). Although the speed range above 100 km s^{-1} is not directly accessible and no laboratory calibration data are present, the physics behind the impact process would contradict to such a shape of the hyperplane. *Bigger grains at a given speed should always generate more impact charge.*

A new fit approach was performed with the emphasis on smooth and continuous rising function with both, increasing speed and increasing mass. The Munich data were considered now which shaped the surface in the required direction. The parameters of this fit result are given in Eq. 3.27.

$$\begin{aligned} \log(m_{QI}) = & -2.16 + 1.03 \cdot \log(QI) + 0.0180 \cdot (\log(QI))^2 - 3.85 \cdot \log(v) \quad (3.27) \\ & - 0.112 \cdot \log(v) \cdot \log(QI) - 0.365 \cdot (\log(v))^2 \end{aligned}$$

However, the price for this function is a slightly higher error factor shown in Fig. 3.25. The factor rises significantly from 1.52 (best fit) to 1.97. We should also not forget that this error factor seems to be quite small in comparison to former calibration approaches (which had factors of ≈ 10). Furthermore, this factor is only valid if the impact speed and the impact charge are determined accurately.

Nevertheless, for an official use, Eq. 3.27 is recommended to derive the dust mass from the QI signal for IIT impacts.

We go one step back by asking the question, if a fit by a hyperplane with a lower degree is possible⁵. The answer is yes, we do find a converging fit with the parameters given in Eq. 3.28:

$$\log(m_{QI}) = -4.24 + 0.597 \cdot \log(QI) - 5.82 \cdot \log(v) - 0.20 \cdot \log(v) \cdot \log(QI) \quad (3.28)$$

As usual, the units are kms^{-1} , C and kg . Due to the lower dimensionality, the error factor rises from 1.97 to 2.09. The diagrams in Fig. 3.26 show the resulting hyperplane for two views. The rise of the $v = \text{const.}$ lines were achieved by including artificial stream particle data before the fit. Without the data points at high speeds and low masses, the slope would be

⁵1-dimensionality in case of a plane means, that the highest degree of the each parameter x or y of the surface $f(x,y)$ is one

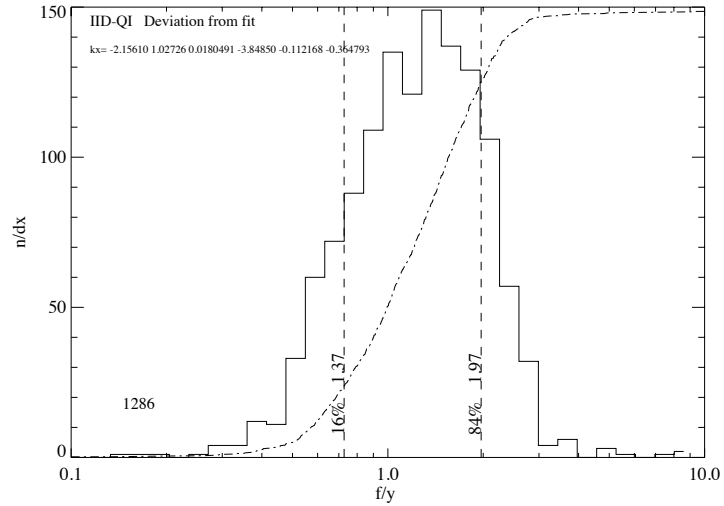


Figure 3.25: Histogram of the ratio f/m using Eq. 3.27 and the QI signal for IIT impacts. If the impact speed and the QI amplitude are accurately known, the error factor is 1.97.

negative. This would again lead to the wrong conclusion that higher charge yields are related to smaller dust masses. This result given in Eq. 3.28 avoids this and provides a consistent way to describe the calibration data of the ion grid signal.

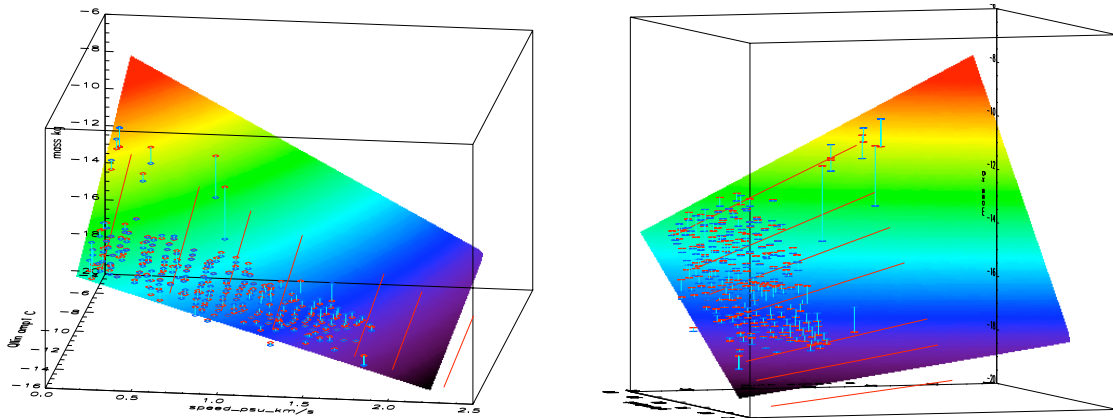


Figure 3.26: Hyperplane $\{v, QI, m\}$ for IIT impacts using Eq. 3.28. Red lines indicate data with $v = \text{const.}$

3.5 Chemical Analyser Target Calibration

3.5.1 Dust Impact Speed

The Chemical Analyser subsystem represents an impact ionisation system like the IID. The calibration methods for the impact speed are therefore similar: The rise time of the electrons collected at the target and the ratio of the target and ion grid signal are the two major calibration procedures. Further possibilities are the shape of the target signal and the type and peak shapes of the time-of-flight spectra.

Another procedure is based on the induced signal of a big dust grains carrying large primary charges: Once the dust grain enters the region between the acceleration grid and the target, the target amplifier detects the induced charge of the dust grain as long as the grain is located between the grid and the target. This behaviour would allow to accurately determine both, the flight time for the 3 mm distance (dust speed) and the primary charge⁶. However, this would require a high sampling frequency to allow the oversampling of the short rise time of the induced charge signal⁷. The CDA pre-trigger sampling frequency is only 375 kHz, and the normal sampling frequency is 6 MHz. Both sampling frequencies are too slow to oversample the short induction pulse. The other disadvantage is, that only big grains with large primary charges could be detected. Micron sized and submicron sized grains would not be detected with surface potentials of +5 V.

The possibility to derive the impact speed from the time-of-flight spectrum properties like peak abundances or peak shapes is under investigation, but never provided a consistent calibration function [Hillier et al., 2006, Postberg, 2007]. This method is not explained here in detail, but the general observation is: The occurrence of cluster ions and sharp mass lines indicate low velocities of $v < 10 \text{ km s}^{-1}$). The impact energy and the plasma temperatures of fast impacts do not allow the formation of cluster ions as observed in Postberg [2007] and Stübig [2002] or in Fig. 4.10. The number of clusters can therefore indicate the impact speed. Variations in dust compositions complicate the application of this procedure.

It is known, that the peak shape is related to the impact energy distribution (and angular distribution) of the plasma ions [Stübig, 2002, Hillier et al., 2006]. The Chemical Analyser is a time-of-flight spectrometer without a reflectron, which could compensate for the initial ion energy (like the instrument CIDA onboard Stardust [Kissel et al., 2004]). The peak shapes are therefore a direct picture of the impact plasma parameters. This sounds trivial, but a careful calibration requires a broad data set, which is provided now basically by the in-flight data. In order to derive the relation between impact speed and peak shape, the speed for at least a subset of the in-flight impact events has to be known. This leads again to the calibration methods introduced at the beginning: Derivation of the impact speed from the rise time or the ratio of the target and ion grid signal.

⁶If the dust grain electrical surface potential is known, this provides also the dust mass.

⁷The signal duration of a dust grain with 10 km s^{-1} is only 330 ns which would require a sampling speed of at least 20 MHz to record the signal.

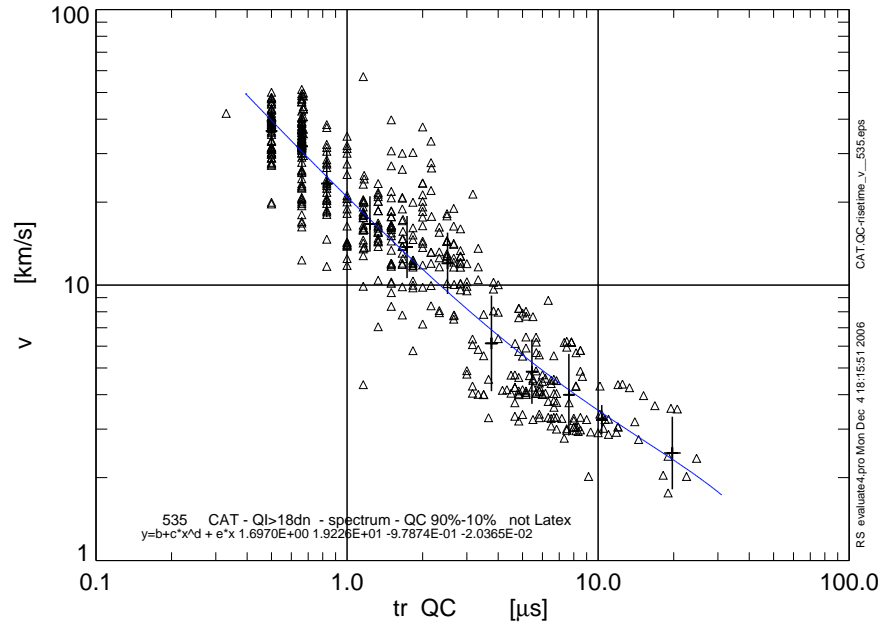


Figure 3.27: Determination of the impact speed by analysing the QC signal rise time.

Fig. 3.27 reveals the dependence of the target signal rise time t_r on the impact speed v . For calibration purposes, the axis labels were exchanged, the rise time is now allocated to the x-axis, which makes the derivation of the speed easier and which allows for a direct fit of the points. Each symbol represents one iron dust impact measured at the accelerator. Although this dependence seems to be rather obvious and strong, it is to be mentioned, that the axis are shown in a logarithmic scale.

For the analysis of the rise time a certain amplitude is required to avoid errors introduced by noisy signals. Signals showing ion signals greater than 10 fC were considered only, and the target signals were accordingly higher (factor 5). The rise time was evaluated by determining the time difference between 10% and 90% of the signal. The signal was converted from the raw dn values to engineering units (Coulomb) before deriving the rise time. Finally, a fit based on the general function $f(t_r) = a_0 + a_1 \cdot t_r^{a_2} + a_3 \cdot t_r$ was applied and the result is given in Eq. 3.29.

$$v_{QC} = 1.7 + 19.2 \cdot t_r^{-0.979} - 0.0204 \cdot t_r \quad (3.29)$$

The physics behind this coupling of signal rise time and the impact speed was explained in section 3.4.1: The strength of the primary impact charge leads to a leading pulse which affects the signal shape and the signal rise time.

How accurate is this method? Does the strong electric field between the acceleration grid and the target destroy the dependency? Which regions strike the ejecta and fragments after the impact? The target is much smaller than the Impact Ionisation Target and its curvature is only weak, since the overall diameter is 16 cm. It is unlikely that the ejecta hit target regions further away, but primarily they will hit the backside of the acceleration grid. The acceleration grid

3 Cosmic Dust Analyser Performance

is made out of a compound from copper beryllium and its yield is moderate; the yield of the rhodium target is certainly higher. The clear trend in Fig. 3.27 is therefore a surprise. Obviously the stronger electric field attracts the generated charges faster and compensates by this means for the disadvantageous facts listed above. The calculation of the error factor of 1.42 is shown in Fig. 3.28. This low factor is not the final error in speed calculation; we have to keep in mind that we used iron impacts only. Other projectile materials cause a further uncertainty such that a total error factor of 2 is more realistic [Stübig, 2002].

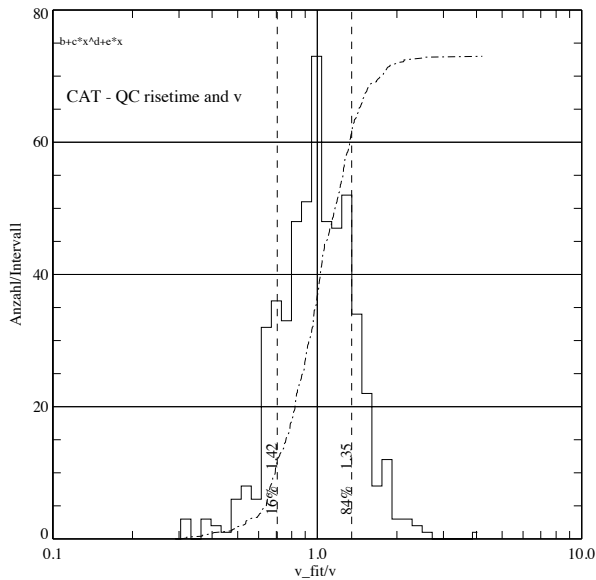


Figure 3.28: Histogram of the ratio of calculated speed to impact speed for CAT impacts. The analysis of the QC signal rise time provides an error factor of 1.42.

A second method to derive the impact speed is the analysis of the ratio between the electron and ion grid signal (QC/QI). Why should there be a dependence of this ratio with speed? It is true, that the acceleration field is quite strong with 3300 V/cm, but it is still not strong enough to focus all ions of the impact plasma to the ion grid. If all ions would be focused the ratio would remain constant under all impact conditions. This is not observed in Fig. 3.29. The left plot shows the ratio QC/QI over the impact speed with logarithmic axes, the second diagram plots the ratio QC/QI on the x-axis and the axis scales are linear. The left plot does not reveal a strong dependence with impact speed, but it shows the influence of the various projectile materials. The blue diamond symbols represent iron and two point clusters are observed: One cluster at high speeds with low QC/QI ratios, and one cluster at low speeds with a greater ratios. This simply means, that more ions are focused to the ion grid for high impact speeds. This would contradict to the theory, that high ion energies related with high impact speeds cause a defocusing of the ion beam. Here, it seems that the vanish of the impact ejecta process with high speeds causes a more natural ratio of the electron to ion signal. The ratios of $QC/QI > 10$ are very high and are obviously related to the fact, that the ions generated by secondary impacts are not sufficiently focused towards the ion grid⁸. This effect is more

⁸The secondary ejecta hit the back side of the acceleration grid and do not get enough field energy to be focused to the central and small ion grid.

pronounced if more ejecta are formed which is related to the projectile material. The high ratios of QC/QI for carbon (red star symbols) are not understood today. The weak aluminium shows only a moderate dependence of the ratio with impact speed (black squares).

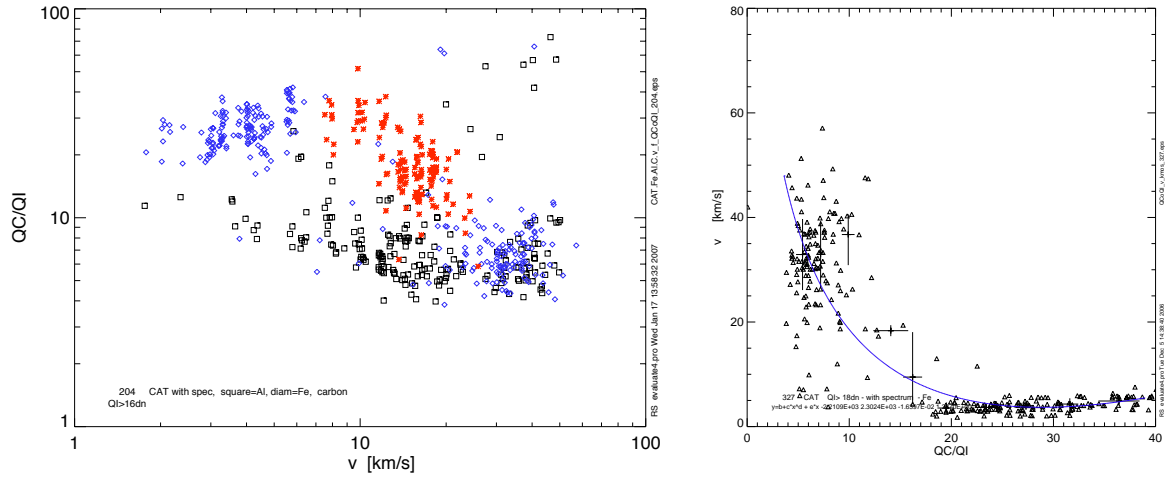


Figure 3.29: Ratio of target and ion signal QC/QI depends on the projectile material (left). Carbon: red, aluminium: black, iron: blue. The right plot has linear axis and uses only iron dust.

If we focus on the dust material iron, we get a picture as shown in the right plot of Fig. 3.29. The symbol clusters clearly separate again the two regions of the ejecta forming low speed process and the high speed process. The points were fitted using a function of the type $v(R) = a_0 + a_1 \cdot R^{a_2} + a_3 \cdot R$ and the parameter results are given in Eq. 3.30.

$$v\left(\frac{QC}{QI}\right) = -2211 + 2302 \cdot \left(\frac{QC}{QI}\right)^{-0.0164} + 1.24 \cdot \frac{QC}{QI} \quad (3.30)$$

The units of the values QC and QI are taken in Coulomb and the function output is defined in km s^{-1} . The function has a significant uncertainty between ratios of 8 and 14, but it can be used to constrain the speed to the low or high speed region.

An investigation of the ion grid signal rise time did not show a valuable dependence which can be used for speed calibration.

3.5.2 Dust Mass Determination

The approximation of the dust mass by fitting a hyperplane to the speed v and QC amplitude data is more difficult than the mass determination for IIT impacts. Consequently, the errors are bigger and the best fit provides a plane slope which changes its sign for very high impact speeds $v > 60 \text{ km s}^{-1}$: Rising impact charges for $v = \text{const.}$ result in a decrease of the dust mass for a certain v -interval. The curves of $v = \text{const.}$ show a minimum. An example of such a fit with a degree n of two is given in Eq. 3.31(iron particles). The cumulative distribution shows, that 68% of the data have values between 0.48 and 2.75, such that the error factor can

3 Cosmic Dust Analyser Performance

to be assumed as 2.7.

$$\log(m_{QC}) = 5.23 + 2.30 \cdot \log(QC) + 0.072 \cdot (\log(QC))^2 - 5.51 \cdot \log(v) - 0.20 \cdot \log(v) \cdot \log(QC) - 0.149 \cdot (\log(v))^2 \quad (3.31)$$

In order to avoid the mass minimum for $v = \text{constant}$, the fit function was modified to a lower degree by decreasing the degree from two to one. The result of such a linear fit is a hyperplane which is not curved. Eq. 3.32 gives the parameters for a plane described by the relation $f(x,y) = a_0 + a_1 \cdot y + a_2 \cdot x + a_3 \cdot x \cdot y$.

$$\log(m_{QC}) = -7.69 + 0.353 \cdot \log(QC) - 5.30 \cdot \log(v) - 0.165 \cdot \log(v) \cdot \log(QC) \quad (3.32)$$

This hyperplane has a slightly higher error factor of 2.99. Fig. 3.30 shows this 3D fit in the $\{v, QC, m\}$ space. Now, the surface shape provides a smooth and constant increase with only gradual changes. But the slope k of $\log(m) \sim k \cdot \log(QC)$ for constant v (rising m for increasing QC) decreases with v . The higher the speed, the lower the dependency of the impact charge from the dust mass. This is surprising and the slope reaches the value of zero around 100 km s^{-1} ! Higher impact speeds would even mean, that the measurement of high impact charges corresponds to smaller dust masses. The imagination of the physics behind this behaviour is again very difficult⁹.

For this reason, a third fit was executed by introducing further constraints to tilt the hyperplane to positive slopes for high velocities. It was decided, to use virtual data points at high impact speeds. The question is of course, which values should be taken in speed, mass and charge? Here the input from modelling of nano-dust streams was considered, since this is the only hint we have to constrain the data. The method to constrain the parameters was performed by S. Hsu and starts with the knowledge of a real dust impact in the outer saturnian system. The impacts considered have rise times which are very short and which are out of the calibration range ($>60 \text{ km s}^{-1}$ impact speed). The possible dust trajectories were traced back to the inner saturnian system taking into account the latest magnetospheric model of Saturn and the common forces like gravity and Lorentz forces. S. Hsu found solutions for the dust properties and normally they have a wide range of parameters (e.g. from 60 to 300 km s^{-1} and from 3 to 30 nm in size). But for selected dust impacts, the parameter ranges of possible solutions (launch at Saturn's ring system and hit the Cassini S/C location) was rather small. Therefore it was possible to found a solution for a specific dust impact event, its trajectory and properties of $[v, QC, m] = [200 \text{ km s}^{-1}, 1 \cdot 10^{-14} \text{ C}, 5 \cdot 10^{-22} \text{ kg}]$. This value was added in the calibration data set to tilt the hyperplane accordingly (to aim for a rising slope at high speeds) and the resulting function for the dust mass calculation by QC impact charges is given by Eq. 3.33. The impact speed v has the unit of km s^{-1} and the charge QC the unit of Coulomb.

$$\log(m_{QC}) = -9.09 + 0.239 \cdot \log(QC) - 3.91 \cdot \log(v) - 0.050 \cdot \log(v) \cdot \log(QC) \quad (3.33)$$

⁹It is possible that nm-sized grains are implanted in a metal surface and the resulting impact crater and impact charges become relatively low for $v > 100 \text{ km s}^{-1}$.

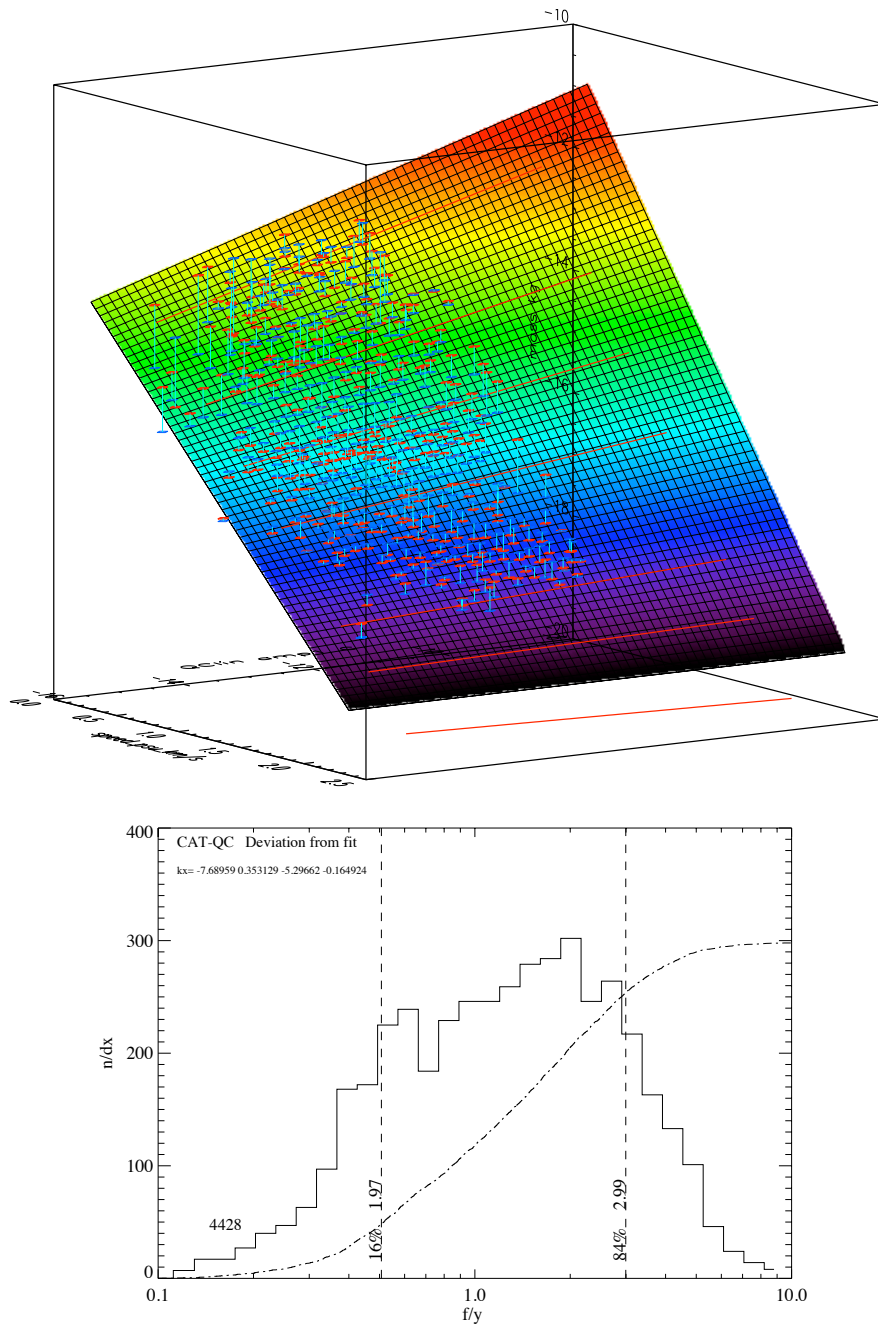


Figure 3.30: Top: Fit of $\{v, QC, m\}$ data for CAT impacts by a hyperplane with the degree 1 as defined by Eq. 3.32. The plane is bend in a way that the slope turns to negative values for impact speeds above 100 km s^{-1} . Bottom: Histogram to determine the error factor of ≈ 3 .

3 Cosmic Dust Analyser Performance

This function describes again a hyperplane with the degree of one and is an even, but tilted surface in the space $\{v, QC, m\}$. We cannot expect to lower the fit accuracy by artificially tilting the plane. The error factor derived by the cumulative distribution function of the ratio histogram is therefore slightly higher for Eq. 3.33 than for Eq. 3.32 and was determined to 3.1. The error histogram and its correlated cumulative distribution is shown in Fig. 3.31. The histogram shows, that 68% of the calculated dust masses have a deviation with a factor between 2.0 and 3.1. Although the error of this function is slightly higher, this formula is recommended for the dust mass determination of CAT impact by the analysis of the QC signal.

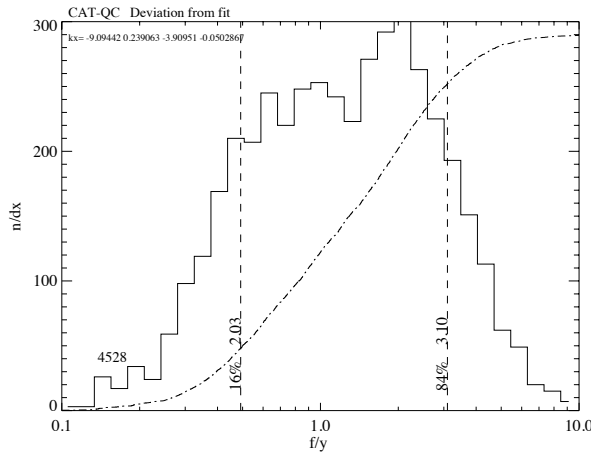


Figure 3.31: The error histogram shows the distribution of the deviation of the calculated dust mass to the real mass. The distribution refers to QC signals of CAT impacts described by Eq. 3.33.

The visualisation of the 3D fit in the $\{v, Q, m\}$ space is difficult and the reader cannot get an impression, how accurate the fitted hyperplane approximates the data points. This is much easier in a 2D view, where a curve goes through individual data points. However, the low degree of one of the hyperplane (no curvature) allows to tilt the plane in a way that an edge-on view is reached. Such an edge-on view was prepared for the fit with Eq. 3.33 and the plot is shown in Fig. 3.32. The space is filled with red symbols (original data points) and blue symbols (projected data points to the fitted hyperplane), which are connected by a bright blue line. The projection is along the mass axis (z), since the parameters speed and charge are known and measured. They do not represent the shortest projection to the surface to allow for a visualisation of the deviation in mass calculation. The red lines with constant speed are now straight and are shown in red. The edge-on view shows impressively, that the deviation of the calculated mass is normally much lower than one order of magnitude.

The second possibility to calculate the dust mass from the impact signals is the relation between, speed v , mass m and ion grid charge QI . Although we have 1000 Volts between the acceleration grid and the impact target, some ions are not focused properly to the ion grid with is a diameter of roughly 7 cm at a distance of 23 cm from the target. Some ions are lost and especially big particles with many fragments and ejecta generate charges on the backside of the acceleration grid. The ions generated at this location only see an effective potential which is much lower than the 3300 V/cm. The number of ejecta is dependent on the dust speed and

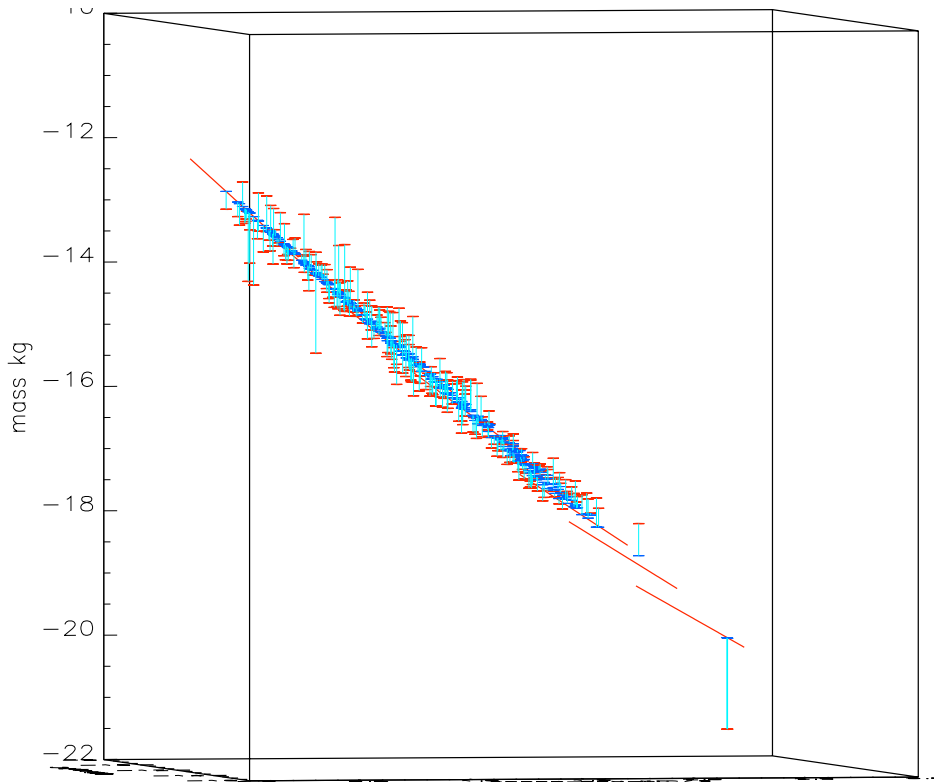


Figure 3.32: Edge-on view of the 3D hyperplane fit of the dust speed, impact charge QC and dust mass. The vertical bright blue lines connect the dust mass (red) with the calculated data (blue). The lines represent the error factor and are typically much smaller than one order of magnitude. The dust speed is plotted along the x-axis (from left to right). Straight red lines are curves with $v = \text{const.}$.

dust mass, whereas we expect a varying loss of ion grid charges. At this point it is therefore not clear, whether the means of the QI signals provides as consistent results for the mass calibration as the means of the QC signal.

Let us try now a three step approach in data approximation: First, fit the data with a hyperplane of degree $n = 2$ (curved hyperplane); second, reduce the dimensionality by one to $n = 1$ (plane hyperplane); and, third, apply further constraints to step 2 (add data points representing nano-sized stream particles).

$$\log(m_{QI}) = 9.63 + 2.13 \cdot \log(QI) + 0.0427 \cdot (\log(QI))^2 - 11.72 \cdot \log(v) - 0.556 \cdot \log(v) \cdot \log(QI) + 0.254 \cdot (\log(v))^2 \quad (3.34)$$

The 2-dimensional fit provides Eq. 3.34 and the next step is to omit the mixed terms (v, QI^2) , (v^2, QI) and (v^2, QI^2) since they do not provide any additional accuracy: The error factor is 1.55 for both cases and the cumulative distributions of the error histograms are almost identical.

3 Cosmic Dust Analyser Performance

For completeness, the full hyperplane function is given by Eq. 3.35, but I do not recommend his application for calibration. This surface is very curved and provides a negative slope in the mid speed range.

$$\begin{aligned} \log(m_{QI}) = & 51.9 + 7.61 \cdot \log(QI) + 0.22 \cdot (\log(QI))^2 - 138 \cdot \log(v) \\ & - 17.3 \cdot \log(v) \cdot \log(QI) - 0.55 \cdot \log(v) \cdot (\log(QI))^2 + 61 \cdot (\log(v))^2 \\ & + 8.0 \cdot (\log(v))^2 \cdot \log(QI) + 0.26 \cdot (\log(v))^2 \cdot (\log(QI))^2 \end{aligned} \quad (3.35)$$

The next step is the reduction of the degree n leading to Eq. 3.36. Unfortunately, this plane is twisted along the x-axis (speed), changing the slope to negative values (Fig. 3.33). This is no surprise as the former relations for the target charge QC (Eq. 3.32), and the mass determination of IIT impacts showed the same behaviour. Equation 3.36 provides an accuracy of a factor of 1.54, but an improvement of the slope trend is necessary.

$$\log(m_{QI}) = 0.0645 + 0.865 \cdot \log(QI) - 9.92 \cdot \log(v) - 0.463 \cdot \log(v) \cdot \log(QI) \quad (3.36)$$

Finally, we introduce constraints at high velocities by adding data points above 100 km s^{-1} . We have some flexibility in their definition as long as we twist the hyperplane to positive slopes at high speeds. The additional data were taken were defined as follows: $v = [60 \dots 200 \text{ km s}^{-1}]$, $QI = 1.2 \dots 2.6 \text{ fC}$ and $m = 5 \cdot 10^{-24} \dots 6 \cdot 10^{-22} \text{ kg}$. The result is given by Eq. 3.37, which turns the plane from Fig. 3.33 to Fig. 3.34. Now, the relation between v , QI and m is consistent, but the error factor increased from 1.54 to 1.83. In summary Eq. 3.37 is recommended for calibration using the ion grid signal of CAT impacts.

$$\log(m_{QI}) = -4.15 + 0.558 \cdot \log(QI) - 5.59 \cdot \log(v) - 0.144 \cdot \log(v) \cdot \log(QI) \quad (3.37)$$

3.6 Laser Yield Measurements

Laser charge yield measurements can significantly improve the calibration range of the impact ionisation process. The charge sensitive amplifiers of the CDA instrument have a measurement range which covers six decades ($1 \cdot 10^{-15} \text{ C} \dots 1 \cdot 10^{-9} \text{ C}$). This range cannot be covered by real dust impact experiments at the Heidelberg dust accelerator. The impact energy of the 2 MV-accelerated, micron sized dust impacts is not high enough to generate charges above $1 \cdot 10^{-12} \text{ C}$. The yield of the CDA gold target (IIT) is 600 C kg^{-1} at typical impact speeds of 10 km s^{-1} . With masses up to $3 \cdot 10^{-15} \text{ kg}$ the total charge produced at a dust impact is of the order of $1.8 \cdot 10^{-12} \text{ C}$.¹⁰

Today it is not difficult to generate laser induced plasmas with charges above 1 pC. However, some environmental conditions have to be considered before comparing laser and dust impact produced plasmas. First, the plasma generation time should be in the same order of magnitude. Dust impacts of 10 km s^{-1} interact with the impact target within 0.1 ns. Furthermore, the laser pulse should be short enough to not disturb or interact with the already generated plasma. No

¹⁰Recent tests of non-metallic materials showed values of 417 C kg^{-1} (Kapton) and 255 C kg^{-1} (Polyimid).

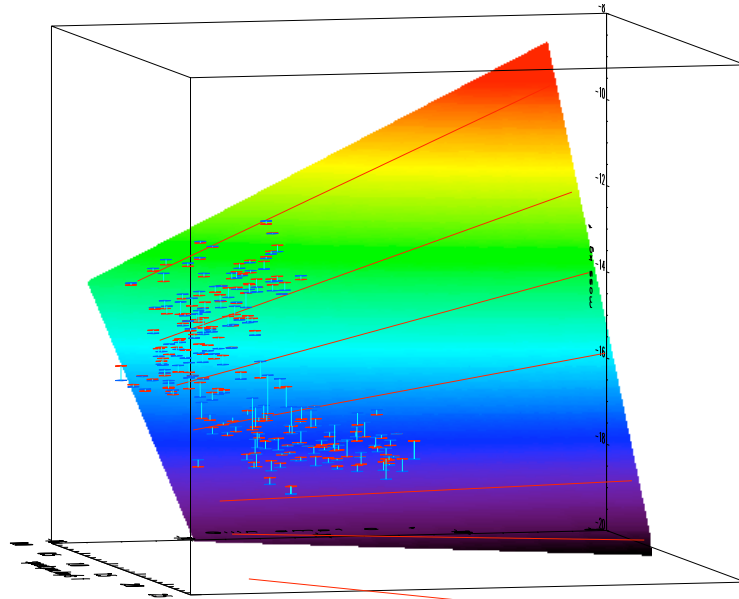


Figure 3.33: Hyperplane approximation for the mass calibration using the QI signal of CAT impacts. The surface function shows the difficulty to find solutions with rising masses (z-axis) for all ion charges (x-axis) for $v = \text{const.}$ (red lines). The slope of the red lines turn from positive to negative values with increasing speed. The lines are drawn for the velocities 2, 5, 10, 20, 60, 100 and 200 km s^{-1} . This hyperplane is not suited as calibration function.

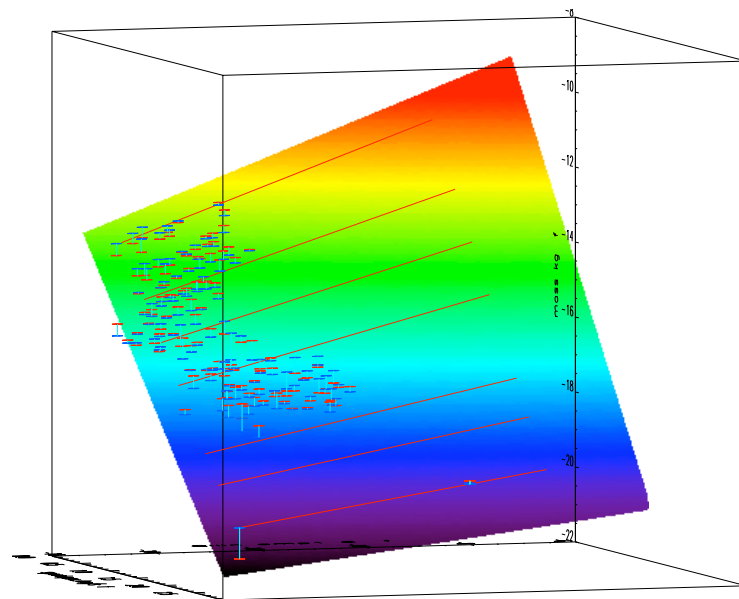


Figure 3.34: Final hyperplane fit of CAT impacts using the ion yield QI. Stream particle data provide an additional anchor point at high velocities ensure a positive slope for constant impact speeds. The error factor of this hyperplane fit is 1.83.

3 Cosmic Dust Analyser Performance

laser energy should be absorbed by the plasma already generated. In order to guarantee this, a pulse duration below 1 ns is needed. The latter effect is mitigated by the means of shorter laser wave lengths. Lasers with wave lengths in the UV range are much better suited than infrared lasers.

The other advantage to use laser induced plasmas during calibration measurements is the independence on the projectile material. Only a target material is necessary and the target material determines the type of ion species in the laser plasma. On the one hand, this is less realistic than the case of the dust impact generated plasma where both, the target and projectile species do occur, on the other hand this provides the advantage to replace the material of the target with cosmo chemistry relevant compounds or even real micrometeorite samples. This, in fact, was done by A. Mocker and the results of ToF mass spectra of dust impacts onto meteorite samples and of laser shots are presented in Mocker [2009]. The goal of her work is to generate time-of-flight mass spectra using existing meteorite samples (provided by M. Trieloff, Univ. Heidelberg) under various conditions. Laser-induced plasma properties are compared with hyper-velocity impact generated plasmas. Since this work is in progress, some facts will be presented here.

The laser energy has to be focused effectively onto the surface which is difficult for long focal lengths as they occur by using big spectrometers and big vacuum chambers. In order to achieve the highest energy density possible, the focal spot width should be minimized using appropriate focussing methods. Here, one focusing lens was used with a focal length of $f = 20$ cm. Then the focal spot size d_0 at the distance f behind the lens is dependent on the focal length f , the laser wavelength λ and the waist width of the input laser beam D_0 as given in Eq. 3.38. A small focal spot size is reached by using small laser wavelengths, a small focal length and a big width of the incident laser beam.

$$d_0 = \frac{M^2 4 \lambda f}{\pi D_0} \quad (3.38)$$

Furthermore, the smallest size is reached for a beam with a single mode TEM₀₀ with a Gaussian beam profile $I(r)$ of the shape

$$I(r) = I_0 \cdot e^{-\frac{r^2}{d_0^2}}$$

with $I(w_0) = I_0/e$. The beam quality has to be considered by the beam propagation factor M . The laser employed is the model PEAK AC of the company Azura Laser AG (Berlin) and provides a single mode with TEM₀₀ $M^2 < 1.4$.¹¹

The laser used is of type Nd:YAG and operates from single pulses up to 200 Hz with a single pulse energy up to $\approx 400 \mu\text{J}$ at a wavelength of 355 nm, a pulse width of 5 to 20 ns, a beam diameter of 0.3 mm and a beam divergence of 1.5 mrad. For plasma yield measurements (19.

¹¹In general, a Gaussian beam profile can be approached also by a multimode combination of beams and the beam-propagation factor M was introduced to describe adequately the laser mode characteristics [Roundy, 1999]. This factor compares the propagation characteristics of the real beam to those of a pure TEM₀₀ Gaussian beam.

Sep. 2005), the beam was widened to a diameter of 30 mm and focused by a lens with $f = 8$ cm onto a rhodium target under 45° incidence angle. The real target module of CDA did not fit into the small target chamber, and a simple experiment of a plane target, a grid and the optical lens was employed. The laser pulse power was modulated using a polarizer and the laser operated with 2 Hz. In a distance of 2 cm a grid was placed to applied a linear electric field of 2000 V. The spot size can be calculated according to Eq. 3.38 to a minimum of $1.7\mu\text{m}$. Due to the simple experiment setup, the spot size was probably a bit larger ($\approx 5\mu\text{m}$). Charge sensitive amplifiers (model Tennelec and self-made amplifiers) were connected to the target and determined the generated impact charges. The measurement results are shown in Fig. 3.35.

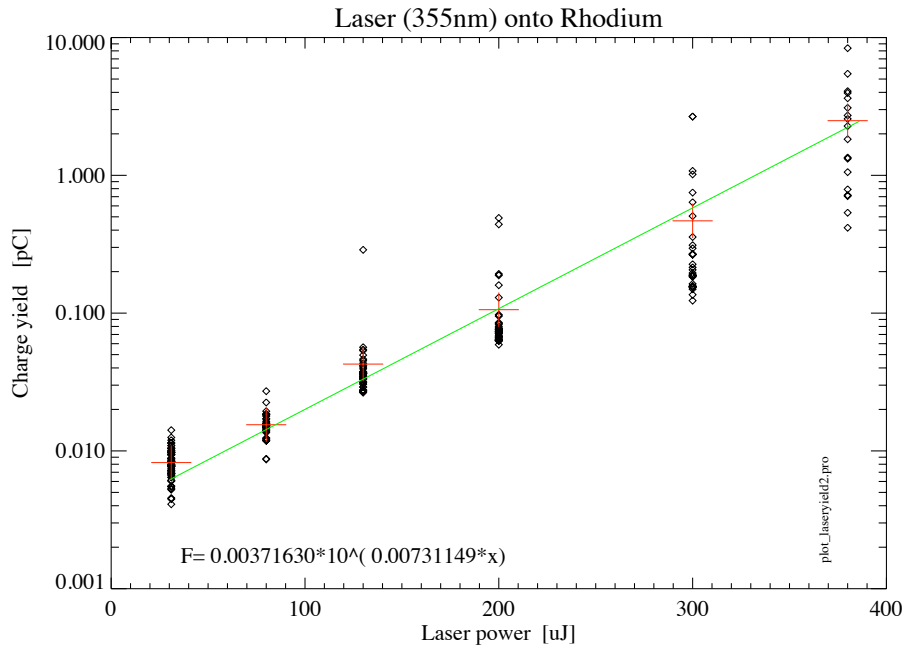


Figure 3.35: Charge yield of a rhodium target using a 355 nm laser with variable laser energy. The yield was measured using charge sensitive amplifiers and a bias voltage of 2000 V.

The laser energy E_L of $100\mu\text{J}$ relates to a power density of

$$L = \frac{E_L}{A \cdot t} = \frac{100 \cdot 10^{-6} \text{J}}{\pi (5 \cdot 10^{-6} \text{m})^2 \cdot 5 \cdot 10^{-9} \text{s}}$$

giving $2.5 \cdot 10^{14} \text{ J m}^{-2} \text{ s}^{-1}$ or $2.5 \cdot 10^{10} \text{ W cm}^{-2}$. The charge yield Y is rising with energy density and empirically Eq. 3.39 was derived.

$$Y = 0.0037 \cdot 10^{0.00731 E_L} \quad (3.39)$$

3 Cosmic Dust Analyser Performance

Here the laser energy is given in μJ and the charge yield has the unit of pC. Although the laser energy is stable and varies only by 3% , the measured yield can vary by a factor of up to 10. This is caused by small vibrations of the sample holder within the vacuum chamber. Small variations of the spot size and spot location irradiate different areas with different surface contaminations. It was shown, that especially for power densities below $3 \cdot 10^{10} \text{ W cm}^{-2}$ the ionisation of surface contaminations play a major role [Mocker, 2009].

Table 3.2: Energy and power densities of dust impacts. The assumed dust density was 1200 kg m^{-3} and the impact duration was set to 0.1 ns. Two impact speeds of 6 km s^{-1} and 18 km s^{-1} were considered. 18 km s^{-1} was the relative impact speed of dust grains during the inclined Enceladus flyby in 2008. Water ice grains were considered with a constant impact duration of $1 \cdot 10^{-10} \text{ s}$. In comparison the impact parameters of interstellar dust (ISD), the Giotto-Halley flyby and dust stream particles are listed. The table shows the dust diameter D , mass m , impact speed v and energy E , energy density E/A and power density L .

D μm	m kg	v km s^{-1}	E J	E/A J cm^{-2}	L $1 \cdot 10^{10} \text{ W cm}^{-2}$	
10 nm	$6.3 \cdot 10^{-22}$	18	$1.0 \cdot 10^{-13}$	0.13	0.13	
200 nm	$5.0 \cdot 10^{-18}$	18	$8.1 \cdot 10^{-10}$	2.6	2.6	
500 nm	$7.9 \cdot 10^{-17}$	18	$1.3 \cdot 10^{-8}$	6.5	6.5	
1 μm	$6.3 \cdot 10^{-16}$	18	$1.0 \cdot 10^{-7}$	13	13	
2 μm	$5.0 \cdot 10^{-15}$	18	$8.1 \cdot 10^{-7}$	26	26	
10 μm	$6.3 \cdot 10^{-13}$	18	$1.0 \cdot 10^{-4}$	130	130	
100 μm	$6.3 \cdot 10^{-10}$	18	0.102	1290	1290	
10 nm	$6.3 \cdot 10^{-22}$	6	$1.1 \cdot 10^{-14}$	0.014	0.014	
200 nm	$5.0 \cdot 10^{-18}$	6	$9.0 \cdot 10^{-11}$	0.29	0.29	
500 nm	$7.9 \cdot 10^{-17}$	6	$1.4 \cdot 10^{-9}$	0.72	0.72	
1 μm	$6.3 \cdot 10^{-16}$	6	$1.1 \cdot 10^{-8}$	1.4	1.4	
2 μm	$5.0 \cdot 10^{-15}$	6	$9.0 \cdot 10^{-8}$	2.9	2.9	
10 μm	$6.3 \cdot 10^{-13}$	6	$1.1 \cdot 10^{-5}$	14	14	
100 μm	$6.3 \cdot 10^{-10}$	6	0.011	144	144	
10 nm	$1.57 \cdot 10^{-21}$	200	$3.14 \cdot 10^{-11}$	40	80000	stream
600 nm	$3.39 \cdot 10^{-16}$	27	$1.24 \cdot 10^{-7}$	44	200	ISD
1 μm	$1.05 \cdot 10^{-15}$	68	$2.42 \cdot 10^{-6}$	308	2100	Giotto

In comparison to the laser energy density of $2.5 \cdot 10^{10} \text{ W cm}^{-2}$, the energy density produced by an impact of a dust particle with a size of $0.1 \mu\text{m}$ ($m=4 \cdot 10^{-15} \text{ kg}$) and an impact speed of 30 km s^{-1} has a value of

$$\frac{\frac{1}{2} \cdot m \cdot v^2}{\pi \cdot r^2} = \frac{1.8 \cdot 10^{-6} \text{ J}}{7.8 \cdot 10^{-13} \text{ m}^2} = 2.3 \cdot 10^6 \frac{\text{J}}{\text{m}^2}$$

which corresponds to energy densities of $230 \frac{\text{J}}{\text{cm}^2}$. Assuming an impact interaction time of the particle surface with the target material of 0.03 ns, the according power density is there-

fore $7 \cdot 10^{12} \frac{W}{cm^2}$ and much higher than the laser power density used in these tests. The power densities of dust impacts are comparable to the laser power densities in the case of low impact speeds ($<5 \text{ km s}^{-1}$) and small grain sizes ($<2 \mu\text{m}$). Generally, the high energy densities as listed in Tab. 3.2 explain the modelled high ion energies of $>50 \text{ eV}$ of the impact generated rhodium target ions [Hillier et al., 2006]. The calculations show, that power densities above $10^{13} \text{ W cm}^{-2}$ might occur during hyper-velocity impacts of jovian or saturnian stream particles and the related mass spectra indicate target ion energies of the order of 100 eV (broad leading flank of the rhodium peak, [Kempf et al., 2005b, Postberg et al., 2006]).

Former results showed, that laser densities of $1 \cdot 10^6$ to $1 \cdot 10^7 \text{ W cm}^{-2}$ at 355 nm cause only light absorption and ions are build by desorption from the material surface, whereas light densities above $1 \cdot 10^8 \text{ W cm}^{-2}$ already generate material ablation, leading to craters in the focus area. The interaction of intense laser light with surfaces was extensively studied by Novodvorsky et al. [1999] and Müller et al. [2003]. Srivastava et al. [2006] worked on the determination of the angular and energy distribution of laser generated plasma ions.

3.7 High Rate Detector

The overall objective of the HRD is to carry out quantitative measurements of particle flux and mass distribution throughout the Saturn ring system. The detector carries two PVDF type foils of different sizes and sensitivities. The big detector has a sensitive area of 50 cm^2 and consists of a $28 \mu\text{m}$ thick foil, whereas the small detector has an area of 10 cm^2 and a thickness of $6 \mu\text{m}$. The foil basically determines the impact energy of the dust grains; impacting particles destroy a permanently polarized plastic foil and electrodes register a current pulse which is proportional to the destroyed volume. During calibration measurements, the number of electrons N of iron and glass particle impacts was determined as given by the Eqs. 3.40.

$$\begin{aligned}
 N_{Fe}(6\mu\text{m}) &= 3.6 \cdot 10^{18} m^{1.3} v^{3.0} \implies m = \left(\frac{N_{Fe}}{3.6 \cdot 10^{18} v^{3.0}} \right)^{\frac{1}{1.3}} & (3.40) \\
 N_{Glass}(6\mu\text{m}) &= 1.36 \cdot 10^{13} m^{0.7} v^{1.3} \\
 N_{Fe}(28\mu\text{m}) &= 3.6 \cdot 10^{18} m^{1.3} v^{3.0} \\
 N_{Glass}(28\mu\text{m}) &= 1.36 \cdot 10^{13} m^{0.7} v^{1.3}
 \end{aligned}$$

The HRD mechanics, electronics and calibration was described in Srama [2000b] and Srama et al. [2004a] and the detector measurement principle is well established. PVDF based detectors were applied in many former space missions due to their simplicity and reliability [Simpson and Tuzzolino, 1985]. However, there are some facts in former publications which were either wrong or not presented in a useful manner. We therefore have to present the calibration formulas again.

The foils are energy detectors and the impact speed has to be known in order to derive the dust mass. The speed might be derived from IIT data or from modelling results. Generally, the HRD is less sensitive than the IID and the mass thresholds are typically above 1 micron .

Grain sizes measured by HRD are big enough to be dominated by gravitational forces. If the grains move on almost circular orbits, simple assumption about their relativ impact speed can be derived directly from Cassini's state vector. Eq. 3.40 shows the relation between the number of generated electrons N , the dust mass m (g) and the impact velocity v (km s^{-1}). Generally, the relation between speed, mass and number of electrons is given by Eq. 3.41 with a constant K .

$$N = K m^\alpha v^\beta \quad (3.41)$$

If we assume spherical grains of radius $r_g = \left(\frac{3}{4\pi\rho}\right)^{\frac{1}{3}} \cdot m^{\frac{1}{3}}$ with density ρ we get the general Eq. 3.42 to calculate the grain radius in dependence on the impact speed v .

$$r_g = \left(\frac{3}{4\pi\rho}\right)^{\frac{1}{3}} \cdot \left(\frac{N}{K \cdot v^\beta}\right)^{\frac{1}{3\alpha}} \quad (3.42)$$

However, we do have two different detectors (small and big) and four charge thresholds for each device. Furthermore, the HRD can be commanded to an unsensitive range (High mass range) by switching an internal relay. We know, that most dust particles in Saturn's E-ring are made out of water ice such we can assume a dust density of 1 g cm^{-3} . The related mass thresholds are given in Tab. A.5 in the appendix on page 196 and they vary with the impact speed. The relative impact speeds on Cassini vary in the E ring between 4 and 18 km s^{-1} . We can use Fig. 3.36 to derive the sensitivity thresholds given as particle diameter of the two HRD detector foils and its four internal electronic thresholds. But it has to be noted, that the figure is applicable only for the low mass range (default) of HRD. The high mass range is approximately a factor of 10 less sensitive (compare Tab. A.5). Furthermore, a comparison of the two detector thresholds shows a nice condition for cross calibration: The threshold **M1** of the big detector is similar to the threshold **m2** of the small detector. HRD measurements were discussed in detail by Kempf [2007].

3.8 Dead Time Correction

Dust instruments measure dust densities and dust fluxes by various methods. Independent on the measurement method, a dead time typically occurs in the measurement processing and data recording cycle. For the CDA instrument, an analysis was performed to define the function behind the dead time process, which is by far non-trivial due to the interaction of software and hardware. Here, some further laboratory measurements and details are given in addition to the results given in Kempf [2007].

The measurement of a dust impact, or generally speaking, of an event, starts with the generation of charge signals which cause rising signals at the charge sensitive amplifiers. A comparator is set with a predefined amplitude threshold and compares the amplifier output signal with the threshold. Signals higher than the threshold release a trigger and the signal processing starts: buffer read-out of the channels QP, QC, QT, QI and QM, amplitude, rise time, base line and integral calculations, signal compression and signal storage. The entire process takes $\approx 800 \text{ ms}$ depending on the compression and data frame settings, before the next measurement

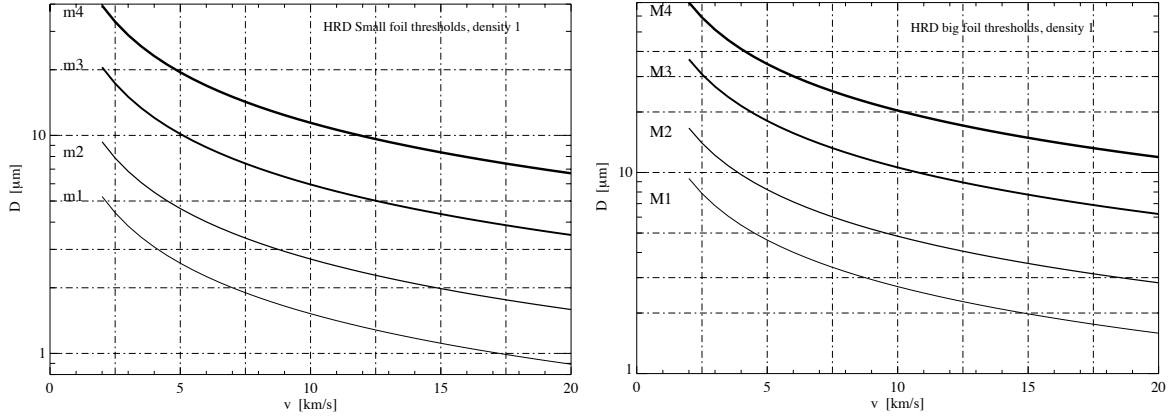


Figure 3.36: HRD dust detection thresholds given as grain diameter for the small foil (left) and the big foil (right). Four lines represent the four different electronic thresholds of the HRD. The small detector measures dust grains with sizes $>1.5 \mu\text{m}$ diameter at impact speeds of 10 km s^{-1} assuming a grain density of 1 g cm^{-3} . The big foil has higher mass detection thresholds due to its thicker PVDF foil which is less sensitive.

cycle is enabled (opening the event definition). The processing parameters are flexible and it is possible to store the data compressed or uncompressed. Furthermore, it is possible to store only selected channels in order to save bandwidth (e.g. neglect noisy channels). But this flexibility means, that the processing time is highly variable. In addition, the CPU speed can be changed by a factor of two. However, for the accurate determination of dust densities and dust fluxes, it is necessary to accurately determine the measured event rates, and a rate correction is necessary. It was decided already in the cruise phase to avoid flexible processing and dead times. The maximum processing time was estimated to almost one second and the flight software was programmed in a way, to always allocate a dead time of (almost¹²) one second after each event trigger.

The number n' is the counted number of dust particles recorded in each time interval T . For each of the n' particles within T , we lose the time $t = n' \cdot \tau$. For a total number of n particles within T , the number of lost particles Δn is then $\Delta n = n \cdot n' \tau = n - n'$ and we receive the common formula (Eq. 3.43) for the real event rate n . This equation is well established and is taken normally in experimental physics (e.g. measurements with the Geiger-Müller tube in nuclear physics) for dead time correction.

$$n = \frac{n'}{1 - n' \tau} \quad (3.43)$$

The parameter τ is the dead time of an individual event and can reach 1 second as a maximum. A good approximation is also the value of $\tau = 0.94 \text{ s}$. However, Eq. 3.43 is applicable for CDA only in case of rather low event rates ($\ll 1 \text{ s}^{-1}$) and we need to correct for the time grid of 0.125 ms given by the real time interrupt cycle, which determines the times of enabling

¹²For details see [Kempf, 2007]

3 Cosmic Dust Analyser Performance

a new measurement. Kempf derived the correct formula for CDA which is given by Eq. 3.44.

$$n = \frac{1}{\Delta} \cdot \ln \left(\frac{\Delta}{\frac{1}{n'} - \tau_{max}} + 1 \right) \quad \text{or} \quad n = 8 \cdot \ln \left(\frac{0.125}{\frac{1}{n'} - 1} + 1 \right) \quad (3.44)$$

The true event rate n is dependent on the measured rate n' , the time step Δ (one real time interrupt cycle, 0.125 s) and the maximum dead time τ_{max} of an individual event which is one second. The difference is not big for moderate impact rates, but becomes significant for higher rates close to 1 s^{-1} . Measured impact rates of 0.9 s^{-1} lead to real rates of 5.76 s^{-1} by Eq. 3.43 and of 6.03 s^{-1} by Eq. 3.44 which represents a deviation of only 4%. For higher rates the correction is significant as a comparison of the measured rate of 0.98 s^{-1} shows: Eq. 3.43 provides a value of 12.06 s^{-1} and Eq. 3.44 gives a rate of 15.7 s^{-1} , which means a difference of already 23%. A more strict application of Eq. 3.43 with a dead time $\tau = 1 \text{ s}$ even leads to rates of 49 s^{-1} which is much too high. The value of $\tau = 0.94 \text{ s}$ represents a mean dead time of 7.5 RTIs which is more realistic.

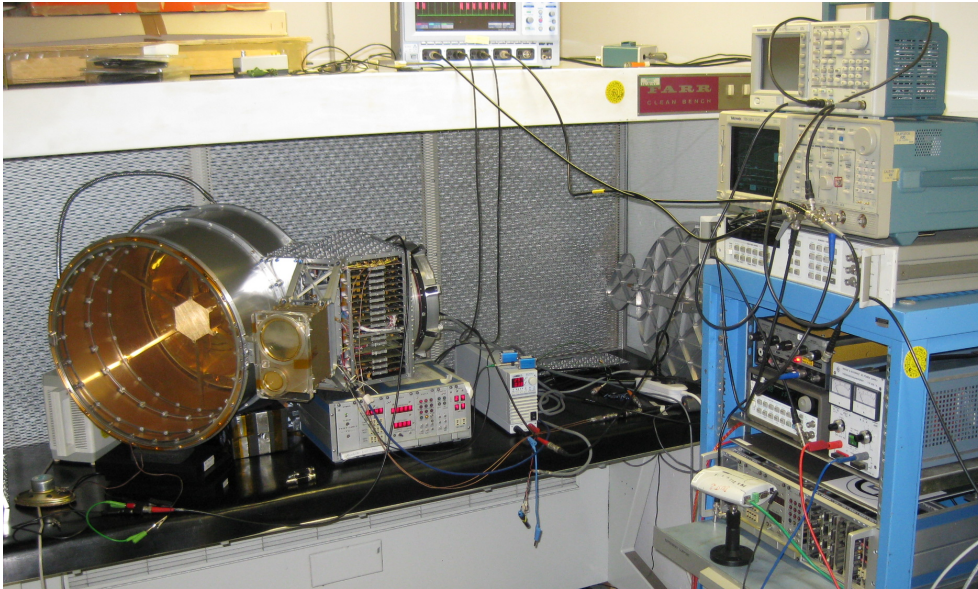


Figure 3.37: Clean bench with the flight spare unit of the CDA instrument. The polycarbonat cover allows the view to the golden DA target. The front side of the main electronics box is open. This test setup was used for dead time investigations.

Now, it was necessary to investigate the rate measurements of the CDA instrument under realistic conditions. Most measurements were performed with the flight software version 10.0 and it was decided to focus on tests with this version (Fig. 3.37). Nevertheless, the rate measurements are, of course, dependent on the flight software. Compiler flags like “time optimised” or “space optimised” influence binary code and the software running conditions. The event processing time and the dead time might also depend on internal parameter settings (wavelet compression parameters like the shrinking parameter). Realistic processing values

which were used during ring plane crossings were selected and remained unchanged. Nevertheless, the default dead time of the CDA system is one second at maximum. After an event trigger, the software is waiting seven RTIs before opening the event definition again. This process leads to an instrument dead time which lies between 7 and 8 RTIs (0.875 s and 1 s). Realistic measurements were performed using stochastic event triggers. No standard pulse generator was used in order to avoid systematic errors and interferences of the stimulating events and the internal interrupt system. Instead the trigger events obeyed the Poisson process. The Poisson distribution is a discrete probability distribution which describes the result of the Bernoulli experiment: A stochastic event with two possible states is executed many times. The probability function is described by Eq. 3.45

$$P_S(x) = \frac{\lambda^x}{x!} e^{-\lambda} \quad (3.45)$$

The parameter λ is a positive number and the expected value and the variance of the distribution. The Poisson statistics is often used to describe timely processes. If we assume a stochastic event which occurs in average once every $t = t_1$ seconds, the Poisson distribution $P_S(x)$ with $\lambda = t_2 \cdot 1/t_1$ describes the probability, that x events occur in the time frame $t = t_2$. The Poisson process is stationary and independent on time. The Poisson distribution describes the number of stochastic events within a time interval and the time between two events is exponentially distributed. The exponential distribution with the probability density parameter λ is described by Eq. 3.46 (probability density function).

$$f_X(x) = \lambda \cdot e^{-\lambda x} \quad (3.46)$$

In a first step exponentially distributed time tags were created which were used to trigger the CDA instrument stochastically.¹³ Before using the data for extended rate measurements, the test data had to be verified. The time series were checked and compared with the expected distribution according to Eq. 3.46. The comparison between the generated test data and the function is shown in Fig. 3.38. Four cases with the mean frequencies of 1, 2, 5 and 10 Hz were investigated. The coincidence between the generated data and the predicted distribution is almost exact and totally sufficient for the foreseen tests. Normalised and detailed results for the frequencies 10 Hz, 1 Hz and 0.5 Hz is given in Fig. 3.39. The fit functions were derived to $f(t) = 9.957 \cdot e^{-9.957t}$, $f(t) = 0.999 \cdot e^{-0.999t}$ and $f(t) = 0.500 \cdot e^{-0.500t}$ showing that the deviations between the expected frequency values and the parameters used for data generation are negligible.

A generated data set with an event frequency of 0.5 Hz was compared with the Poisson statistics and its result is shown in Fig. 3.40. A slight deviation around the maximum of 30 min^{-1} of the artificial data set and the ideal function does occur, but will not be relevant for the following tests.

After this verification of the data generation process for stochastic events, various data sets have been created with mean frequencies between 0.1 Hz and 50 Hz. The generated lists of

¹³The c-program genexp was used to create the data.

3 Cosmic Dust Analyser Performance

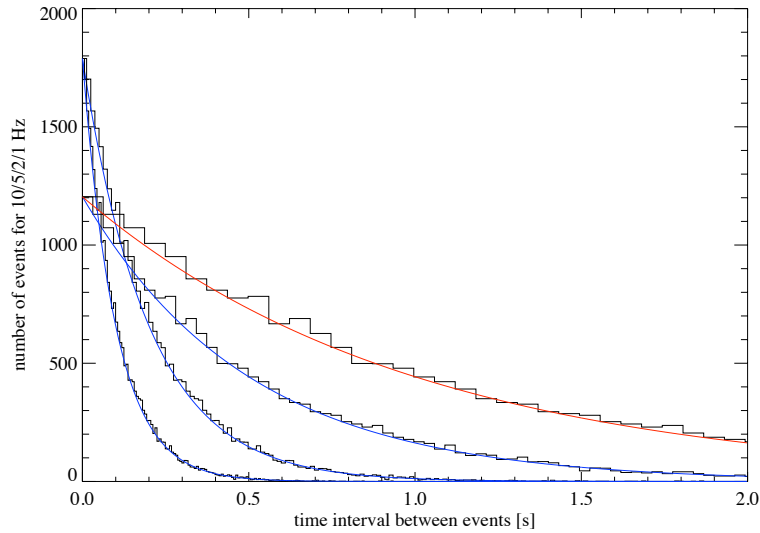


Figure 3.38: Comparison of generated test data (histogram) following a Poisson statistics and the exponential distribution function (smooth continuous line). The time difference between individual events is exponentially distributed.

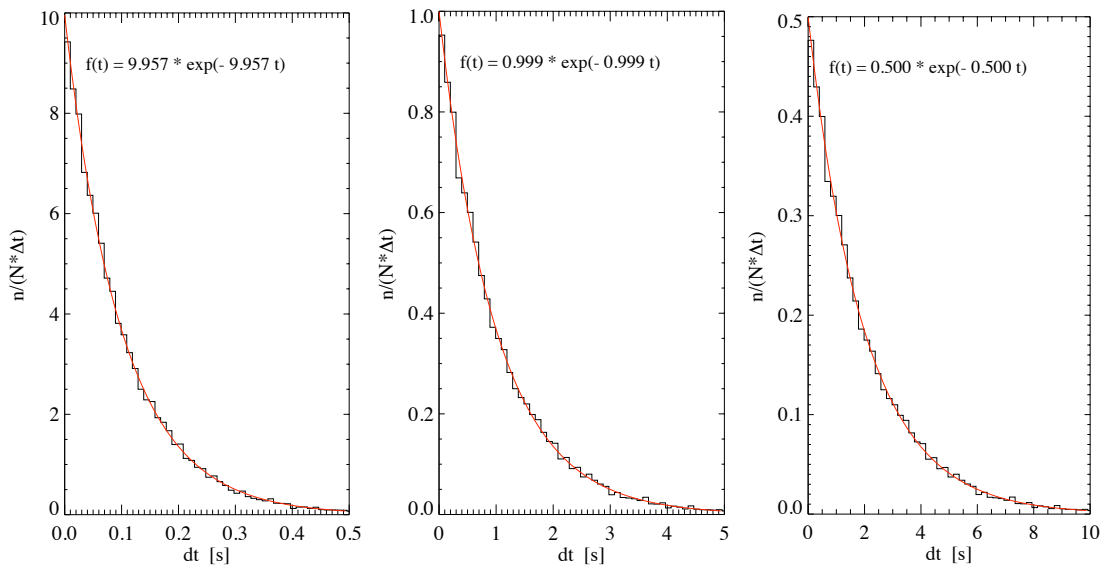


Figure 3.39: Data verification of generated stochastic events and the exponential distribution. The excellent correlation validates and qualifies the generated test data.

event times were read by a special program running on a notebook of the ground equipment. Each event changed the status of one pin of a parallel connector, and this signal was used to trigger a pulse generator. The pulse generator produced a typical pulse shape of the ion grid and the signal was routed over a capacitance into the preamplifier of the ion grid channel (QI),

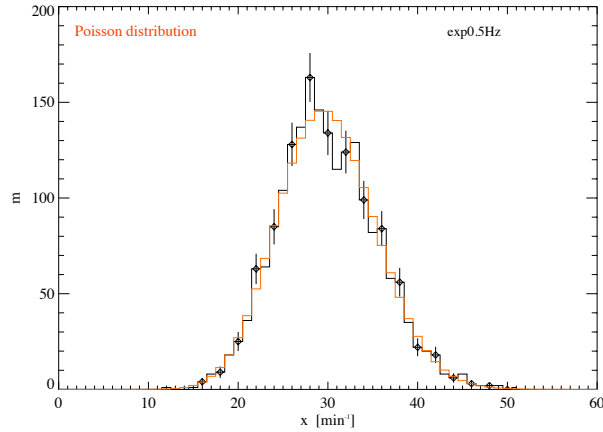


Figure 3.40: Stochastic data set (black histogram) with a maximum at 0.5 Hz and Poisson distribution function (red line). The coincidence verifies the data generation process.

which finally triggered the CDA instrument. Although various flight software version were tested, results only of the flight software version 10.0 will be displayed. The test setup used allows to feed stochastic distributed events (and any other arbitrary event distribution) into the flight spare unit CDA system. By this method, a realistic test setup was achieved to study dead time effects of the CDA trigger and counting system under various loads (event frequencies). However, no time delay shall occur between the computer generated pulse chain and the input into the preamplifier. Measurements showed, that the delay of the pulse generators is negligible (order of ns) and the delay at the parallel port is rather constant and approximately 1 ms. This delay time was accepted due to the fact that the highest mean event rates were 50 Hz.

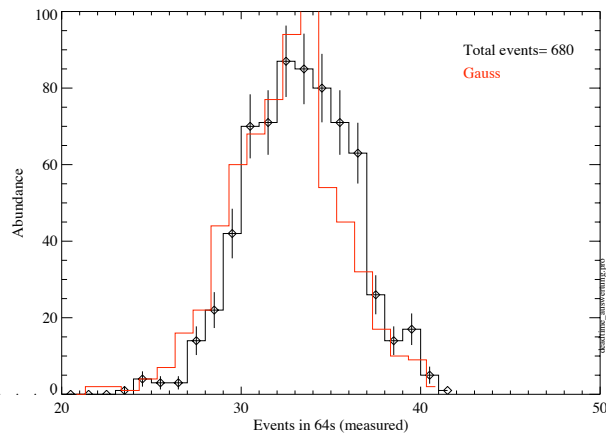


Figure 3.41: Measured event distribution by CDA using flight software version 10.0. Two event distributions (Poisson and Gauss) with a mean rate of 1 Hz triggered the instrument. In average only 33 events within 64 s were registered.

3 Cosmic Dust Analyser Performance

The distribution of the measured event rates with the CDA instrument using a Poisson and Gauss distributed process is shown in Fig. 3.41. A mean frequency of 1 Hz was used for this experiment. The dead time clearly reduces the measured rate to 33 events within 64 s (0.51 Hz), which means a reduction by a factor of two. In average only every second event was registered and counted by the flight software. The dead time correction factor is already a factor of two for such low event rates of 0.5 Hz (compare Eq. 3.44).

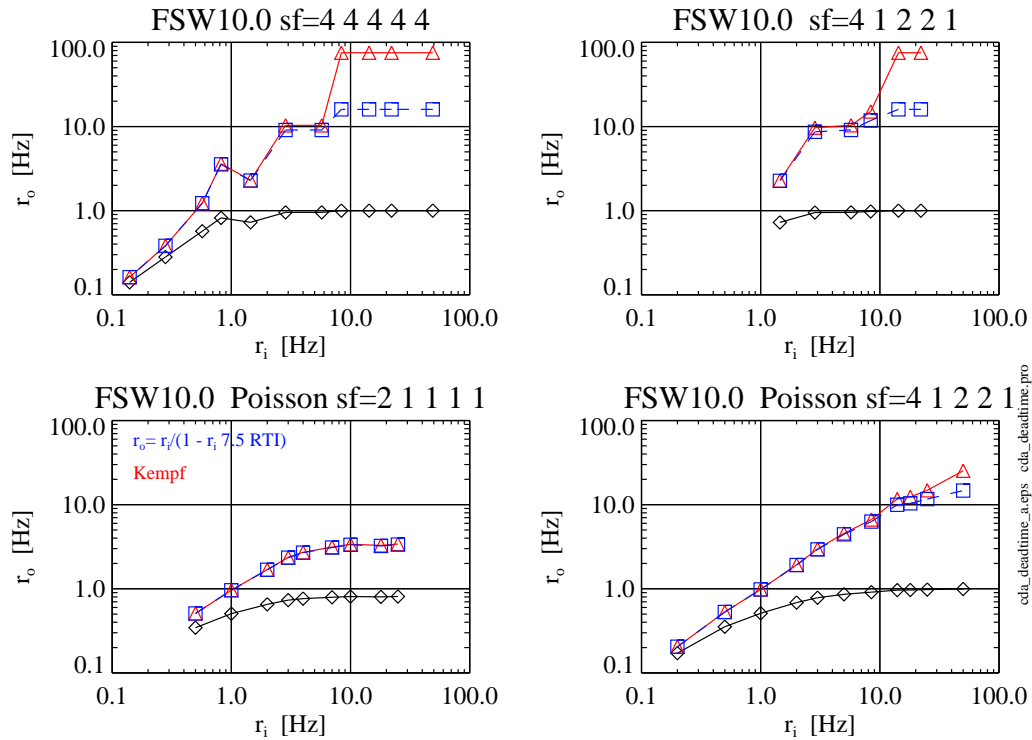


Figure 3.42: Event rates recorded by the CDA instrument under different conditions using the flight software version 10.0. This software is active onboard Cassini since 2005-150. Two cases were used, a time constant pulser (upper diagrams) and a stochastic event distribution (bottom diagrams). The measured rates are given as the black line (diamonds, lowest rates). A dead time was applied using Eq. 3.43 (blue squares) and Eq. 3.44 (red triangles).

The dependence of the measured event rate from the expected value is shown in Fig. 3.42. Four diagrams show the increase of the measured rate which goes into saturation (black curve) at input rates of approximately 10 Hz. Both, evenly time spaced events (constant frequencies) and exponentially distributed time series were used as input signals. The upper plots used constant input frequency generated by a standard pulse generator. The measured count rates by the CDA system are not smooth but provided fluctuating values due to interferences between the internal interrupt system and the constant event frequency. Higher input frequency did not necessarily lead to increased counting rates (upper left plot around 1 Hz input frequency). The

“load” of the software determines the saturation limit and accuracy of the dead time correction.

The shortest processing time is achieved when the raw data are not wavelet compressed, not stored in a raw data frame and are not lossless compressed (zipped). Dead time tests were performed using a typical instrument setup, which is used during Saturn ring plane crossings. The titles of the four diagrams in Fig. 3.42 consist of a string of numbers representing the five signal channel shrinking factors (sf). The numbers indicate the divisor for the back transformation of the wavelet compression. A number of 4 means, that only a quarter of the wavelet coefficients of one channel are back transformed. Higher numbers mean a smaller number of points to be transformed and the algorithm works faster - the processing time decreases. Each of the five channels has its own wavelet compression processing parameter and the numbers represent the channels entrance grid (QP), Chemical Analyser Target (QC), ion grid (QI), big target (QT) and multiplier (QM). Generally higher values lead to a faster event processing and the event triggering should work undisturbed: The dead time correction is applicable without major corrections. The string 4 4 4 4 4 provides the best processing conditions and the string 2 1 1 1 1 is leading to the longest event processing time in this test run. The comparison of the two upper and the two lower diagrams confirm, that measurement conditions under a low CPU load (short processing times, higher shrinking factors) lead to a faster event processing and, accordingly, to a later saturation behaviour.

The difference between the top and bottom diagrams is the means of the event time distribution. The top diagrams were recorded by a pulse generator using a constant time interval between two events, whereas the bottom diagrams refer to the advanced method using stochastic generated values of the Poisson statistics. The latter ones show a much smoother relation between the measured count rate and the rate of the expected values.

In summary, the application of the dead time correction leads to the correct input rates for mean input frequencies of up to 10 Hz. This requires already instrument setup parameters which allow a short event processing time (e.g. sf=[4, 1, 2, 2, 1]). Furthermore, the difference between the established dead time correction of Eq. 3.43 using a dead time of 7.5 RTIs (0.875 s) and the exact function of Eq. 3.44 is negligible for event rates below 30 Hz.

3.9 Calibration Outlook

Each hypervelocity impact is a unique process depending on many parameters like, dust speed and mass, dust density, impact angle and target surface properties. Only a subset of parameters was used to derive the calibration functions defined in the previous sections. How shall we proceed with calibration, which further information will become available?

We should also not forget the information already on ground to derive further information, where the man power until today was just not available to trigger detailed investigations. For example we already have many mass spectra on ground with known impact velocities and known dust masses. We have already seen, that fast impacts generate an impact plasma of higher energies and temperatures (>20.000 K). Here, the acceleration field is not strong enough in order to disregard the ion energies of the impact plasma. The result are broad peaks

3 Cosmic Dust Analyser Performance

in the mass spectrum in contrast to sharp lines of low impact velocities. Especially the peak shapes of the target ion species are a measure for the dust impact speeds. The impact process and the mass spectra were modelled by J. Hillier at Open University [Hillier et al., 2006], but a calibration function between peak shapes or peak widths and impact speeds is outstanding. There is another information we can derive from the time-of-flight mass spectra, namely the number of cluster ions. Postberg has in shown in Postberg [2007], that cluster ions are abundant in mass spectra of impact velocities below 10 km s^{-1} . Two major cluster processes are observed: The formation of clusters from target and projectile ion species (mixed clusters like rhodium-silicon), and the formation of clusters from the projectile species alone. The major component of dust grains in Saturn's E-ring is water ice. Water ice spectra are dominated by a polar molecule, the hydronium ion H_3O^+ which attracts further water molecules and clusters are formed of the type $(H_2O)_iH_3O^+$ with $i=0 \dots 10$. The clusters become unstable for higher plasma temperatures and the number of clusters i and their relative abundance is a measure of the impact plasma conditions. On the other side the plasma conditions are related to the impact speed. An analysis of the CDA flight data should be performed to investigate the relation between impact speed and cluster abundance (e.g. abundance of H_3O^+ ions to ions of the type $(H_2O)_iH_3O^+$ with $i > 0$).

In some sense, self-calibration with in-flight data is possible at the end of the Cassini tour. Once hundreds or even thousands of data sets are on ground, statistical analysis of particle speeds, masses and compositions allow for a correlation with dynamical models of E ring grains and with compositional information of the dust sources (icy satellite surfaces and the plume of Enceladus). If the particle composition is known, the dust mass determination becomes more accurate, too.

Dynamical ring models constrain the impact speed limits at certain positions of Cassini in the ring. This means, that the impact speed range of bound dust particles is known and the most likely relative impact speeds can be predicted. An analysis of the velocity of the dust impacts show a certain distribution which has to match the prediction. Then a correction factor for the impact speed calculation can be derived. This procedure requires an accurate dynamical ring model which was outstanding for a long time. Recent results of Horányi and Beckmann do reproduce the dust densities quite accurate [Horányi et al., 2008]. Beckmann [2008] was able to reproduce dust impact rates of CDA measured during S/C rolls. It seems that the models are now accurate enough to constrain and predict dust impact parameters in the ring.

From new laboratory tests we have further time-of-flight spectra of hypervelocity dust impacts. The new data set includes projectile materials like silicates as well as latex (polystyrene) based samples. Furthermore, the mass spectra were recorded using new instrumental technologies (Large Area Mass Analyser with a mass resolution of 200). The results of those laboratory tests have to be compared with in-flight data of CDA. Laboratory mass spectra of high mass resolution do not reflect the ion energy distribution and represent a reference in terms of possible mass lines and their relative abundancies. However CDA flight spectra often show broad features which might be attributed to both, an insufficient mass resolution (merged peaks) or a single peak of high energy spread. The question, if broad mass lines of CDA are caused by

multiple mass lines or by high ion energies can be answered. In general, the acceleration of new projectile materials generate a new data base to derive calibration functions of the CDA subsystems.

Another important source for calibration points is the growing knowledge about the dust sources. The Cassini mission studies the sources of dust grains since the beginning of the tour in 2004. The surface of the icy satellites act as a dust source by surface sputtering and the active ice geysers of Enceladus continuously release icy dust grains into the ring system. Optical spectrometers gave information about the surface composition and measurements of the Enceladus gas and dust plumes constrain the composition and mass distribution of the dust grains. The Cassini flyby at Enceladus through the dust plume provides freshly ejected dust grains from the surface with a speed, which is almost identical to the velocity of Enceladus itself. At this location, the relative impact speed of the dust grains is exactly known (by better than 3%). Why is the speed known so accurately although there are many dust grains from the E-ring background on eccentric orbits and with velocities exceeding the circular dust speed? The background dust density reaches values of up to 1 dust particle per m^3 . The reason is the extreme high density of the dust plume released by the moon. The dust densities in the plumes are a factor of 10 or even 100 higher than the E ring background. The dominating number of impacting dust grains own the dynamical properties of the moon itself and have circular dust speeds of almost exactly 12.6 km s^{-1} . The grain speeds in the plume reach values of only up to 300 m s^{-1} with respect to the surface of Enceladus and is therefore negligible. The exact knowledge of the relative impact speed is beneficial for both detectors, the Impact Ionisation Targets of the Dust Analyser, and the High Rate Detector. The signal strength of the HRD foils depend strongly on the impact speed (exponent of 3), but only slightly from the dust mass (exponent ≈ 1).

In section 3.1 it was shown, that the signal rise time, which is normally taken to derive the impact speed, consists of two components. The current calibration is based on this combined signal with a leading flank and a slowly rising component. A deconvolution of this signal will separate the fast peak from the slow signal. A result is a much stronger and clearer dependence between of impact speed and the amplitude ratio of the both signal components. Although this is not proven in this work, the author recommends an investigation of this behaviour.

We have even more possibilities to refine the calibration with in-flight data. First, it was already noted that the QP channel provides the most accurate velocity information of dust grains. Unfortunately, the signals are seldom and only grains bigger than $5 \mu\text{m}$ provide clear parameters. The progress is depended on the number of signals and some further years of in-flight are necessary to use statistical methods for a better dust mass determination.

Extensive effort is spent on the modelling of the nanometre sized dust grains ejected from the saturnian system. Tiny grains ($< 20 \text{ nm}$) reach the CDA instrument when Cassini is outside of the magnetosphere. Individual dust impacts are traced back to the inner saturnian system and solutions in the phase space of (v, m, q) are determined [Hsu, 2010]. Normally, the solution space is rather big, velocities range from 50 to 300 km s^{-1} and the grain masses from

3 Cosmic Dust Analyser Performance

10^{-24} to 10^{-21} kg. However, under some special conditions in time and geometry, only a few solutions for the dust trajectories exist (very constrained speed and mass range). These special cases can be used in order to define rise times and impact yields of nanometre sized grains. Some preliminary results were already successfully applied to extend the range of data points in the fits using hyperplanes for a dust mass calibration.

Some further calibration methods might evolve due to the rising knowledge and the growing data set of in-flight impact signals with time. The knowledge of the composition, structure and density of dust particles in space is very sparse. In the year 2006 the Stardust mission returned cometary and interplanetary dust particles to Earth [Brownlee and Stardust Mission Team, 2006]. Their analysis and results have to be merged with the knowledge of in-situ measurements, having in mind especially the dust impacts of interplanetary particles during the cruise phase. Unfortunately, we will not have the chance to return dust samples from the saturnian system.

In general, self-calibration will be the most fruitful method in order to improve and refine the current calibration for the dust speeds and masses. Learning about the exact parameters like the dust speed in certain areas of the Cassini tour immediately lead to a lower error in the dust mass determination. This in turn, has an impact to theoretical models and open new self-calibration possibilities.

4 CDA Measurements and Selected Results

4.1 Dust Analyser Operations

The work and the importance of operations is generally underestimated, especially from scientists doing only science analysis or using the results once they are there. It is a long lasting process which takes tremendous efforts from many engineers and scientists behind the scenes. In contrast to former dust instrumentation, the Cosmic Dust Analyser requires a very detailed and intense operations process caused by many factors. The main reason is the complexity of both, the spacecraft Cassini and of the instrument itself. Cassini is the most capable and complex interplanetary spacecraft ever built. Ten instruments onboard with distinct requirements, a complex tour with numerous flybys and variable inclinations (Fig. A.2) lead to a difficult prioritisation of science observations. Spacecraft constraints and flight rules cause further complications and narrow down the allowed observational profile. Especially the flight rule to avoid Sun light (and therefore heating) on the spacecraft +X direction (opposite of the former Huygens probe side) shall keep the temperature of the radiators of the infrared remote sensing instruments low.

The start of the planning process was the tour selection of the Cassini mission. Tour designers worked out various trajectories with different inclination and azimuthal profiles. Icy moon encounters and Titan flyby altitudes, as well as star occultation possibilities showed many deviations. For the dust instrument CDA, a global coverage of the latitude-longitude regions as well as the number of icy satellite flybys was essential. Furthermore, the opportunity for inclined ring plane crossings at various distances from Saturn are useful in order to determine the shape of the E ring. For the analysis of the radial E ring profile, an equatorial orbit with a priority for dust measurements is required and was negotiated with the project science working groups (orbit 149).

Following the tour selection and the coarse segmentation of orbit parts to the individual science disciplines (magnetosphere and plasma, rings, surfaces, atmospheres, titan), the mission planning took place in the science working groups, where a complete observation timeline with prime instrument phases and downlinks was established. Here, the general spacecraft flight rules were considered as far as possible in order to come up with a conflict-free timeline for a later smooth integration. It is clear that this was not always the case, since it was not possible to take into account all details of the (later) fully implemented timeline. Late changes in the downlink scheme (e.g. by the requirements of other missions or failures of ground receivers), pointing violations and too high data volumes often require the adjustment of the

4 CDA Measurements and Selected Results

already implemented observations – meaning sometimes even a loss or degradation of the planned prime-observations. Fortunately, this was not often the case for the CDA instrument prime observations. CDA is primarily a rider instrument adjusting its observation profile (and its articulation profile) to the implemented timeline. Requested prime observations, especially during ring plane crossings, were often degraded or deleted by high-priority science of other instruments or by project needs (e.g. stellar or radio occultations, moon flyby science, dust hazard regions etc.).

Once the timeline is worked out, the implementation starts approximately four month before execution onboard the spacecraft. The sequence has varying durations which lies normally between four and ten weeks. The instrument prime teams prepare their spacecraft pointing profile and the sequence leads merge the individual inputs in order to prepare the sequence data products (c-kernel with pointing information, operational mode listings, data volume report, activity spreadsheet). Taking part at the distributed operations concept¹ the CDA instrument team is preparing all uplink products for the sequences in a conflict-free manner and it is fully responsible for monitoring, data processing and archiving as well.

For the operations of an impact ionisation detector like CDA several rules have to be applied. The rules are classified in health- and safety conditions and in general operational constraints. The health and safety rules are of major concern and shall protect an instrument from any harm during the mission. These rules are part of the official CDA Operation Procedure and software tools at the spacecraft office (Jet Propulsion Laboratory) and the operational team at Max Planck Institute Heidelberg control any violations during the sequence generation phase. The official health and safety rules of CDA cover the Replacement heater operation (avoid longer off-times and ensure the operational temperature range), the phase of Main Engine Burns (avoid high voltages and a low-contamination orientation of CDA), the decontamination heater usage (avoid high voltages and Sun light in the aperture during and shortly after the decontamination of the Chemical Analyser Target) and the restriction of the CDA articulation speed (in order to avoid imbalances of the spacecraft). The latter rule is analysed in detail in Srama [2000b], but is not explained in the official flight rule documentation.

Special attention is necessary in the planning of flybys at small bodies with atmospheres or at moons with active geysers or volcanoes. The high densities of dust or gas particles might cause contamination, saturation effects in the electronics or high voltage break-downs. The latter effect is of health and safety concern and has to be considered seriously.

The operational pressure range of the CDA multiplier device at a nominal voltage of 2700 V is below $1 \cdot 10^{-4}$ mbar. Further high voltages (1000 V) are applied at the CDA Chemical Analyser Target section with a distance of ≈ 3 mm between the electrodes. According to the Paschen curve of electrical arcing between electrodes the most critical pressure lies around 0.6 Torr where arcing occurs already at field strengths of only 40 V mm^{-1} (normal air). The significant parameter is the product of pressure p and distance d and the empirical law was

¹The distributed operations concept was introduced by NASA in 1996 in order to save costs in Cassini operations. Each instrument team is fully responsible for the **uplink** products, which have to be in accordance with project guidelines and constraints. Spacecraft office tools are used by the prime teams in order to prepare the pointing commands of the spacecraft.

found in experiments using pressures of 0.01 to 2000 Torr². The breakdown is, of course, dependent on many further factors like radiation, dust and surface roughness. The breakdown voltage $V_{breakdown}$ rises quickly with lower pressures and Paschen's law (Eq. 4.1) gives values of 40 kV for distances of 1 cm at a pressure of 0.06 Torr.

$$V_{breakdown} = \frac{B \cdot p \cdot d}{C + \ln(p \cdot d)} \quad \text{with} \quad C = \ln(A) - \ln(1 + \gamma^{-1}) \quad (4.1)$$

γ is the Townsend secondary ionisation coefficient and represents the net number of secondary electrons produced per incident positive ion or photon. Electronegative gases (oxygen, CO₂) reattach electrons quickly and have low γ values. The γ value of air is set to 0.01. A and B are constants given by the Clausius law describing the mean free path length in a gas and B depends on the ionisation energy. For air the values of $A = 15 \text{ cm}^{-1} \text{ Torr}^{-1}$ and $B = 365 \text{ V cm}^{-1} \text{ Torr}^{-1}$ are used such that the value C becomes 1.18. Kim [2006] studied breakdown voltages in the context of the development of gas sensors and he found a critical voltage of 1000 V at an electrode distance of 0.5 mm and a pressure of 0.06 Torr using normal air. The breakdown voltage is dependent on the gas type, but air is a good approximation for passing the nitrogen rich atmosphere of Titan. However, Paschen's law reflects the Townsend breakdown mechanism in gases (cascading of secondary electrons emitted by collisions in the gap) and the Eq. 4.1 does not describe the arcing mechanism at lower pressure products of $p \cdot d = 0.03 \text{ Torr} \cdot \text{cm}$. The logarithmic function forbids the calculation of breakdown voltages in pressure ranges below 0.01 Torr and the author recommends to not exceed approximately $1 \cdot 10^{-3} \text{ mbar}$ due to the many unknown factors (type of gas, degree of ionisation, surface contamination and roughness). This will provide a safety factor of 10 which is appropriate.

Which dynamic pressures are expected during low altitude Titan flybys or Enceladus plume crossings? The dynamic pressure is given by Eq. 4.2 with the dynamic pressure p_d , the static pressure p_s and the velocity v .

$$p_d = \frac{1}{2} \cdot p_s \cdot v^2 \quad (4.2)$$

The relative flyby speeds of Cassini at Titan and Enceladus are above 6 km s^{-1} and Eq. 4.2 has to be multiplied by approximately a factor of two in order to take the rather high speeds into account. This leads to Eq. 4.3.

$$p_d = p_s \cdot v^2 \quad (4.3)$$

Let's assume now a Titan flyby altitude of 900 km with an atmosphere density of $3 \cdot 10^{-9} \text{ kg m}^{-3}$ and a flyby speed of 6 km s^{-1} , consequently Eq. 4.3 provides a dynamic pressure of 0.108 Pa or $1.08 \cdot 10^{-3} \text{ mbar}$. More often are Titan flybys at altitudes of 950 km and the atmosphere density is a bit lower with $2 \cdot 10^{-9} \text{ kg m}^{-3}$ leading to dynamic pressures of $7.2 \cdot 10^{-2} \text{ Pa}$ or $7.2 \cdot 10^{-4} \text{ mbar}$. These values are very close to the allowed pressure values and protective measures for the CDA high voltages have to be initiated. Since the multiplier electrodes are partly protected by a housing, the limiting device is the Chemical Analyser Target with its

²The unit Torr does not comply with the SI system of units, but is still used in the scientific literature. 1 Torr = 133,3 Pa and 760 Torr = 1013 mbar

4 CDA Measurements and Selected Results

high voltage of 1000 V.

The Titan atmosphere is not the only danger in this regard. After the discovery of the Enceladus gas and dust plumes at the south pole region, a second hazardous region was found. Which dynamic pressures are now expected at Enceladus plume crossings?

Here a gas peak density of up to $6.0 \cdot 10^{-11} \text{ kg m}^{-3}$ was measured by the neutral gas instrument and the Attitude Articulation Subsystem in 2008 and the flyby speed was, due to the inclined orbit, 17 km s^{-1} . However, this provides a dynamic pressure of only 0.017 Pa ($1.7 \cdot 10^{-4} \text{ mbar}$). In contrast to the Titan flybys the crossing of the Enceladus plumes take only approximately 40 seconds. On November 2, 2009, Cassini goes deeper into the plume (orbit 120) and higher densities are expected but with a rather low flyby speed of approximately 7 km s^{-1} (equatorial orbit). Nevertheless, the high voltage of the Chemical Analyser was reduced during the November 2009 Enceladus flyby.

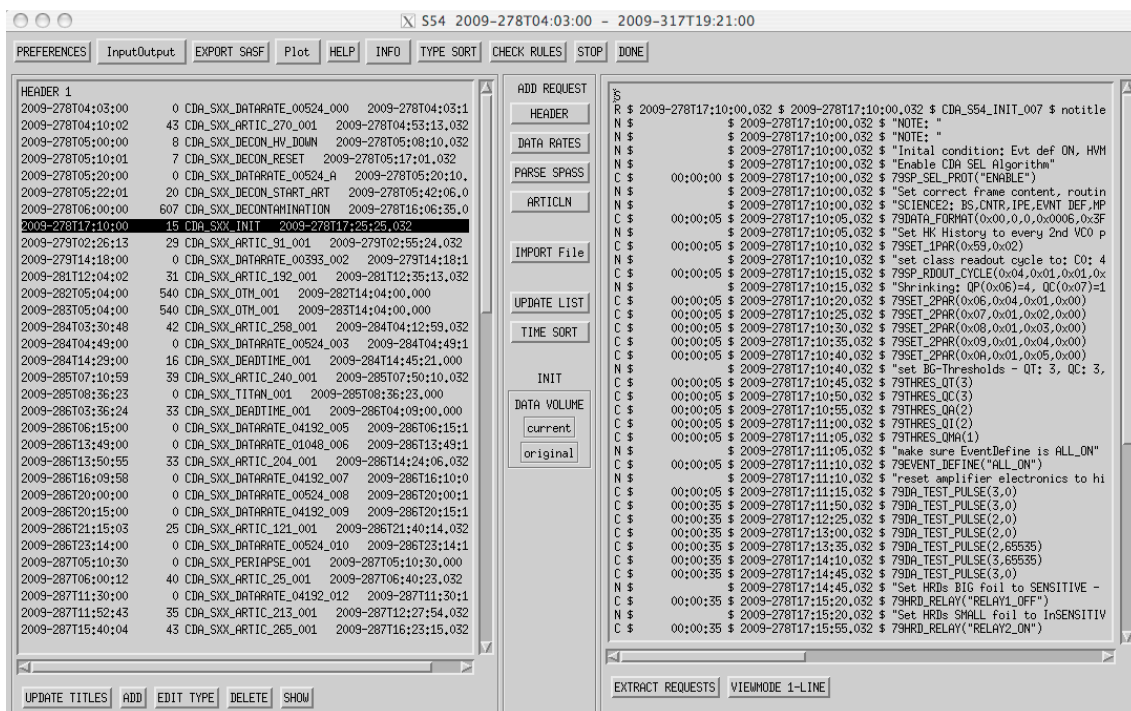


Figure 4.1: Uplink tool based on IDL in order to edit and generate command files (SASF-Editor). The tool is able to import data rate reports, the Science Planning Attitude Strategy Spreadsheet (SPASS) and time ordered listing of the Cassini request data base (CIMS-TOL). The main purpose is the visualisation and adjustment of the CDA articulation profile. The main dust targets are bound ring particles (prograde and retrograde) and interstellar dust. The SPASS file provides an overview of dead times, spacecraft maneuvers, pericenter-, apocenter- and flyby events.

The used software for operations planning is manifold and self-developed by the CDA team members in order to fulfill the specific CDA needs in terms of pointing analysis and internal commanding rules. Most software packages are based on the Interactive Data Language (IDL)

and are named *Science Analyser* (pointing analysis of directionality compatibility of the CDA boresight and the dust RAM directions), *SASF³ Generator* (reading project file products and generate the CDA articulation and data rate commanding) and *SASF Editor* (compare Fig. 4.1 and 4.2, reading command sequences or project output files and edit or generate CDA command products, overview of the CDA articulation profile and the dust RAM directions).

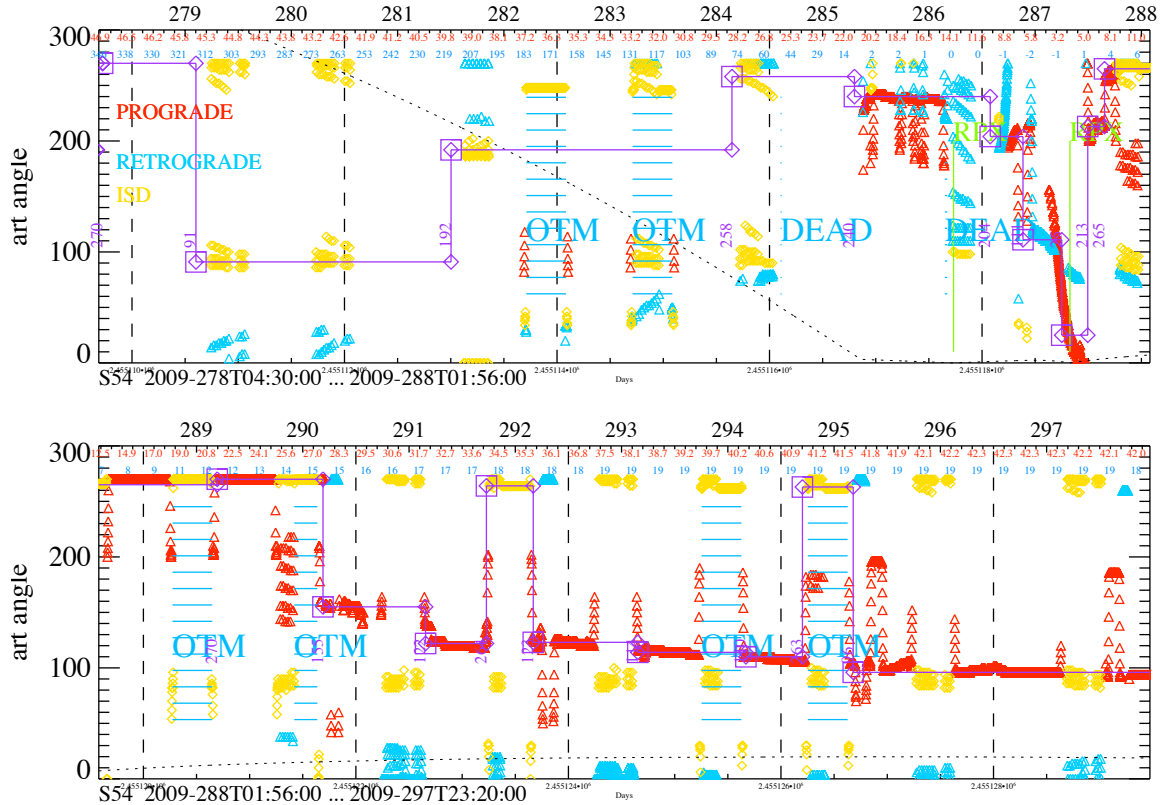


Figure 4.2: Overview of commanded CDA articulation profile in the sequence S54. The plot shows the required CDA articulation angle over time in order to point to various dust targets (small symbols for prograde (red), retrograde (blue) or interstellar dust grains (yellow)). The pink line gives the commanded articulation profile. The analysis is based on the spacecraft C-kernel and the top labels belong to the DOY (black), distance from Saturn in Saturn radii (yellow) and distance from the ring plane in tkm (blue symbols and black dashed line).

A further important uplink software package is the java-based *CDAcommandList* tool, which read the command files and checks the project and CDA flight rules like the command timing, high-voltage states, dead times and OTMs⁴, data rates and operational modes. In addition, a variety of smaller tools and scripts are used for file handling and information extraction.

The instrument **monitoring** occurs either in real-time (project tools) or by transferring CDA housekeeping data from the project data base and the consecutive analysis by self-developed

³Spacecraft Activity Sequence File, standard file format used in the uplink process.

⁴Orbital Trim Maneuvers

tools. The project tools do include new web based tools like RAMPAGE and non-web based tools running on NASA provided Sun workstations (DMD). The self-developed software package BCE7⁵ is used for processing, debugging and monitoring the downlink data stream of the housekeeping and science data packets, respectively (compare Fig. A.8). Recently, a Java-based tool was developed by Pentamino GmbH, which allows both, commanding the Flight Spare Unit of CDA (JBCE), and processing and displaying science and housekeeping data (JShow).

For scientific analysis, a MySQL data base is the core for CDA data product archiving and IDL based interface programs allow for an extraction and analysis of its contents in many ways [Kempf, 2007]. Furthermore, the CDA data are included in the Planetary Data Archive (PDS) according to the Cassini project archiving guidelines. The University of Chicago is responsible for PDS archiving of High Rate Detector data products.

4.2 The HRD and CDA Noise Rate

Dust detectors using PVDF foils are very reliable and they have been used in space onboard many interplanetary missions and Earth satellites. The noise rate of the HRD onboard Cassini shows outside the dense E ring region a negligible number of events and the counter values remain unchanged for a couple of days giving a noise level of $< 10^{-5} s^{-1}$. However, the big foil sensor became noisy after the G-ring crossing of Cassini at September 5, 2005 (248T10:40). Cassini crossed the ring plane at a distance of only 2.93 R_S which was very close to the known G-ring of Saturn which extends from 166.000 km to 173.200 km. The HRD was hit by a few dust grains and one impact exceeded the highest threshold M4, which corresponds to a grain size of at least 25 μm at the relative impact speed of 8 $km s^{-1}$. From this moment on, the HRD big foil sensor showed an increased noise behaviour with characteristic time variations as shown in Fig. 4.3, Fig. 4.4 and Fig. A.9. The noise rate fluctuates between two different noise levels of approximately 0.1 s^{-1} and 0.01 s^{-1} forming an almost periodic pattern. Generally, the two noise levels did not change with time very much and no drift or alteration was observed from 2005 to 2008. A detailed rate analysis of the days 150 to 160 in 2008 revealed that the rate changes not by a factor of ten but typically with a smaller factor between 6 and 8.

Fig. 4.3 has shown, that there is a partly correlation of the HRD noise rate and the spacecraft attitude. A closer investigation between various pointing characteristics and the noise rate revealed especially a moderate correlation with the HRD-Sun angle (Fig. 4.4). When the angle rises above approximately 70° the HRD noise drops significantly. But this rule is violated at the beginning of day 171 and at the end of day 175.

Are other correlations of the HRD noise rate possible and which are they? No convincing coincidence with spacecraft pointing characteristics, like the angle between the instrument boresight and the dust-RAM, Sun, Plasma or Saturn direction, was found. However, Fig. 4.4

⁵BCE stands for Bench Checkout Equipment

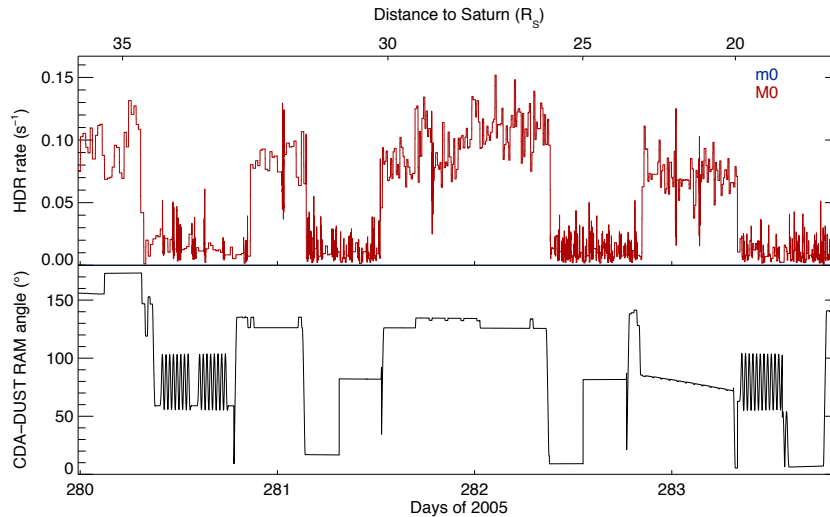


Figure 4.3: Increased HRD noise rate and CDA pointing in 2005 (between DOY 280 to 284). The boresight of HRD and CDA are identical and the bottom plot shows the angle between the CDA and the dust RAM direction of prograde Kepler particles around Saturn. The plots do only partly correlate, in the second half of day 282 the curves are decorrelated (courtesy Kempf, 2007).

also indicated a correlation of the HRD and the CDA noise rate⁶. This means that the noise source obviously influences both subsystems, either directly or indirectly. An inside noise source could be the power supply or unstable grounding, an outside noise source could be of either acoustic, plasma, radiation, dust or temperature type. For an investigation of the periodicity, a fourier analysis has been performed of the time frame 2008-150 to 2008-160 in order to check for any Saturn system related properties like moon orbit periodicities.⁷

The result of the frequency analysis is shown in Fig. 4.5. The figure includes the FFT analysis (left), the HRD rate of M1 (top right) and the angle of the HRD boresight to the ring plane (bottom right). As expected, the FFT reveals major periodicities between 20 and 40 hours. Five main periodicities were identified in the diagram with the times of 22.1 h, 25.1 h, 29.2 h, 32.8 and 34.9 h. The frequency of 22.1 h is very close to 22.08 h which is the relative frequency of the Enceladus orbital period of 32.88 h and Saturn's rotation frequency of 10.8 h⁸.

This result is amazing and surprising. Is this correlation just by chance? Spacecraft activities are always related to observations of moons, of the rings or of Saturn, and those observations are repetitive by its nature leading to artificial frequencies in the data set. However, in

⁶This correlation is more obvious in Fig. 4.5 which is discussed later.

⁷This method of frequency analysis was successfully applied to the Galileo dust rate data set. The result was the identification of the moon Io and its volcanoes as source for high impact rates by nanometre sized grains [Graps et al., 2000]. However, the HRD-M foil with its thickness of 28 μm does not react to submicron dust grain impacts.

⁸The orbit of Tethys has a periodicity of 45.288 hours which is too long to be correlated with the HRD data. The frequency of 32.8 h is very close to half of Dione's orbit of 32.845 h. Furthermore, the difference of Dione's and Enceladus' orbit is 32.81 h as well.

4 CDA Measurements and Selected Results

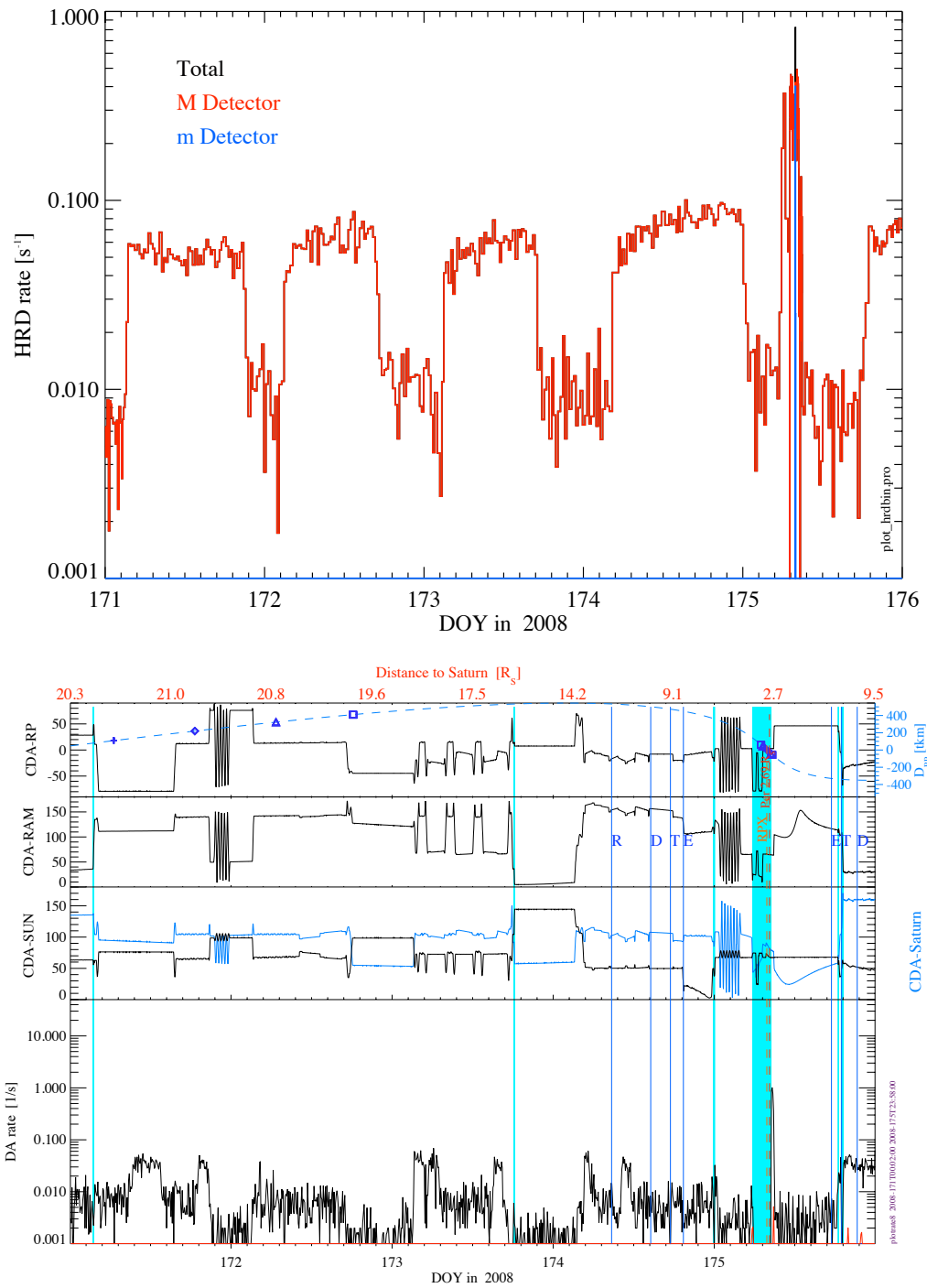


Figure 4.4: Noise of the channel M1 of the HRD (top) and event rate with pointing information of the CDA (bottom). Both subsystems show increased event rates lasting many hours. The event rates have two rate levels which are slightly modulated by spacecraft pointing activities. Both HRD and CDA show strong event rates during the ring plane crossing at 2008-175T07:55 which occurred at 2.71 Saturn radii distance. The event rate is correlated to pointing changes, but not with the angle to the dust RAM direction.

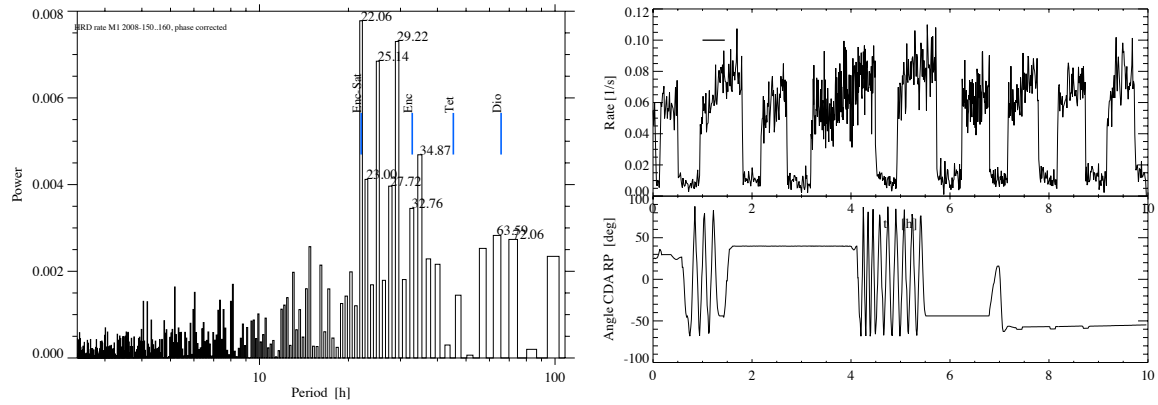


Figure 4.5: Fourier analysis of the HRD M1 rate (left), HRD event rate (top right) and pointing profile (boresight angle towards the rings plane) in the time frame 2008-150...2008-160. The HRD M1 noise rate and the CDA pointing are not correlated.

this time frame, no special observations with the highlighted frequencies were made although the activity list showed imaging observations of the icy satellites. This leads to the question, if there is a noise source in the saturnian system which is related to the motion of Enceladus and Saturn's rotation and which affects the HRD instrument. Is there any electromagnetic radiation produced by the interaction of Enceladus' geysers and Saturn's magnetosphere? This scenario is very unlikely since the HRD was quiet in the years 2004 and 2005. A closer investigation of the HRD noise shows only a partly correlation with pointing characteristics like the boresight-Sun angle or the boresight-dust RAM angle.

Is stronger acoustic noise possible to cause the observed phenomena? Generally yes, but the only known (relevant) acoustic noise source onboard Cassini are the reaction wheels. Under certain revolution conditions, they generate vibrations and it was shown, that a mirror of an optical instrument onboard Cassini was affected leading to degraded observations. However, the strong periodic noise pattern excludes the strong influence of acoustic noise. Any influence of temperature variations was checked and can be ruled out as well.

The high sensitivity of the preamplifiers of both HRD and CDA, and its correlation by the noise rate shown in Fig. 4.4 indicates a joint source. Such a source could be the internal power subsystem. Any changes of the instrument ground or in power supply stability would immediately be picked up by the measurement channels. However, no current or voltage peaks were observed using the existing monitoring methods (housekeeping data frames). This does not exclude the existence of power spikes since the sampling of housekeeping values on both sides, the spacecraft and instrument side, is very slow (once every minute). Strong loads of the system influence the noise on the grounding and affect the sensitivity of the amplifiers. A known strong load is the Bus Interface Unit (BIU) of CDA of the 1553 bus subsystem. This board was provided by NASA and consumes for milliseconds 500 mW during the packet transfer to the bus. The rhythm of packet transfers is dependent on the telemetry mode of the

Central Data Subsystem (CDS). In early cruise, the bus was still quiet and packet requests were seldom (no science data packet transfer until the middle of the year 2000). After the definition of the final telemetry modes, a higher noise rate was registered – The BIU activity seems to have a strong influence on the observed noise rates.

There are basically two packet pick-up rates of 0.125 Hz^9 and of 1 Hz^{10} . This means, that every second a power spike on the electrical ground occurs. It was amazing how accurate the noise event rates of CDA and especially HRD correlate with the changes of the telemetry modes (Fig. 4.6). Each time the operational status shows a high-rate mode (1 Hz packet pick-up rate), the noise of HRD rises by a factor of 8. This factor is in fact identical with the increase of the packet pick-up cycle of a factor of 8 from the 524 bps to the 4192 bps modes. Fig. 4.7 shows the rate distribution of HRD events for a 10 day period in 2008 starting on day 150. The amplitude distribution shows two maxima at $\log(r) = -1.15$ and $\log(r) = -2.05$ corresponding to the rates of $r_1 = -0.0089 \text{ s}^{-1}$ (lower rate periods) and $r_2 = 0.0708 \text{ s}^{-1}$ (higher rate phases), respectively. The HRD noise rate seems to rise linearly with the data pickup cycle, and $r_2 \approx 8 \cdot r_1$. Although the telemetry mode was identified as the major noise source, it was not possible to investigate the detailed feedback mechanism over the power and ground lines due to a lack of monitoring data.

As already pointed out, the noise rate of both subsystems, HRD and CDA, is correlated with the telemetry bus onboard Cassini. In order to analyse this behaviour, tests in the laboratory using the CDA flight spare unit were performed under the application of distinct packet transfer rates. However, no correlation between the noise event rate and the CDA data rate was observed using the standard test setup and a high stabilised power supply from the company Lambda. However, after the replacement of the power supply in March 2009 by an old model of the company TET, the picture changed. Now, a clear dependence of the CDA trigger rate on the telemetry mode was observed (Fig. 4.8). The test started with the normal mode of 524 bps, meaning that one CDA packet of 524 bytes is transferred every 8 seconds between the CDA Bus Interface Unit (BIU) and the Remote Terminal Interface Unit (RTIU). The thresholds used for this test were QT=2, QC=4, QA=5, QI=15 and QMA=15¹¹. No high voltages were applied and the HRD was switched on in the first part of the test.

The next question was, if the trigger rate is linked to the *type* of CDA packets. Basically there are two types of data packets: science data packets filled with real data, and zero length packets (ZLP), filled with arbitrary data. ZLPs are transferred to the onboard data subsystem, but are not stored on the solid state recorder of Cassini. ZLPs are used to control the CDA data rate in addition to the packet pickup cycle. The idea behind this test was to identify any software-hardware correlation. The telemetry mode used was S&ER-3 with a packet pickup cycle of one packet per second, but the observed CDA trigger rate remained constant, regard-

⁹Science data rate of 524 bps corresponds to the transfer of one 524-byte science packet every 8 seconds, used during e.g. downlink modes until 2009-263 and in the modes S&ER-5 and S&ER-5a.

¹⁰CDA modes with 4192 bps, one science packet per second, telemetry modes: S&ER-2, S&ER-3, S&ER-4, S&ER-6, downlink modes after 2009-263. The S&ER-2 mode was changed to a packet cycle of 4 Hz in 2009 leading to a CDA maximum science data rate of 16 kbps.

¹¹Please compare with Srama [2000a] for a translation from threshold to coulomb

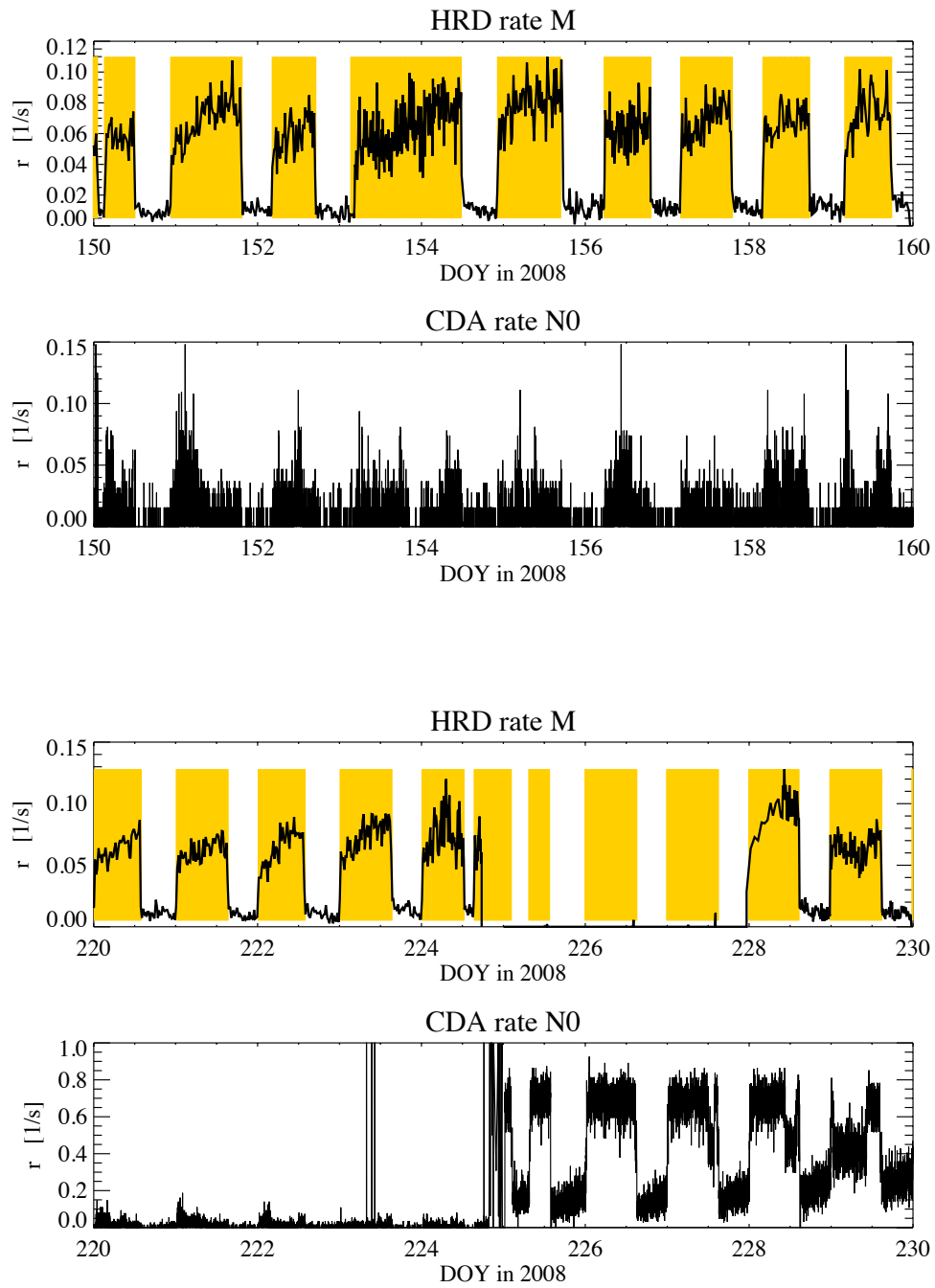


Figure 4.6: Correlation of the HRD M1 and CDA event rate with the onboard telemetry mode. The yellow marked areas represent modes of 8-times increased data pickup rates (1 Hz instead of 0.125 Hz). The proofs, that the Bus Interface Unit of CDA disturbs the sensitive measurements of HRD and CDA.

4 CDA Measurements and Selected Results

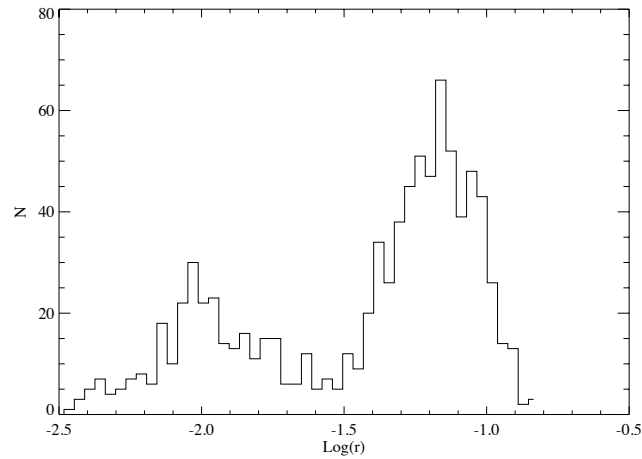


Figure 4.7: Distribution of the HRD noise rate $\log(r)$ over ten days starting at 2008-150. The HRD noise rate shows two maximima at $\log(r) = -2.05$ and $\log(r) = -1.15$.

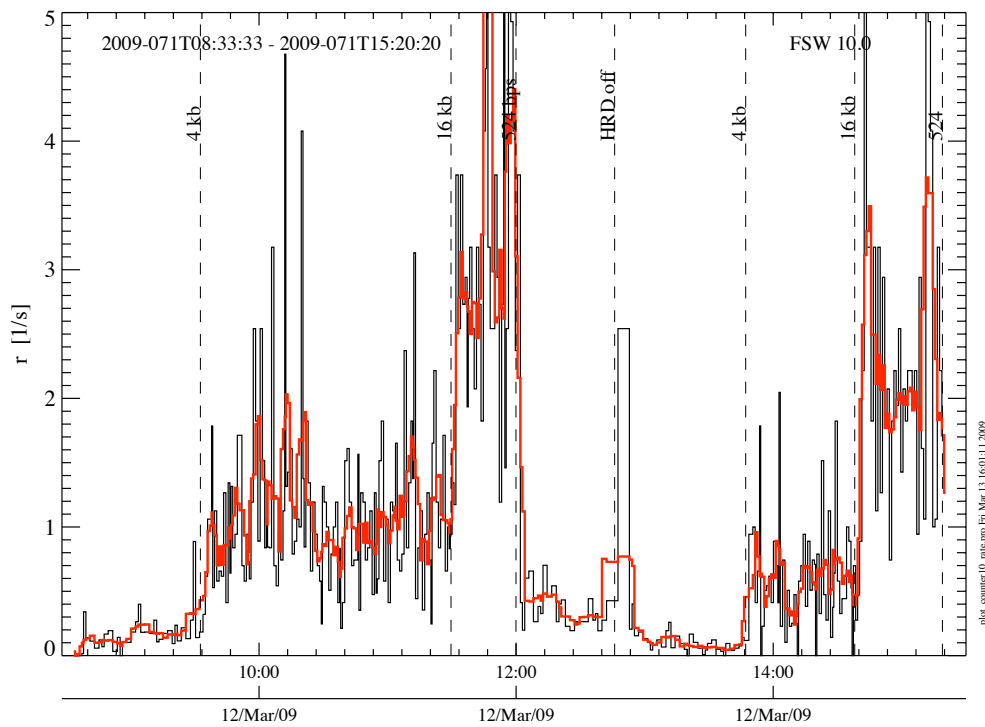


Figure 4.8: Correlation of the CDA event rate (noise) and the packet pickup cycle (telemetry mode/data rate). The test started with a low data rate of 524 bps and included the High Rate Detector (HRD). The change to the 4192 bps mode and to the 16 kbps mode increased the noise rate accordingly. At 12:45 the HRD was switched off leading to slightly lower trigger rates, but the overall correlation remained. The red curve shows an average over five sample intervals.

less of the percentage of ZLPs.

The laboratory investigations clearly show, that the preamplifiers of CDA react to BIU activities. This correlation is not only given by the strength of the noise (rates), but also by the periodicities found in the time distribution of the events (Fig. 4.9). Specific frequencies related to the BIU packet cycle are found and the periodicity of 8 seconds is clearly the strongest mode ruling out a random distribution of trigger events. Electromagnetic compatibility checks during the Assembly Test and Launch Operations phase revealed a power consumption of the BIU board of up to 500 mW causing significant disturbances on the electrical ground. Therefore both disturbances, the CDA and the HRD noise behaviour is attributed to interferences caused by the BIU activities.

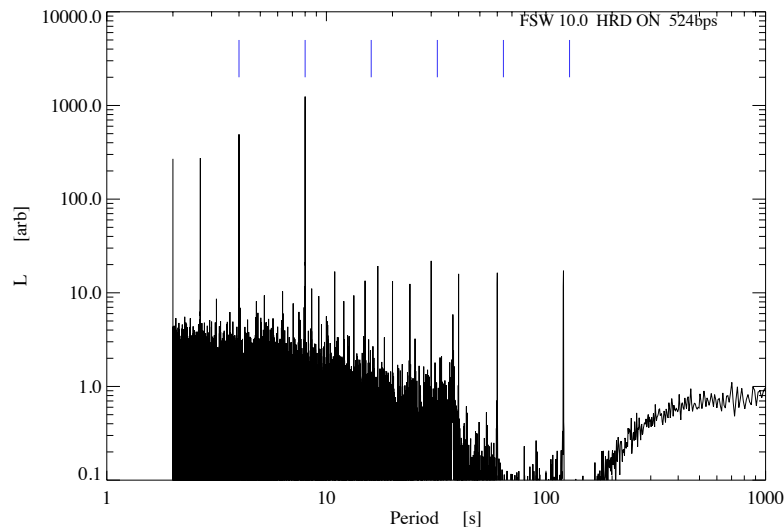


Figure 4.9: Lomb normalised periodogram of the CDA event times recorded during a telemetry mode with a packet pickup cycle of 8 seconds. The strong peaks at the periodicity of 8 seconds and its higher modes identify the BIU as the major noise source of the subsystem. The periodicities of 4, 8, 16, 32, 64 and 128 seconds are labeled by a short vertical line.

4.3 Comparative Impact Signals

Since Cassini's dust detector is the first sensor providing a full data set of raw impact signals, an overview about the achieved signal shapes and its interpretation will be given. Each raw data set includes the primary charge signal (QP), the CAT electron signal (QC), the IIT electron signal (QT), the ion grid signal (QI) and the multiplier signal (QM) (compare Fig. 2.5). An overview of CAT impacts is shown in Fig. 4.10. For CAT impacts, the QC signal shows the strongest amplitude, a mass spectrum is observed in the channel QM (peaks within the first 6 μs) and the rise time of the QI signal is rather short (below 15 μs). Furthermore, stronger

4 CDA Measurements and Selected Results

impacts show a high QP signal after the impact time. This signal is caused by unfocused ions not hitting the ion grid or multiplier.

For an efficient description of the events, a tuple was defined as label: [UTC, Distance from Saturn in R_S , latitude with respect to ring plane in degree, relative impact speed of bound prograde ring particles in km s^{-1}]. The upper left event shows very weak target, ion and multiplier signals. Nevertheless, a mass spectrum of water ice clusters is shown by the QM signal. Such events are typically classified as noise events onboard by the flight software. It is obvious, that such small impact events would be lost by rather simple impact detectors using higher trigger thresholds. Here, the ion grid signal shows an amplitude of only 3 dn values ($2 \cdot 10^{-15}$ C) and the electron target charge (QC) was approximately $15 \cdot 10^{-15}$ C. These signals were measured at 11 R_S distance from Saturn and the relative impact speed of bound, prograde dust grains would be 7.5 km s^{-1} . The author apologizes for the small scale of all plots and the small axis labels, but details are readable in the electronics pdf-version.

The upper right and middle left event in Fig. 4.10 are typical impact signals of water ice grains. The known water ice clusters in the lower left plot window show peaks starting at the mass 19 u with following cluster peaks of the type $\text{H}(\text{H}_2\text{O})_n^+$ and the red ion signal shows steep rise times below 12 μs .

The middle right event was recorded about 4 hours after the ring plane crossing at latitudes of -4.4° and the typical pattern of water ice clusters is not visible. Instead, an asymmetric peak around 3.5 μs flight time indicates a mineralic/metallic type particle. *Generally, four different types of grain compositions were found in the E ring of Saturn: pure water ice grains, water ice grains containing high amounts of salts (sodium content), water ice grains with mineralic and/or organic impurities and pure mineralic/metallic grains* [Postberg et al., 2009a].

The bottom left event shows a typical Saturn stream particle ($\approx 15 \text{ nm}$, 100 km s^{-1}). Very sharp rise times and a mass spectrum containing mainly lines of hydrogen, carbon, sodium and rhodium are typical for this particle class. This stream particle was measured at a Saturn distance of 36 R_S and a latitude of 4° .

The bottom right event is again a CAT impact, but the mass spectrum shows very high amplitudes and rather broad features. Furthermore, the QP signal shows only the quantisation noise explained by a saturated signal. Those mass spectra were not analysed further, but might contain valuable information as well. More details about compositional measurement of dust grains by CDA can be found in our publications about the composition of interplanetary grains [Hillier et al., 2007a], the composition of jovian and saturnian stream particles [Kempf et al., 2005b, Postberg et al., 2006] and the composition of Saturn E ring particles [Hillier et al., 2007b, Postberg et al., 2008, Postberg et al., 2009b]. A more general overview about ring measurements is given in Kempf [2007] and Postberg et al. [2009a] describes the process to interpret mass spectra and the possible relevance of target contaminations.

More likely than CAT impacts are IIT impacts (Fig. 4.11). The much lower electric field strength of about 1 V/cm in front of the target (the total applied voltage is 350 V between target and grid) and its big shape lead to slow rise times of the electron and ion signal. The rise times normally exceed 20 μs . The criteria to separate between CAT and IIT impacts was defined in Srama [2000b] and further constrained in Kempf [2007]. The QT electron signal is

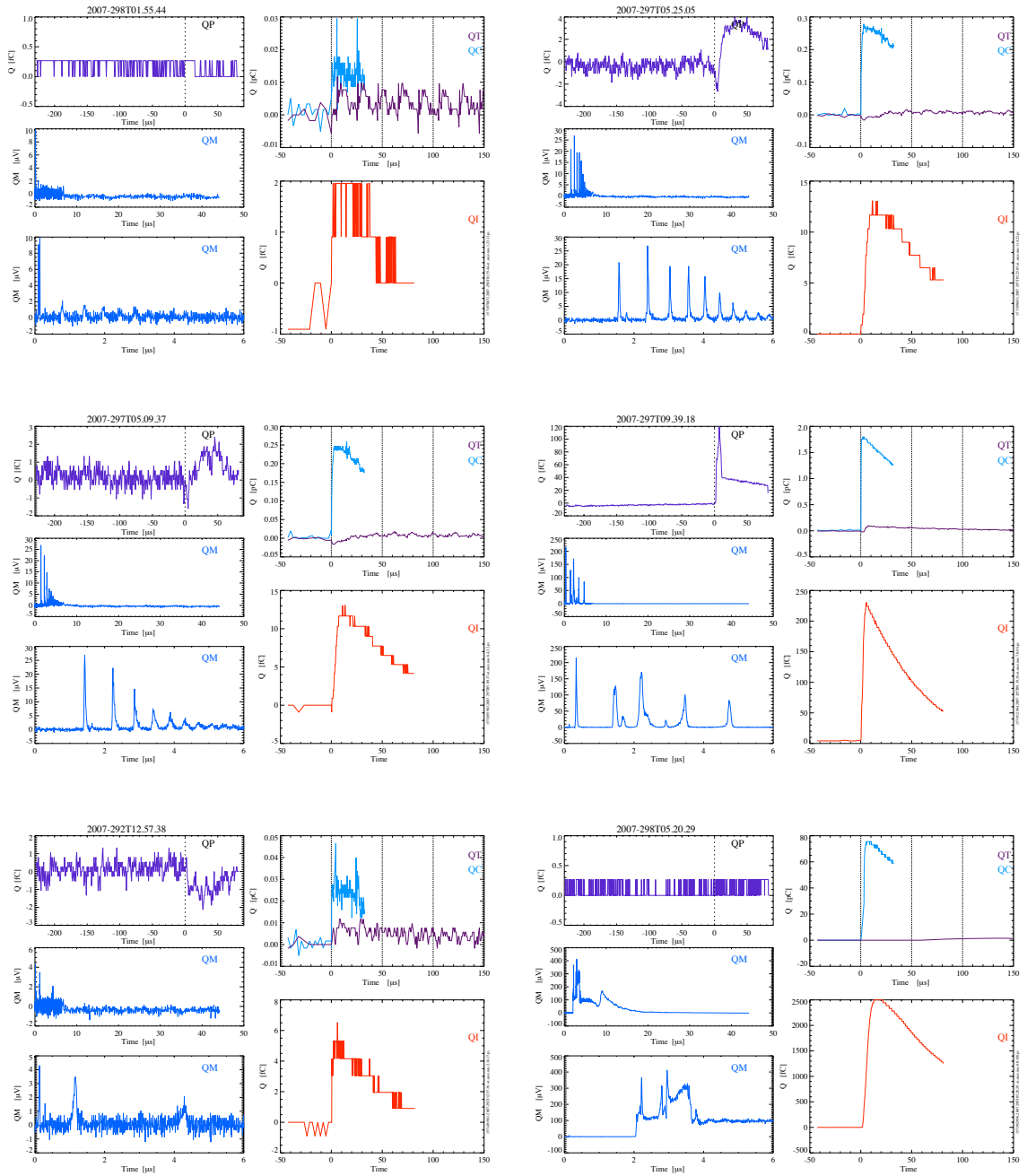


Figure 4.10: Representative signals of impacts onto the CAT providing a mass spectrum. Five plots belong to each impact event, three small plots (left top: QP, left middle: full QM signal, left bottom: first 6 μs of QM signal with TOF mass spectrum) and two bigger plots (right top: QC and QT signal, right bottom: QI signal). In order to better separate the both target channels, the dark pink curve represents the QT signal. The event properties are from top left to bottom right: [2007-298T01:55:44, 11.2, -2.35, 7.5], [2007-297T05:25:05, 4.2, 0.11, 6.25], [2007-297T05:05:37, 4.28, 0.35, 6.41], [2007-297T09:39:18, 3.99, -4.44, 5.46], [2007-292T12:57:38, 36.5, 4.1, 3.6] and [2007-298T05:20:29, 12.6, -1.9, 7.2].

4 CDA Measurements and Selected Results

roughly by a factor of five stronger than the QI signal. For big or fast dust grains, a leading flank of the electron signal is observed. This first and steep rise is caused by electrons of the impact plasma followed by a slower peak due to secondary particle impacts onto adjacent target regions (the curved target allows for ejecta impacts). The multiplier signal shows only very broad features in contrast to the sharp mass lines of CAT impacts.

The impact speed of the left event in Fig. 4.11 derived by the QI signal and Eq. 3.14 is 8.0 km s^{-1} , which is rather close to the impact speed of prograde circular particles of 6.48 km s^{-1} . The event occurred at the ring plane crossing in 2007-297T05 at a distance of $4.3 R_S$ and a latitude of 0.47° . The right event occurred almost five hours later at 2007-297T09:48 and shows a much steeper rise time providing an impact speed of 20 km s^{-1} . Such speeds are not possible for bound prograde particles, such that it is either an impact of a retrograde particle or of interstellar origin. The calculated mass of this event is $1.6 \cdot 10^{-16} \text{ kg}$ (density 2500 kg m^{-3} , diameter $0.5 \mu\text{m}$) in good agreement of the maximum of the interstellar dust population.

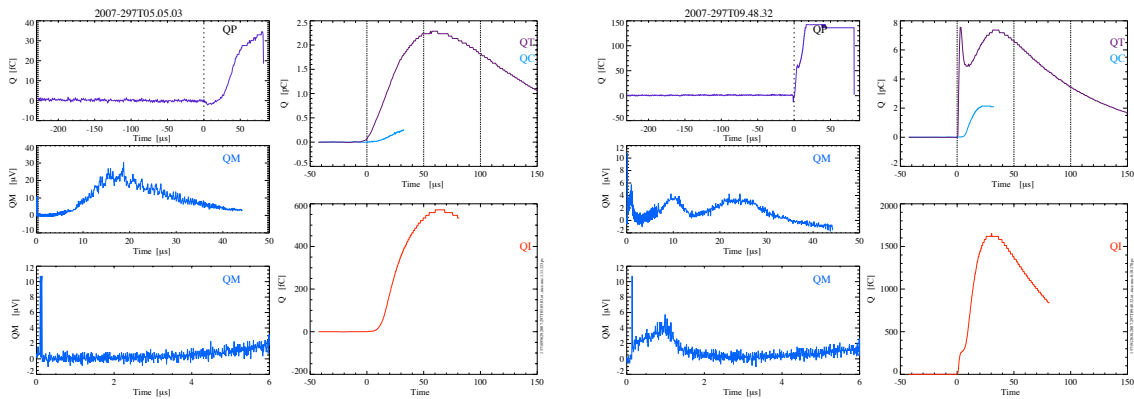


Figure 4.11: IIT impact signals of the events [2007-297T05:05:03, 4.3, 0.47, 6.48] and [2007-297T09:48:32, 4.24, 0.23, 6.3]. The left event represents a typical prograde particle impact (8 km s^{-1} , $1.9 \mu\text{m}$), whereas the impact speed of the right event is either of retrograde or interstellar origin ($> 20 \text{ km s}^{-1}$, $< 0.5 \mu\text{m}$).

CAT and IIT impacts are identified very reliably, but the CDA instrument is normally operated in the discovery mode, meaning that very low detection thresholds on all channels are active. This leads to a high noise rate, but provides the advantage, that many Saturn stream particles of sizes below 10 nm and with speeds of approximately 100 km s^{-1} are measured. Nevertheless, even the raw data do not clearly allow the identification of stream particles (bottom right event in Fig. 4.12). Generally, the noise events are classified either as wall impacts, as events showing a high baseline on the QC channel, events showing no amplitudes besides a steep and high QI signal, or they remain unclassified (no special features). In addition, the QP channel shows frequently a very low noise indicating simply the saturation of this channel¹².

¹²The QP channel saturation is correlated with the spacecraft plasma environment, but was not investigated in detail.

Wall impacts are identified by small or medium amplitudes at the QI channel and strong, but early signals at the QP channel. The event at 2007-297T05:21:24 shows a strong rise at about $40 \mu\text{s}$ before the trigger time (at $0 \mu\text{s}$). The rise of QP is time variable, but shall always occur for impacts onto the inner housing structures. The impacts generate charges which are detected by the sensitive primary charge channel and the generated ions drift to the ion grid triggering the signal recording. For wall impacts, often a small QT signal is observed as well. The origin of the QI-only signals and the QC high-baseline signals is unclear, but they were already observed during the Cassini cruise phase through interplanetary space. No correlation with pointing changes or spacecraft and instrument events was found until today.

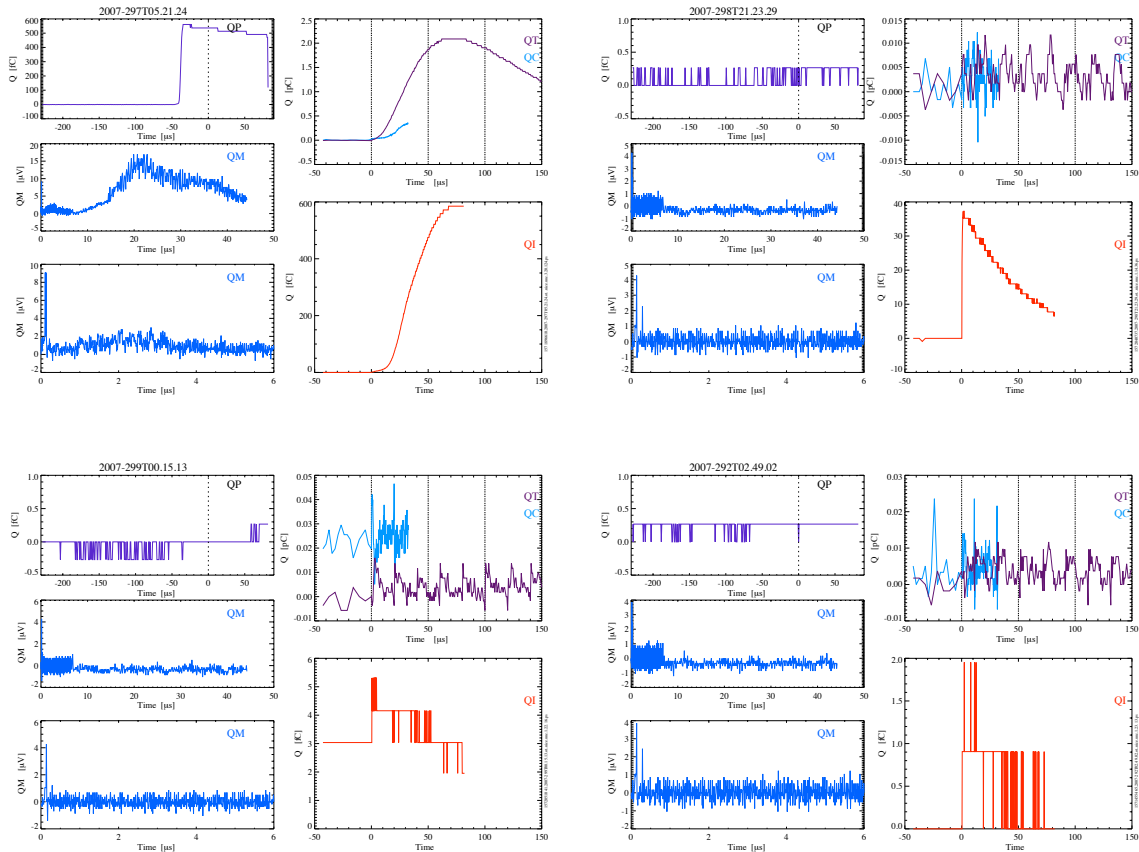


Figure 4.12: From top left to bottom right: Wall impact [2007-297T05:21:24, 4.22, 0.1, 6.2], QI-flare noise event [2007-298T21:23:29, 18.6, -0.6, 6.0], QC high baseline noise event [2007-299T00:15:13, 19.5, -0.4, 5.86] and noise event / Saturn stream particle [2007-292T02:49:02, 38.2, 4.06, 3.4].

There is a category of impact events of very high impact speed showing also clear mass spectra of mineralic/metallic particles (Fig. 4.13). The ion channel signals with its rise times $< 10 \mu\text{s}$ indicate impact speeds between 40 km s^{-1} and 60 km s^{-1} . This speed is even too high for retrograde particles, which lies in the range of 13 km s^{-1} (2009-113) or 24 km s^{-1} (2009-263), respectively. Where do the particles come from? Are these Saturn stream particles which

gained high energies in the saturnian magnetosphere? Can we really exclude retrograde orbits?

Retrograde particles with a semi major axis of $a = 16 R_S$ and an eccentricity of $e = 0.7$ reach speeds of 15 km s^{-1} at pericentre distances of $r_{peri} = (1 - e) \cdot a = 4.8 R_S$ as given by Eq. 4.4. We use $\mu = G \cdot M_S$ with the constant of gravitation $G = 6.6726 \cdot 10^{-11} \text{ N m}^2 \text{ kg}^{-2}$ and the mass of Saturn $M_S = 5.69 \cdot 10^{26} \text{ kg}$.

$$v_{peri} = \sqrt{\frac{(1+e)\mu}{(1-e)a}} \quad \text{and} \quad v_{apo} = \sqrt{\frac{(1-e)\mu}{(1+e)a}} \quad (4.4)$$

Such high retrograde grain velocities lead to impact speeds aboard Cassini of higher than 25 km s^{-1} at the perisaturnium. Furthermore, the impact speed derived from the raw impact signals underlies error factors of up to 1.5. So the answer has to be: no, we cannot exclude retrograde orbits per default and a case-by case analysis has to be done.

But there exist also other possibilities in order to explain the high relative impact velocities. The grains enter the saturnian system from interplanetary space. Here, we have to distinguish between bound particles (interplanetary dust grains) and unbound particles on hyperbolic orbits (β -meteoroids, interstellar grains). Retrograde IDPs might have relative impact speeds \vec{v}_{rel} above 20 km s^{-1} as well, since we have to add the velocities of Saturn ($\vec{v}_S \approx 10 \text{ km s}^{-1}$), the IDP motion with respect to the Sun ($\vec{v}_{IDP} \approx 10 \text{ km s}^{-1}$) and Cassini's velocity with respect to Saturn ($\vec{v}_{Cas} \approx 10 \text{ km s}^{-1}$) in order to achieve the relative impact speed aboard Cassini. Therefore retrograde IDPs are therefore not excluded.

$$\vec{v}_{rel} = \vec{v}_{Cas} + \vec{v}_S - \vec{v}_{IDP}$$

The dust grains following unbound orbits in our Solar System are further candidates for relative impacts speeds of 30 km s^{-1} or beyond. β -meteoroids are accelerated by the solar radiation pressure in the inner Solar System such that they gain hyperbolic speeds depending on their size, optical properties and mass. The last (known) considered population are interstellar dust grains entering our Solar System (compare section A.9). These grains enter the system with $\approx 26 \text{ km s}^{-1}$ and the motion of Saturn in 2009 adds further 10 km s^{-1} such that impact speeds of $>36 \text{ km s}^{-1}$ are expected. Such impact signals are therefore good candidates for interstellar dust impacts and a later statistical analysis and further modelling efforts are necessary to give the proof.

A special high-speed flight software was used onboard CDA, in order to record CAT impacts and mass spectra with a high frequency. This mode was developed and used during the Enceladus flybys like e.g. on DOY 2008-283. In order to avoid saturation effects in the dense plume region (compare Fig. A.4), the event trigger was set to the multiplier channel only with a slightly reduced multiplier voltage. Furthermore, the ion grid voltage was set to 0 V for a further reduction of multiplier anode signals of the very frequent IIT impact events. Impact rates of up to 1 million events per second were expected by the developed model. Such high impact rates lead to charge accumulation at the electrodes, floating baselines and a broad multiplier signal background. Nevertheless, the CDA instrument succeeded to record

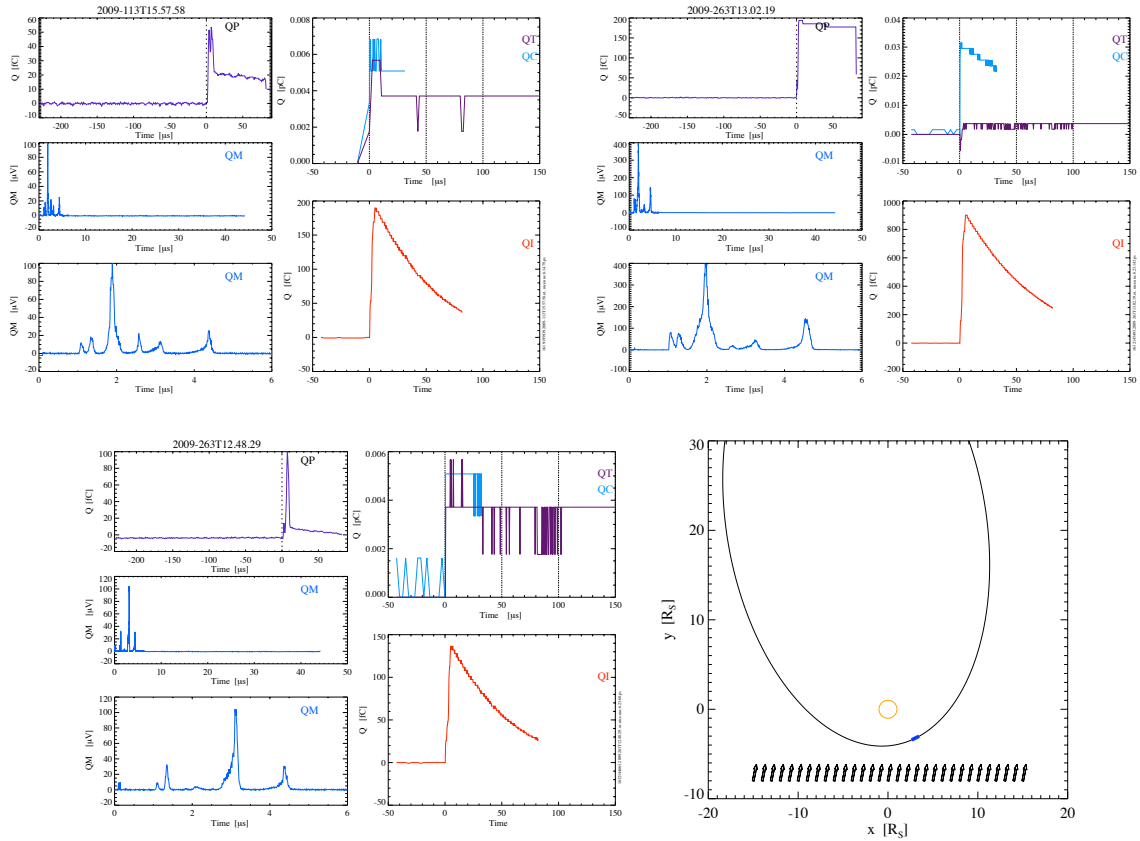


Figure 4.13: Impact events with steep ion grid signals and fast rise times described as [2009-113T15:57:58, 17.0, -60, 1.4], [2009-263T13:02:19, 4.75, -0.97, 6.37] and [2009-263T12:48:29, 4.69, -1.54, 6.24]. All event show mass spectra with strong asymmetric peaks of rhodium ($\sim 4.5 \mu\text{s}$), iron or nickel ($\sim 3.2 \mu\text{s}$), calcium ($\sim 2.6 \mu\text{s}$) and magnesium/silicon ($\sim 1.9 \mu\text{s}$). The first two peaks are probably attributed to carbon and oxygen. The origin of the grains is unclear - possible sources are retrograde dust, interplanetary and interstellar dust. The CDA pointing on day 2009-113 was favorable for ISD observations (a minor deviation of 20° to the upstream ISD direction). The CDA boresight pointing at 2009-263T13 was compatible with the saturnian retrograde direction, but off from the direct upstream ISD direction by 70° . The Cassini orbit number 118 with the marked ring plane crossing at 2009-263T12:30 is shown in an ecliptic J2000/Saturn centered coordinate frame.

200 spectra in the time frame from 2008-283T19:06:42 to 19:07:20. The number of registered impact events was significantly higher, but the internal data processing filtered and stored only spectrum-like signals. The achieved average spectrum recording rate was 5.2 s^{-1} . The Enceladus closest approach occurred at 19:06:40 (all times UTC¹³).

The signals recorded showed a variety of features and spectral shapes (Fig. 4.14), which is no surprise in the very challenging measurement environment. Spectra with sharp lines are mixed with signals showing only rather broad peaks or signatures. The data are currently under an in-depth analysis by F. Postberg of MPI-K/Univ. Heidelberg, since the spectra have to be cal-

¹³Universal Time Coordinated

4 CDA Measurements and Selected Results

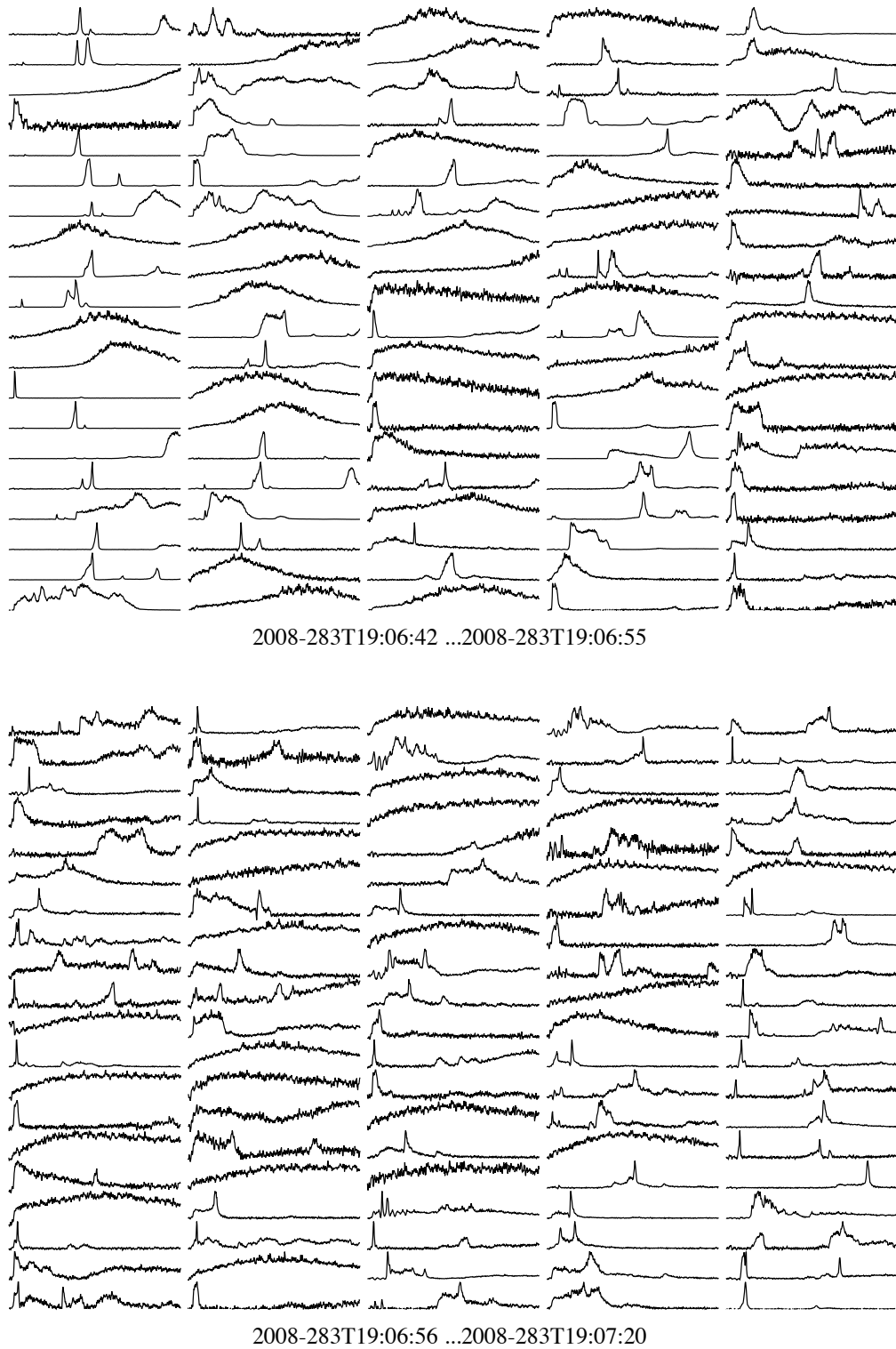


Figure 4.14: All raw mass spectra recorded during the Enceladus flyby between 2008-283T19:06:42 and 2008-283T19:07:20. The closest approach occurred at 2008-283T19:06:40 at an altitude of 25 km. The dense plume region was passed between 19:06:50 and 19:07:05 (compare Fig. A.4). In the dense plume region more spectra showing broad features rather than sharp lines were observed.

ibrated manually. The analysis focuses on the abundance and yield of the sodium features in order to derive information about the possible salt contents in the water ice grains. The flyby speed of 17.7 km s^{-1} reduced the number of water molecule clusters and the mass line at 19 u of the hydronium ion H_3O^+ shall dominate in conjunction with atomic lines. Detailed results of Saturn ring particle compositions can be found in Postberg et al. [2009b], Postberg et al. [2008] and Hillier et al. [2007b].

4.4 Rate and Density Measurements in Saturn's E Ring

In order to summarise the importance and meaning of this section at the beginning: The effort, processing and interpretation of rate measurements is often underestimated. This is more than true for the CDA onboard Cassini based on two facts. First, the high dust densities lead to high impact fluxes showing significant dead time effects (compare section 3.8), and, second, the impacts recorded were filtered and processed by the onboard software due to the limited playback bandwidth. Once the real event rate was derived, a correction and filtering of noise events, wall impacts and counter overflows has to be applied. Generally, two different methods are possible to derive the dust impact rate. The first method is a direct method and based on the analysis of the onboard counter scheme [Srama et al., 2006]. The reliable counter classes (no noise or wall impact counters) are corrected by overflows and dead times with no further interpretation. This approach is employed in this work. The second approach is the analysis of all raw signals on ground. The benefit is a better decision process (CAT impact, IIT impact, Wall impact, noise event, etc.), but the disadvantage is the limited amount of data. Not all signals recorded and classified by the onboard counter scheme are played back to Earth. The amount of downlinked data might be as high as 100% in the outer saturnian system, but can drop down to 5% during ring plane crossings. Therefore these data have to be corrected by an appropriate comparison with the counter data.

Counter values have to be correlated with a mass threshold, and, if possible, with the impact location. From Srama et al. [2006] we get the mass threshold of CDA M_T in dependence of the impact speed v in Eq. 4.5.

$$M_T [kg] = 3.037 \cdot 10^{-13} \cdot v^{-3.75} [km s^{-1}] \quad (4.5)$$

This function was established during laboratory measurements with iron particles and depends on the projectile material and the current threshold settings of the CDA instrument. Since the threshold settings onboard Cassini are lower than or equal to the settings of the former laboratory measurements, one can assume that this formula is quite conservative for the estimation of the lower mass limit¹⁴. Assuming a typical relative impact speed of 8 km s^{-1} , the lower mass threshold would be $1.2 \cdot 10^{-16} \text{ kg}$. This mass corresponds to compact water ice particles with a diameter of $0.6 \mu\text{m}$. Faster impact speeds decrease this mass threshold significantly: Impact speeds of 20 km s^{-1} already produce enough impact charge for water

¹⁴The threshold deviations between laboratory and flight do not exceed a factor of two.

4 CDA Measurements and Selected Results

ice grains with diameters above 200 nm to be detected.

The CDA instrument is generally switched on and in a measurement configuration all the time. The measurement times are interrupted by short periods (max. 40 minutes, approximately once per day) during articulations of the CDA platform, by checkout phases (a few hours of duration), by CDA decontaminations (duration approximately 12 hours), by orbit maneuvers (approximately 4 hours for each OTM) and segments of CDA anomalies (reset and reboot of the instrument after interrupt problems or commanding errors).

The following paragraphs will describe the findings during some selected ring plane crossings. The data recorded during consecutive crossings differ significantly mainly caused by the pointing changes of the Cassini spacecraft. The plots shown in Fig. 4.15 and Fig. 4.16 to Fig. 4.19 are composed of three sections, the upper two give trajectory and pointing information, with the dust impact rates onto the Dust Analyser (DA) at the bottom.

The upper section of Fig. 4.15 shows the angle in degrees between the CDA boresight and the ring plane (RP). A positive angle is defined such that CDA points upwards into the northern hemisphere. 0° corresponds to the CDA boresight parallel to the ring plane. The blue curve shows the distance of Cassini to the ring plane (right y-axis with distance in thousand kilometers).

The middle section shows the angle between the CDA boresight and the dust RAM direction. For this calculation we assume circular prograde dust orbits. Above an angle of 50° , no particles on circular prograde orbits can hit the impact target of DA. However, impacts on the inner wall of DA might be detected up to impact angles of almost 90° (note the central Chemical Analyser Target has an aperture with a half cone angle of 28° , compare Srama et al. [2004a]). An angle of zero corresponds to a normal incident direction.

The bottom section shows the overall DA event rate of (black curve) and the impact rates with small impact charges (blue) and big impact charges (red). Vertical bright blue stripes mark times when the DA was not in a measurement configuration (mainly caused by articulations with a duration of 15 to 30 minutes). During the activation of the articulation platform the event definition has to be switched off and no events can be recorded.

The impact rates are based on two different classification schemes. The flight software before version 10.0 used 20 counters and processed the data until DOY 150 in 2005. The three rate curves are: Red representing class 3 events including the counters 2, 3, 6, 7, 8, 9, 14 and 15 (counter definitions are given in Srama et al. [2006]). This class covers highly reliable dust impacts with amplitudes well above the noise level and a mass threshold of approximately $5.0 \cdot 10^{-15}$ kg (the mass threshold is velocity dependent and here we assume an impact speed of 7.5 km s^{-1} ; ice particle with 2.1 micron diameter); Blue covering the counters 10, 11, 12, 13, 17 and 18, which represent the class 2 events (mass threshold of $1.0 \cdot 10^{-16}$ kg or ice grains with a diameter of 0.55 micron). 90-95% of these events are considered to be true dust impacts with moderate amplitudes; the black line includes all counters (including the noise counters 16 and 19) and shows the highest rates.

Impact events represented by the counters of the red curve are called hereinafter big particle impacts and the events related to the blue curve are called small particle impact. However, the

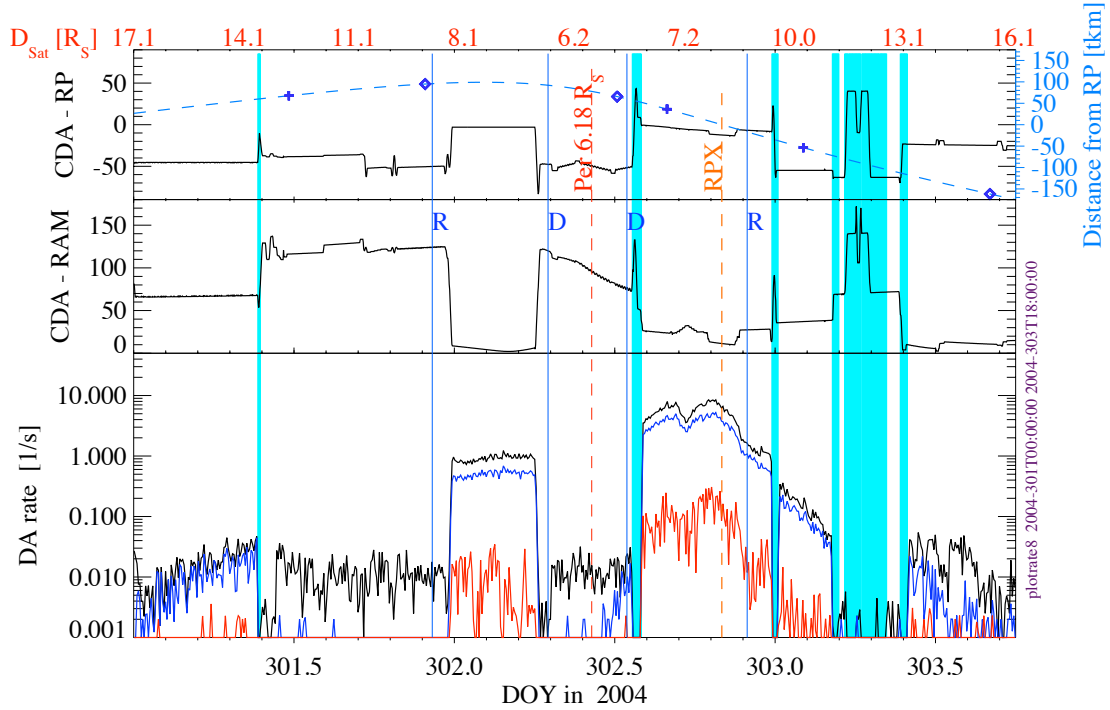


Figure 4.15: Pointing geometry and dust impact rates for the first inner ring plane crossing of Cassini at Saturn (orbit A). The top panel shows the angle in degrees between the CDA boresight and the ring plane (black line) as well as the distance of Cassini from the ring plane in units of 1000 km (dashed blue line). The symbols on the dashed line indicate crossings of different latitudes (cross: 5° , diamond: 10° , triangle: 15° , square: 20°). The middle panel shows the angle between the CDA boresight and the dust RAM direction assuming circular prograde orbits. The lower panel shows impact rates based on a flight software 9.x-classification scheme: red line are class 3 events, blue line are class 2 events and a black line for all events (see text for details). The red numbers at the top are Cassini's distance from Saturn in units of R_S . The vertical red line labelled 'PER' indicates the time of periapsis and the dashed red line labelled 'RPX' indicates the time of ring plane crossing. The lines labelled R, D, T, E and M indicate the time of crossings of the orbits of the moons Rhea, Dione, Tethys, Enceladus and Mimas respectively. The vertical bright blue bars indicate the time periods where CDA was not in a nominal measurement configuration (CDA did articulate, CDA was off or in a standby mode).

detection thresholds of the counters react to impact charges and the particle speed has a dominant influence on the impact charge. The separation between big and small impacts becomes only true by considering a constant impact speed.

The measured rates after 2005-150 are based on the classification and onboard processing with flight software version 10.0. Here, we define the red curves as the sum of class 2 and class 3 events, which are true dust impacts with a mass threshold of $5.0 \cdot 10^{-15}$ kg. Class 3 events describe strong impacts and cover the counters 0, 2, 8, 9 and 11, whereas class 2 events are used for medium sized dust impact charges and include the counters 1, 3, 10, 12 and 7. The blue curve includes the counters 4, 5, 6, 17 and 18 of class 1, which count small dust impacts

4 CDA Measurements and Selected Results

on the IID or the CAT with a mass threshold of $3.5 \cdot 10^{-16}$ kg (ice grain with a size of $0.87 \mu\text{m}$). Even class 1 events are dominated by real impacts, due to a reliable onboard evaluation scheme. The noise and low quality counters are 13, 14, 16, 19, 20, 21, 22 and 23 and they correspond to class 0. These counters might include many real dust impacts like dust stream particles with low impact charges or impacts on the inner wall or struts of the dust analyser aperture. The ratio of real impacts to noise¹⁵ is highly variable but can reach values of more than 50% of real impacts during ring plane crossings. The black curve shows the highest rate and is composed of the sum of class 0, class 1 class 2 and class 3.

The first ring plane crossing data were obtained around DOY 2004-302 and the corresponding rate profiles are shown in Fig. 4.15. At 2004-302T04:17 Cassini reached a Saturn distance of $7.0 R_S$ and a latitude of 13.5° which corresponds to an altitude of $100\,000$ km. Periapsis occurred at $6.18 R_S$ and the ring plane crossing occurred at DOY 302T20 at a distance of $8.0 R_S$. For the first time, DA measured dust at high altitudes as far as $100\,000$ km above the ring plane (early on DOY 2004-302). Beyond distances of $10 R_S$ the impact rate is still significant (early on DOY 303). The onset of dust impacts occurred at a distance of $17 R_S$ and altitude above $20\,000$ km at the beginning of DOY 2004-301. After an unfavorable pointing geometry during the second half of DOY 301, the dust analyser registered clear dust signals between 8 and $6.5 R_S$ at altitudes of $100\,000$ km with an impact rate of approximately 1 per second. The impact rate increased with approach to Saturn and at lower altitudes (DOY 302). Between 8 and $9 R_S$ distance, the impact rate was still very high and close to the saturation limit of the instrument (1 second dead time). The rates are dead time corrected and therefore show values above 1 s^{-1} .

The measurement geometry was different for the second ring plane crossing around DOY 2004-350 (Fig. 4.16). The rolling downlinks during which the CDA - ring plane angle changed significantly (DOY 349 and DOY 350) are very obvious. The second roll was interrupted due to Cassini internal flight rules. During this part of the orbit Cassini stayed within a distance of $30\,000$ km of the ring plane except at the end of this segment when it finally reached a distance of $60\,000$ km. The rolls led to strong variations of the dust impact rates. This can be observed at low dust densities further out (around $15 R_S$), as well as within $7 R_S$. Nevertheless, the envelope of the rate maxima during rolls still follows a clear trend; it rises during the approach phase on DOY 349 and increases and decreases before and after the ring plane crossing on DOY 350. As soon as the CDA boresight angle to the dust RAM direction exceeds $\sim 60^\circ$, the impact rate falls by orders of magnitude (DOY 351T00). On its outgoing pass, DA observed significant impact rates beyond $10 R_S$ (between 0.2 s^{-1} and 0.5 s^{-1}).

The geometry changed significantly in orbit 3 with its targeted Enceladus encounter at 2005-048T03:30 and a flyby altitude of 1260 km. Furthermore, Fig. 4.17 shows that this orbit had a low inclination and Cassini remained close to the ring plane for the entire time. This would have been optimal for investigations of dust densities during satellite orbit crossings. How-

¹⁵Noise caused by plasma fluctuations, sounder events, mechanical noise and disturbances on the electrical ground

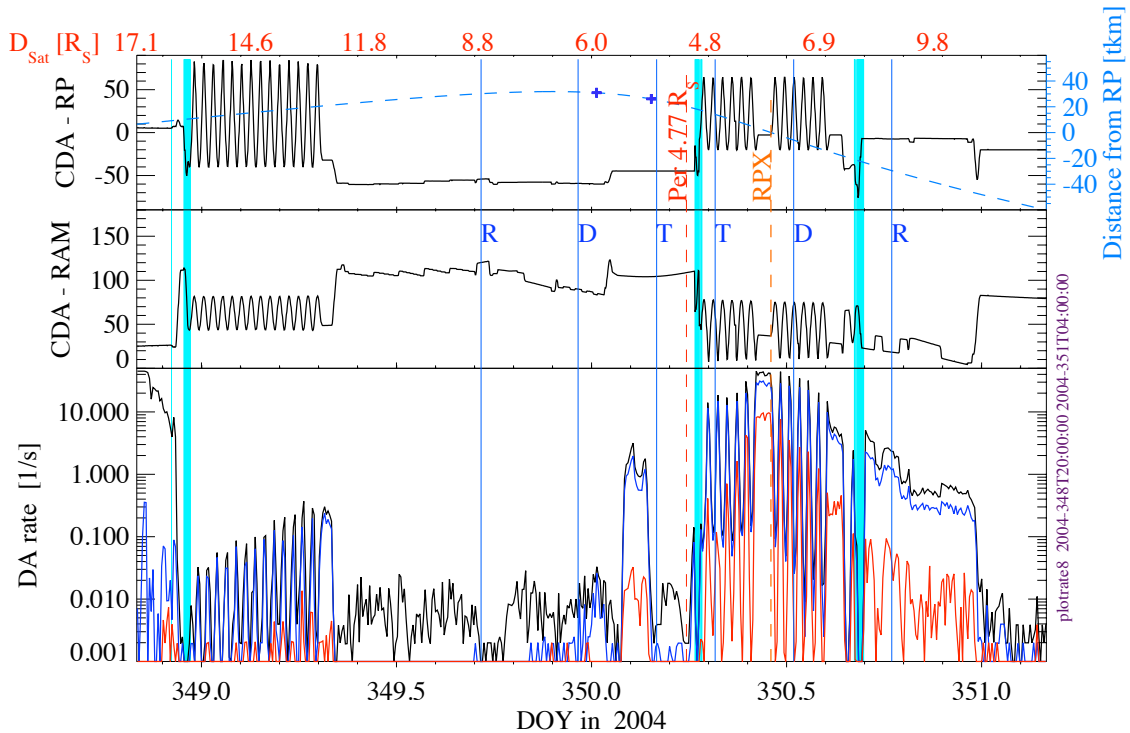


Figure 4.16: CDA pointing and dust impact rates at the inner ring plane crossing in orbit B.

ever, many pointing changes occurred close to the moons orbital distances and no significant variations of dust impact rates during the orbit crossings could be observed. Close to the perapsis and ring plane crossing the spacecraft went into a safe attitude with the high gain antenna pointing towards dust RAM (in order to protect the subsystems from big dust impacts). This orbit segment shows quite a number of interesting features. First, the approach phase showed a high number of impacts (ring particles and stream particles) between 16 and 10 R_S . Due to the marginal pointing, small impacts (i.e. low signals) dominated with a low rate of big particle impacts. Within 6.3 R_S the instrument was saturated, but a decrease of dust impacts was observed on the outgoing pass outside 6.3 R_S . Therefore, DA could not resolve a dust impact rate profile during the Enceladus encounter. However, the HRD instrument showed dust flux variations which were high at the orbit of Enceladus. These results were reported in Kempf [2007]. Fortunately, the observing geometry was stable and convenient outside 10 R_S and a decrease of the impact rate of 1 s^{-1} at 10 R_S down to 0.1 s^{-1} at 15 R_S was detected.

A rocking downlink was performed on day 2005-088 leading to impact variations of two orders of magnitude (Fig. 4.18). The instrument was in saturation again in the inner saturnian system. The first rate variations were observed on the outgoing part of the trajectory starting at 4.5 R_S . On the other hand, the boresight was approximately 50° away from the dust RAM direction which limited the observable number of particles. CDA had good pointing for dust measurements for only a short period before noon on DOY 89. The rate measurements around

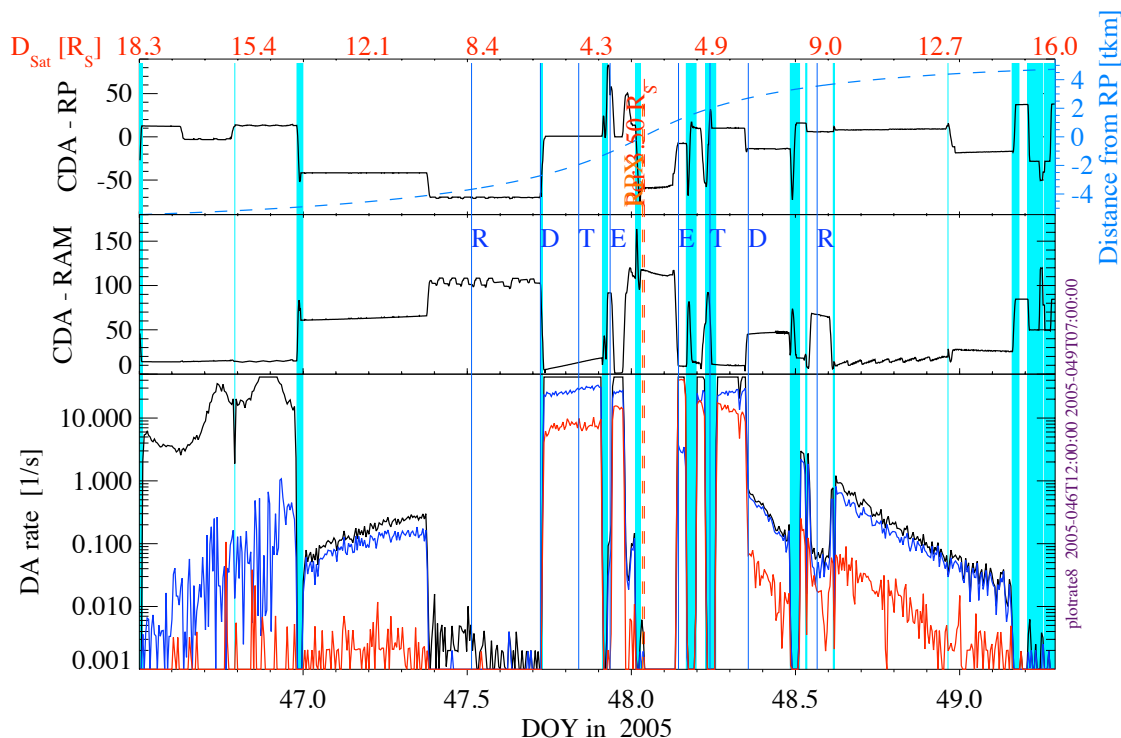


Figure 4.17: CDA pointing and dust impact rates at the ring plane crossing on orbit 3.

8 R_S still have values of 3 s^{-1} and confirm the high rates monitored in previous orbits. More interesting is the phase between 10 and 12 R_S showing an increasing dust flux with increasing distance from Saturn. This was caused by changes of the geometry: The CDA boresight went closer to the dust RAM direction leading to a larger sensitive area for circular prograde particles.

The ring plane crossing of orbit 7 had only a few major changes in spacecraft attitude. This allowed rather excellent and smooth dust flux measurements with CDA between 5 R_S on the ingoing part and 17 R_S on the outgoing part. Minor changes in the spacecraft pointing are reflected in small increases of the impact rate (123T12:00 - 124T00:00). On the other hand this orbit had a higher inclination and therefore big elevations above or below the ring plane. The result of the impact rate measurements is shown in Fig. 4.19. The peak impact rate of small impact charges shows a small slump at the ring plane crossing at 122T23:36. This causes two maxima before and after the ring plane crossing separated by approximately 35 minutes. In this time the spacecraft moved from about -2° latitude to $+0.8^\circ$ latitude. The relation between small (dark blue curve) and big impact charges (red curve) are anti-correlated at the time of the ring plane crossing (122T23:36). However, the measurement geometry was very stable leading to the conclusion that the dust population changes with distance from the ring plane. The profile is reminiscent of the shape of Jupiter's Gossamer ring where the vertical ring extension is related to the inclination of the moons [Hamilton, 2003]. Here, the only

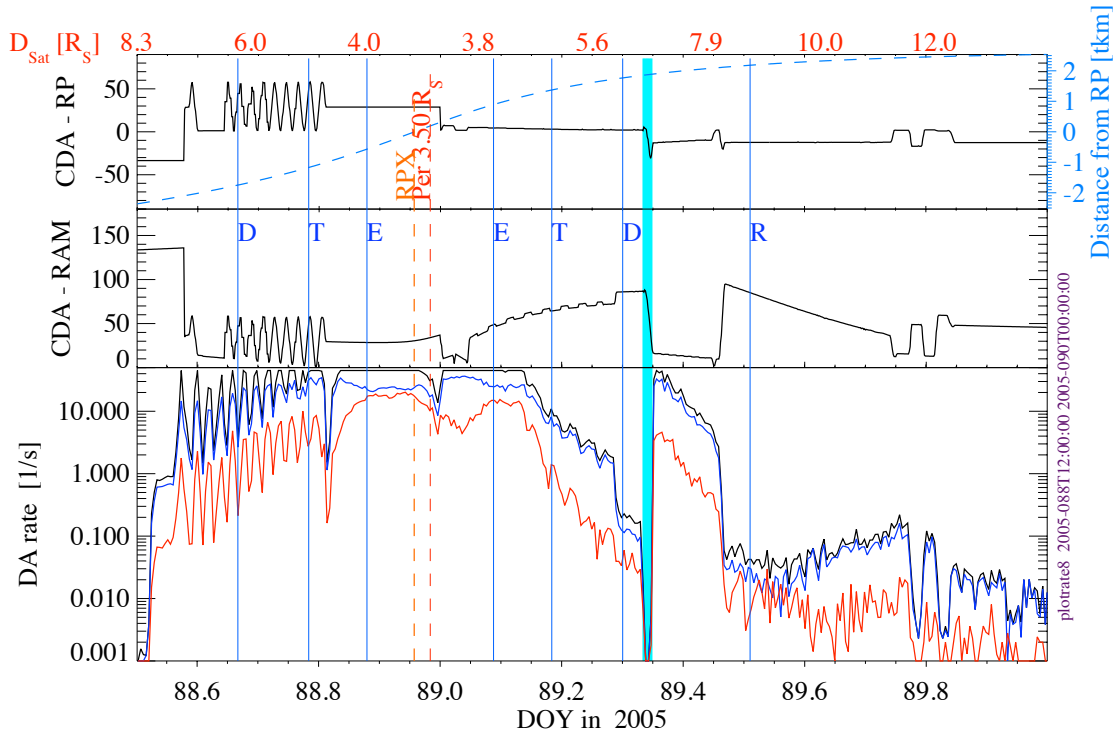


Figure 4.18: CDA pointing and dust impact rates at the inbound ring plane crossing on orbit 5. The fixed pointing angles around DOY 88.6 are caused by CDA data gaps.

moons with an inclination above 1° are Tethys and Mimas. The relative impact velocity for circular prograde particles was 8 km s^{-1} . Later measurements on day 2005-177 showed a similar counter profile.

The quick rise of Cassini elevation above the ring plane was accompanied by a fast decrease of the impact rate. Changes of the CDA angle towards the ring plane in mid DOY 123 (Dione orbit crossing) led to dust detections at elevations above the ring plane as far as 120 000 km (at $7 R_S$, 17° latitude). This was followed by only a gradual decrease in the impact rate with distance from Saturn. However, one has to take into account that Cassini came closer to the ring plane with increasing distance. Although only minor pointing changes occurred, due to the high ring plane elevations, this data set is again not suited for an analysis of dust densities around satellite orbit crossings. Some impact rates based on this data set are listed in Tab. 4.1.

The rate measurements obtained on day 2005-122 and 123 remain the most consistent data set until today due to its stable outgoing pointing profile. The second best ring profile determination occurred in orbit 8 (2005-141/142). Within $7 R_S$ more pointing changes occurred and the rate profile was more fragmented. Starting at $7 R_S$ on the outgoing segment, continuous coverage of the ring was possible until $17 R_S$. However, during the scan the elevation to the ring plane changed again significantly. It fell from 120 000 km at $7 R_S$ down to 55 000 km at $17 R_S$. Once again high impact rates of dust particles were observed by DA at high altitudes

4 CDA Measurements and Selected Results

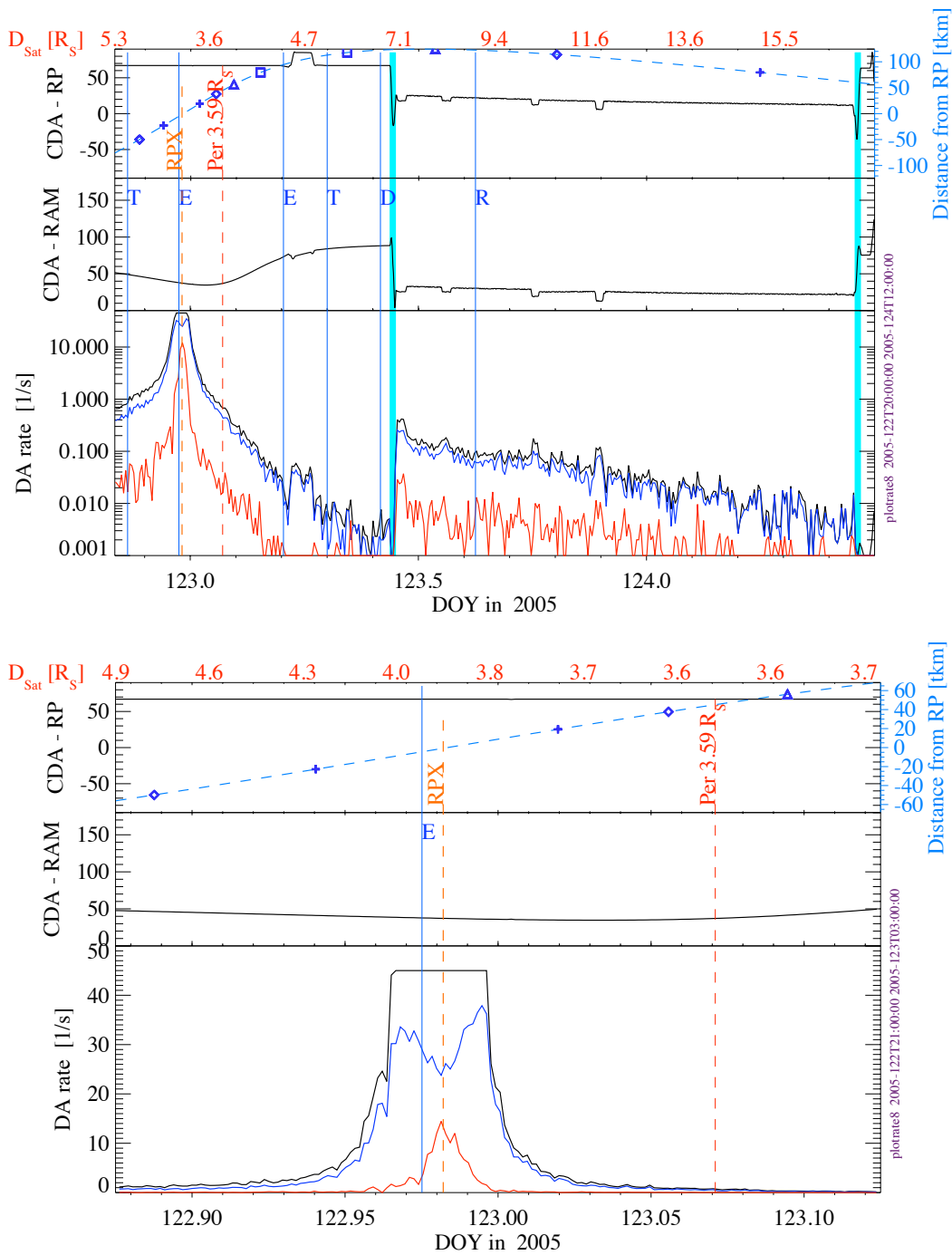


Figure 4.19: CDA pointing and dust impact rates for the inbound ring plane crossing on orbit 7 (top). The DA impact rate of the ring plane crossing of orbit 7 with a higher time resolution (bottom).

Table 4.1: Impact rates derived from the data set on DOY 2005-123.

DA impact rate	Distance from Saturn	Elevation above ring plane
1 s^{-1}	$5 R_S$	-50 000 km
1 s^{-1}	$3.6 R_S$	+40 000 km
0.2 s^{-1}	$7 R_S$	+120 000 km (17° latitude)
0.01 s^{-1}	$14 R_S$	+75 000 km

above the ring plane. The rate observed was 0.3 s^{-1} at a distance of $10 R_S$ and an elevation of 100 000 km. An inspection of the raw data revealed reliable dust impacts with impact speeds between 7 and 40 km s^{-1} .

The entire ingoing pass on orbit 9 was lost due to unfavorable measurement geometries. The outgoing pass had many changes in spacecraft attitude and a rolling downlink on DOY 160. An inspection of raw impact signal data showed evidence for water ice particles at elevations of 50 000 km and above (at $\approx 4 R_S$). At distances of $7.8 R_S$ water ice particles were identified at latitudes as high as 15° . Further data of CDA ring plane crossing measurements are shown and discussed in Srama et al. [2006].

The Cosmic Dust Analyser measures continuously at all distances and latitudes from Saturn. Normally, the impact rates show high values in the inner saturnian system (inside Titan's orbit), but there are many exceptions. Rates above 0.1 s^{-1} are often observed outside Titan's orbit up to distances of $50 R_S$. One example is shown in Fig. 4.20 where the instrument reached saturation levels at distances around $30 R_S$ from Saturn. A closer look to the pointing profile showed a strong correlation with both, the angle of the CDA boresight towards the prograde dust RAM direction and the Saturn direction (dust stream direction). Furthermore, the profile clearly shows, that high fluxes occurred while the CDA has a low angle towards the saturnian ring plane (top diagram, Fig. 4.20).

What is the nature of such particles? As shown by the black line of the rate plot (bottom diagram), the events showed only very small electrode charges, which means, that the impacts were caused either very slow or very tiny dust grains. A closer look into the raw data revealed some tiny impact signals related to CAT impacts. These signals do show a weak multiplier spectrum only (peaks with amplitudes of less than 5 dn), and the electron signal of the QC channel is smaller than 4 dn ($< 7 \cdot 10^{-15} \text{ C}$, the signals of the QI channels do not exceed amplitudes of $\sim 2 \cdot 10^{-15} \text{ C} \approx 3 \text{ dn}$). The low thresholds of CDA did allow to trigger to such small signals, and only the raw data can reveal the real nature of such features.

High rates outside Titan's orbit were found at times around e.g. DOY 2005-281, 2006-185, 2006-225, or 2007-266 (rates up to 0.5 s^{-1} at $47 R_S$ and 250 000 km below the ring plane). Assuming a sensitive area of CDA of only 0.06 m^2 ¹⁶ the measured dust fluxes could

¹⁶The detection threshold of CAT impacts is lower than of IIT impacts due to the mass lines in the multiplier spectrum, which are taken as trigger signal.

4 CDA Measurements and Selected Results

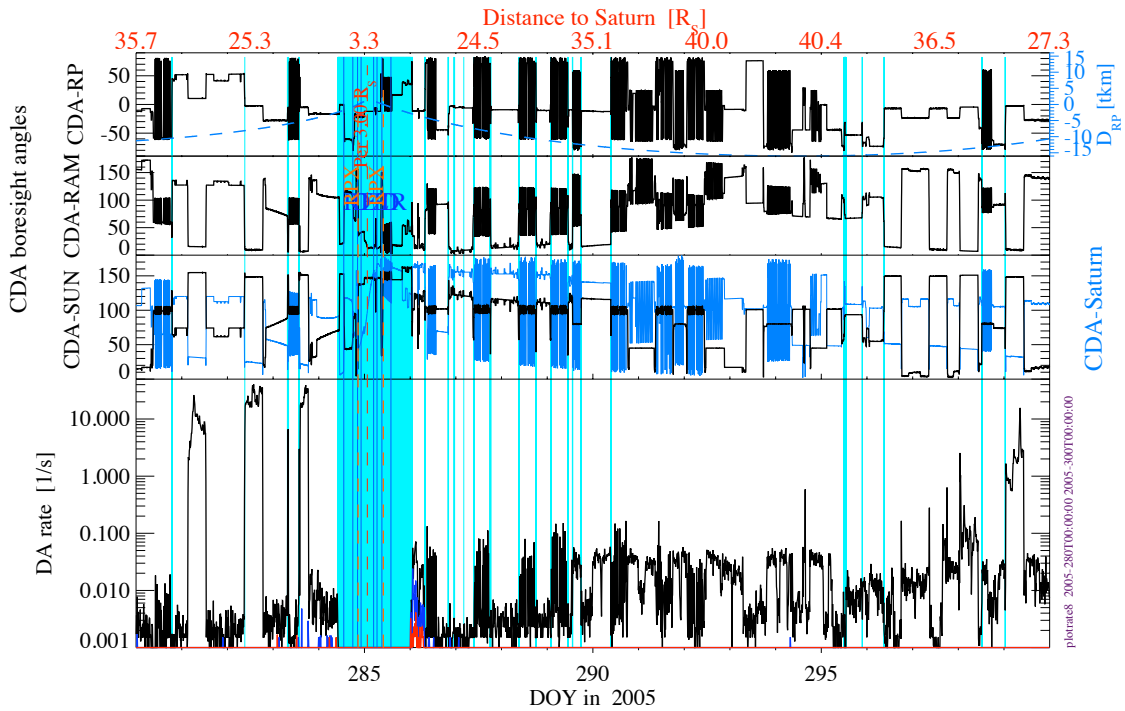


Figure 4.20: CDA impact rate (bottom) and pointing information (top plots). In addition to previous figures, the angle between the CDA boresight and the Sun and Saturn direction was added (middle-bottom panel). High impact rates were registered well outside Titan’s orbit at distances of 30 R_S on the days 281, 282 and 283. The rates of the noise/small impact counters reached saturation levels. The rates are correlated with the CDA-dust RAM direction and the CDA-Saturn direction. Small angles between the CDA boresight and Saturn provide high fluxes of nano-sized dust stream particles.

reach values of up to $33 \text{ m}^{-2} \text{ s}^{-1}$ at distances of $47 R_S$). – The mass threshold of prograde bound dust particles detected around 2006-225 can be estimated by taking the expected relative impact speed of 4 km s^{-1} and the QI amplitudes of maximal 2 fC. The calculated mass is $1.8 \cdot 10^{-15} \text{ kg}$ which corresponds to water ice grains with sizes of at least $1.4 \mu\text{m}$. A source for such big grains with local densities high enough to partly saturate the CDA instrument is unknown. Although Phoebe (retrograde), Iapetus and Hyperion can act as a dust source in the outer saturnian system [Banaszkiewicz and Krivov, 1997], only saturnian dust stream particles are considered as a source strong enough to explain these observations. Furthermore, saturnian dust streams (nanometre sized silicate grains with speeds of $\approx 100 \text{ km s}^{-1}$) were discovered with high rates during the approach of Cassini to Saturn in 2004 [Kempf et al., 2005a].

A good correlation of the CDA measured dust fluxes with the Cassini pointing on DOY 225 in 2006 is given in 4.21. The dust rate (bottom diagram) shows clear maxima of 1 s^{-1} as long as the CDA boresight is close to the dust RAM direction (prograde grains) and the angle of CDA and Saturn is within 50° . The modulation between 225T02:00 and 225T10:00 is caused by one of Cassini’s downlink rolls. The high gain antenna points towards Earth and

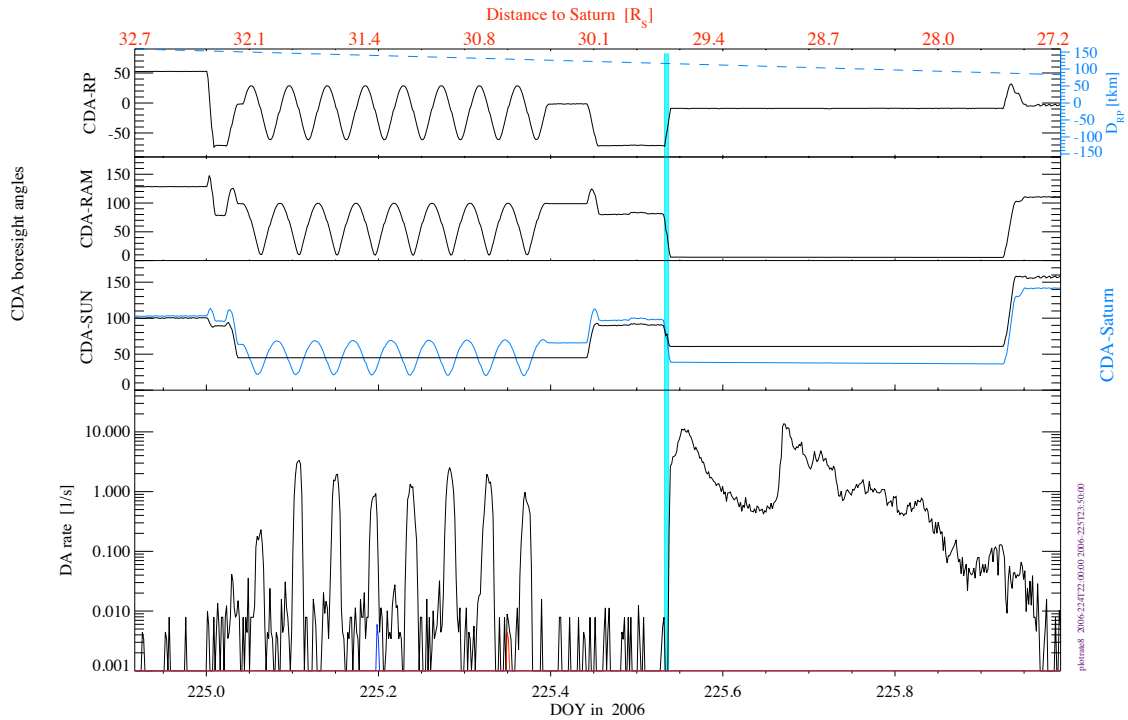


Figure 4.21: Modulation of the CDA impact rates of Saturn dust stream particles on day 2006-225 during a spacecraft roll. High impact rates occurred during phases of low angles between the CDA boresight and the Saturn direction (blue curve, middle bottom panel). The fixed pointing during the second half of day 225 lead to minor variations of the rates (interaction of stream particles with the magnetosphere of Saturn).

the spacecraft rolls about its z-axis with a speed of up to 26 min. per revolution. Here the CDA instrument showed rates even above 1 s^{-1} at distances between 28 and 32 R_S . A detailed analysis of the dynamics of the saturnian dust streams using the real parameters of the saturnian magnetosphere and back-tracing methods is done by Hsu [2010].

Impact Rate Analysis

What are all the impact rate data good for? One answer is, that local dust densities can be derived by correcting the data for the detector sensitive area, its mass threshold and the Cassini velocity. This will be done in the next section. Another common method is the spectral analysis of rate data in order to learn about the nature of their sources and forces. If the dust sources show any time variable behaviour (rotating bodies with volcanoes, orbiting moons), or if the forces acting upon the dust grains on their way from the source to the observer are subject to periodic phenomena (rotating magnetospheres, rotating Sun and the IMF), time variable impact rates will be detected. The study performed by Graps et al. [2000] revealed the origin of the jovian dust streams. The extraction of Io's orbit and of Jupiter's rotation frequency in

the Galileo dust data identified the source of the nanometre sized dust streams: Jupiter’s moon Io and its volcanoes.

Can we do something similar with the saturnian dust impact rates of the interplanetary cruise phase? Cassini approached Saturn in august 2004 and the dust instrument pointed towards Saturn within the time period of 2003-220 to 2003-259. Other observational periods are very fragmented and were not taken for an analysis.

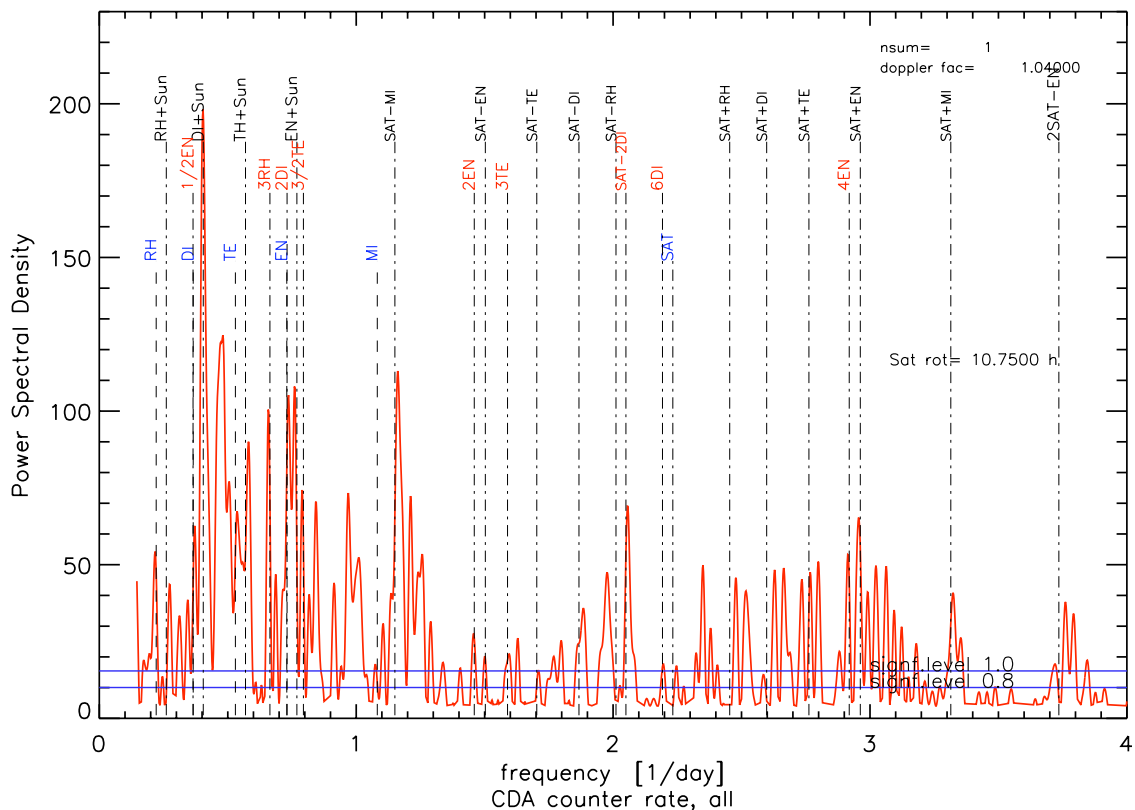


Figure 4.22: Lomb periodogram of CDA noise counter events in 2003 from day 220 to 259. Periodicities of the saturnian moons and of Saturn’s rotation period are marked with vertical lines. The labels indicate the orbital periods of the moons Rhea (RH), Dione (DI), Enceladus (EN) and Tethys (TE). Further rotation frequency labels are from Saturn (SAT) and the Sun. Possible combinations of the Saturn or Sun rotation period and moon orbital frequencies are labeled.

The IDL program *rs_rate2periodogram.pro* was developed based on the spectral analysis code of A. Graps in order to investigate any periodicities of the CDA counter data in the mentioned time period. The filter works with non-uniform sampled rate values as they occur for in-situ space instrumentation. Data gaps, pointing changes, checkout times and maneuvers normally interrupt the data sampling. Problems arise when the data gaps become large and any patching technique (replacement or interpolation of the missing data) introduces spurious frequencies at the low frequency end. In order to avoid this, Lomb’s method was used, which involves least square fitting of the time domain samples to a sine and cosine series of different

frequencies [Lomb, 1976]. The Lomb algorithm provides the power spectral density P_N of a given frequency ω_i (Lomb periodogram). For each frequency ω_i a probability P is determined, that the null hypothesis is true (i.e. that the frequency peak is random). Fig. 4.22 shows the lomb periodogram of the noise event rates¹⁷ derived from the housekeeping data in 2003 of the days between 220 and 259. The upper blue horizontal line marks the threshold of reliable frequencies and peaks exceeding the line are considered to be real. The frequencies were doppler corrected by a factor of 1.04 in order to account for the finite dust stream velocities of $\approx 100 \text{ km s}^{-1}$ in relation to the Cassini velocity of $\approx 5 \text{ km s}^{-1}$. This correction is important for a valid interpretation of the power spectrum, but unfortunately, the exact dust speed is not known (likely between 90 and 150 km s^{-1}). Furthermore, the rotation frequency of Saturn is time variable. A period of 10.75 hours (10:45 h) was selected, which is slightly longer than the rotation period determined by Voyager of 10:39, but closer to the value measured by the radio plasma instrument onboard Cassini in 2004 (the SKR value provided 10:45:45) [Read et al., 2009].

First, it is remarkable, that many frequencies are found in the data set, ranging from 0.4 to 3 per day. A strong dominance of the Enceladus orbital period cannot be observed, but some peaks correlate with 1/2, 1 and 4 orbital periods. The highest peak might be attributed to the interference of Dione and the Sun. Further frequencies might be explained by Enceladus+Sun, Saturn–Mimas and Saturn+Enceladus combinations. The occurrence of many lines and the manifold combinations of moon, Saturn and Sun frequencies make the analysis very difficult and questionable. Nevertheless, the saturnian system is very complex and the E ring of Saturn embeds the moons Mimas, Enceladus, Tethys, Dione and Rhea, such that an influence of many bodies is not excluded.

High Rate Detector Rates

In addition to the measurements by the impact detector DA, dust impact rates are determined by the High Rate Detector sensor. As explained in section 3.7, the foil detectors measure impact rates up to $10\,000 \text{ s}^{-1}$ although with a higher mass threshold and low reliability. A summary of HRD measurements is given by Kempf [2007] and Kempf et al. [2008], but two recent examples will be given in this section showing the registered dust flux during the Enceladus plume crossings in 2008.

One closest approach at Enceladus occurred at 2008-224T21:06:19 with an altitude of 46 km and a flyby speed of 17.7 km s^{-1} (Fig. A.4, 11. Aug. 2008, rev. 80, E4), and a second flyby occurred at 2008-283T19:06:40 (9. Oct. 2008, rev. 88, E5) with the same flyby speed but with an altitude of only 19.2 km.¹⁸ The Cassini orbits had a high inclination of more than 70° and the closest approach was at equatorial latitudes of Enceladus. Cassini entered the plume region (south pole) therefore 10 to 20 seconds after the closest approach and the highest impact

¹⁷It was found that the noise counter corresponds to the saturnian stream particles which are affected by Lorentz forces in the magnetosphere.

¹⁸No HRD and DA data were recorded during the Enceladus flyby at 2008-072 due to an unexecuted software patch command.

4 CDA Measurements and Selected Results

rates were measured also after the closest approach (Fig. 4.23).

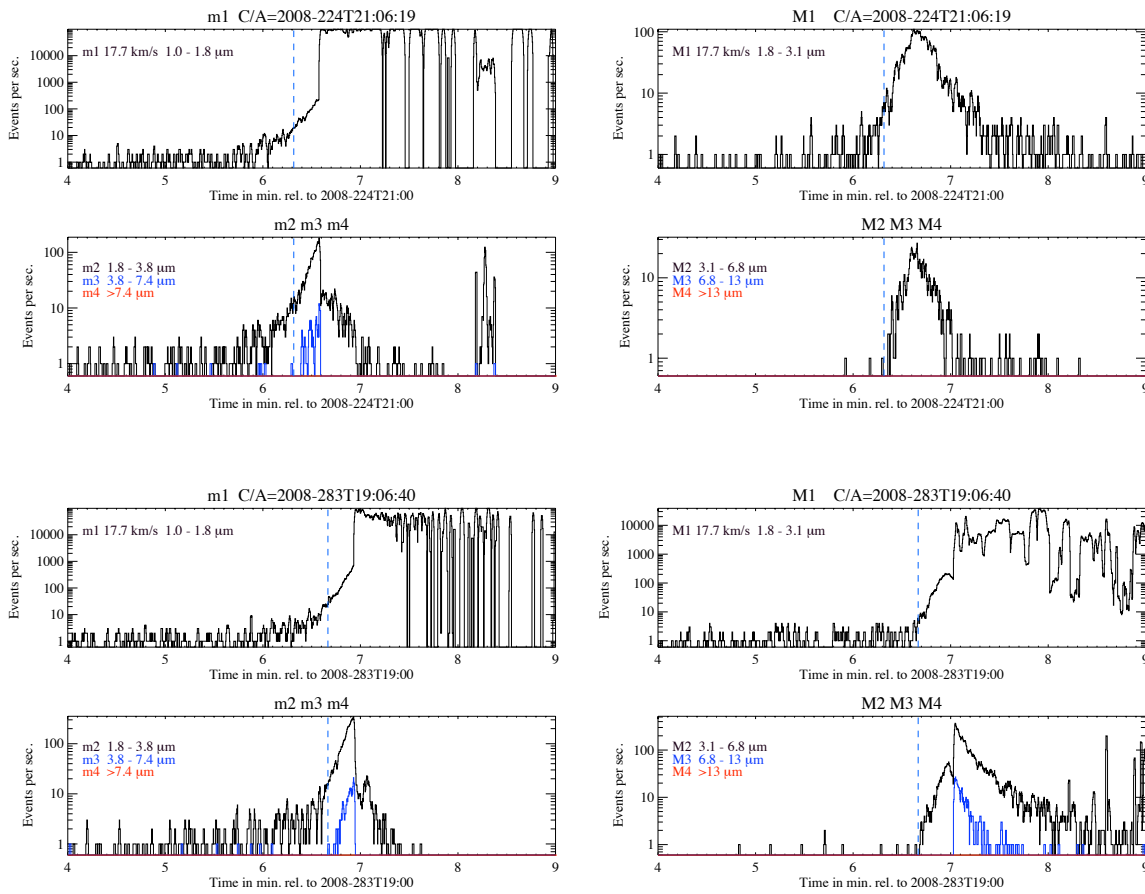


Figure 4.23: Counting rates of the two HRD sensor foils (m and M) during the Enceladus flybys at 2008-224T21:06:19 (top diagrams) and 2008-283T19:06:40 (bottom diagrams). The closest approach to Enceladus is shown by the dashed vertical line (46 km at 2008-224 and 19 km at 2008-283) and the relative flyby speed was 17.7 km s^{-1} . The four thresholds for the grain sizes of the individual counter channels is labeled. Consistent results were achieved until about 20 seconds after closest approach, where a step rise of the counter $m1$ occurs. These high rates are considered to be noise and dead time effects lead to falling rates in the channels of $m2$ and $m3$. The data were recorded using the encounter mode with a time resolution of 0.2 s and the rates are not dead time corrected. Rates of $10\,000 \text{ s}^{-1}$ lead to dead times of 5% [Srama et al., 2004a].

The rate data of the HRD detector are classified in total by eight counters: Four counters with four different mass thresholds for each detector. The mass thresholds (trigger thresholds) are dependent on the impact speed and the values are shown in each diagram of Fig. 4.23 (compare Tab. in section A.7). The sensors are named m for the small $6 \mu\text{m}$ thick foil, and M for the $28 \mu\text{m}$ thick foil. The mass thresholds for the big foil are accordingly higher and the corresponding water ice grain diameters are as follows: $m1 = 1.0 \mu\text{m}$, $m2 = 1.8 \mu\text{m}$, $m3 = 3.8 \mu\text{m}$ and $m4 = 7.4 \mu\text{m}$ for the thin foil, and $M1 = 1.8 \mu\text{m}$, $M2 = 3.1 \mu\text{m}$, $M3 = 6.8 \mu\text{m}$ and

$M4 = 13 \mu\text{m}$ for the big foil. The $m1$ and $M1$ counters are the most sensitive ones and show the highest rates accordingly (top diagrams in each diagram set). The amount of dust grains bigger than $3.8 \mu\text{m}$ is a factor of 50 lower than of grains with a diameter bigger than $1.0 \mu\text{m}$. This was observed during both flybys and indicates consistent measurements.

The results of the small $m2$ channel and the big $M1$ channel should show comparable results, since their mass threshold is identical ($\approx 1.8 \mu\text{m}$). However, the maximum rate of $M1$ was 100 s^{-1} and the rate of $m2$ was 150 s^{-1} . We have to correct for the sensitive area of the detectors in order to compare the dust fluxes. The thick foil has a sensitive area of 0.0050 m^2 and the thin foil detector has an area of only 0.0010 m^2 . This provides the fluxes of $F_{M1} = 20\,000 \text{ m}^{-2} \text{ s}^{-1}$ and for the small sensor we calculate $F_{m2} = 150\,000 \text{ m}^{-2} \text{ s}^{-1}$. The measured fluxes are therefore off by a factor of seven, but the overall rate profiles are similar.

The flux measured by the thin foil counting all particles bigger than $\approx 1 \mu\text{m}$ was about $R_{m1} \approx 300 \text{ s}^{-1}$ giving fluxes of $F_{m1} \approx 300\,000 \text{ m}^{-2} \text{ s}^{-1}$. This translates to maximum dust densities along the Cassini trajectory of $d_{>1\mu\text{m}} \approx 17 \text{ m}^{-3}$ – but most of the grains in the plume are smaller than $1 \mu\text{m}$ leading to orders of magnitude higher densities [Schmidt et al., 2007].

The values given refer to the maximum values up to about 20 seconds after the closest approach, where a very steep rise occurs and the rates reach values above $10\,000 \text{ s}^{-1}$ ($m1$ at 2008-224 and 2008-283, and $M1$ at 2008-283). Such high rates are unrealistic and are probably caused by the interaction of the thin foils and the quickly changing plume environment during the flyby. The rising gas and dust densities in the plume might lead to thermal gradients or acoustic noise which invalidates the data in the second half of the flybys. The high rates did also cause high dead time effects such that the $m2$ and $m3$ rates drop down with the onset of the very high $m1$ rates at 2008-224T21:06:33 and 2008-283T19:06:55. Even the more insensitive foil showed strong noise and decreasing $M2$ and $M3$ rates starting at 2008-283T19:07:00.

Such saturation and noise effects were not observed in previous PVDF space instruments and no experience exist in the operation of PVDF based detector in high gas or dust densities. Nevertheless, the sensitive reaction of such foils to small thermal gradients is known¹⁹ and gradients of 1° C within a few seconds are considered to provide unreliable counting results [James, 2009].

Dust densities in Saturn's E Ring

In section 4.4 CDA impact rates were discussed. The data presented have clearly shown a wide distribution of dust particles around Saturn. The first indication of high-altitude dust was measured in the year 2004 on DOY 302 (October 28) at elevations as high as $100\,000 \text{ km}$ above the ring plane at distances of $7 R_S$ from Saturn. The derived dust densities for particles bigger than $0.5 \mu\text{m}$ is rather high and reaches values as high as 0.001 m^{-3} . These results confirm the discovery of dust particles outside the ring plane measured by the plasma wave instrument onboard Voyager 20 years ago [Gurnett et al., 1983].

¹⁹Extensive tests with PVDF foils were performed in preparation and operation of the New Horizon Student Dust Counter (Univ. of Colorado, Boulder).

4 CDA Measurements and Selected Results

The dust number densities n_d can be derived from impacts rate n_r , the sensitive detector area A and the relative impact speed v_{imp} as defined by Eq. 4.6.

$$n_d = \frac{n_r}{A \cdot v_{imp}} \quad (4.6)$$

The number density and the sensitive area are time dependent and we get for the impact rate n_r

$$n_r = \frac{n(t)}{\Delta t} = n_d(t) \cdot v_{imp}(t) \cdot A(t) \quad (4.7)$$

where $n(t)$ describes the number of impacts in the time interval Δt . We have to integrate over the time t and we get Eq. 4.8 under the assumption that the number density n_d is constant in the time interval $t \dots t + \Delta t$. S is named the integrated sensitivity.

$$n(t, t + \Delta t) \approx n_d \cdot \int_t^{t+\Delta t} v_{imp}(t) \cdot A(t) = n_d \cdot S(t, t + \Delta t) \quad (4.8)$$

Although this seems to be trivial, neither of the parameters needed is known with accuracies better than 10%. The impact rate is derived from the counter values and some contribution of noise events cannot be excluded. Taking only the reliable counter classes (as done in this work), the real impact rates are higher and the result is a rather conservative (minimum) number density. Furthermore, the time interval Δt has to be small in order to avoid changes in the dust number density n_d . The minimum time interval considered in this work is 128 seconds and Cassini moves already between 500 and 2000 km in this time. There is no reason to assume, that the number density is constant in the inner E ring over such extended spatial regions. The situation gets worse in the outer ring system where we have to handle with a poor statistics and with just few number of impacts within time intervals of e.g. 10 minutes. Here, we have to integrate over longer time scales in order to derive a mean impact rate and mean density.

In principle, the detector area A is known very well, but its projection towards the dust RAM direction requires the knowledge about the dust trajectories. Eccentric, retrograde or even unbound stream particles have very different relative impact speeds v_{imp} leading to distinct projected sensitive areas A . For coarse density estimates, only prograde circular orbits were assumed for dust density calculations.

In order to even complicate the calculation, it has to be noted, that further uncertainties are introduced by the unknown mass distribution of E ring particles, which vary with distance and latitude. Further distances from Saturn shall contain smaller grain sizes than the inner region close to the ring plane. Furthermore, the relative impact speed of prograde circular grains decreases with increasing distances from Saturn. Both, the grain speeds and the spacecraft velocity are small in the outer region of Saturn. The low relative impact speeds produce only small impact charges and, depending on the grain mass distribution, not all impacts are counted and show up in the event rate (compare Eq. 4.5). In addition, the outer ring region shall contain smaller grain masses, which amplifies the underestimation of the dust density in Saturn's outer ring region. In order to correct for this effect, we need a correction factor, or better, exponent α , in Eq. 4.6 for the speed dependence leading to Eq. 4.9. The value of α

shall reflect the speed-dependent mass threshold, which is of the order of 3.5.

$$n_d = \frac{n_r}{A \cdot v_{imp}^\alpha} \cdot C(\vec{r}) \quad (4.9)$$

Here, the correction factor $C(\vec{r})$ was introduced, which depends on the location \vec{r} of Cassini in the ring and which takes the variable grain mass distribution into account. In this section, the influence of B will be neglected and is set to 1. Furthermore, the inclusion of dust stream particle impacts in the count rates would lead to overestimated grain densities, especially in the outer saturnian region; for this reason only higher counter classes were taken for dust density calculations.

As already mentioned, that dust impact speed determines the mass detection threshold defined in Eq. 4.5, smaller dust grains are detected at higher impact speeds. On the other hand, a steep grain mass distribution leads to the fact that the impact rate is dominated by the density of tiny particles which are smaller than e.g. 0.5 micron. Slight increases of the spacecraft speed (or more correctly the relative dust impact speed) will cause significant higher fluxes if the dust environment is dominated by tiny ($<0.5 \mu\text{m}$) grains (compare Eq. 4.5). One good example is the rate observed in orbit 10 between 2005-177T11:00 and 2005-177T16:00. Although the ring plane crossing was fully symmetric, the relative impact speeds changed from 8.6 km s^{-1} before the crossing to 6.5 km s^{-1} after the crossing. This changed the mass threshold of particles reliably detected from $9.4 \cdot 10^{-17} \text{ kg}$ to $2.7 \cdot 10^{-16} \text{ kg}$ (from $0.28 \mu\text{m}$ radius to $0.4 \mu\text{m}$ radius assuming water ice particles). If the dust population is dominated by grains below $0.4 \mu\text{m}$ in radius, the rate profile can vary over orders of magnitude although the dust density might be constant.

A dust density profile along Cassini's trajectory was derived for the ring plane crossing on day 2005-122 in orbit 7 and is shown in Fig. 4.24. The dust number density n [m^{-3}] is shown in dependence of radial distance from Saturn (x-axis, [R_S]) and height above the ring plane (y-axis, [10^3 km]). The maximum density observed during this periapse was in the order of 0.5 m^{-3} . For example a rate of 1 s^{-1} , a sensitive area of 0.05 m^2 and a common relative dust impact speed of 7 km s^{-1} refers to a dust density of 0.0028 m^{-3} . A maximum dust density of approximately 1 m^{-3} in the vicinity of Enceladus is therefore compatible with the rate measurements by DA. A clear decrease of the dust density to further distances can be observed and density values below 0.0001 m^{-3} were observed at regions beyond $15 R_S$ from Saturn. The curve in Fig. 4.24 takes into account Cassini's speed and the sensitive area of DA, but does not consider variations of the DA measurement thresholds caused by changes of relative dust impact speeds. This is a rather conservative estimation and the real dust density might be much higher due to the limited impact rate measurement capabilities of the Dust Analyser (dead time, mass threshold).

Fig. 4.25 shows the dust densities, derived from the impact rates, measured along Cassini's trajectory from 2004 until 2008. The data processing took into account the CDA checkout times, the Cassini velocity, the sensitive target area towards circular prograde particles and the

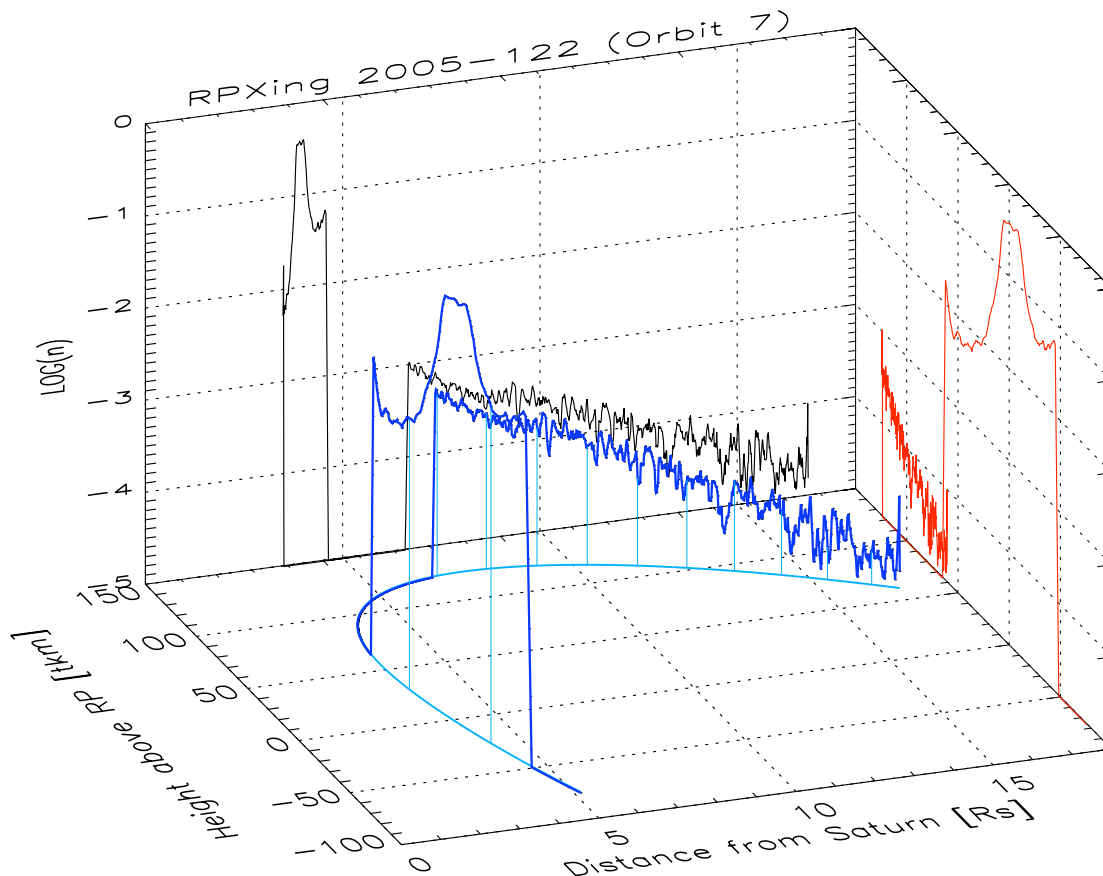


Figure 4.24: Three-dimensional dust density profile (blue) along Cassini's trajectory of the ring plane crossing and periapses of orbit 7 in 2005. Two projections of the density profile are shown on the side panels (black and red curve). The vertical axis gives the dust density n in units of $\log(m^{-3})$. The maximum dust density measured at this periapses was $\approx 0.5 m^{-3}$.

dead time correction. The highest dust densities in the inner saturnian region (along Enceladus orbit at $4 R_S$) are a few particles per cubic metre and they are consistent with former modelling work. Surprising is certainly the high dust density inside Titan's orbit at $20 R_S$ with altitudes up to $4 R_S$ ($250\,000$ km) from the ring plane. In the outer region, fluxes below $1 \cdot 10^{-6} m^{-3}$ are measured, interrupted by segments of higher densities of up to $1 \cdot 10^{-6} m^{-3}$ (green trajectory segments at distances beyond $30 R_S$). However, it was shown by the occurrence of mass spectra in the raw signals of noise data, that such impacts were caused by much faster grains of saturnian stream particles with speeds above $100 km s^{-1}$. By using the much lower relative impact speeds of a few $km s^{-1}$ of bound prograde particles, these dust densities are overestimated by at least a factor of 20.

Eliminating the saturnian dust stream particles from the data set (neglecting impacts with small impact charges) lead to another picture of the dust density around Saturn, which is

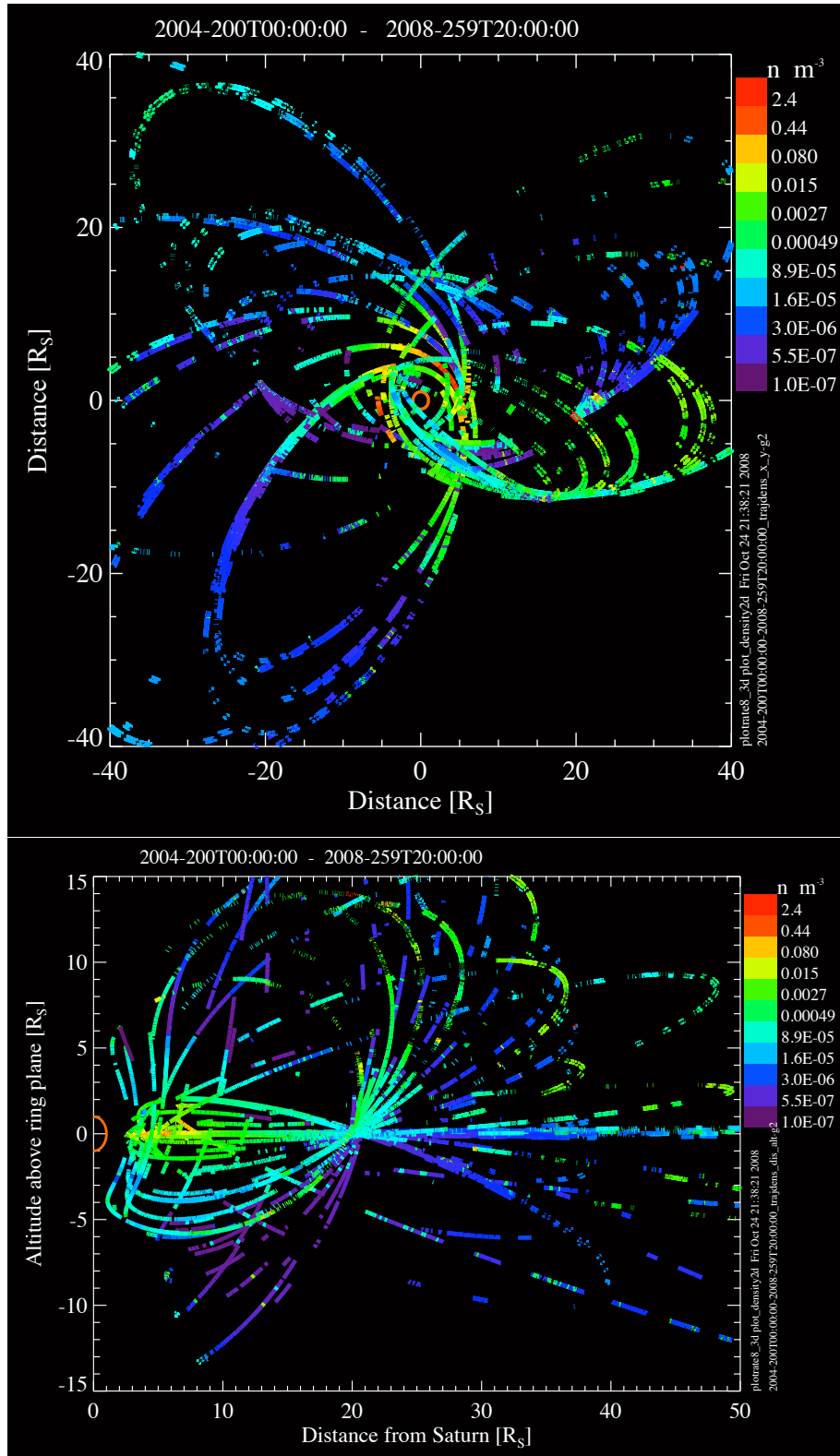


Figure 4.25: Global dust density measured by CDA in the saturnian system. The densities are color coded along the Cassini trajectory in the time range of 2004-200 to 2008-259. High impact rates and densities are observed outside the known E ring ranging from 3 to 9 R_S . The plots use a J2000, Saturn centered coordinate system, with the x- and y-axis in Saturn's ring plane and the positive x direction pointing towards the vernal equinox. Details are readable in the electronic version of this document.

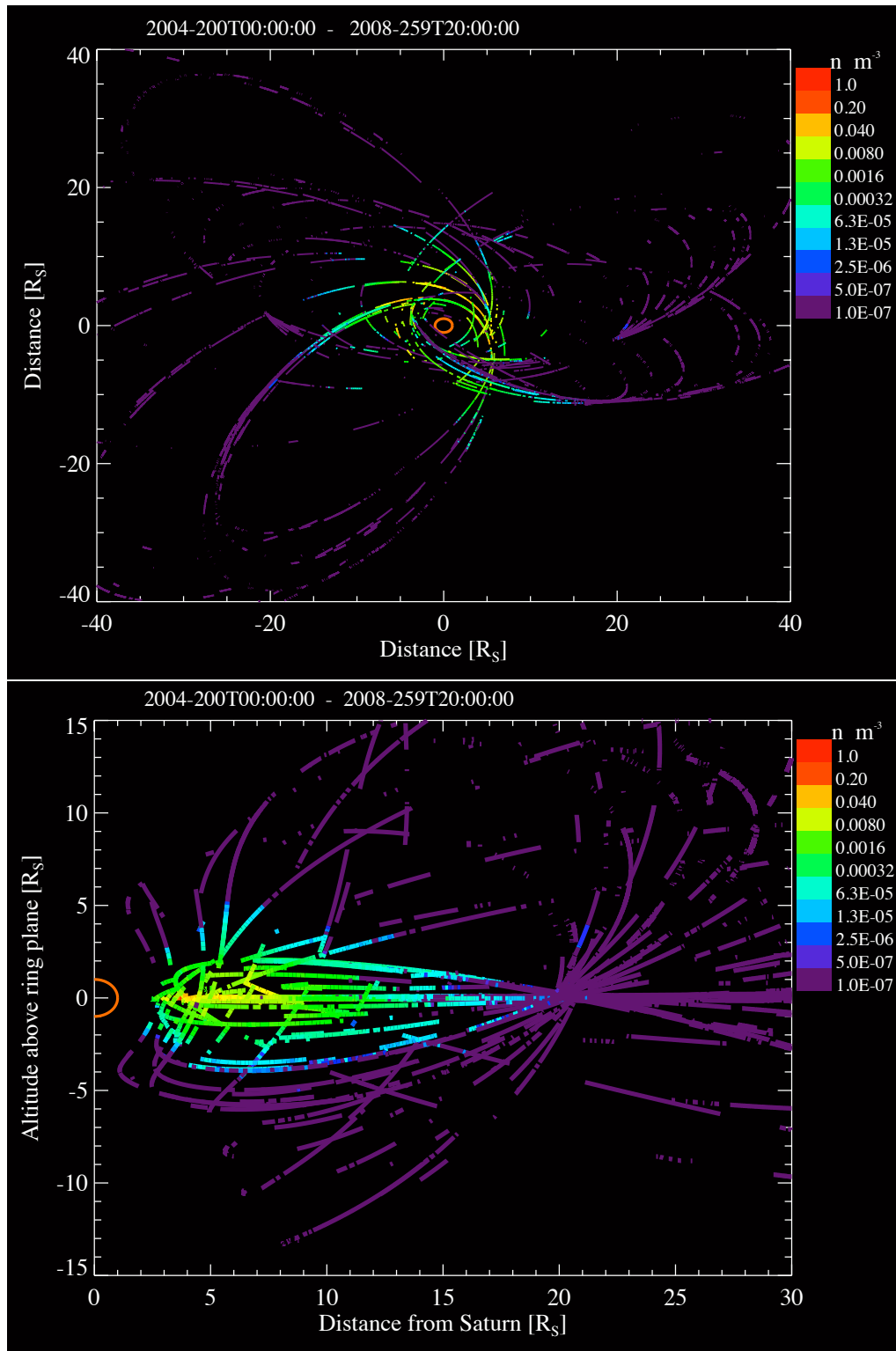


Figure 4.26: Dust density distribution around Saturn after the removal of dust stream particles and retrograde particles. The coordinate system used is a Saturn centered J2000 system with the x- and y-axis in the ring plane. Top: Top view; Bottom: Side view.

4.4 Rate and Density Measurements in Saturn's E Ring

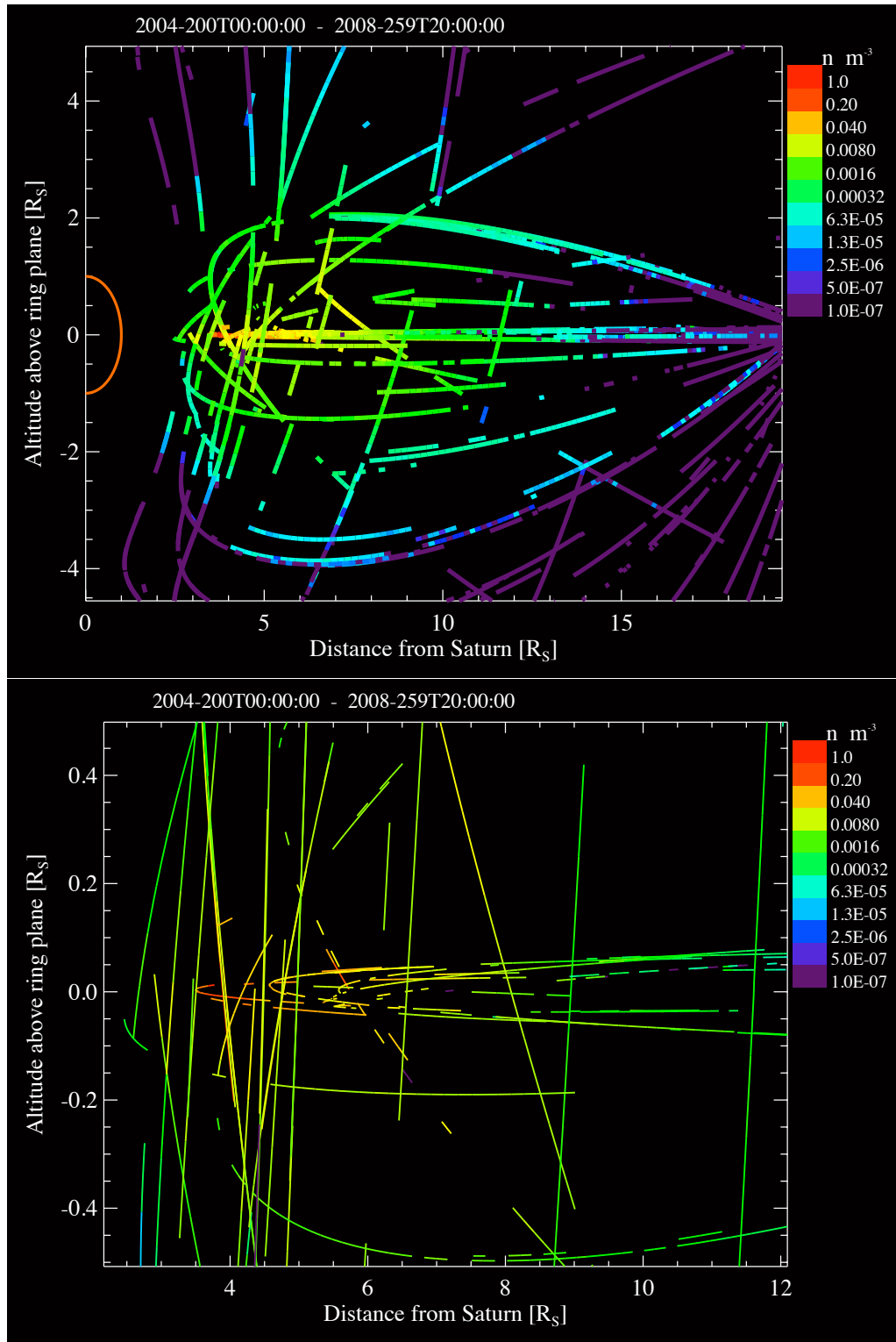


Figure 4.27: Edge-on view of the dust density within the extended E ring (inside 20 R_S).

4 CDA Measurements and Selected Results

much more consistent and shown in Fig. 4.26 and 4.27. The high densities outside Titan's orbit vanished and the density profile is smooth and gradually decreasing with Saturn's radial distance. Fig. 4.26 shows two overview plots from top and from the side. Enhanced data processing and filtering (removal of dust stream particles and low impact charges) lead to dust densities more concentrated in the inner saturnian system, inside Titan's orbit and within $4 R_S$ of the ring plane. The color coded densities vary between $1 \cdot 10^{-6} \text{m}^{-3}$ and 1m^{-3} . Two zoomed edge-on views are shown in Fig. 4.27 in the range $[x,y]=[0:20,-5:+5]R_S$ (left) and $[x,y]=[0:12,-0.5:0.5]R_S$ (right).

Cassini's dust detector performed in-situ measurements of dust fluxes along its trajectory covering only a minor fraction of the overall 3D-space. Therefore Fig. 4.26 still does not provide a general view of the dust distribution. How do we achieve a more global view? Based on the analysis by Showalter et al. [1991] of optical measurements, a model was defined which describes the vertical ring profile by a Gaussian whose width σ linearly depends on the radial distance to Saturn r as

$$\sigma(r) = \sigma(3R_S) \left(\frac{\sigma(8R_S)}{\sigma(3R_S)} \right)^{(r-3R_S)/5R_S} \quad (4.10)$$

using $\sigma(3R_S) \sim 2500 \text{ km}$ and $\sigma(8R_S) \sim 15\,900 \text{ km}$. Kempf et al. [2008] investigated HRD rate measurements of grains with diameters $>3.5 \mu\text{m}$ in order to derive parameters for the vertical and radial profile. Power laws on the basis of the HRD data were found, but no big grains outside $7 R_S$ were detected such that the results are not applicable to the extended E ring in global.

What do we get, if no assumptions are made with respect to the density gradients and if we ignore a ring structure defined by Eq. 4.10? In order to get a global impression of the CDA dust density data, a contour plot using the Interactive Data Language was performed, and the result is shown in Fig. 4.28 for two different scales. The left plot shows the region up to $16 R_S$ and the right plot gives more details in the range up to $10 R_S$ and with a vertical scale up to $0.8 R_S$. In contrast to optical measurements where brightnesses are determined for an entire region, we only have a few tracks of density measurements mapped to the r-z space (compare Fig. 4.27). Therefore the rate and density data of CDA were treated in a special way. For this contour fit the dust density data points (n) below the ring plane were turned to positive values in order to achieve more measurement points ($n_z = \text{ABS}(n_z)$). The contoured dust densities are colour coded using a rainbow-like colour table.

It is obvious that this distribution is very different from a profile defined by Eq. 4.10. The vertical extension is much broader and high densities are widely seen even at altitudes of $1.5 R_S$ and $r = 10 R_S$. As a reminder, one Saturn radius is more than $60\,000 \text{ km}$. Stripes of higher densities rise from the ring plane to higher latitudes shown as red bands. The contours provide the impression that the orbits of Enceladus, Tethys and Dione have some local influence on the vertical density profile.

Now we have to rise the inconvenient question, whether these features are real. Do we have enough data points and enough tracks which allow for gapless contour fit results? We do have

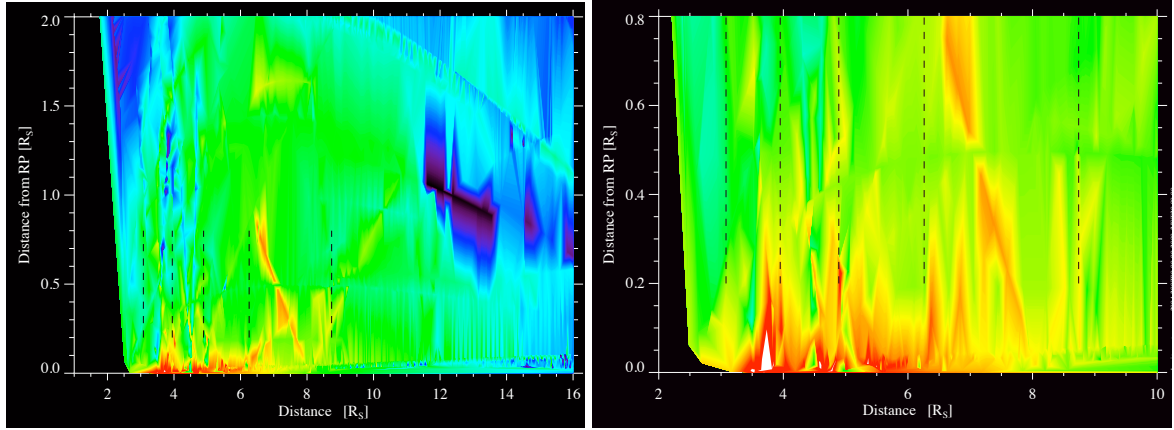


Figure 4.28: Contour plot of the dust densities of Fig. 4.27 using a rainbow-like colour table. Red regions mark higher dust densities. The data basis are dust impacts in the time frame 2004-200 to 2008-060 (left) and 2004-200 to 2008-259 (right). Cold colours are both, missing data or low dust densities, respectively. The orbital distances of the moons Mimas, Enceladus, Tethys, Dione and Rhea are marked by vertical dashed lines.

data points at inclined crossings for the following 15 ring plane crossings:

RPX UTC	Distance	Altitude range
2007-337T06:47	2.66 R_S	0.5 ... -0.1 R_S
2005-248T10:37	2.937 R_S	0.05 ... -0.5 R_S
2006-252T19:07	3.16 R_S	0.5 ... -0.5 R_S
2008-051T17:54	3.45 R_S	0.02 ... -0.4 R_S
2007-146T22:44	3.496 R_S	0.4 .. -0.4 R_S
2005-122T23:41	3.88 R_S	0.4 ... -0.2 R_S
2005-141T03:59	3.89 R_S	0.4 ... -0.2 R_S
2005-177T13:32	3.92 R_S	0.4 ... -0.4 R_S
2008-003T22:08	4.35 R_S	0.01 ... -0.3 R_S
2008-131T00:06	4.48 R_S	0.3 .. -0.3 R_S
2008-092T18:10	4.49 R_S	0.4 .. -0.4 R_S
2007-130T19:39	4.73 R_S	0.1 ... -0.4 R_S
2006-337T00:36	4.96 R_S	0.3 ... -0.4 R_S
2006-301T03:04	4.96 R_S	0.4 ... -0.3 R_S
2007-114T14:04	6.53 R_S	0.4 ... -0.22 R_S

By applying n_z as $ABS(n_z)$ to the z-component of the dust densities n , the contour data are based on 30 individual vertical or inclined tracks with only a few horizontal scans (Fig. 4.27). This figure does therefore provide a first global perspective onto the dust density distribution. The variable fine structure makes clear, that no global function is suited to describe the vertical ring profile over larger scales. In the future, this figure has to be updated with data of the Cassini extended mission. Unfortunately, the instrument sensitivity changed twice in 2008 (compare chapter 3.2).

We have enough data points close to the ring plane in order to derive a function for the radial profile. Plotting the data within the ring plane we achieve Fig. 4.29. When we do that, we have to be careful in two spatial regions for two different reasons. The inner distance boundary is given by the dead time of DA by one second; the data inside Dione's orbit were not considered due to saturation effects. Second, the number of impacts per time or radial interval in the outer E ring becomes too low for a meaningful interpretation. Therefore the fit of the decline of the radial dust density was based on the measured dust densities between 6 and 15 R_S . The bottom plot in Fig. 4.29 shows a comparison with modelled data by Horányi et al. [2008]. The Cassini data show a radial density $n(r)$ which can be described by Eq. 4.11.

$$n(r) = \frac{20}{(r - 2.8)^{4.6}} \quad (4.11)$$

Starting at a distance $r = 6R_S$ with a density of 0.095 m^{-3} the density falls down to $2.0 \cdot 10^{-4} \text{ m}^{-3}$ at $15 R_S$. This is a bit less than the decrease found by modelling work.

The overall amount of dust within Titan's orbit was very surprising. The questions that are immediately raised are: Do these particles belong to one big, faint and extended E ring, which was defined between 3 and 9 R_S earlier in the literature? Are there gaps or short scale density gradients in the extended dust environment? Are there dust density enhancements or different dust mass distributions along satellite orbits? The most likely answer is yes, there is one big E ring showing a very complex fine structure which is not explained until today.

The strong variations of the DA impact rate with the boresight angle towards the dust RAM direction show that the impact rates are dominated by prograde keplerian particles. A separate retrograde dust population has not been identified in the data set so far. The predicted dust densities of retrograde particles is very low (10^{-9} m^{-3}) and its detection in the inner saturnian system would still be difficult due to the high noise and particle background. Three-dimensional simulations predict a tenuous ring of captured interplanetary particles into retrograde orbits [Mitchell et al., 2005]. This dust, which has a typical size of $0.1 \mu\text{m}$, forms a thick ring around the planet between the main rings and 9 planetary radii with a thickness of approximately 3 planetary radii. However, due to the very low density, only 20 retrograde grains would be detected by DA during the first four years of the Cassini mission. Dust produced by the outer moon Phoebe might contribute significantly to a retrograde dust population [Verbiscer et al., 2009].

What are the particles at high latitudes made of? Are there compositional variations of particles within the E ring and the extended dust environment? This question was not addressed in this work, but CDA was able to record and deliver the data necessary to answer this question to the ground. An analysis of this topic has started and is ongoing [Hillier et al., 2007b, Postberg et al., 2008, Postberg et al., 2009b]. However, it can be stated that water ice particles were found in the entire dust environment, at high and low latitudes and at all distances from Saturn within $17 R_S$. The mass spectra of water ice particles with impact speeds of approximately 10 km s^{-1} are very characteristic with their repetitive mass lines of water molecule

4.4 Rate and Density Measurements in Saturn's E Ring

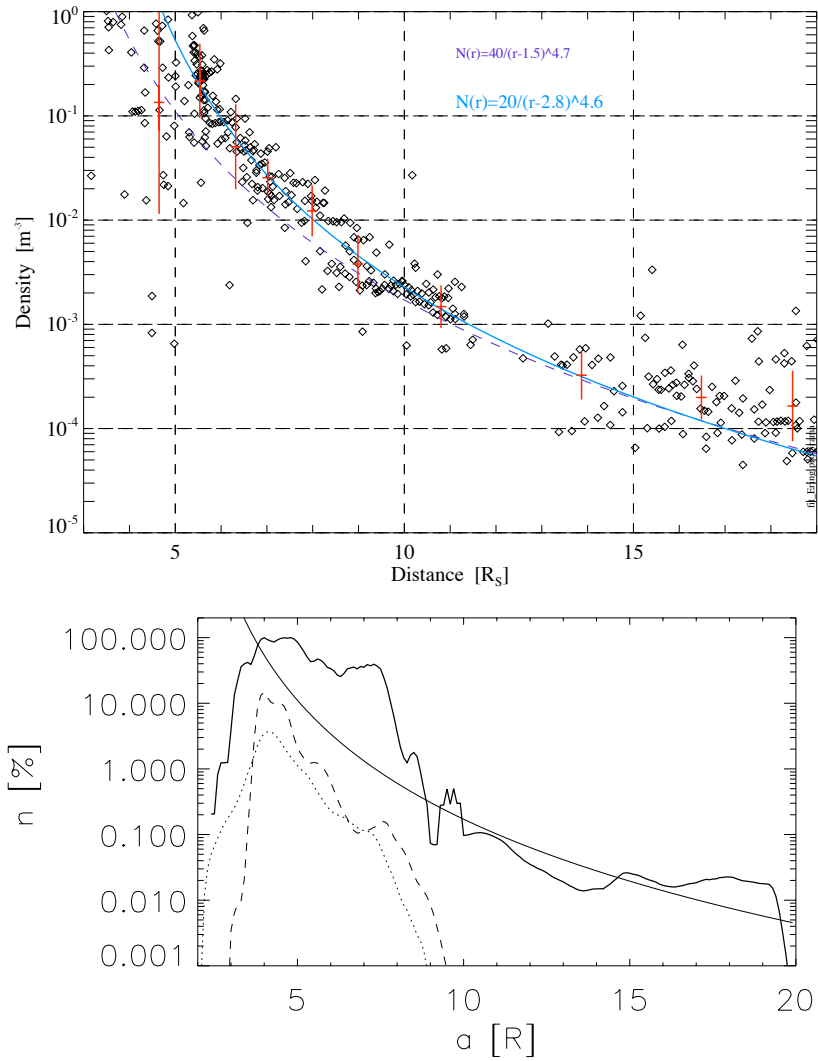


Figure 4.29: Top: CDA measured dust density in the ring plane with a power law fit (blue line). Bottom: Column densities as function of distance a from Saturn for three groups of particle sizes: $0.1 < r_g < 0.5 \mu\text{m}$ (continuous line), $0.5 < r_g < 0.1 \mu\text{m}$ (dashed line), and $1 < r_g < 3 \mu\text{m}$ (dotted line). These curves are normalised by setting the maximum density of the smallest grains to 100, corresponding to a real column density of 0.3 m^{-2} . For comparison the power law fit from the upper plot is shown. The bottom plot is taken from Horányi et al. [2008].

clusters (Fig. 4.10). Such features were recognised in the mass spectra of the majority of the micron sized grains. Furthermore, silicate features were identified in some spectra [Hillier et al., 2007b, Postberg et al., 2008].

4.5 Dust Measurements in the Equinox Mission

What are the next steps and possible discoveries of CDA? NASA has already developed plans to extend the Cassini mission until summer 2017. The shallow solar angle towards Saturn's ring plane gives the extended Cassini mission its name in the years between 2010 and 2017. The tour is already designed and allows for a couple of exciting new measurements. First, Cassini will cross the ring plane in Saturn's shadow and this allows for dust grain charge studies under solar UV and non-UV conditions. The grain potential should change in the shadow region and grains bigger than $3 \mu\text{m}$ carry enough charges to provide primary QP signals which can be analysed.

Second, further vertical ring plane crossings at different azimuth angles (angle towards the solar direction in the ring plane) might show vertical asymmetries of the E ring.

The overall data set has to be unpeeled in order to separate bound E ring grains, Saturn stream particles, bound retrograde particles, interplanetary and interstellar dust. In order to do this, the identification of interstellar grains at great distances from Saturn will be done first. The overall geometry is convenient for this kind of study (compare Sec. A.9 and Fig. A.10). The outer saturnian region is well suited for the discovery and characterisation of interstellar grains, since their relative impact velocities are much higher ($>30 \text{ km s}^{-1}$) than from bound prograde or retrograde dust particles ($<10 \text{ km s}^{-1}$). However, the fast interstellar grains have still to be separated from the abundant, but tiny Saturn stream particles. The identification and compositional analysis of interstellar grains would be of major importance for the astronomy community.

The characterisation of retrograde dust would shed light on their origin and the properties of their parent bodies. Retrograde dust are either caught by Saturn, or they originate from retrograde moons like Phoebe. An inclined Phoebe dust ring with densities of $\approx 20 \text{ km}^{-3}$ was recently proposed between 130 and 210 R_S [Verbiscer et al., 2009]. These particles spiral inwards entering the E ring or striking the moons.

Another puzzle is still the predicted Halo dust population, dust grains on bound orbits, but never crossing the ring plane [Howard et al., 2000]. However, the modelled dust particles at rather short distances and high latitudes are supposed to be below the detection threshold of CDA at the expected relative impact speeds (assuming grain sizes $<100 \text{ nm}$).

4.6 Outreach

The best scientific or technological results are useless if nobody knows about them. For this reason, scientific publications in refereed journals are one of the main tasks in scientific research. But this does not necessarily mean, that the results distribute widely in the community. The access to journals is restricted and constrained by the limited budgets of universities, companies and institutes, and only a limited number of people become aware of the latest developments. This accounts for an unused potential for the development of our society. If only 10% of the gained knowledge of humankind would be accessible worldwide, our technology, scientific research and our society in global would change much faster, and, hopefully, much

smarter.



Figure 4.30: Start screen of the of the movie produced for the Open Day presenting Cassini mission and Dust Analyser results (background image: NASA/JPL).

The public and scientific colleagues have to be engaged in the progress of running projects. One attempt in order to achieve this was the production of a movie called *Saturns Ringe, Monde und Eisvulkane – Ergebnisse der Weltraummission Cassini* (Fig. 4.30), which got a lot of attention during the Open Day of the Max Planck Institute for Nuclear Physics in 2008. The movie²⁰ summarises some main results of the Cassini mission and presents the most exciting finding, namely the ice volcanoes on the surface of Enceladus. The Dust Analyser measured the composition, size distribution and density of ice particles in Saturn’s E ring, which originates from the plumes of the ice geysers at the south pole of Enceladus. The ice grains contain high amounts of salts, implying the existence of liquid water in contact with the rocky core of the moon. Today, astrobiologists state, that the oceans below the surface of Enceladus are the most habitable worlds in space. Did you know that?

Movies are the most attractive medium today. The second attractive medium is sound or music. How can we use that? Unfortunately, the Dust Analyser does not *sound* during an impact of a micron sized dust particle. The grains would have to be much bigger before natural sound could be recorded by a microphone in the frequency range of the human ear (20 Hz to 15 kHz). However, the Stardust team was able to translate the results of their acoustic sensors during the flyby with a speed of 6 km s^{-1} at the comet Wild 2. But comets have many bigger grains, with sizes up to $100 \mu\text{m}$ or even larger.

Which possibilities has CDA in order to make their impacts sound? A method was found such that one can hear the dust impacts onto the various parts of the instrument. Four different event classes like IIT impacts, CAT impacts, Wall impacts and Noise were defined, and individual sounds to each class were assigned. Sounds, which can be correlated with a hit

²⁰<http://www.mpi-hd.mpg.de/dustgroup/news/TdoT.html>

4 CDA Measurements and Selected Results

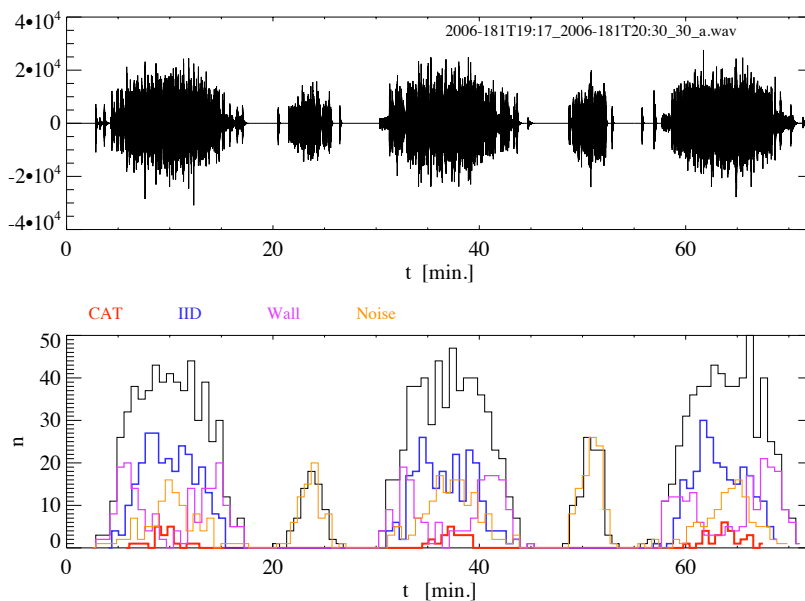


Figure 4.31: Example for a translations of impact rates per minute from the year 2006 (bottom) into a sound file (top). The total impact events (black) were classified in CAT impacts (red), IIT impacts (blue), Wall impacts (pink) and noise/small events (yellow). The data were recorded on day 2006-181 between 19:17 and 20:30 during a spacecraft downlink roll at a distance of $6.7 R_S$ in the ring plane.

onto a surface, were taken and four different drum sounds were selected and recorded in a wave-data format. Software was written which translates the rhythm of the dust impacts into an interfering sound composition²¹. For each event, the corresponding sound-file was added to the overall composition and a wave-file was written using binary data output procedures. The result was a 16 bit resolved, 44.1 kHz stereo composition, which is well known as the Compact Disc format. Furthermore, the timeline was compressed by a factor of 16 such that a spacecraft roll of 26 minutes is expressed by a sound file of 97 seconds length.

Mission phases of fast changing pointing orientations with oscillating impact rates are most interesting for rate-to-sound translations (Fig. 4.31). Such observations are for example downlink rolls or spacecraft rocking modes²². By playing the sound file, one can clearly hear first the impacts on the instrument walls, followed by rising hits onto the big IIT, and followed by some impacts onto the CAT during a downlink roll. The sound files were made available as 128 kbps coded MPEG3 version for a fast distribution over the internet²³.

Here, just two examples of today's outreach activities are given, in addition to public talks, public flyers, Open Days, wikipedia entries or group web pages. It is no question, that new media will raise the visibility in both communities, the scientific and the public community.

²¹The software package counter2sound.pro translates CDA counter data into a binary RIFF-wave file, it is written in the Interactive Data Language. Wave files use the standard RIFF structure which groups the file contents (sample format, digital audio samples, etc.) into separate chunks

²²Downlink roll: continuous turn about the spacecraft z axis; rocking mode: windshield wiper turns of $\pm 60^\circ$ about the spacecraft z-axis during which the CDA boresight scans through the dust RAM direction.

²³http://www.mpi-hd.mpg.de/dustgroup/CDA_outreach/CDAImpactSounds.html

5 New Dust Instrumentation

5.1 Introduction

The analysis of micron sized particles in the vicinity of the Earth provides knowledge about the relative fluxes of interplanetary dust, interstellar dust and space debris. Many particles entering our solar system encounter the Earth and they are heated up in the upper atmosphere without reaching the surface. Dust samples on Earth are limited and those reaching the surface are processed and chemically altered in the Earth's atmosphere. The only way to perform unbiased measurements and to separate natural meteoroids from space debris, are in-situ measurements in the Earth environment. For this purpose, it is required to determine the grain trajectory and elemental composition quite accurately.

The overall problem of the sensitive detection of space debris and micro meteoroids is the low flux which requires a large sensitive area. On the other hand the accurate in-situ determination of particle properties like speed, trajectory and composition is difficult with a big instrument. High-resolution dust mass analysers that provide elemental composition of dust particles have been flown on missions to the comet Halley [Kissel, 1986] and are currently flying on the Stardust mission [Kissel et al., 2003] (Tab. 5.1). The instruments employed a time-of-flight mass spectrometer in order to obtain the elemental composition of the impact plasma generated upon an impact of cometary dust particles. A mass resolution of $\frac{m}{\Delta m} > 100$ was achieved by the means of a reflectron that provided energy focusing of the ion beam. Because of the very high dust fluxes expected near the comet, only a very small sensitive area of 5 cm² was necessary in order to obtain thousand, high resolution dust mass spectra.

Table 5.1: Mass resolution of impact ionization time-of-flight spectrometers.

Mission	Area(cm ²)	$\frac{m}{\Delta m}$	Type
Helios	120	5-20	1m linear drift tube
Cassini	100	20-50	0.2 m linear drift tube
Giotto, VeGa	5	100	1 m reflectron
Stardust	90	100	1 m reflectron
LAMA	1000	>120	1 m reflectron

The Stardust spacecraft carrying the Cometary and Interstellar Dust Analyzer instrument (CIDA) flew by comet Wild 2 in 2004. CIDA, too, is an impact mass analyser employing a reflectron stage in order to provide high resolution ($\frac{m}{\Delta m} > 100$) mass spectra. The sensitive area of this instrument is 90 cm² and an analysis of a few tens of cometary grains was achieved [Kissel et al., 2004].

A medium resolution impact mass spectrometer ($\frac{m}{\Delta m} = 20 - 50$) of 100 cm^2 sensitive area is part of the Cassini CDA instrument [Srama et al., 2004a]. On its way to Saturn it has measured several impact spectra of interplanetary or interstellar dust particles and in the vicinity of Saturn several hundred spectra of Saturn stream particles [Kempf et al., 2005b].

What will be the future of dust detection technology? Are there new concepts for dust impact detection? The Cosmic Dust Analyser onboard Cassini is based upon induced charge detection and impact ionisation – is this still state of the art? The answer is yes. The basic principle of both, induced charge detection and impact ionisation count to the most sensitive and reliable methods, but both methods can be improved.

Cassini CDA demonstrated successfully the measurement of dust grain charges in space [Kempf et al., 2004], which was the basis for the development of the *Trajectory Sensor* (see section 5.2.1). The other method, impact ionisation, can only marginally be improved by alterations of the target surface and material. But very promising is the method of TOF mass spectrometry of impact generated plasmas. Here, the integrated Chemical Analyser of CDA provided thousands of TOF mass spectra of interplanetary dust grains, jovian and saturnian nanometre-sized grains and of saturnian E ring particles. This measurement principle is very reliable and sensitive [Postberg, 2007], opening its application range to particles over a wide velocity range ($1 \dots > 100 \text{ km s}^{-1}$). Therefore this concept was investigated further and a large area mass analyser was designed and tested (section 5.2.2). The following chapter therefore concentrates on these two development activities.

This does not mean, that there are more activities in dust sensor technology development. Recent activities focus on the flux measurement of nanometre sized grains using foil coated MCPs. The BepiColombo mission will carry a japanese dust detector based on piezo materials currently in the development phase [Nogami et al., 2009]. It is also known, that dust impacts generate short light flashes which can easily be detected by avalanche detectors or photomultipliers. The problem here is, that in space there are many light sources which act as a noise source. But even the PVDF based foil detectors are investigated for future missions, their simplicity and low costs are still attractive for selected applications. Dust detection technology has still a high potential for future improvements caused by the progress in electronics and material technology.

5.2 Dust Telescope Technology

A *Dust Telescope* is a combination of a *Trajectory Sensor* and an analyser for the elemental composition of micrometeoroids or space debris. It was introduced by Grün et al. [2000] and Srama et al. [2004b] and its development and test is described in Srama et al. [2005b] and Srama et al. [2005a]. Dust particle trajectories are determined in the *Trajectory Sensor* by the measurement of the electric signals that are induced when a charged grain passes through a position sensitive electrode system. The position sensitive system consists of four planes of wires where each wire is connected to a separate charge sensitive amplifier. This system allows the accurate determination of the particle velocity vector. The elemental composition of particles is analysed by a time-of-flight system for the ions which are generated upon the

particle impact. The large area of this mass analyser is 0.1 m^2 and has a mass resolution >100 for all possible impact locations.

5.2.1 The Trajectory Sensor

The trajectory sensor determines in-situ the speed, mass, primary charge and trajectory of micrometeoroids and its underlying concept was first described by Auer [1975]. The measurement is based on charge induction of the particle primary charge onto individual metal wires. Each wire is connected to a separate charge sensitive amplifier (CSA) of high sensitivity. Particles in interplanetary space carry normally a positive potential of approx. 5 Volts due to the dominating photo electron current. Particles with a radius of $r = 1 \text{ }\mu\text{m}$ carry already a charge of $Q = 4\pi\epsilon_0 r\Phi = 5.6 \cdot 10^{-16} \text{ C}$, where ϵ_0 is the permittivity ($8.85 \cdot 10^{-12} \frac{\text{C}}{\text{Vm}}$) and Φ is the surface potential in Volts. This charge corresponds to 3500 electrons and can easily be measured with advanced techniques. Here, an ASIC (Application Specific Integrated Circuit) based on $0.18 \text{ }\mu\text{m}$ CMOS technology was developed by A. Srowig which shows a noise of only 90 electrons in a bandwidth range between 10 kHz and 10 MHz [Srowig, 2005]. The noise of a CSA is depending on the detector capacitance. Therefore, the capacitance of the wires with respect to signal ground (detector frame) has to be as low as possible. It is $\approx 5 \text{ pF}$ for a thin wire with a length of 300 mm. A charged particle flying through a set of wires generates an induced charge on the most adjacent wires. The wire geometry determines how much charge is measured at the individual channels. Here, only 30% of the primary charge might be detected at one channel for the instrument shown in Fig. 5.1.

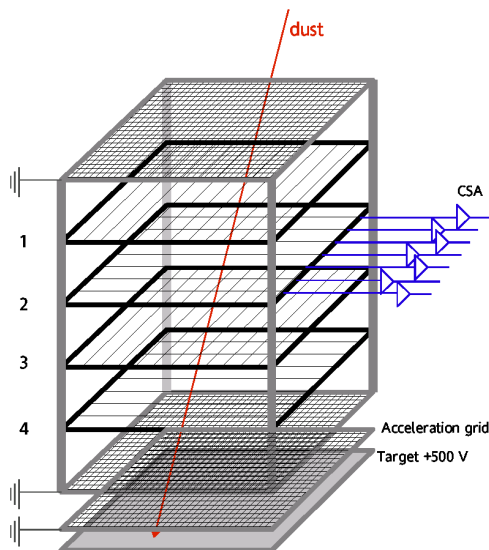


Figure 5.1: Schematics of the *Trajectory Sensor*. Four planes with perpendicular wires allow the reconstruction of the particle trajectory. The distance between the wires and the planes are 20 mm and 40 mm, respectively. The connection of CSAs to individual wires is shown only for one plane. An impact detector at the bottom will trigger the signal recording.

For the trajectory information it is necessary to locate the particle at two positions in the instrument volume. Each position sensor consists of two perpendicular planes separated by 40 mm from each other. Each plane is formed by a quadratic frame holding 16 parallel wires.

An electronics board is located inside the metal frame and carries the 16 front-end (FE) amplifiers (ASICs) connected to the individual wires. The FE-ASIC also includes a logarithmic amplifier to allow for a measurement range between 10^{-17} and 10^{-13} C and an undisturbed signal transfer to the transient recorder (TR) (Fig. 5.2).

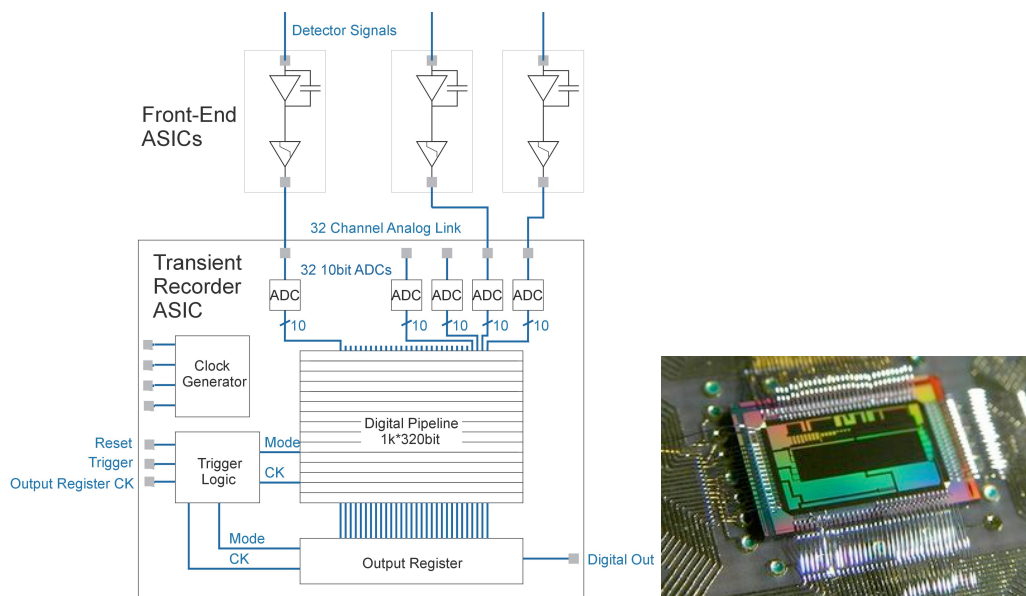


Figure 5.2: Left: Electronics concept of the FE-ASIC and the TR-ASIC after Srowig [2005]. The transient recorder converts and stores up to 32 signals with a buffer depth of 1024 samples. Right: The DUNE-1.1 TR-ASIC developed by the ASIC Laboratory Heidelberg in cooperation with the MPI-K, Heidelberg.

The CSA of the ASIC consists of a folded cascade with a capacitive feedback of 270 fF. The net signal is a bipolar current and the net charge after the measurement is zero. A feedback resistor minimizes the influence on the signal and keeps the signal noise very low. For this reason, the feedback resistor can be chosen rather high such it cannot affect the signal shape and signal noise. On the other hand, the ambient plasma might lead to significant baseline shifts. This problem is addressed by the possibility to decrease the CSA feedback resistor for some time leading to a suppression of DC signals. The FE (CSA and logarithmic amplifier) has a conversion gain of 404 mV/fC and shows a noise of approx. 90 electrons. The logarithmic amplifier behind the CSA is implemented as a series of two differential amplifiers with on-chip biasing. A feedback circuit controls the operating point and stabilises the baseline. The 10 bit ADC is based on successive approximation, consumes only 3 mW and runs with up to 25 MHz (Fig. 5.2). Therefore the power consumption of the total recording system (FE and TR) is dominated by the CSA of approx. 50 mW per channel.

The ASICs have been manufactured and integrated at the laboratory model of the *Trajectory Sensor* (Fig. 5.3) and the recorded signals are shown in the right plot. The tests confirmed the simulated low-noise behaviour of the electronics.

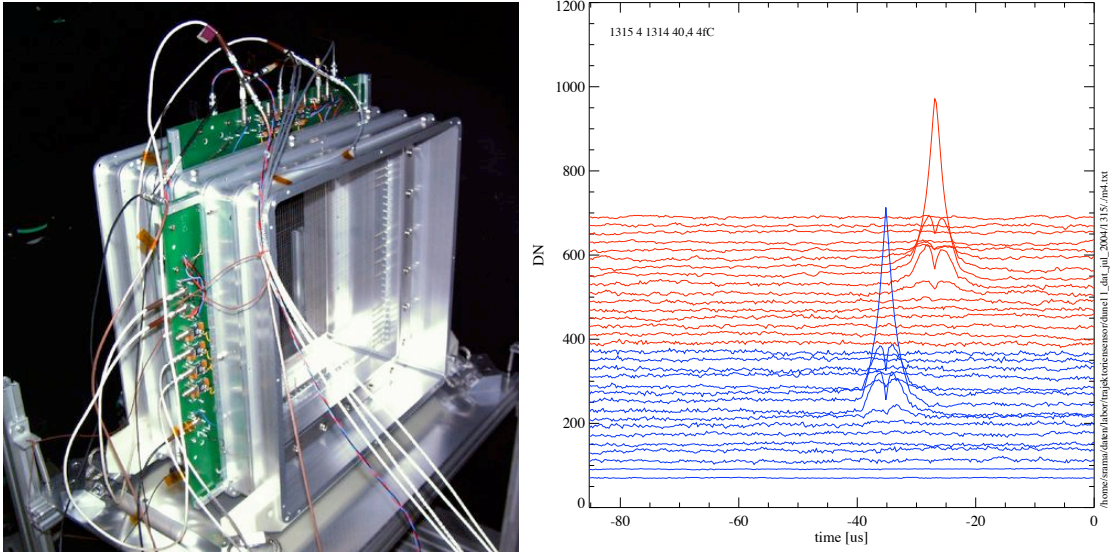


Figure 5.3: Left: Laboratory model of the *Trajectory Sensor* during tests at the Heidelberg dust accelerator facility. The wires of this laboratory model have a length of 300 mm leading to a cross section of the frame of 360x360 mm. The height of the *Trajectory Sensor* is 240 mm. Right: Signals of a particle passing the wire planes of the *Trajectory Sensor*. The particle speed and charge was 5 km/s and 4 fC, respectively.

A particle with a radius of 1 micron and a surface potential of 1 Volt carries a charge of 700 electrons. Assuming an induction efficiency on the wires of 50% , a signal of 350 electrons is expected. The amplifier noise of 100 electrons gives a SNR ratio of 3.5 which is sufficient under normal conditions. However, the grain surface potential is low under the low energy plasma conditions in the Low Earth Orbit (-0.5 V) leading to a higher mass threshold of approximately 10^{-10} g. The high energy plasma conditions in the Geostationary Orbit lead to surface potentials between -30 and +3 V. The measurement threshold of those particles is expected to be as low as 10^{-15} g (50 nm). In contrast, in interplanetary space the photo emission dominates the grain charging process leading to surface potentials of $\Phi \approx +5$ V. Here, a 0.1 micron particle carries 350 electrons. Tab. 5.2 gives the mass threshold m for particles with a surface charge Q of 1000 electrons by the application of Eq. 5.1.

$$m = \frac{4\pi\rho}{3} \left(\frac{Q}{4\pi\epsilon_0\Phi} \right)^3 \quad (5.1)$$

The error factor of the grain mass calculation is dominated by the uncertainty of the grain surface potential and the particle density ρ . Due to the logarithmic compression of the analog signal between the CSA and the ADC, the quantization noise has no significant influence on the grain mass determination. However, the sensitive charge measurements might be affected by the ambient plasma (spacecraft environment, solar wind). This requires operating tests of

Table 5.2: Mass threshold for the detection of grains with a charge of 1000 electrons.

Φ [V]	Size r [μm]	mass [g]
0.5	3	$2.3 \cdot 10^{-10}$
1	1.5	$2.8 \cdot 10^{-11}$
5	0.3	$2.3 \cdot 10^{-13}$
10	0.15	$2.8 \cdot 10^{-14}$
30	0.05	$1.0 \cdot 10^{-15}$

the *Trajectory Sensor* in a vacuum chamber under environmental plasma conditions.

An analysis of the signal times observed at the wire planes (Fig. 5.3) gives a start and stop signal to calculate the particle speed with an accuracy of $\approx 1\%$. This accuracy is sufficient in order to derive the orbital parameters of individual grains, which in turn are characteristic for their sources (interstellar, space debris, interplanetary).

Furthermore, this detector type measures accurately the grain charge Q and thus provides directly the grain mass m by Eq. 5.1. Parameters are the particle density ρ , the permittivity ϵ_0 , and the particle surface potential Φ . The detection of micrometeoroid primary charges in space by the Cassini-CDA instrument was reported in Kempf et al. [2004] and it was shown, that the described approach to determine particle masses is more accurate than other methods.

5.2.2 Large Area Mass Analyser

The low dust flux in interplanetary space (approx. $10^{-4} \text{ m}^{-2} \text{ s}^{-1}$) requires a dust analyser with a large (0.1 m^2) sensitive area and a wide field-of-view ($> 50^\circ$) [Srama et al., 2004b]. This was not achieved with the previous dust analysers in space. Therefore a new Large-Area Mass Analyzer (LAMA) was developed that meets the requirements of a sensitive impact area and a mass resolution of $\frac{m}{\Delta m} > 100$ [Srama et al., 2005a, Rachev et al., 2004, Rachev, 2005]. For LAMA, a configuration with cylindrical symmetry has been chosen with a ring-shaped impact target. Two different configurations were studied: LAMA1 has a short tube length in order to minimize the instrument size [Sternovsky et al., 2007], whereas LAMA2 is slightly larger due to an increased field free region between the acceleration grid and the ion reflector in order to incorporate a *Trajectory Sensor* (Fig. 5.4).

The impact detector consists of a flat annular shaped impact target at +5 kV potential and a grounded acceleration grid mounted 50 mm in front of the target. Potential rings provide a smooth electric field close to the edges. The acceleration distance of 50 mm is several times bigger than the 3 mm for Cassini CDA or the 10 mm of CIDA onboard Stardust. Thereby, the effect of shielding within the impact plasma cloud is reduced because the ion cloud is allowed to expand into a much wider volume before acceleration becomes effective.

The main tool to model and analyse the large-area mass spectrometer was SIMION 3D, a software package developed by David A. Dahl at the Idaho National Engineering & Environ-

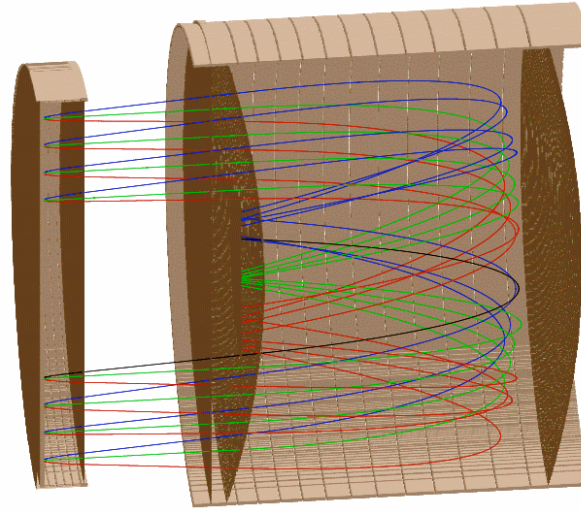


Figure 5.4: LAMA2 Simion simulation of ion trajectories starting at the target (left) with the ion emission angles of -90° , 0° and $+90^\circ$ [Rachev, 2005]. The starting ion energy at the annular target was set to 50 eV. An ion detector of 110 mm radius is necessary in order to collect all ions. Ion trajectories are shown for different impact positions on the target. LAMA2 uses two parabolic grids with a focal length of $f_{o1} = 540 \text{ mm}$ and $f_{o2} = 600 \text{ mm}$.

mental Laboratory. This software allowed us to model complex structures, to calculate the electric field distribution, and to determine ion trajectories and flight times .

In front of the impact detector there is a field-free drift region and the ion reflector has two parabolic shaped grids on the potential of 0 V and approx. +6000 V. Ion trajectories originating from different impact positions are shown in Fig. 5.4, which are spatially and timely focused onto the ion detector. It was assumed that ions have up to 50 eV energy spread and that they are emitted at different angles with respect to the target normal. An ion detector with a radius of about 120 mm measures highly resolved spectra. Parabolically shaped reflectron grids have been selected because of enhanced spatial focusing characteristics. For a given potential of the upper reflectron grid, the axial position of the ion detector with optimum spatial focusing was determined. After the ion detector position was found for a given reflectron configuration, the distance of the impact detector and the potential of the reflectron grid were varied to find the optimum mass resolution. The grid curvatures and the distance of the reflectron grids have been varied as well.

Ions of the impact plasma are described by a variety of properties like starting positions at the target, emission angles, and initial energies. These parameters strongly influence the spectrometer capabilities and finally the mass resolution. Here, impact locations from 120 to 240 mm radius, ion energies between 0 and 50 eV, and emission angles between -90° and 90° have been considered for the calculation of the mass resolution. However, only ions with initial energies below 3 eV reach an ion detector (microchannel plate) with a radius of 25 mm.

Higher ion energies up to 50 eV require an ion detector size as large as 110 mm radius. Several different configurations were found that provide a mass resolution $\frac{m}{\Delta m} > 150$ for all

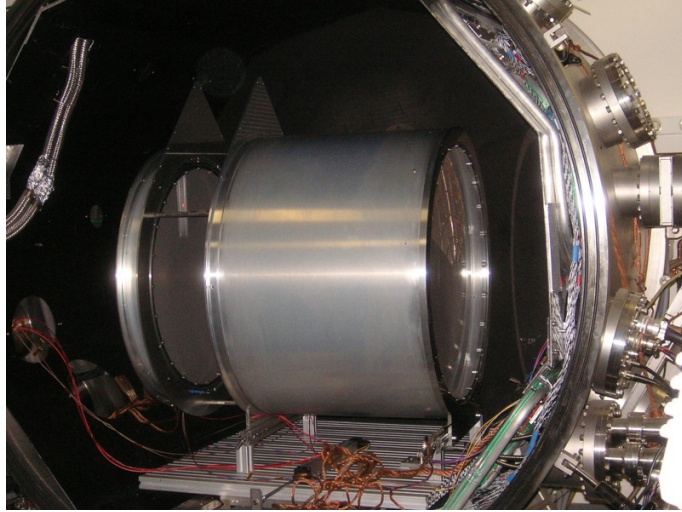


Figure 5.5: The laboratory model of LAMA2 at MPI-K.

impact locations on the target. There is also a weak dependence of the the mass resolution on the impact location at the target and on the width of the ion beam in the detector plane. For all impact positions between radius 120 and 240 mm the mass resolution is $\frac{m}{\Delta m} > 170$ using an ion detector diameter of 120 mm.

A laboratory model of LAMA2 was manufactured by the company Astro- und Feinwerktechnik, Berlin, and tested at the Heidelberg dust accelerator facility (Fig. 5.5). The reflector was manufactured with a reduced open area in order to simplify the manufacturing. However, the electric field geometry was fully preserved. An overview about the properties of *LAMA* and the *Trajectory Sensor* are listed in Tab. 5.3.

Table 5.3: Properties of the *Trajectory Sensor* and *LAMA*. The instrument mass, power and dimensions are estimations. The dust mass ranges assume a particle density of 2000 kg/m³ and a surface potential of 5 V.

Property	<i>Trajectory Sensor</i>	LAMA2
Mass [kg]	7.5	15
Power [W]	8	11
Sens. area [m ²]	0.25	0.1
Dimensions [m]	0.5x0.5x0.25	0.65Dx0.72
Aperture [+/-deg]	56	40
Measurement range		
Dust velocity [kms ⁻¹]	3-100	1-100
Dust charge [fC]	0.1-100	-
Dust mass [kg]	$5 \cdot 10^{-17} - 5 \cdot 10^{-8}$	$10^{-18} - 10^{-8}$
Dust trajectory accuracy	+/-2°	+/-40°
Dust composition $\frac{m}{\Delta m}$	-	>100

How do mass spectra of *LAMA* look like? Does the achieved mass resolution meet the simulated predictions in mass resolution? The answer is clearly yes, the expected performance was confirmed by a variety of impact tests at the dust accelerator using iron, nickel, latex or even mineralic dust particles with speeds between 4 and 40 km s⁻¹. Mass spectra using organic micrograins are of special interest for astrobiological questions. Organic time-of-flight spectra show a variety of mass lines at low impact speeds and are demanding for the instrumentation. Fig. 5.6 shows typical hyper-velocity impact spectra using coated latex projectiles [Srama et al., 2009b]. The spectrometer shows individual resolved mass lines over a simultaneous large dynamic range. A high dynamic range is required for the identification of minor species. The two-stage MCP device for ion detection (7 cm diameter) was normally operated at -1.5 kV and the weakest lines are composed of approximately 100 ions. Typical line widths are 14 ns (H) and 30 ns (Ag) providing mass resolutions $\frac{m}{\Delta m} > 200$. Narrow mass lines lead to high sensitivities, but require fast electronics with broad analog bandwidths and fast sampling rates >300 MHz.

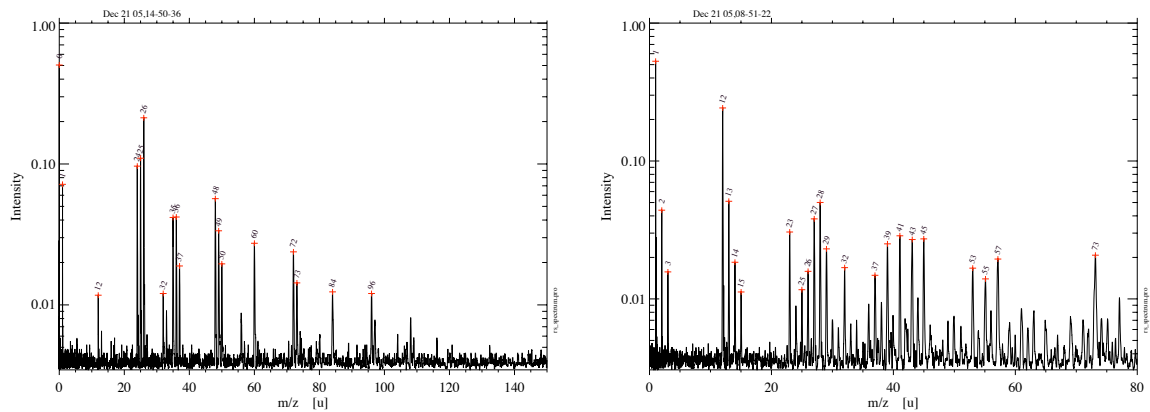


Figure 5.6: Left: Anion spectrum obtained for a 0.35 μm diameter PPy-PMPV latex at an impact velocity of about 20 km s⁻¹. A series of hydrogen-free carbon clusters can be followed from the C₂-cluster (mass 24) to the C₈-cluster (mass 96). For clusters with an even number of C atoms, species with one and two hydrogens are also found. The mass lines at 35 u and 37 u are due to chloride. The sulfur anion can barely be identified at 32 u. Right: Mass spectrum with a stretched mass scale. Cation spectrum obtained for a 0.30 μm diameter PPy-PMPV latex at an impact velocity of 20 km s⁻¹. The pattern of the carbon clusters ends with the C₄-cluster. At higher masses the isotopic patterns of [Ag₂]⁺ and [Ag₃]⁺ clusters are found. The ³²S⁺ line can be identified clearly.

5.3 Types of Dust Telescopes

First, the *Trajectory Sensor* has to be combined with the spectrometer for simultaneous measurements of the grain properties, speed, trajectory, electrical charge, mass and composition. For data acquisition, the mass spectrum has to be recorded in conjunction with the induced charge signals of the individual wires of the *Trajectory Sensor*. However, the storage depth

of the TR-ASIC connected to the wire amplifiers is only 1024 samples which corresponds to $\approx 20 \mu\text{s}$. The fast ADC of the ion detector is not running continuously, but has to be triggered by a dust impact. The trigger time for event recording has to be defined accordingly in order to record both signals, the trajectory sensor information before the target impact, and the mass spectrum of the MCP after the impact. Fig. 5.7 shows the combined signals of a dust grain with a primary charge of $1.7 \cdot 10^{-15} \text{ C}$ and an impact speed of 20.1 km s^{-1} . The trajectory sensor detects both, the primary charge signal of the dust grain, and the positive plasma ions upon the particle impact. The charge sensitive amplifier turns the positive signals into negative amplitudes. The mass spectrum shows typical lines of hydrogen, carbon and the target material silver (double peak at mass 107 u and 109 u).

The *Dust Telescope* development started with the scientific requirement of a large sensitive area for the detection of low interplanetary and interstellar dust fluxes. This leads to large detector volumes and masses, such that multi-purpose spacecrafts do not have the resources for its accommodation – as a consequence own dust observatory missions were proposed to ESA and NASA in the last years.

There are new missions for planetary or moon environments which do not require necessarily large sensitive areas. Therefore a down-scaling of the *Dust Telescope* was investigated and the result are two further telescope proposals as shown in Fig. 5.8.

One design carries a quadratic *Trajectory Sensor* and a round, but much smaller chemical analyser. This design was chosen for a german moon orbiter currently in the study phase by industry¹. It combines the ability to accurately measure dust fluxes, dust velocity vectors and dust mass distributions. For about 40% of the infalling particles a compositional analysis by the integrated TOF spectrometer with a mass resolution $\frac{m}{\Delta m} \approx 100$ is performed. This design is very well suited for the study of dust clouds around moons as discovered in the vicinity of Europa, Ganymed or Callisto. For an Europa orbiter with an altitude of 200 km, 100 000 impacts were predicted by the Open University for a mission life time of two months. A similar number of dust impacts was predicted for an orbiter around the Earth's moon. Such high dust fluxes allow for smaller sensitive areas making the instrument more compact. However, scaling down the TOF mass spectrometer has the disadvantage of a decreasing mass resolution. The small spectrometer shown in Fig. 5.8 allows measurements with $\frac{m}{\Delta m} \approx 100$, which is still a factor of three better than the integrated spectrometer of CDA onboard Cassini.

The most compact spectrometer type was designed with the goal of a total instrument mass of $\approx 2 \text{ kg}$, such that it can be employed for smaller missions like the Europa Orbiter, the Ganymed Orbiter or the Solar Probe Plus mission². The TOF spectrometer was persevered, but the Trajectory Sensor was replaced by one plane of wires screened by two grids. By this means, all impacting grains still provide compositional information by a simultaneous determination of the dust charge and mass by the wires. The dust speed information is derived from the flight time between the plane of wires in the front and the target plane.

¹LEO : Lunar Exploration Orbiter, the dust instrument proposed is names LEOPARD standing for LEO dust PARTicle Detector

²The name for this design is SODA : Solar Orbiter Dust Analyser or JEDI : Jupiter Europa Dust Instrument.

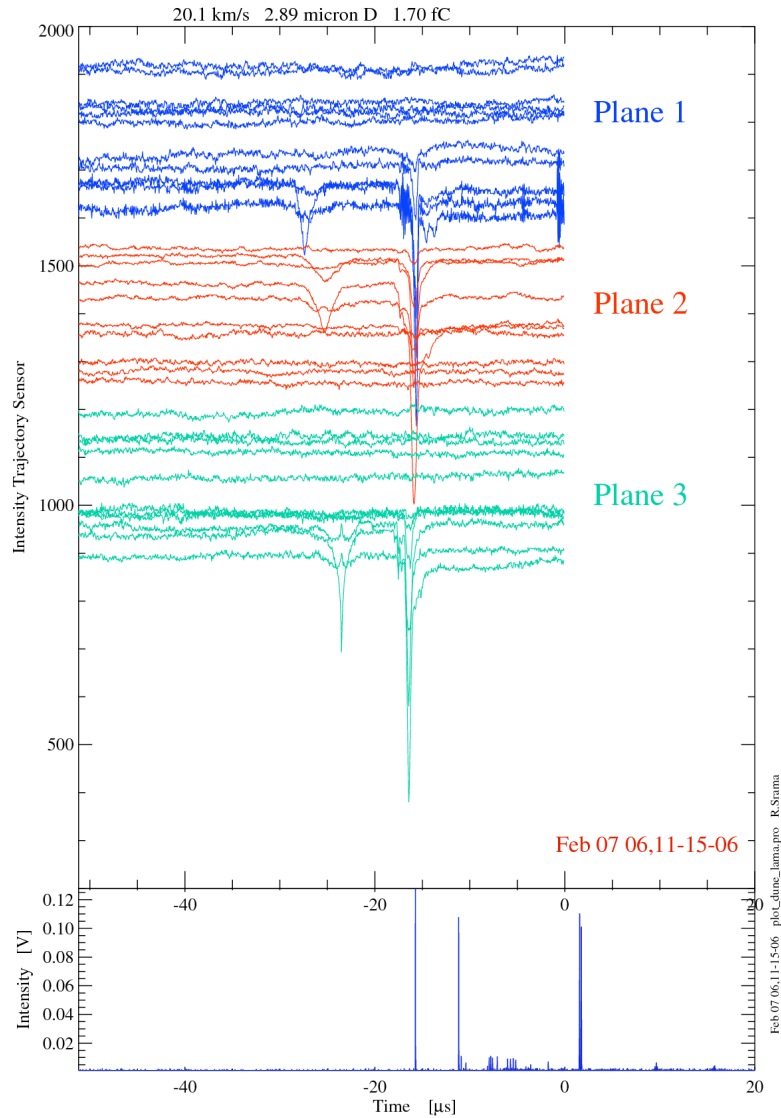


Figure 5.7: Combined signals of a dust grain with 20 km s^{-1} and a primary charge of 1.7 fC measured by a LAMA2-type Dust Telescope at the Heidelberg dust accelerator. The signals of individual wires for three planes of the Trajectory Sensor are shown in three different colors. The mass spectrum with its H, C and Ag line is shown at the bottom using the same time axis.

Tab. 5.4 gives the overview about the instrumental properties of the big *Dust Telescope*, the intermediate design LEOPARD, and the compact design SODA. A laboratory model of the compact mass spectrometer SODA was already manufactured and tested in the laboratory. Its spectrometer shows the predicted performance and TOF spectra examples are given in Fig. 5.9.

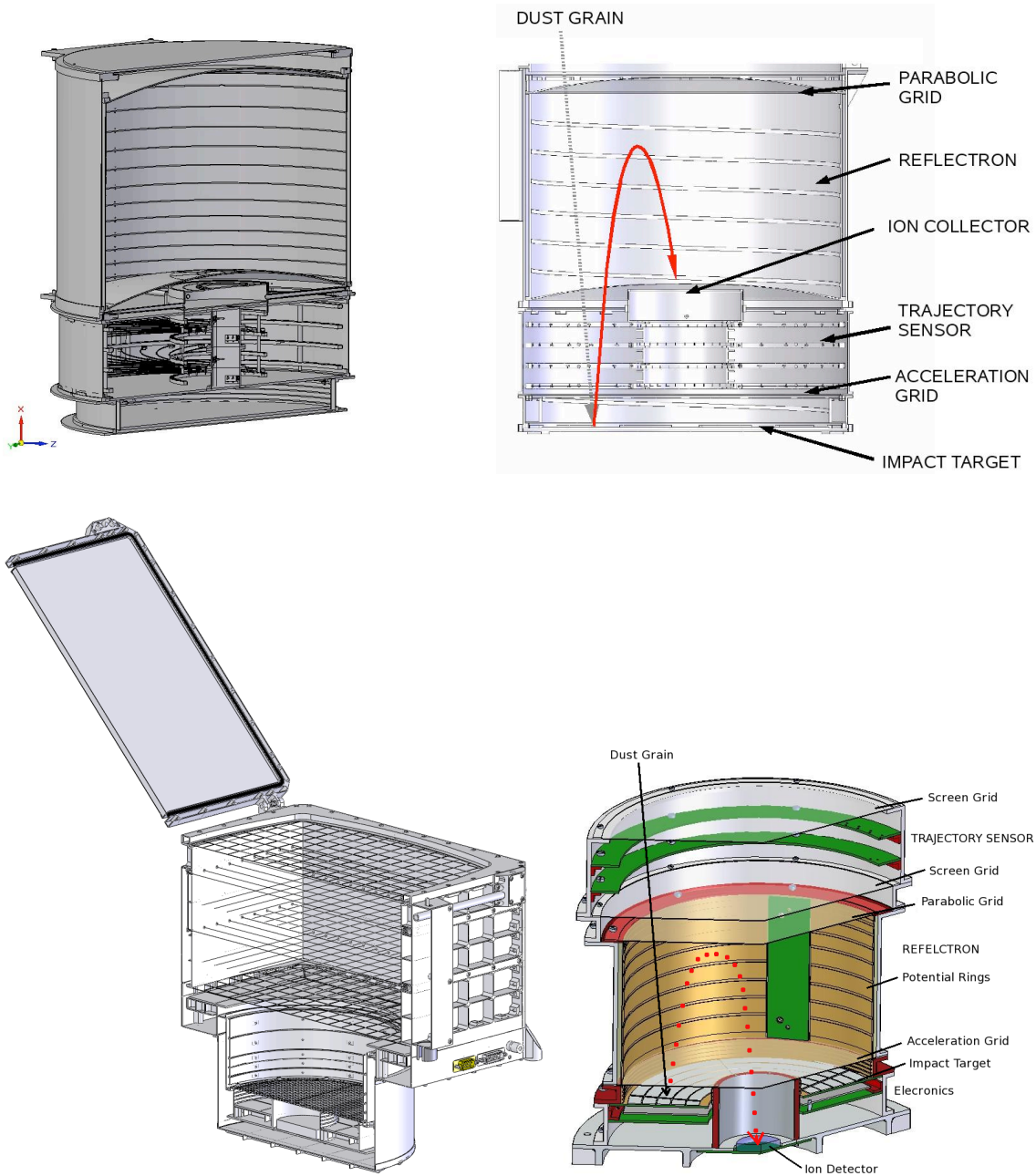


Figure 5.8: Design studies of three different Dust Telescopes. Top: TS+LAMA with a target diameter of 60 cm (von Hoerner & Sulger). Bottom left: LEOPARD with a Trajectory Sensor side length of 30 cm (G. Pahl). Bottom right: SODA with a target diameter of 20 cm (V. Schlemmer).

The flight time of the ions in the spectrometer from the target to the MCP are described by Eq. 5.2, using the stretch parameter a , the ion mass m in u, the ion charge q and a constant b .

$$t = a \cdot \sqrt{m/q} + b \quad (5.2)$$

Table 5.4: Properties and measurement thresholds for three different Dust Telescopes DT (big), LEOPARD (medium size) and SODA (small).

Property	DT	Leopard	SODA
Mass [kg]	≈ 22	≈ 8	< 2.5
Power [W]	< 19	< 19	≈ 10
Area [cm ²]	2200	750	240
FOV	$\pm 38^\circ$	$\pm 50^\circ$	$\pm 45^\circ$
Datarate [kbps]	1 - 10	0.5 - 10	0.5 - 4
Dimension m ³	$0.65 \times 0.65 \times 0.72$	$0.23 \times 0.23 \times 0.35$	$0.32 \times 0.37 \times 0.35$
Dust speed [km s ⁻¹]	1 - 50	1 - 50	1 - 50
Dust mass [kg]	$1 \cdot 10^{-18} - 1 \cdot 10^{-8}$	$1 \cdot 10^{-18} - 1 \cdot 10^{-8}$	$1 \cdot 10^{-18} - 1 \cdot 10^{-8}$
Dust flux [m ⁻² s ⁻¹]	$< 1 \cdot 10^{-5}$	$< 3 \cdot 10^{-5}$	$< 6 \cdot 10^{-5}$
Dust charge [C]	$3 \cdot 10^{-16} - 1 \cdot 10^{-13}$	$3 \cdot 10^{-16} - 1 \cdot 10^{-13}$	$5 \cdot 10^{-16} - 1 \cdot 10^{-13}$
Dust trajectory ($1 \cdot 10^{-15}$ C)	$\pm 1^\circ$	$\pm 1^\circ$	$\pm 10^\circ$
Dust composition $\frac{m}{\Delta m}$	yes, > 200	yes, ≈ 100	yes, ≈ 100

Using the big LAMA2 spectrometer (Fig. 5.5), stretch factors of $a = 1.79 \cdot 10^{-6}$ are nominal. The parameters of the small SODA spectrometer are $a = 1.03 \cdot 10^{-6}$ ($V_{target} = 2500$ V) and $a = 5.47 \cdot 10^{-7}$ ($V_{target} = 5000$ V), respectively.

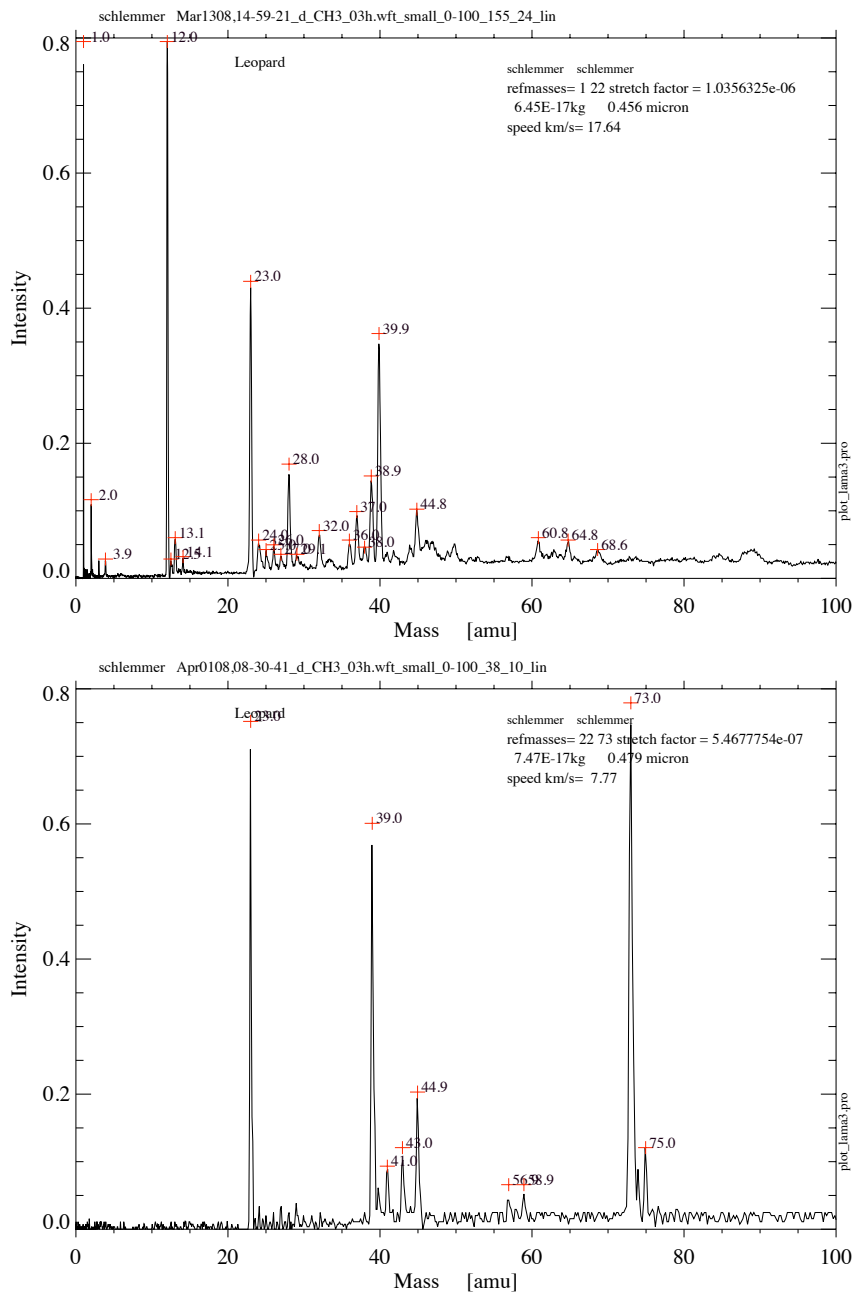


Figure 5.9: TOF spectra recorded in April 2008 with the small Dust Telescope SODA at the dust accelerator. The projectiles used were coated PMPV latex grains and the target was gold plated. The applied voltages were 2.5 kV (target), 2.7 kV (reflectron grid) and -1.5 kV (MCP) (top spectrum). The target voltage of the right spectrum was higher and 5 kV. The projectile properties were $17.7 \text{ km s}^{-1} / 0.46 \text{ }\mu\text{m}$ (top) and $7.8 \text{ km s}^{-1} / 0.48 \text{ }\mu\text{m}$ (bottom). The mass resolution of this compact spectrometer is ≈ 100 .

6 Future Dust Missions

Dust transports information over space and time – therefore it is an excellent medium to learn about the history of our Solar System, our interstellar neighborhood and even about the origin of life. Dust grains are charged and are affected by planetary magnetospheres, by the interplanetary magnetic field and by the interstellar medium. The growing interest and its significance for astronomers, planetologists, geophysicists and astrobiologists lead to a sequence of international mission proposals under the leadership of Germany (Univ. Stuttgart, MPI Nuclear Physics) and the USA (Univ. Colorado). These proposals were triggered by the knowledge gained by the interplanetary missions Giotto, Ulysses, Galileo, Cassini and Stardust. Ulysses discovered and characterised the interstellar dust, Cassini made excellent compositional measurements and detected for the first time grain charges, and Stardust brought cometary (and interplanetary or even interstellar) dust samples back to Earth. The community is now aware of the unique possibilities of current dust detector technology, such that international researchers do support, or even depend on such future activities. Three new mission concepts are described in this chapter. In addition, the latest PVDF-type dust sensor onboard New Horizon provides results from the outer Solar System already today [Horanyi et al., 2009] and an impact ionisation detector is in preparation for the Lunar Atmosphere and Dust Environment Explorer (LADEE)[Horanyi et al., 2009].

6.1 Cosmic DUNE

Cosmic DUNE¹ is a dust observatory for the study of interstellar and interplanetary dust. ESA issued a *call for missions* in order to reuse the Mars Express Bus to safe costs. Out of the 50 proposals, four proposals were selected for study by ESA. The Cosmic DUNE proposal was selected and a mission definition report was prepared by ESA [Svedhem, 2005].

Galactic interstellar dust constitutes the solid phase of matter from which stars and planetary systems form. Interplanetary dust, from comets and asteroids, represents remnant material from bodies at different stages of early Solar System evolution. Thus, studies of interstellar and interplanetary dust with Cosmic DUNE in Earth orbit would provide a comparison between the composition of the interstellar medium and primitive planetary objects. Hence Cosmic DUNE will give insights into the physical conditions during planetary system formation. This comparison of interstellar and interplanetary dust is highly important for both planetary science and astrophysics, respectively.

The discoveries of interstellar dust in the outer and inner solar system during the last decade

¹DUNE : DUSt Near the Earth



Figure 6.1: Cosmic DUNE spacecraft in the vicinity of the Earth.

suggest an innovative approach to the characterisation of cosmic dust. Cosmic DUNE establishes the next logical step beyond NASA's Stardust mission, with four major advancements in cosmic dust research:

- Analysis of the elemental and isotopic composition of individual cosmic dust grains
- Determination of the size distribution of interstellar dust
- Characterisation of the interstellar dust flow through the planetary system
- Analysis of interplanetary dust of cometary and asteroidal origin

Additionally, in supporting the dust science objectives, Cosmic DUNE would characterise and monitor the ambient plasma conditions near the Earth's magnetotail.

The science payload consists of a dust telescope, comprising space-proven instruments based on dust detection techniques successfully used on Giotto, VeGa, Cassini, Stardust, Rosetta and other missions. Tab. 6.1 gives the mass and power summary of the payload instruments CDA, CIDA, D2S, ISIDE and PLASMON.

Table 6.1: Instrument payload properties. All instruments except PLASMON point towards the dust RAM direction.

Property	CDA	CIDA	D2S	ISIDE	PLASMON	total
mass [kg]	13.0	11.0	32.0	6.0	1.3	63
power [W]	7.2	15.0	14.7	15.0	1.5	53
sens. area [m ²]	0.1	0.012	7×0.11	4×0.015	NA	1

The payload instruments were selected on the basis of space-proven detectors and are optimised for the large area impact detection and trajectory analysis of micron sized and larger

dust grains. They ensure the determination of fluxes, masses, speeds, electrical charges, and especially, the high resolution chemical analysis of cosmic dust. The instruments employ various detection techniques and have different sensitivities (Fig. 6.2). The physical techniques are impact ionisation (CDA, CIDA), electrical induction (D2S-QP), depolarisation of a permanently polarised foil (D2S-PVDF) and momentum detection (ISIDE). CIDA and CDA have the highest sensitivity for fast particles. The instruments are capable of analysing particles with masses between $1 \cdot 10^{-4}$ and $1 \cdot 10^{-14}$ g and speeds between 1 and 100 km s^{-1} as required by the observation scenario and the scientific goals. A large sensitive area of 1 m^2 is guaranteed by the D2S instrument (Dust Detector System), whereas the best chemical analysis is achieved by the CIDA instrument (Cometary and Interstellar Dust Analyser, mass resolution 250). A combination of CDA and D2S allows a simultaneous measurement of the dust properties including a moderate resolution of mass spectra for chemical analysis.

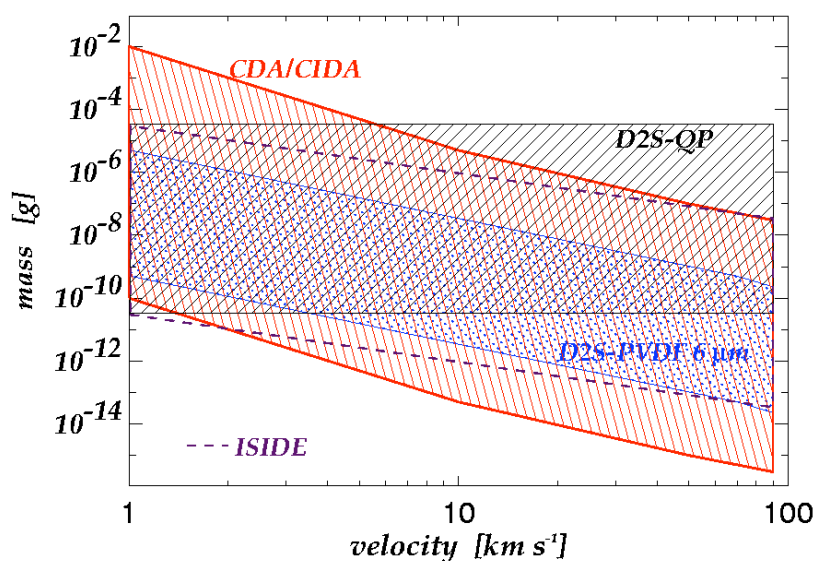


Figure 6.2: Sensitivity ranges of the payload instruments. CDA and CIDA have the same sensitivity. The charge measurement threshold of D2S-QP is $1 \cdot 10^{-15}$ C. This corresponds to a dust particle with a surface potential of 5V and a particle radius of $2 \mu\text{m}$ (mass $3 \cdot 10^{-11}$ g and density 1 g cm^{-3}). Very large particles above the range indicated in the figure can be detected by all instruments, but the signals would be in saturation.

Particles impacting onto CIDA or CDA will provide an independent particle speed and mass determination with medium resolution, based on the impact charge liberated and signal profile. While CIDA provides a high resolution mass spectra of the elemental composition, it cannot determine the speed and mass of the particles over a wide mass range – CDA offers a much wider mass dynamic range. However, particles triggering the D2S-QP system (thus determining an accurate speed) and then impact onto CDA, will offer an accurate mass determination (i.e. within a factor of 2 or 3 compared with a factor of 10).

Another accurate mass determination relies on D2S-QPs synergy with ISIDE. The ISIDE sub-

system provides a measurement of the particle momentum and thus, when combined with a direct speed measurement from D2S-QP, the mass can be calculated more accurately than with either D2S-QP or ISIDE alone.

The same scheme is applied to the combination of the signals from D2S-PVDF (essentially related to particle impact energy) with signals from D2S-QP (giving accurate particle speed), although with the following difference. The PVDF detector output voltage U is proportional to a function of the form $U \sim v^\alpha m^\beta$. Here, the D2S-QP provides an independent determination of the particle speed and the particle mass can be calculated using this formula. Without a combination of D2S-QP and D2S-PVDF, that mass determination would not be possible.

The D2S-QP instrument directly determines the electrical charge and the trajectory of single dust grains, and the CDA and CIDA instruments indirectly measure the charge based on the plasma generated by the dust particles hypervelocity impacts. For this reason, it is desirable that the plasma environment is monitored by an appropriate sensor system. This plasma monitoring is achieved by the PLASMON instrument, which is mounted such that it can permanently track the solar wind conditions and the spacecraft local plasma environment.

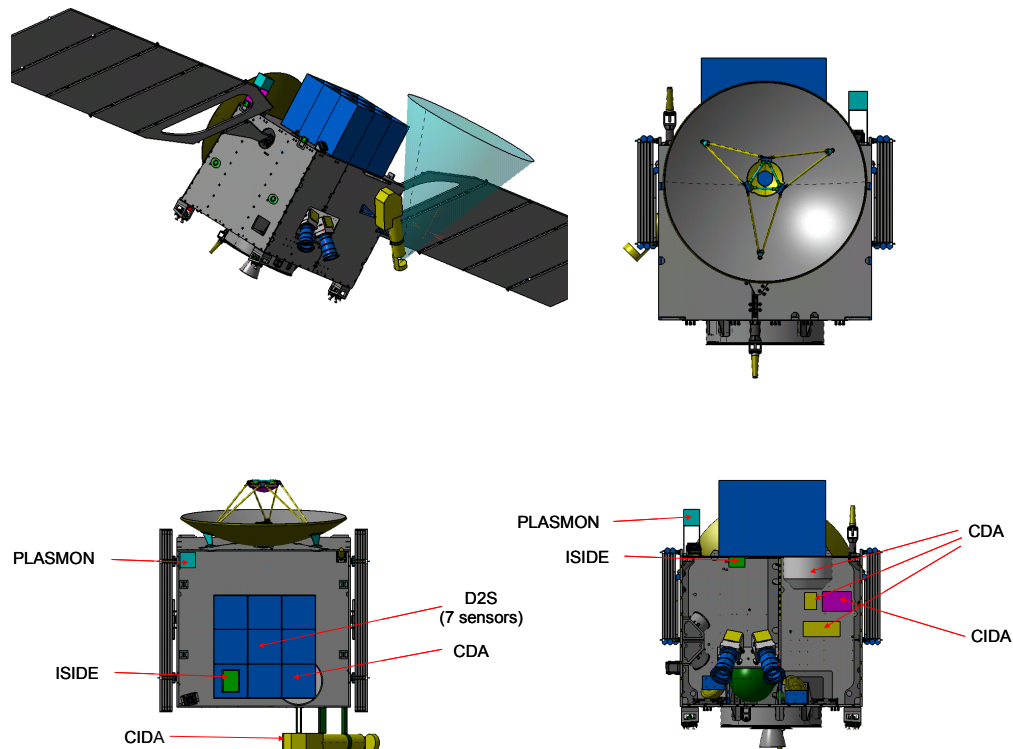


Figure 6.3: The Mars Express Bus with the integrated Dust Telescope payload. Nine modules of the Dust Detector System (D2S) are integrated [Svedhem, 2005].

The dust particles surface properties are determined via a coupled relationship between the particles mass and charge potential. The elemental composition constrains the optical proper-

ties of the dust, which leads to a better understanding of the particle surface potential Φ . The surface potential Φ and the particle radius r (assuming a spherical shape) then give the particle charge: $Q = 4\pi r\Phi\epsilon_0$. Since the charge is directly measured by D2S-QP, the calculated mass and potential constrains either the particle density or, using a known density, the particle shape (fluffiness or porosity).

The instrument subsystems form an integrated dust telescope (Fig. 6.3) with a shared pointing direction. About 1000 grains are expected to be recorded by this payload every year, with 10% of these providing elemental composition.

An orbit about the collinear Lagrangian point L2 of the Sun-Earth system meets the requirement of being at large distances from Earth's orbital debris belts, and it provides a very stable thermal environment. A Lissajous orbit about L2 was selected as the baseline orbit for Cosmic DUNE. The L2 point is about $230 R_E$ (Earth radius) behind the Earth (away from the Sun). For most of the time, a spacecraft on an orbit about L2 will be in the solar wind with possible tail crossings. The geometry as well as the plasma properties in the tail are highly variable. Typical plasma densities are $\sim 0.5 \text{ cm}^{-3}$ and the temperatures are high (keV). The photoemission process dominates and the dust surface potential remains around +5 V. The distant tail has an approximately circular cross section, $30 R_E$ in diameter, and of uncertain length, although it has been detected downwind beyond $1500 R_E$.

Unfortunately, no technical or scientific weak points were identified in the study, but finally, Cosmic DUNE was not selected by ESA in favour of Venus Express.

6.2 DuneXpress

Based on the scientific goals defined for the Cosmic DUNE mission, the Dust Astronomy mission DuneXpress was proposed to ESA in response to the Cosmic Vision program 2015-2025 [Grün et al., 2009]. The DuneXpress mission has two major advantages. The payload employs new developed dust instrumentation, and a bus concept ConeXpress of Dutch Space was selected as a low-cost spacecraft bus in order to carry the DUNE instrument package. The new payload instrumentation with increased sensitivity (charge threshold) and performance (mass resolution) defines the following measurement goals considering the overall scientific goals listed in Grün et al. [2009]:

- Measurement of dust charges down to $1 \cdot 10^{-16} \text{ C}$
- Determine dust trajectories with an accuracy of better than 3% in speed and 3° in direction in order to distinguish interstellar from interplanetary dust by their trajectories
- Analyse the elemental and isotopic composition of individual cosmic dust grains at a mass resolution $\frac{m}{\Delta m} > 100$
- Characterise the ambient plasma conditions
- Determine the physical properties of individual dust grains

The ConeXpress generic platform was developed under ESA/telecom by a European industrial team led by Dutch Space. The total mission cost CaC was estimated to be below 100 M€. This platform makes use of an Ariane 5 adaptor as a primary structure and uses electric propulsion to go within 600 days from GTO to a halo orbit around L2. L2 is preferred over L1 because the spacecraft configuration has the high-gain antenna pointing to the opposite direction than the dust instruments. During downlinks the instruments point away from the Sun, which is required for thermal reasons. The orbit geometry is shown in Fig. 6.4; Fig. 6.5 presents the spacecraft bus with the integrated dust instrumentation.

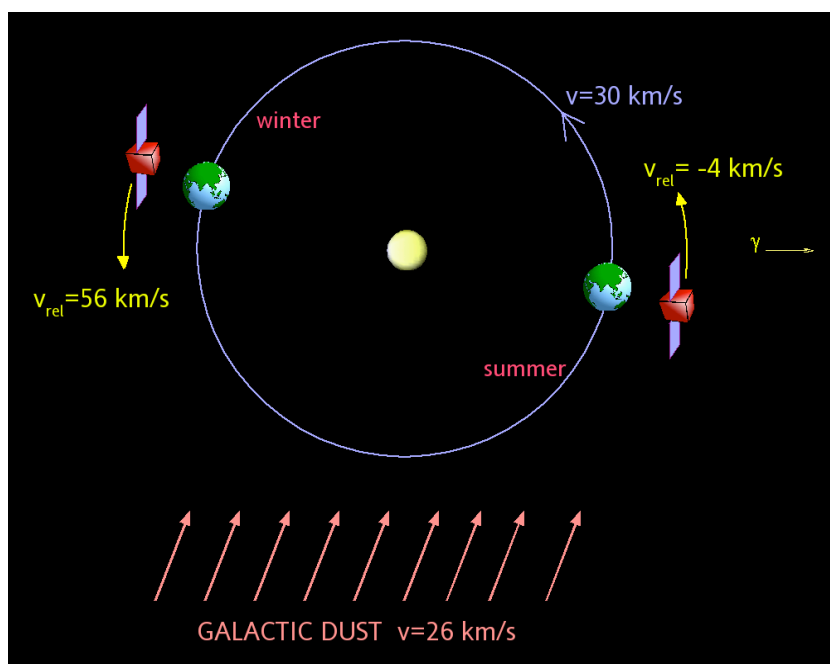


Figure 6.4: Mission scenario of DuneXpress at L2 of the Sun-Earth system. The interstellar dust flux direction, two positions of the Earth and the spacecraft are shown (right: late summer, and left: late winter). The orbital geometry leads to a yearly modulation of the interstellar flux. The corresponding fluxes are $F = 4.5 \cdot 10^{-4} \text{ m}^{-2} \text{ s}^{-1}$ in winter and $F = 6.6 \cdot 10^{-5} \text{ m}^{-2} \text{ s}^{-1}$ in summer. Further information can be found in Grün et al. [2009] and Grün et al. [2003].

The S/C mass is 1200 kg, with two drivable wings of three panels each generating a power output of 4 kW. Communication is provided by an omnidirectional S-band and an X-band system that will use a 0.5 m parabolic antenna reflector. DuneXpress will be 3-axis stabilised using star trackers as primary sensors and reaction wheels for actuation.

DuneXpress will be launched into GTO as an auxiliary payload of an Ariane 5 ECA flight. From there, the perigee will be raised by electric propulsion to 20 000 km, the apogee will be brought to 1.5 million km, and the spacecraft will be injected into a halo orbit around L2 where scientific operation begins. The spacecraft provides pointing of the dust telescope to better than one degree and the measurements will be divided into observation segments of fixed duration from a few days to about 4 weeks. Within each observation segment, the spacecraft will maintain a fixed orientation, while all instruments collect data simultaneously (staring

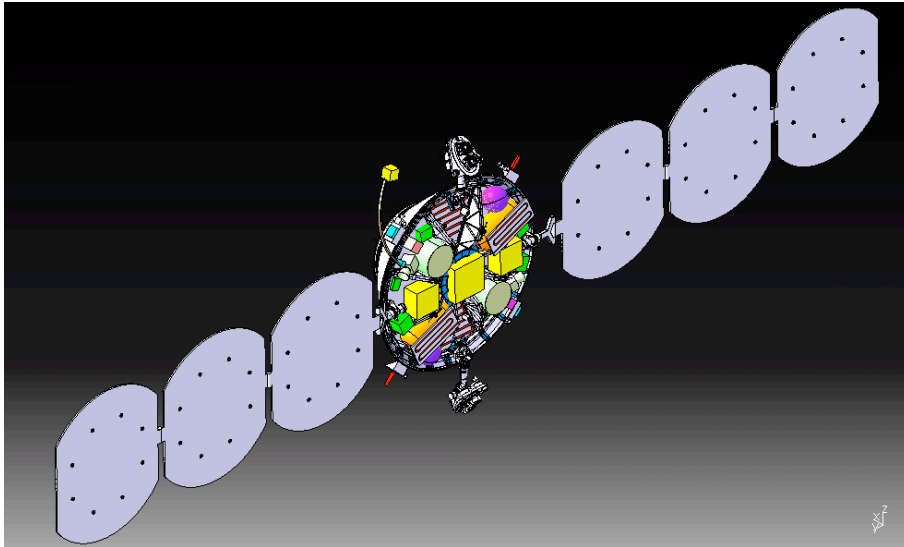


Figure 6.5: DuneXpress bus with two integrated Dust Telescopes (bright green) and three Dust Cameras (yellow boxes). The plasma monitor is mounted at a short boom (yellow box). (Dutch Space)

mode). For a few days in between observational segments, data will be downloaded and new commands will be received. Within two years observation time 1000 interstellar grains will be measured, 200 of which will be with high-resolution chemical analysis; also about three times more interplanetary particles will be analysed. The spacecraft will take sufficient fuel to enable scientific measurements of over four years.

The payload consists of two Dust Telescopes (compare Fig. 5.8), i.e. combinations of Dust Trajectory Sensors (DTS) and Large-Area-Mass Analyzers (LAMA), three Dust Cameras, a dust detector for nanometer-sized dust (Aluminum Film Interplanetary Dust Detector, AFIDD), and a Plasma Monitor (PLASMON) (Tab. 6.2). The Dust Cameras are combinations of DTS with various kinds of impact detectors (compare Fig. 5.1). This provides complementary information and extends the overall measurement range of DTS.

Table 6.2: Summary of the payload instruments onboard DuneXpress. Combinations of Trajectory Sensors with various impact stages (Dust Cameras, DC) are employed. Two types of Dust Telescopes (DT) provide trajectory and compositional information of impacting interstellar or interplanetary dust grains. Some instruments share a data processing unit (not shown). The total payload mass and power is 56 kg and 95 W, respectively. A further description is given in Grün et al. [2009].

Instrument	DT1	DT2	DC1	DC2	DC3	AFIDD	PLASMON
Type	LAMA1	LAMA2	PVDF	Piezo	Ionisation	Al film+MCP	Plasma
Area [m ²]	0.05	0.05	0.1	0.1	0.2	0.004	NA
Mass [kg]	15	19	4.9	5.6	8	1	1.3
Power [W]	16	25	8	< 30	9	2	1.5
Size [cm]	44×49	48×48	30×30×34	36×36×29	50×50×23	13×13×2	15×15×15

The *Dust Camera DC1* uses a polyvinylidene fluoride (PVDF) film to measure the mass of a dust particle passing through a Trajectory Sensor. The PVDF film (or a variant, vinylidene fluoride/trifluoroethylene i.e. a PVDF copolymer) consists of a permanently polarized material [Simpson and Tuzzolino, 1985]. A particle impacting the sensor surface makes a crater (or hole) which produces a local destruction of dipoles. This results in a rapid current pulse (of order $10 \mu\text{s}$) which can be detected by relatively simple electronics. No bias voltage need be applied to the PVDF, although the PVDF is coated with a thin (typically 70 nm) conducting layer to act as sensing electrodes. The pulse signal (charge liberated) depends on particle mass and velocity. This instrument comprises 25 discrete (in a 5×5 array) PVDF film modules, each with approximate dimensions $6 \text{ cm} \times 6 \text{ cm}$. Each PVDF film is held by an acoustically isolating housing around its perimeter. For maximum sensitivity, thin PVDF is used ($6 \mu\text{m}$ thick with 70 nm thick conducting layers on both sides). The PVDF rear surface will be coated (e.g. with Chemglaze Z-306/307 or SiO) to increase the emissivity and aid temperature control. Using 25 modules minimises capacitance of each sensor element and improves the sensitivity and reliability of the instrument. The segmented detector also allows discrimination between impact sites. The PVDF instrument contributes less than 3 kg and 2 W to the total mass/power budget of the whole camera.

The *impact sensor of DC2* is a momentum sensor placed at the bottom of the Trajectory Sensor, which was developed for the GIADA instrument onboard the Rosetta mission [Colanageli et al., 2007]. The detection method is based on a metal diaphragm exposed to the impact of grains. The plate is equipped with piezoelectric sensors (PZT, e.g., lead zirconate titanate crystals); their number is adequate to have multiple measurements of a single impact, which give impact position and an intrinsic redundancy in the sensor. Impact position knowledge helps in both calibration and trajectory reconstruction by coupling it with data from the Trajectory Sensor. Referring to previous experiences made on specific configurations, a minimum momentum of $6.5 \cdot 10^{-10} \text{ kg m s}^{-1}$ can be detected. The detection limits of this impact stage correspond to grain masses of $1.3 \cdot 10^{-13} \text{ kg}$, $6.5 \cdot 10^{-14} \text{ kg}$ and $3.2 \cdot 10^{-14} \text{ kg}$ at impacts speeds of 5, 10 and 20 km s^{-1} .

Dust Camera 3 utilises the process of impact ionisation, which occurs when a particle at hypervelocity impacts a target. Impact ionisation techniques are reliable and established in space (see this work). This detector carries a flat target plate (at 0V), and impact cations are accelerated towards an electrode grid (at 100V). The total charge collection at this electrode is related to the particle mass and velocity (by $Q \sim m v^{3.4}$) leading to sensitivities of $5 \cdot 10^{-16} \text{ kg}$ (5 km s^{-1}) and $5 \cdot 10^{-18} \text{ kg}$ (20 km s^{-1}). In order to ensure low detector capacitances, 25 sensing modules are mounted in an 5×5 array.

Even more sensitive is the nano-particle detector *AFIDD*. Nano-diamonds were identified in meteoritic material and spectroscopic data have shown, that nano-diamonds are abundant in interstellar space [Meyer-Vernet et al., 2009, Mutschke et al., 2004] and in cometary environments [Ip and Chow, 1997]. *AFIDD* consists of four circular MCPs detectors bearing Al films with two thicknesses, $2 \times 10 \text{ nm}$ and $2 \times 100 \text{ nm}$. Hypervelocity dust grains penetrate a thin Al film and generate a signal at the underlying MCP device. The MCP detectors are

operated in a low-gain mode, whereby the voltage across the channels is low compared with a standard photon or electron detecting MCP detector. The result is that the pulse height becomes a function of the total energy deposited in the microchannel and can therefore be used to discriminate between dust and radiation induced events. Its mass sensitivity is extremely high and given as $8.3 \cdot 10^{-19}$ g (10 nm foil, 5 km s^{-1}) and $4.1 \cdot 10^{-20}$ g (20 km s^{-1}), respectively.

The *PLASMON* sensor uses channeltrons in a counting mode and a small electrostatic plasma analyser measures the electron and ion distribution in a wide energy range. Its measurement range is 40 – 8000 eV (ions), 0.35 – 4200 eV (electrons) and 5 pT (magnetic field at 1 Hz) [Auster et al., 2007].

Two different types of *Dust Telescopes* are foreseen for ConeXpress, one DT is developed by MPI-K/Heidelberg and one DT is designed by the Univ. Boulder/USA. The Boulder version of the DT has a lower mass and a more compact design, but a slightly reduced mass resolution for compositional measurements [Sternovsky et al., 2007]. The design and capabilities of a *Dust Telescope* is described in detail in section 5.2.

6.3 SARIM – Sample Return of Interstellar Matter

Cosmic DUNE and DuneXpress are missions using in-situ techniques exclusively. This is an excellent approach as long as the sensor technology is able to answer all scientific questions. But even a Dust Telescope is limited in its performance and cannot determine dust grain morphologies or specific compositional questions. Laboratory analysis techniques are still better in comparison to in-situ space instrumentation (mass resolution, sensitivity, spatial resolution). However, sensitive laboratory methods do require unaltered and uncontaminated samples, such that special precautions are necessary in collector handling, spacecraft integration and sample return.

After the success of Stardust [Brownlee and Stardust Mission Team, 2006], which brought cometary dust grains back to Earth, planetologists are therefore strongly supporting future sample return missions like Marco Polo (asteroid sample return) or Triple F².

Stardust focused on the collection of cometary dust samples, but did not succeed to clearly identify and characterise interstellar dust grains although some particles were collected. For this reason, the mission SARIM (Sample Return of Interstellar Matter) was proposed in the framework of the ESA Cosmic Vision program [Srama et al., 2009a].

The SARIM spacecraft will be launched into an orbit around the Sun-Earth Lagrange point L2 which is 1.5 million km away from Earth outwards. The scientific instruments collect and measure ISD during a three year mission to meet the objectives before dust samples will be returned to Earth within a small reentry capsule. A low delta-v and low complexity strategy was chosen for the transfer to L2 and the return to Earth trajectory, minimising systems and operations costs. Europe's future small low-cost launch vehicle VEGA offers 2300 kg into

²Fresh From the Fridge – a comet nucleus sample return mission [Küppers and the Triple F team, 2009]

a 5.2° inclination low Earth orbit and provides enough performance to deliver SARIM as a primary payload of 200 kg total launch mass into an intermediate low Earth orbit. The 480 kg SARIM spacecraft (including the 130 kg return capsule) uses an additional hydrazine-based propulsion module of 225 kg dry mass for transfer orbit injection. The propulsion module containing 1395 kg propellant provides the necessary delta- v of $3,65 \text{ m s}^{-1}$ for a single-burn maneuver into transfer orbit to L2. After separation from the propulsion module the transfer of the SARIM spacecraft takes approximately 75 days followed by direct propellant-less insertion into the Halo orbit of $205\,000 \text{ km} \times 650\,000 \text{ km}$ around L2. All instruments of the three-axis stabilised spacecraft are fixed and provide a data volume of approx. 150 Mb per day which are downlinked every 2 weeks.

After three years of collection and in-situ measurements around L2, the SARIM spacecraft with the return capsule attached, performs an Earth return transfer maneuver demanding a delta- v of less than 15 m s^{-1} . After a 7 months journey the return capsule is released from the SARIM bus approximately 1 h before Earth reentry for precise and safe guidance. The spacecraft is transferred into a heliocentric orbit with a rescue maneuver of 57 m s^{-1} delta- v after capsule separation for possible mission extension. The ROM costs of the spacecraft bus (excluding payload) are approx. 125 M€ including the sample return mechanism and capsule; the preferred launcher of type VEGA requires an additional budget of 20 M€.

SARIM is optimised for the collection and discrimination of interstellar dust grains. Improved active dust collectors on-board allow the in-situ determination of individual dust impacts and their impact location. Nevertheless, SARIM requires some knowledge about the grains to be collected. Only dedicated sensor instrumentation is capable to collect interstellar grains efficiently and prohibit processing during the collection process (high impact speeds lead to grain heating, chemical and physical alteration). What are the pointing requirements for the collector and what are the relative impact speeds?

In order to optimise the collection strategy, first, a DuneXpress-like mission is helpful or even required. The knowledge gained (fluxes, directionality, composition) will impact the SARIM mission design and collector development significantly. But what can we do already now, if we would have to launch SARIM first? So let's have a look at the ISD velocity vectors with the assumption, that SARIM follows a halo orbit in L2 of the Earth Sun system (basically at 1 AU distance from the Sun on a DuneXpress-like orbit of Fig. 6.4).

In order to collect and measure interstellar dust in the inner Solar System, the interstellar particles have to penetrate the heliosphere to reach distances as close as 1 AU. The motion of interstellar grains through the Solar System is parallel to the flow of neutral interstellar hydrogen and helium gas. However, many grains are deflected by radiation pressure forces due to their optical properties (Fig. A.10, Fig. 6.6), and the relative pointing profile of SARIM has to be adjusted accordingly. Nevertheless, interstellar dust was identified by in-situ measurements as close as 0.3 AU from the Sun and the grain size ranges from 0.1 to $1 \mu\text{m}$ with a maximum at about $0.3 \mu\text{m}$ [Altobelli et al., 2006]. The predicted range of the dust grain impact speeds with different values of $\beta = 1 = F_{rad}/F_{grav}$ is shown in Fig. 6.7.

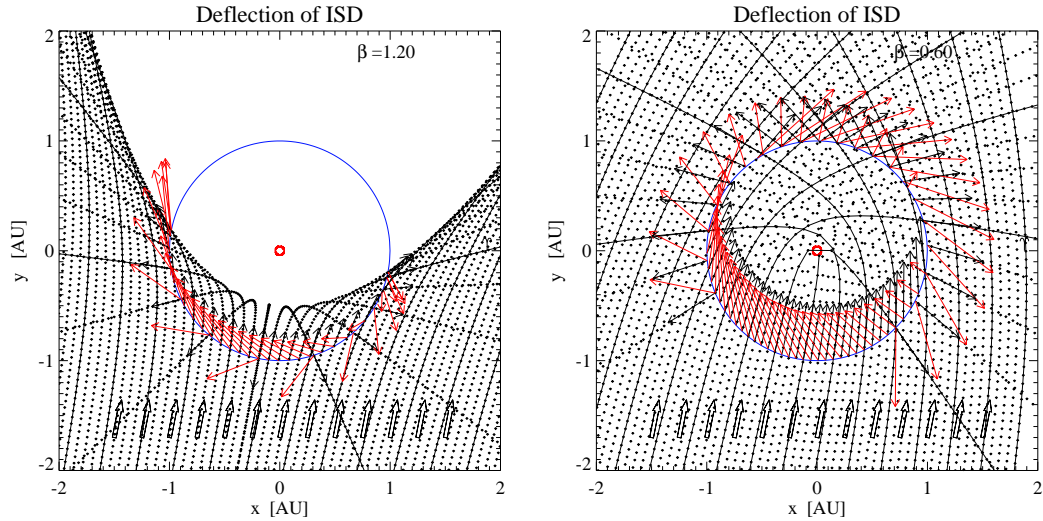


Figure 6.6: Flow of interstellar dust through the Solar System affected by gravity and radiation pressure. A dust mission on an Earth-like orbit observes a variation of the relative grain velocities \vec{v} (red arrow), and the collector or Dust Telescope boresight has to be adjusted. Left: radiation pressure dominated grain trajectories ($\beta = 1.2$); right: gravity dominated dust particle trajectories ($\beta = 0.6$).

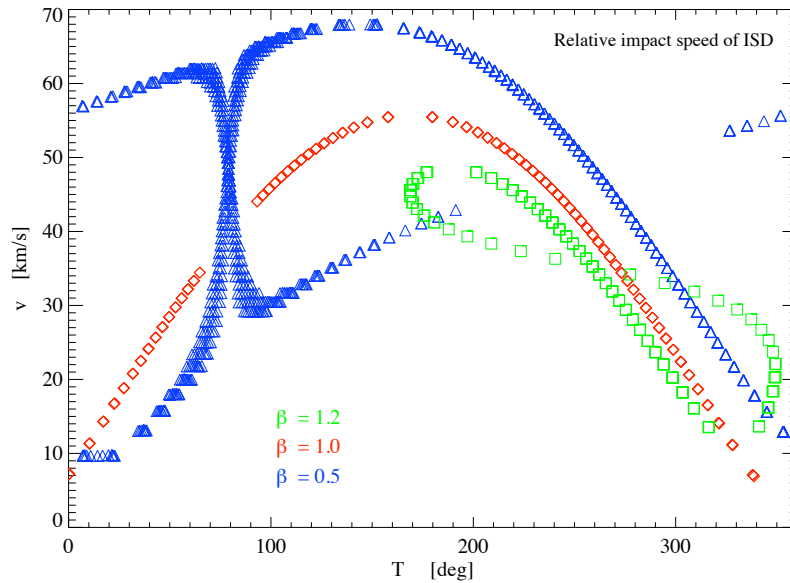


Figure 6.7: Relative impact speeds of ISD for a DuneXpress-like orbit for different angular distances from the point of periaresis (True anomaly T). The colours belong to particles with $\beta = 0.5$ (gravity dominated, big dust grains), $\beta = 1.0$ (radiation force and gravity are equal) and $\beta = 1.2$ (radiation force dominated, reflected by solar radiation pressure).

The dust speed v and particle flux $F = \frac{n}{t \cdot A}$ are modulated by the orbital period of one year. The dust instrumentation and the collector design have to cover a rather broad range of relative impact speeds from 5 to 55 km s^{-1} . Unfortunately, the time windows of highest flux are correlated with the highest impact speeds, which makes it difficult to collect samples unaltered. Relevant is therefore the number of particles below a certain threshold speed which was set to $v_{thres} = 20 \text{ km s}^{-1}$ based on the investigations of the Stardust project (aerogel collector materials). On an Earth-like orbit, SARIM would collect ≈ 100 interstellar grains with speeds below 20 km s^{-1} (Fig. 6.8). But even particles entering an aerogel-type collector with speeds above 20 km s^{-1} can be analysed in the collector matrix in order to determine their composition (e.g. by TOF-SIMS techniques).

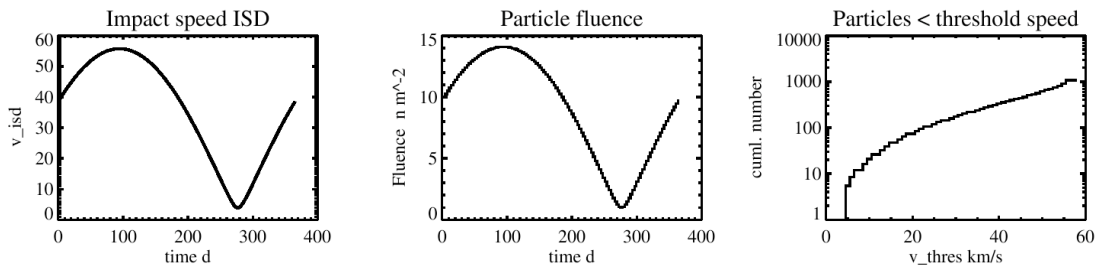


Figure 6.8: Relative impact speeds, particle fluence and cumulated number of collected interstellar dust grains below a threshold speed v_{thres} ($\beta = 1$).

The **in-situ instruments** will analyse the dust flux, size distribution, dust trajectories (dynamics and origin), and coarse elemental composition. They will also study time variability of the interstellar dust stream through the heliosphere and its coupling to the solar cycle. The preliminary payload consists of Active dust Collectors (AC), one Dust Telescope (DT), one Nano-particle detector, a plasma monitor, and one Sample Return Capsule (SRC). This payload allows a sensitive and reliable determination of individual dust grain characteristics such as speed, mass, charge, trajectory and composition. The total science payload mass is 86 kg and requires 170 W.

Seven **Active Collectors** (AC) are used onboard SARIM to monitor the dust flux with a total sensitive area of 1.1 m^2 (Fig. 6.9). These sensors are capable of determining the impact time, velocity vector, trajectory (hence grain origin), primary charge, impact location at the collector surface and mass of individual micrometeoroids. Each AC consists of a Dust Trajectory Sensor (DTS), a movable dust collector unit, and an impact detector (ID). The combination of DTS with ID is also called a Dust Camera (DC). A robotic mechanism pushes the collector between the DTS and the ID for the exposure to interstellar grains during parts of the orbit (i.e. July to October). For non-exposure times the collector is removed and the dust grains pass through the DTS and impact onto the ID, which itself is a separate dust sensor applying a variety of detection techniques to get complementary information about the dust grains. Detection techniques of these impact detectors are either impact ionisation (used by five modules), depolarisation of foils (one module), or acoustic signals (one module). The

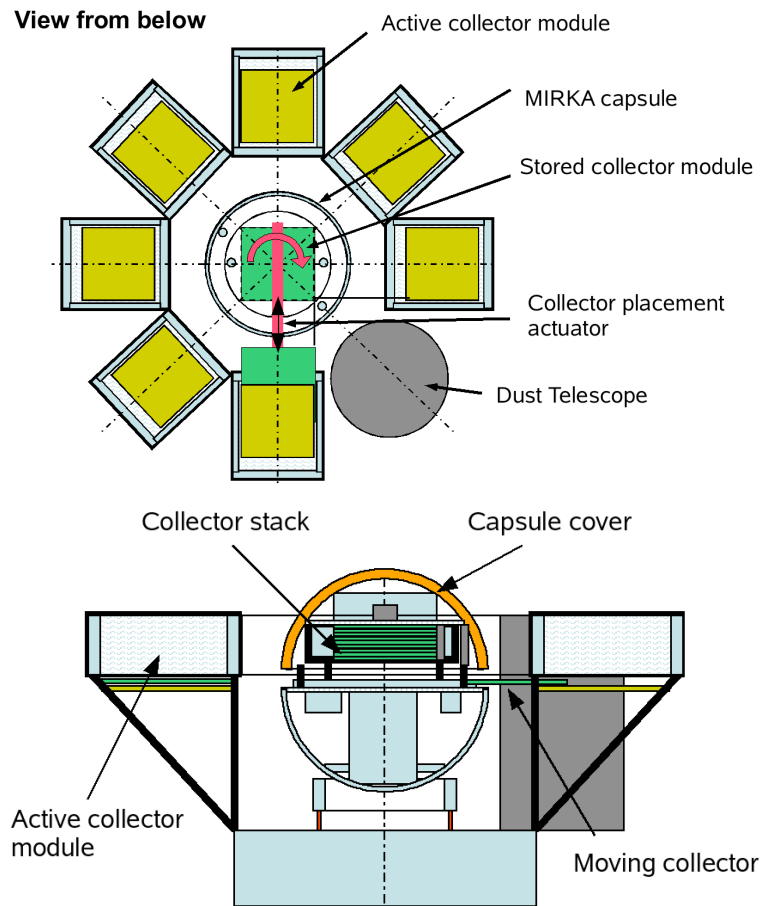


Figure 6.9: SARIM payload configuration with seven collector modules, one Dust Telescope and the Sample Return Capsule in the centre [Srama et al., 2009a](Astrium/EADS). Dust collectors are arranged in a stack mounted in a turn table housing within the front heat shield, which opens and thereby unseals simultaneously with the movement of the front heat shield. Seven dust collectors with a size of 400 mm × 400 mm × 20 mm and a total mass of 0.5 kg per collector plus supporting structure mechanism and a collector storage housing have to be accommodated within the MIRKA based return capsule. A collector handling system consisting of two linear actuators for vertical movement and a container bridge-like sliding mechanism picks up a single collector for delivery to each of the active collectors.

nano-particle AFIDD detector and the plasma monitor PLASMON provide complementary information about the environment [Srama et al., 2009a].

Most of the payload instruments were discussed in previous sections, DTS is explained in 5.2.1, the Dust Telescope is discussed in section 5.2 and the impact and plasma detectors are introduced in section 6.2. How do the **dust collectors** look like and what are they made of? For deep-space collection of interplanetary and interstellar particles (dominated by silicate-, sulfide-, oxide-minerals with very small grains including amorphous, non-crystalline materials, diamond, exotic carbides and nitrides), the ideal collector substrate must not contain

elements likely to be of major significance in captured particles (Na, Mg, Al, Si, P, S, K, Ca, Ti, Cr, Mn, Fe, Ni). H, C, N, and O should be absent, or their isotopic composition in the substrate should be highly distinctive if they are to be distinguished from captured organic material. Furthermore, the collection medium should: capture any particle between 10 nm and 1 mm size, regardless of particle structure, mass or velocity; result in no structural or compositional modification during or subsequent to capture; allow rapid and unambiguous location of all captured particles on return to the laboratory; give no interference with in-situ analysis techniques, and no ambiguity as to the origin of specific elemental signatures; permit perfect physical separation of the captured particle prior to further, sophisticated analysis. At present no material meets all of the desirable criteria perfectly. However, three materials probably provide the best available compromise: silica aerogel, polymer, and metal foil surfaces, albeit in modified form to those deployed on previous missions, and each with different limitations.



Figure 6.10: Aerogel material of low density with a paper clip on top. The top surface shows a dark grey spot caused by the impact of thousands of micron sized iron particles with a few km s^{-1} .

Silica aerogel as collector substrate material is very low in density (as low as 0.002 g cm^{-3}) and highly porous (Fig. 6.10). Impactors can tunnel with varying degrees of damage depending on the particle structure, composition, size and speed [Burchell, M.J. et al., 2006, Westphal et al., 2004]. Dense and robust particles penetrate deeply, and little material is lost or dust structure modified. The peak pressure at 6 km s^{-1} is likely to be only a few GPa. Coarser grained silicates, oxides, and carbonates are known to survive relatively intact, suitable for both mineralogical and petrological analyses and determination of major, minor and trace elemental composition as well as isotopic characterisation.

Recent studies focus on the development of non-silicate aerogels to allow for a detection of silicates in the collected dust grains. Non-silicate materials studied are of type carbon, alumina, titania, germania, zirconia, niobia, tin oxides and hafnia with densities between 20 and 100 mg cm^{-3} . Although such materials are opaque, synchrotron X-ray microprobe studies (SXR) allow the measurement of elemental abundances. But also polymer foils and metal plates and foils have been studied as collector material and further references are given in Srama et al. [2009a].

A S/C design was developed by Astrium/EADS on the heritage of former missions (Fig. 6.11). The mission consists of one three-axis stabilised **spacecraft** with rotating solar cells,

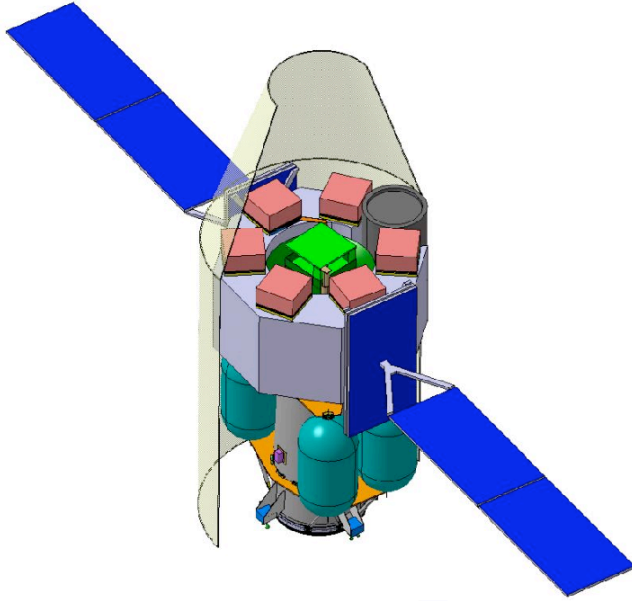


Figure 6.11: SARIM spacecraft in a VEGA payload fairing with extended solar sails (Astrium/EADS). Six Active Collectors (red cubes), one Dust Telescope (grey cylinder) and the collector sample stack (green) are mounted on the S/C body. The Sample Return Capsule encloses the collector samples in the centre (not shown).

body mounted payload and one return capsule. The MIRKA based return capsule has a diameter of 1.1 m and is located in the centre of the S/C bus. The collector modules are placed around the sample return capsule which contains the sample holder (Fig. 6.9).

The scientific success of SARIM is related to the quality of the subsequent laboratory analysis of dust samples extracted from the collectors. Contemporary interstellar dust has never been analysed in terrestrial laboratories so far. Therefore all kind of information that can be retrieved from returned samples is of great value for astronomers and planetary scientists, and can, in principle, not be foreseen. First analyses of the dust grains should try to focus on four major issues: isotopic composition, inorganic chemical composition, organic chemical composition and mineralogical/petrologic composition. Each of these issues requires specific techniques and has its special demands on sample properties.

DuneXpress and SARIM have common scientific goals. DuneXpress is a highly cost-effective small mission of high scientific return, of course, without sample return. On the other side, SARIM answers the same questions by its in-situ instrumentation and provides sample return of cosmic dust but at a much higher cost and increased risk. *DuneXpress and SARIM open a new window to the dusty universe, that will provide unprecedented information on cosmic dust – the tools for Dust Astronomy are defined.*

The successful space mission Cassini demonstrated the potential of state-of-the-art dust instrumentation by its many discoveries. Now, advanced sensor technologies open a new window for the exploration of our universe.

Bibliography

- N. Altobelli, S. Kempf, M. Landgraf, R. Srama, V. Dikarev, H. Krüger, G. Moragas-Klostermeyer, and E. Grün. Cassini between Venus and Earth: Detection of interstellar grains. *J. Geophys. Res.*, 108(A10):7–1, 2003.
- N. Altobelli, S. Kempf, H. Krüger, M. Landgraf, M. Roy, and E. Grün. Interstellar dust flux measurements by the Galileo dust instrument between the orbits of Venus and Mars. *J. Geophys. Res.*, 110:7102–+, July 2005a. doi: 10.1029/2004JA010772.
- N. Altobelli, S. Kempf, H. Krüger, M. Landgraf, R. Srama, and E. Grün. In-Situ Monitoring of Interstellar Dust in the Inner Solar System. In C. C. Popescu and R. J. Tuffs, editors, *AIP Conf. Proc. 761: The Spectral Energy Distributions of Gas-Rich Galaxies: Confronting Models with Data*, pages 149–+, April 2005b.
- N. Altobelli, E. Grün, and M. Landgraf. A new look into the Helios dust experiment data: Presence of interstellar dust inside the Earth's orbit. *Astron. Astrophys.*, 448:243–252, 2006.
- S. Amari and K. Lodders. Pre-solar grains from supernovae and novae. In Karel A. van der Hucht, editor, *Highlights of Astronomy*, volume 14, pages 349–353. Intern. Astronomical Union, 2006.
- S. Amari, X. Gao, L. R. Nittler, and E. Zinner. Presolar grains from novae. *Astrophys. Journ.*, 551:1065–1072, 2001.
- S. Auer. *Interplanetary Dust*, chapter Instrumentation, pages 387–438. Springer, 2001.
- S. Auer. Two high resolution velocity vector analyzers for cosmic dust particles. *Rev. Sci. Instrum.*, 46:127–135, 1975.
- S. Auer, E. Grün, R. Srama, S. Kempf, and R. Auer. The charge and velocity detector of the Cosmic Dust Analyser on Cassini. *Planetary and Space Science*, 50:773–779, 2002.
- H. U. Auster, I. Apathy, G. Berghofer, A. Remizov, R. Roll, K. H. Fornacon, K. H. Glassmeier, G. Haerendel, I. Hejja, E. Kührt, W. Magnes, D. Moehlmann, U. Motschmann, I. Richter, H. Rosenbauer, C. T. Russell, J. Rustenbach, K. Sauer, K. Schwingenschuh, I. Szemerey, and R. Waesch. Romap: Rosetta magnetometer and plasma monitor. *Space Sci. Rev.*, 128:221–240, 2007.
- W. J. Baggaley. Advanced Meteor Orbit Radar observations of interstellar meteoroids. *J. Geophys. Res.*, 105: 10353–10362, May 2000. doi: 10.1029/1999JA900383.
- M. Baguhl, E. Grün, and M. Landgraf. In Situ Measurements of Interstellar Dust with the ULYSSES and Galileo Spaceprobes. *Space Science Reviews*, v.78, Issue 1/2, p.165-172., 78:165–172, 1996.
- M. Banaszekiewicz and A. V. Krivov. Hyperion as a Dust Source in the Saturnian System. *Icarus*, 129:289–303, October 1997. doi: 10.1006/icar.1997.5781.
- U. Beckmann. *Dynamik von Staubteilchen in Saturns E-Ring*. phdthesis, Universität Heidelberg, 2008.
- O.E. Berg and F.F. Richardson. The pioneer 8 cosmic dust experiment. *The Review of Scientific Instruments*, 40: 1333, 1968.
- F. Bertoldi, C. L. Carilli, P. Cox, X. Fan, M. A. Strauss, A. Beelen, A. Omont, and R. Zylka. Dust emission from the most distant quasars. 2003. URL <http://hal.archives-ouvertes.fr/hal-00005416/en/>.

Bibliography

- A. C. A. Boogert and P. Ehrenfreund. Interstellar Ices. In A. N. Witt, G. C. Clayton, and B. T. Draine, editors, *Astrophysics of Dust*, volume 309 of *Astronomical Society of the Pacific Conference Series*, pages 547–+, May 2004.
- J. Bradley, Z. Rong Dai, R. Erni, N. Browning, G. Graham, P. Weber, J. Smith, I. Hutcheon, H. Ishii, S. Bajt, C. Floss, F. Stadermann, and S. Sandford. An astronomical 2175 Å feature in interplanetary dust particles. *Science*, 307(5707):244–247, 2005.
- D. E. Brownlee and Stardust Mission Team. Science Results from the Stardust Comet Sample Return Mission: Large Scale Mixing in the Solar Nebula and the Origin of Crystalline Silicates in Circumstellar Disks. In *Bulletin of the American Astronomical Society*, volume 38 of *Bulletin of the American Astronomical Society*, pages 953–+, December 2006.
- M. J. Burchell, M. J. Cole, S. F. Lascelles, M. A. Khan, Chr. Barthet, S. A. Wilson, D. B. Cairns, and S. P. Armes. Acceleration of conducting polymer-coated latex particles as projectiles in hypervelocity impact experiments. *J. Phys. D*, 32:1719–1728, 1999.
- Burchell, M.J., M. J. Willis, Armes, S.P., Khan, M.A., M. J. Percy, and Perruch C. Impact ionisation experiments with low density conducting polymer-based micro-projectiles as analogues of solar system dusts. *Plan. Space Sci.*, 50:1025–1035, 2002.
- Burchell, M.J., G. Graham, and A. T. Kearsley. Cosmic dust collection in aerogel. *Annual Review of Earth and Planetary Science*, 34:385–418, 2006.
- L. Colangeli, J. J. Lopez Moreno, P. Palumbo, J. Rodriguez, E. Bussoletti, V. Della Corte, F. Esposito, M. Heranz, J. M. Jeronimo, A. Lopez-Jimenez, E. Mazzotta Epifani, R. Morales, E. Palomba, A. Rotundi, S. Vergara, and the inter. GIADA team. Giada: The grain impact analyser and dust accumulator for the rosetta space mission. *Adv. Space Res.*, 39(3):446–450, 2007.
- M. J. Devlin, P. A. R. Ade, I. Aretxaga, J. J. Bock, E. L. Chapin, M. Griffin, J. O. Gundersen, M. Halpern, P. C. Hargrave, D. H. Hughes, J. Klein, G. Marsden, P. G. Martin, P. Mauskopf, L. Moncelsi, C. B. Netterfield, H. Ngo, L. Olmi, E. Pascale, G. Patanchon, M. Rex, D. Scott, C. Semisch, N. Thomas, M. D. P. Truch, C. Tucker, G. S. Tucker, M. P. Viero, and D. V. Wiebe. Over half of the far-infrared background light comes from galaxies at $z > 1.2$. *Nature*, 458:737–739, April 2009. doi: 10.1038/nature07918.
- H. Dietzel, G. Eichhorn, H. Fechtig, E. Grun, H.-J. Hoffmann, and J. Kissel. The HEOS 2 and HELIOS micrometeoroid experiments. *Journal of Physics E Scientific Instruments*, 6:209–17, March 1973.
- J. Dorschner. *Interplanetary Dust*, chapter Interstellar Dust and Circumstellar Disks, pages 727–786. Springer, 2001.
- J. Dorschner and T. Henning. Dust metamorphosis in the galaxy. *Astron. and Astrophys. Rev.*, 6(4):271–333, 1995.
- S. P. Driver, C. C. Popescu, R. J. Tuffs, A. W. Graham, J. Liske, and I. Baldry. The energy output of the universe from 0.1 to 1000 microns. *Appl. Phys. Jour.*, L101, 2008.
- E. Dwek. The Evolution of the Elemental Abundances in the Gas and Dust Phases of the Galaxy. In E. P. Smith and A. Koratkar, editors, *Science With The NGST*, volume 133 of *Astronomical Society of the Pacific Conference Series*, pages 249–+, 1998.
- E. L. Gibb, D. C. B. Whittet, W. A. Schutte, A. C. A. Boogert, J. E. Chiar, P. Ehrenfreund, P. A. Gerakines, J. V. Keane, A. G. G. M. Tielens, E. F. van Dishoeck, and O. Kerkhof. An Inventory of Interstellar Ices toward the Embedded Protostar W33A. *Astrophys. J.*, 536:347–356, June 2000. doi: 10.1086/308940.

- B. J. Goldsworthy, M. J. Burchell, M. J. Cole, S. P. Armes, M. A. Khan, S. F. Lascelles, S. F. Green, J. A. M. McDonnell, R. Srama, and S. W. Bigger. Time of flight mass spectra of ions in plasmas produced by hyper-velocity impacts of organic and mineralogical microparticles on a cosmic dust analyser. *Astron. Astrophys.*, 409:1151–1167, October 2003. doi: 10.1051/0004-6361:20031087.
- J. R. Göller, E. Grün, and D. Maas. Calibration of the DIDSY-IPM dust detector and application to other impact ionisation detectors on board the P/Halley probes. *Astron. Astrophys.*, 187:693–698, 1987.
- J.R. Göller and E. Grün. Calibration of the galileo/ulysses dust detectors with different projectile materials and at varying impact angles. *Planetary and Space Science*, 37(10):1197–1206, 1989.
- I. S. Grant and W. R. Phillips. *Elements of Physics*. Number ISBN 0-19-851878-1. Oxford Univ. Press, 2005.
- A. L. Graps, E. Grün, H. Svedhem, H. Krüger, M. Horanyi, A. Heck, and S. Lammers. Io as a source of the jovian dust streams. *Nature*, 405:48–50, 2000.
- J. M. Greenberg, A. Li, C. X. Mendoza-Gomez, W. A. Schutte, P. A. Gerakines, and M. de Groot. Approaching the Interstellar Grain Organic Refractory Component. *Astrophys. J. Lett.*, 455:L177+, December 1995. doi: 10.1086/309834.
- E. Grün and M. Landgraf. Collisional consequences of big interstellar grains. *J. Geophys. Res.*, 105:10291–10298, 2000.
- E. Grün, H. Fechtig, R. H. Giese, J. Kissel, D. Linkert, D. Maas, J. A. M. McDonnell, G. E. Morfill, G. Schwehm, and H. A. Zook. The ulysses dust experiment. *Astron. Astrophys. Suppl. Ser.*, 92:411–423, 1992a.
- E. Grün, H. Fechtig, M.S. Hanner, J. Kissel, B.-A. Lindblad, D. Linkert, D. Maas, G.E. Morfill, and H.A. Zook. The galileo dust detector. *Space Science Reviews*, 60:317–340, 1992b.
- E. Grün, H. A. Zook, M. Baguhl, A. Balogh, S. J. Bame, H. Fechtig, R. Forsyth, M. S. Hanner, M. Horányi, K. K. Khurana, J. Kissel, M. Kivelson, B. A. Lindblad, D. Linkert, G. Linkert, I. Mann, J. A. M. McDonnell, G. E. Morfill, J. L. Phillips, C. Polanskey, G. Schwehm, N. Siddique, P. Staubach, J. Svestka, and A. Taylor. Discovery of jovian dust streams and interstellar grains by the ulysses spacecraft. *Nature*, 362:428–430, 1993.
- E. Grün, B. Gustafson, I. Mann, M. Baguhl, G. E. Morfill, P. Staubach, A. Taylor, and H. A. Zook. Interstellar dust in the heliosphere. *Astron. Astrophys.*, 286:915–924, June 1994.
- E. Grün, M. Landgraf, M. Horanyi, J. Kissel, H. Krüger, R. Srama, H. Svedhem, and P. Whithnell. Techniques for galactic dust measurements in the heliosphere. *Jour. of Geophys. Res.*, 105:10403–10410, 2000.
- E. Grün, B. A. S. Gustafson, S. Dermott, and H. Fechtig. *Interplanetary Dust*. 2001.
- E. Grün, S. Kempf, H. Krüger, G. Moragas-Klostermeyer, and R. Srama. Dust astronomy. *Meteoritics & Planetary Science*, 38:5208–+, 2003.
- E. Grün, Srama, R., Altobelli, N., K. Altwegg, J. Carpenter, L. Colangeli, K. H. Glassmeier, S. Helfert, H. Henkel, M. Horanyi, A. Jäckel, S. Kempf, M. Landgraf, McBride, N., Moragas-Klostermeyer, G., P. Palumbo, H. Scholten, A. Srowig, Z. Sternovsky, and X. Vo. Dunexpress. *Experimental Astronomy*, 23(3):981–999, 2009.
- D. A. Gurnett, E. Gruen, S. C. Gallagher, W. S. Kurth, and F. L. Scarf. Micron-sized particles detected near saturn by the voyager plasma wave instrument. *Icarus*, 53:236–254, 1983.
- D. P. Hamilton. Jupiter’s gossamer rings explained. *AAS/Division for Planetary Sciences Meeting Abstracts*, 35, 2003.
- J. K. Hillier, N. McBride, S. F. Green, S. Kempf, and R. Srama. Modelling CDA mass spectra. *Planet. Space Sci.*, 54:1007–1013, August 2006. doi: 10.1016/j.pss.2006.05.013.

Bibliography

- J. K. Hillier, S. F. Green, N. McBride, N. Altobelli, F. Postberg, S. Kempf, J. P. Schwanethal, R. Srama, J. A. M. McDonnell, and E. Grün. Interplanetary dust detected by the cassini cda chemical analyser. *Icarus*, 2007a. in press.
- J. K. Hillier, S. F. Green, N. McBride, J. P. Schwanethal, F. Postberg, R. Srama, S. Kempf, G. Moragas-Klostermeyer, J. A. M. McDonnell, and E. Grün. The composition of Saturn's E ring. *Mon. Not. Roy. Astron. Soc.*, 377:1588–1596, June 2007b. doi: 10.1111/j.1365-2966.2007.11710.x.
- J. K. Hillier, S. Sestak, Green, S.F., Postberg, F., Srama, R., and M. Tieloff. The production of platinum-coated silicate nanoparticle aggregates for use in hyper-velocity impact experiments. *Jour. of Geophys. Res.*, page in press, 2009.
- C. D. Hines, O. Krause, G. H. rieke, X. Fan, M. Blaylock, and G. Neugebauer. Spitzer observations of high-redshift qsos. *Astrophys. Journ.*, 641:L85–L88, 2006.
- H.-J. Hoffmann, H. Fechtig, E. Grün, and J. Kissel. Messungen des Mikrometeoritenflusses im Erde-Mond-System mit dem HEOS 2-Satelliten. *Mitteilungen der Astronomischen Gesellschaft Hamburg*, 36:67–+, 1975.
- M. Horányi. Dust stream from Jupiter and Saturn. *Phys. of Plasmas*, 7(10):3847–3850, 2000.
- M. Horányi, A. Juhasz, and G. E. Morfill. Large-scale structure of saturn's e-ring. *Geophys. Res. Lett.*, 35(4): 4203, February 2008. doi: 10.1029/2007GL032726.
- M. Horanyi, V. Hoxie, D. James, A. Poppe, C. Bryant, B. Grogan, B. Lamprecht, J. Mack, F. Bagenal, S. Batiste, N. Bunch, T. Chanthawanich, F. Christensen, M. Colgan, T. Dunn, G. Drake, A. Fernandez, T. Finley, G. Holland, A. Jenkins, C. Krauss, E. Krauss, O. Krauss, M. Lankton, C. Mitchell, M. Neeland, T. Reese, K. Rash, G. Tate, C. Vaudrin, and J. Westfall. The student dust counter on the new horizons mission. *New Horizons*, pages 387–402, 2009. URL http://dx.doi.org/10.1007/978-0-387-89518-5_13.
- M. Horanyi, Z. Sternovsky, E. Grün, Srama, R., M. Lankton, and D. Gathright. The lunar dust experiment (ldex) on the lunar atmosphere and dust environment explorer (ladee) mission. In *40th Lunar and Planetary Science Conf. LPSC, Texas*, page id 1741, 2009.
- F. Hörz, R. Bastien, J. Borg, J. P. Bradley, J. C. Bridges, D. E. Brownlee, M. J. Burchell, M. Chi, M. J. Cintala, Z. R. Dai, Z. Djouadi, G. Dominguez, T. E. Economou, S. A. J. Fairey, C. Floss, I. A. Franchi, G. A. Graham, S. F. Green, P. Heck, P. Hoppe, J. Huth, H. Ishii, A. T. Kearsley, J. Kissel, J. Leitner, H. Leroux, K. Marhas, K. Messenger, C. S. Schwandt, T. H. See, C. Snead, F. J. Stadermann, T. Stephan, R. Stroud, N. Teslich, J. M. Trigo-Rodríguez, A. J. Tuzzolino, D. Troadec, P. Tsou, J. Warren, A. Westphal, P. Wozniakiewicz, I. Wright, and E. Zinner. Impact Features on Stardust: Implications for Comet 81P/Wild 2 Dust. *Science*, 314:1716–, December 2006. doi: 10.1126/science.1135705.
- J. E. Howard, H. R. Dullin, and M. Horanyi. Stability of halo orbits. *Phys. Rev. Letters*, 84(15):3244–3247, 2000.
- S. Hsu. *Modeling the dynamics of saturnian dust streams*. PhD thesis, University Heidelberg, 2010.
- D. H. Humes. Results of Pioneer 10 and 11 meteoroid experiments - Interplanetary and near-Saturn. *J. Geophys. Res.*, 85:5841–5852, November 1980.
- D. H. Humes, J. M. Alvarez, R. L. O'Neal, and W. H. Kinard. The interplanetary and near-jupiter meteoroid environments. *J. Geophys. Res.*, 79:3677, 1974.
- E. Igenbergs, A. Huedepohl, K. T. Uesugi, T. Hayashi, H. Svedhem, H. Iglseider, G. Koller, A. Glasmachers, E. Grün, G. Schwehm, H. Mizutani, A. Fujimura, T. Yamamoto, H. Araki, N. Ishii, K. Yamakoshi, and K. Nogami. *Origin and Evolution of Interplanetary Dust*, chapter The Munich Dust Counter - A cosmic dust experiment on board of the MUSES-A mission of Japan, pages 45–48. Kluwer, Dordrecht, 1991.

- E. Igenbergs, S. Sasaki, R. Münzenmayer, H. Ohashi, G. Färber, F. Fischer, A. Glasmachers, E. Grün, Y. Hamabe, H. Iglseider, D. Klinge, H. Miyamoto, W. Naumann, K. Nogami, G. Schwehm, H. Svedhem, and K. Yamakoshi. The mars dust counter. *Earth Planets Space*, 50:241–245, 1998.
- W.-H. Ip and V.W. Chow. On hypervelocity impact phenomena of microdust and nano x-ray flares in cometary comae. *Icarus*, 130(1):217–221, 1997.
- D. James. *Operating Principles and Applications of PVDF Dust Detectors in Space*. PhD thesis, University of Colorado, 2009.
- A. P. Jones. Dust formation, propagation and survival in the ISM. In A. Wilson, editor, *ESA Special Publication*, volume 577 of *ESA Special Publication*, pages 239–244, January 2005.
- A.P. Jones, A.G.G.M. Tielens, and D.J. Hollenbach. Grain Shattering in Shocks: The Interstellar Grain Size Distribution. *Astrophys. J.*, 469:740–+, 1996.
- J. Jones and M. G. Poole. Gravitational focusing and shielding of meteoroid streams. *Mon. Not. R. Astron. Soc.*, 375(925-930), 2007.
- M. Jura. Astrophysical implications of the laboratory studies of pre-solar material. In T. J. Bernatowicz and E. K. Zinner, editors, *American Institute of Physics Conf. Proc.*, volume 402, page 379, 1996.
- S. Kempf. *Saturnian Dust: Rings, Ice Volcanoes, and Streams*. Habilitation, Univ. Braunschweig, 2007.
- S. Kempf. Interpretation of high rate dust measurements with the Cassini dust detector CDA. *Planet. Space Sci.*, 2007. in press.
- S. Kempf, R. Srama, N. Altobelli, S. Auer, V. Tschernjawski, J. Bradley, M.E. Burton, S. Helfert, T.V. Johnson, H. Krüger, G. Moragas-Klostermeyer, and E. Grün. Cassini between Earth and asteroid belt: First in-situ charge measurements of interplanetary grains. *Icarus*, 171:317–335, 2004.
- S. Kempf, R. Srama, M. Horányi, M. Burton, S. Helfert, G. Moragas-Klostermeyer, M. Roy, and E. Grün. High-velocity streams of dust originating from Saturn. *Nature*, 433:289–291, 2005a.
- S. Kempf, R. Srama, F. Postberg, M. Burton, S. F. Green, S. Helfert, J. K. Hillier, N. McBride, J. A. M. McDonnell, G. Moragas-Klostermeyer, M. Roy, and E. Grün. Composition of saturnian stream particles. *Science*, 307:1274–1276, 2005b.
- S. Kempf, U. Beckmann, R. Srama, M. Horanyi, S. Auer, and E. Grün. The electrostatic potential of E ring particles. *Planet. Space Sci.*, 54:999–1006, August 2006. doi: 10.1016/j.pss.2006.05.012.
- S. Kempf, U. Beckmann, G. Moragas-Klostermeyer, F. Postberg, R. Srama, T. Economou, J. Schmidt, F. Spahn, and E. Grün. The e ring in the vicinity of enceladus i: Spatial distribution and properties of the ring particles. *Icarus*, 193(2):420–437, 2008.
- S. Kempf, U. Beckmann, and R. Srama. How the enceladus dust plumes form saturn’s e ring. *Icarus*, (revised), 2009.
- S. J. Kim. Gas sensors based on paschen’s law using carbon nanotubes as electron emitters. *Jour. Physics D: Appl. Phys.*, 39(3026-3029), 2006.
- J. Kissel. The giotto particulate impact analyzer. *ESA SP*, 1077, 1986.
- J. Kissel, R. Z. Sagdeev, J. L. Bertaux, V. N. Angarov, J. Audouze, J. E. Blamont, K. Büchler, E. N. Evlanov, H. Fechtig, M. N. Fomenkova, H. von Hoerner, N. A. Inogamov, V. N. Khromov, W. Knabe, F. R. Krueger, Y. Langevin, V. B. Leonas, A. C. Lvasseur-Regourd, G. G. Managadze, S. N. Podkolzin, V. D. Shapiro, S. R. Tabaldyev, and B. V. Zubkov. Composition of comet halley dust particles from vega observations. *Nature*, 321:280–282, 1986.

Bibliography

- J. Kissel, A. Glasmachers, E. Grün, H. Henkel, H. Höfer, G. Haerendel, H. von Hoerner, K. Hornung, E. K. Jessberger, F. R. Krueger, D. Möhlmann, J. M. Greenberg, Y. Lnagevin, J. Silen, D. Brownlee, B. C. Clark, M. S. Hanner, F. Hoerz, S. Sandford, Z. Sekanina, P. Tsou, and N. G. Utterback. Cometary and interstellar dust analyzer for comet wild 2. *Jour. of Geophys. Res.*, 108(E10):8114, 2003.
- J. Kissel, F. R. Krueger, J. Silen, and B. C. Clark. The cometary and interstellar dust analyzer at comet 81p/wild 2. *Science*, 304(5678):1774–1776, 2004.
- A. V. Krivov and D. P. Hamilton. Martian dust belts: waiting for discovery. *Icarus*, 128:335–353, 1997.
- A. V. Krivov, I. Wardinski, F. Spahn, H. Krüger, and E. Grün. Dust on the Outskirts of the Jovian System. *Icarus*, 157:436–455, June 2002. doi: 10.1006/icar.2002.6848.
- A. V. Krivov, M. Sremčević, F. Spahn, V. V. Dikarev, and K. V. Kholshchevnikov. Impact-generated dust clouds around planetary satellites: spherically symmetric case. *Planet. Space Sci.*, 51:251–269, March 2003.
- H. Krüger. *Jupiter's dust disc, an astrophysical laboratory*. Habilitation, Ruprecht-Karls-Univ. Heidelberg, 2003.
- H. Krüger, A. V. Krivov, D. P. Hamilton, and E. Grün. Detection of an impact-generated dust cloud around ganymed. *Nature*, 399, 1999.
- H. Krüger, A. V. Krivov, and E. Grün. A dust cloud of Ganymede maintained by hypervelocity impacts of interplanetary micrometeoroids. *Planet. Space Sci.*, 48:1457–1471, December 2000.
- H. Krüger, P. Geissler, M. Horányi, A.L. Graps, S. Kempf, R. Srama, G. Moragas-Klostermeyer, R. Moissl, T.V. Johnson, and E. Grün. Jovian dust streams: A monitor of io's volcanic plume activity. *Geophys. Res. Let.*, 30: 3–1, 2003.
- H. Krüger, G. Linkert, D. Linkert, R. Moissl, and E. Grün. Galileo long-term dust monitoring in the jovian magnetosphere. *Planet. Space Sci.*, 53:1109–1120, September 2005. doi: 10.1016/j.pss.2005.04.009.
- M. Küppers and the Triple F team. Triple f – a comet nucleus sample return mission. *Exp. Astron.*, 23:809–847, 2009.
- M. Landgraf. Modeling the motion and distribution of interstellar dust inside the heliosphere. *J. Geophys. Res.*, 105:10303–10316, 2000.
- M. Landgraf, K. Augustsson, E. Grün, and B. Å. S. Gustafson. Deflection of the local interstellar dust flow by solar radiation pressure. *Science*, 286:2319–2322, December 1999. doi: 10.1126/science.286.5448.2319.
- M. Landgraf, W.J. Baggaley, E. Grün, H. Krüger, and G. Linkert. Aspects of the mass distribution of interstellar dust grains in the solar system from in situ measurements. *J. Geophys. Res.*, 105:10343–10352, 2000.
- M. Landgraf, H. Krüger, N. Altobelli, and E. Grün. Penetration of the heliosphere by the interstellar dust stream during solar maximum. *Journal of Geophysical Research (Space Physics)*, 108:5–1, August 2003. doi: 10.1029/2003JA009872.
- S.F. Lascelles, S.P. Armes, P.A. Zhdan, S.J. Greaves, A.M. Brown, J.F. Watts, S.R. Leadley, and S.Y. Luk. Synthesis and characterization of micrometer-sized, polypyrrole-coated polystyrene latexes: verification of a 'core-shell' morphology. *Journal of Material Chemistry*, 7(8):1349–1355, 1997.
- N. R. Lomb. Least-squares frequency analysis of unequally spaced data. *Astrophys. and Space Sci.*, 39:447–462, 1976.
- F. Markwick-Kemper, S. C. Gallagher, D. C. Hines, and J. Bouwman. Dust in the wnd: crystalline silicates, corundum, and periclase in pg 2112+059. 2007. URL <http://edoc.mpg.de/358660>.

- J. A. M. McDonnell, W. M. Alexander, W. M. Burton, E. Bussoletti, D. H. Clark, G. C. Evans, S. T. Evans, J. G. Firth, R. J. L. Grard, E. Grün, M. S. Hanner, D. W. Hughes, E. Igenbergs, H. Kuczera, B. A. Lindblad, J.-C. Mandeville, A. Minafra, D. Reading, A. Ridgeley, G. H. Schwehm, T. J. Stevenson, Z. Sekanina, R. F. Turner, M. K. Wallis, and J. C. Zarnecki. The giotto dust impact detection system. *ESA SP-1077*, page 85ff, 1986.
- J. A. M. McDonnell, P. L. Lamy, and G. S. Pankiewicz. Physical properties of cometary dust. In R. L. Newburn, Jr., M. Neugebauer, and J. Rahe, editors, *IAU Colloq. 116: Comets in the post-Halley era*, volume 167 of *Astrophysics and Space Science Library*, pages 1043–1073, 1991.
- J. A. M. McDonnell, M. J. Burchell, S. F. Green, N. McBride, B. A. M. Vaughan, J. C. Zarnecki, P. Tsou, M. S. Hanner, A. J. Tuzzolino, F. DiDonna, D. E. Brownlee, and B. Clark. The stardust dust flux monitor. *Adv. Space Res.*, 25(2):335–338, 2000.
- S. Messenger and R. M. Walker. Evidence for molecular cloud material in meteorites and interplanetary dust. In E. K. Zinner and T. J. Bernatowicz, editors, *American Institute of Physics Conference Series*, volume 402 of *American Institute of Physics Conference Series*, pages 545–564, March 1997. doi: 10.1063/1.53336.
- N. Meyer-Vernet, M. Maksimovic, A. Czechowski, I. Mann, I. Zouganelis, K. Goetz, M. L. Kaiser, O. C. St. Cyr, J. L. Bougeret, and S. D. Bale. Dust detection by the wave instrument on stereo: nanoparticles picked up by the solar wind? *Solar Physics*, 256:463–474, 2009.
- C. J. Mitchell, J. E. Colwell, and M. Horanyi. Tenuous ring formation by the capture of interplanetary dust at saturn. *J. Geophys. Res.*, 110:A09218, 2005.
- A. Mocker. *Time-of-flight mass spectrometry of laser induced plasmas and of hyper-velocity dust impacts*. PhD thesis, Univ. Heidelberg, in prep., 2009.
- Th. Müller, B. K. Sinha, and K. P. Rohr. Direction-selective free expansion of laser-produced plasmas from planar targets. *Phys. Rev. E*, 67(2):026415, Feb 2003. doi: 10.1103/PhysRevE.67.026415.
- H. Mutschke, A. C. Anderson, C. Jaeger, Th. Henning, and A. Braatz. Optical data of meteoritic nano-diamonds from far ultraviolet to far-infrared wavelengths. *Astron. and Astrophys.*, 423(983), 2004.
- K. Nogami, M. Fujii, H. Ohashi, T. Miyachi, S. Sasaki, S. Hasegawa, H. Yano, H. Shibata, T. Iwai, S. Minami, S. Takechi, E. Grün, and R. Srama. Development of the mercury dust monitor (mdm) onboard the bepicolombo mission. *Plan. Space Sci.*, page in press, 2009.
- O. A. Novodvorsky, O. D. Khramova, E. O. Filippova, C. Wenzel, and J. W. Bartha. Energy distribution of ions in plasma formed by laser ablation of metallic nb and ta targets. *Optics and Lasers in Engineering*, 32(5):449 – 457, 1999. ISSN 0143-8166. doi: DOI:10.1016/S0143-8166(00)00013-0.
- V. Ossenkopf and T. Henning. Dust opacities for protostellar cores. *Astron. Astrophys.*, 291:943–959, November 1994.
- M. A. Perkins, J. A. Simpson, and A. J. Tuzzolino. A cometary and interplanetary dust experiment on the vega spacecraft missions to halley’s comet. *Nucl. Instr. and Methods in Physics Res.*, A239:310–323, 1985.
- F. Postberg. *A new view on the composition of dust in the Solar System: Results from the Cassini Dust Detector*. PhD thesis, University Heidelberg, 2007.
- F. Postberg, S. Kempf, R. Srama, S. F. Green, J. K. Hillier, N. McBride, and E. Grün. Composition of jovian dust stream particles. *Icarus*, 183:122–134, July 2006. doi: 10.1016/j.icarus.2006.02.001.
- F. Postberg, S. Kempf, J. K. Hillier, R. Srama, S. F. Green, N. McBride, and E. Grün. The e ring in the vicinity of enceladus ii: Signatures of enceladus in the elemental composition of e-ring particles. *Icarus*, 193(2): 438–454, 2008.

Bibliography

- F. Postberg, S. Kempf, D. Rost, T. Stephan, R. Srama, M. Tieloff, A. Mocker, and M. Goerlich. Discriminating contamination from particle components in spectra of cassini's dust detector cda. *Plan. Space Sci.*, 57:1359–1374, 2009a.
- F. Postberg, S. Kempf, J. Schmidt, N. Brilliantov, A. Beinsen, B. Abel, U. Buck, and R. Srama. Sodium salts in e-ring ice grains from an ocean below the surface of enceladus. *Nature*, 459:1098–1101, 2009b.
- M. Rachev. *A new time-of-flight spectrometer for impact generated ions*. PhD thesis, Ruperto-Carola University of Heidelberg, 2005.
- M. Rachev, A. Srowig, and E. Grün. Large area mass analyser. *Nucl. Instr. and Methods in Physics Res. A*, 535 (1-2):162–164, 2004.
- P.R. Ratcliff, F. Gogu, E. Grün, and R. Srama. Plasma production by secondary impacts: implications for velocity measurements by in-situ dust detectors. *Adv. Space Res.*, 17(12):111–115, 1995.
- P.R. Ratcliff, M.J. Burchell, M.J. Cole, T.W. Murphy, and F. Allahdadi. Experimental measurements of hypervelocity impact plasma yield and energetics. *International Journal of Impact Engineering*, 20:663–674, 1997.
- P. L. Read, T. E. Dowling, and G. Schubert. Saturn's rotation period from its atmospheric planetary-wave configuration. *Nature*, 460:608–610, 2009.
- C. Roundy. Propagation factor quantifies laser beam performance. *Laser Focus World*, 12, 1999.
- R. Z. Sagdeev, R. Pellat, F. Salo, and et al. *Venus-Halley Mission*. Imprimerie Louis-Jean, Gap., 1985.
- S. Sasaki. Dust ring/torus around mars, waiting for detection by nozomi. *The Moon and Mars*, 23(11):1907–1910, 1999.
- J. Schmidt, N. Brilliantov, F. Spahn, and S. Kempf. Formation of enceladus' dust plume. *Nature*, 2007. in press.
- E. Sedlmayr and D. Krüger. *Astrophysical Implications of the Laboratory Study of Presolar Materials*, chapter Formation of dust particles in cool stellar outflows. American Institute of Physics, 1997.
- M. R. Showalter, J. N. Cuzzi, and S. M. Larson. Structure and particle properties of saturn's e ring. *Icarus*, 94: 451, 1991.
- J. A. Simpson and A. J. Tuzzolino. Polarized polymer films as electronic pulse detectors of cosmic dust particles. *Nucl. Instr. Meth.*, 187(A236), 1985.
- G. C. Sloan, M. Matsuura, A. A. Zijlstra, E. Lagadec, M. A. T. Groenewegen, P. R. Wood, C. Szyszka, J. Bernard-Salas, and J. Th. van Loon. Dust formation in a galaxy with primitive abundances. *Science*, 323(5912): 353–355, 1 2009/1/16.
- F. Spahn, J. Schmidt, N. Albers, M. Hörning, M. Makuch, M. Seiß, S. Kempf, R. Srama, V. Dikarev, S. Helfert, G. Moragas-Klostermeyer, A. V. Krivov, M. Sremčević, A. J. Tuzzolino, T. Economou, and E. Grün. Cassini Dust Measurements at Enceladus and Implications for the Origin of the E Ring. *Science*, 311:1416–1418, March 2006. doi: 10.1126/science.1121375.
- R. Srama. *Kombination von Messsystemen zur simultanen Messung der Eigenschaften von kosmischen Staub*. PhD thesis, Technische Universität München, Garching, 2000a.
- R. Srama. *Vom Cosmic-Dust-Analyser zur Modellbeschreibung wissenschaftlicher Raumsonden*. PhD thesis, Technische Universität München, 2000b.
- R. Srama and S. Auer. Low charge detector for the monitoring of hyper-velocity micron-sized dust particles. *Meas. Sci. Technol.*, 19:doi:10.1088/0957-0233/19/5/055203, 2008.

- R. Srama, T.J. Ahrens, N. Altobelli, S. Auer, J.G. Bradley, M. Burton, V.V. Dikarev, T. Economou, H. Fechtig, M. Görlich, M. Grande, A. Graps, E. Grün, O. Havnes, S. Helfert, M. Horányi, E. Igenbergs, E.K. Jeßberger, T.V. Johnson, S. Kempf, A.A. Krivov, H. Krüger, A. Mocker-Ahlreep, G. Moragas-Klostermeyer, P. Lamy, M. Landgraf, D. Linkert, G. Linkert, F. Lura, J.A.M. McDonnell, D. Möhlmann, G.E. Morfill, M. Müller, M. Roy, G. Schäfer, G. Schlotzhauer, G.H. Schwehm, F. Spahn, M. Stübig, J. Svestka, V. Tschernjawski, A.J. Tuzzolino, R. Wäsch, and H.A. Zook. The Cassini Cosmic Dust Analyser. *Space Sci. Rev.*, 114:465–518, 2004a.
- R. Srama, M. Rachev, A. Srowig, S. Kempf, G. Moragas-Klostermeyer, H. Krüger, S. Auer, A. Glasmachers, and E. Grün. Dust astronomy with a dust telescope. In *Proc. 37th ESLAB Symposium, Tools and Technologies for Future Planetary Exploration*, volume 543 of *ESA SP*, Noordwijk, Netherlands, 2004b.
- R. Srama, M. Rachev, A. Srowig, V. Dikarev, S. Helfert, S. Kempf, D. Linkert, G. Moragas-Klostermeyer, and E. Grün. Performance of an advanced dust telescope. *ESA SP*, 587:171–176, 2005a.
- R. Srama, A. Srowig, M. Rachev, E. Grün, G. Moragas-Klostermeyer, T. Conlon, D. Harris, S. Auer, A. Glasmachers, S. Helfert, H. Linnemann, and V. Tschernjawski. Development of an advanced dust telescope. *Earth Moon and Planets*, 95:211–220, 2005b.
- R. Srama, S. Kempf, G. Moragas-Klostermeyer, S. Helfert, T. J. Ahrens, N. Altobelli, S. Auer, U. Beckmann, J. G. Bradley, M. Burton, V. V. Dikarev, T. Economou, H. Fechtig, S. F. Green, M. Grande, O. Havnes, J. K. Hillier, M. Horanyi, E. Igenbergs, E. K. Jessberger, T. V. Johnson, H. Krüger, G. Matt, N. McBride, A. Mocker, P. Lamy, D. Linkert, G. Linkert, F. Lura, J. A. M. McDonnell, D. Möhlmann, G. E. Morfill, F. Postberg, M. Roy, G. H. Schwehm, F. Spahn, J. Svestka, V. Tschernjawski, A. J. Tuzzolino, R. Wäsch, and E. Grün. In situ dust measurements in the inner Saturnian system. *Planet. Space Sci.*, 54:967–987, August 2006. doi: 10.1016/j.pss.2006.05.021.
- R. Srama, T. Stephan, E. Grün, N. Pailer, A. T. Kearsley, A. Graps, R. Laufer, P. Ehrenfreund, N. Altobelli, K. Altwegg, S. Auer, W. J. Baggaley, M. J. Burchell, J. Carpenter, L. Colangeli, F. Esposito, S.F. Green, H. Henkel, M. Horanyi, A. Jäckel, S. Kempf, N. McBride, G. Moragas-Klostermeyer, H. Krüger, P. Palumbo, A. Srowig, M. Trieloff, P. Tsou, Z. Sternovsky, O. Zeile, and H. P. Röser. Sample return of interstellar matter (sarim). *Experimental Astronomy*, 23:303–328, 2009a.
- R. Srama, W. Woiwode, F. Postberg, S.P. Armes, S. Fujii, D. Dupin, J. Ormond-Prout, Z. Sternovsky, S. Kempf, G. Moragas-Klostermeyer, A. Mocker, and E. Grün. Mass spectrometry of hyper-velocity impacts of organic micrograins. *Rapid Commun. Mass Spectrom.*, page in press, 2009b.
- M. Sremčević, A. V. Krivov, H. Krüger, and F. Spahn. Impact-generated dust clouds around planetary satellites: model versus Galileo data. *Planet. Space Sci.*, 53:625–641, May 2005. doi: 10.1016/j.pss.2004.10.001.
- S. N. Srivastava, B. K. Sinha, and K. P. Rohr. Ions and ion-energy spectra of a collisional laser plasma produced from multi-species targets of aluminium and titanium. *J. Phys. B: At. Mol. Opt. Phys.*, 39:3073–3086, 2006.
- A. Srowig. *Trajectory sensor and readout electronics of a cosmic Dust Telescope*. PhD thesis, Ruperto-Carola University of Heidelberg, 2005.
- Z. Sternovsky, K. Amyx, G. Bano, M. Landgraf, M. Horanyi, S. Knappmiller, S. Robertson, E. Grün, Srama, R., and S. Auer. Large area mass analyzer instrument for the chemical analysis of interstellar dust particles. *REV. Sci. Instr.*, 78, 2007.
- M. Stübig. *New insights in impact ionization and in time-of-flight mass spectroscopy with micrometeoroid detectors by improved impact simulations in the laboratory*. PhD thesis, Heidelberg University, 2002.
- M. Stübig, G. Schäfer, Tra-Mi Ho, Ralf Srama, and Eberhard Grün. Laboratory simulation improvements for hypervelocity micrometeorite impacts with a new dust particle source. *Plan. Space Sci.*, 49:853–858, 2001.

Bibliography

- H. Svedhem. Cosmic dune - an observatory for the study of interstellar and interplanetary dust. Mission Definition Report ESA-SCI(2001)5, ESA, 2005. URL <http://solarsystem.estec.esa.nl/Flexi2005/CosmicDUNE.pdf>.
- M. V. Sykes and R. Greenberg. The formation and origin of the IRAS zodiacal dust bands as a consequence of single collisions between asteroids. *Icarus*, 65:51–69, January 1986. doi: 10.1016/0019-1035(86)90063-1.
- K.-U. Thiessenhusen, H. Krüger, F. Spahn, and E. Grün. Dust Grains around Jupiter-The Observations of the Galileo Dust Detector. *Icarus*, 144:89–98, March 2000. doi: 10.1006/icar.1999.6277.
- A. G. G. M. Tielens. Interstellar Depletions and the Life Cycle of Interstellar Dust. *Astrophys. J.*, 499:267–+, May 1998. doi: 10.1086/305640.
- A. J. Verbiscer, M. F. Skrutskie, and D. P. Hamilton. Saturn’s largest ring. *Nature*, 8515:1–3, 2009.
- S. J. Weidenschilling. Formation of Planetesimals and Accretion of the Terrestrial Planets. *Space Science Reviews*, 92:295–310, April 2000. doi: 10.1023/A:1005259615299.
- A. J. Westphal, C. Snead, A. Butterworth, G. A. Graham, J. P. Bradley, S. Bajt, G. G. Patrick, G. Bench, S. Brennan, and P. Pianetta. Aerogel keystones: Extraction of complete hypervelocity impact events from aerogel collectors. *Meteoritics & Planetary Science*, 39:1375–1386, 2004.
- D.C.B. Whittet. *Dust in the galactic environment/Second Edition*. Institute of Physics Publ., Bristol, 2002.
- M. E. Zolensky, T. J. Zega, H. Yano, S. Wirick, A. J. Westphal, M. K. Weisberg, I. Weber, J. L. Warren, M. A. Velbel, A. Tsuchiyama, P. Tsou, A. Toppani, N. Tomioka, K. Tomeoka, N. Teslich, M. Taheri, J. Susini, R. Stroud, T. Stephan, F. J. Stadermann, C. J. Snead, S. B. Simon, A. Simionovici, T. H. See, F. Robert, F. J. M. Rietmeijer, W. Rao, M. C. Perronnet, D. A. Papanastassiou, K. Okudaira, K. Ohsumi, I. Ohnishi, K. Nakamura-Messenger, T. Nakamura, S. Mostefaoui, T. Mikouchi, A. Meibom, G. Matrajt, M. A. Marcus, H. Leroux, L. Lemelle, L. Le, A. Lanzirotti, F. Langenhorst, A. N. Krot, L. P. Keller, A. T. Kearsley, D. Joswiak, D. Jacob, H. Ishii, R. Harvey, K. Hagiya, L. Grossman, J. N. Grossman, G. A. Graham, M. Gounelle, P. Gillet, M. J. Genge, G. Flynn, T. Ferroir, S. Fallon, D. S. Ebel, Z. R. Dai, P. Cordier, B. Clark, M. Chi, A. L. Butterworth, D. E. Brownlee, J. C. Bridges, S. Brennan, A. Brearley, J. P. Bradley, P. Bleuet, P. A. Bland, and R. Bastien. Mineralogy and Petrology of Comet 81P/Wild 2 Nucleus Samples. *Science*, 314:1735–, December 2006. doi: 10.1126/science.1135842.

About the Author

The main part of this work addresses the Cosmic Dust Analyser (CDA) of the Cassini mission to Saturn. I am leading this project now for many years and I accompanied all steps of this project since its beginning. After the study of physics (Dipl.-Ing.), I joined the CDA project in 1992 in the definition and design phase. During this time, I was responsible to ensure the measurement capabilities of CDA with respect to the scientific requirements. I tested the instrument functionality at the dust accelerator and I defined electronic requirements for signal acquisition. Then, I was leading the calibration phase which was performed at the accelerator laboratories in Munich and Heidelberg. After the instrument integration phase, I wrote ground software in order to decode and analyse the binary data of the instrument. Instrument operations, security and archiving documents were prepared shortly before the launch of Cassini in 1997. Finally, the science planning and instrument operations phase of Cassini started to become very active. I was the instrument operations team lead and investigation team lead for many years until I became the Principal Investigator of the CDA instrument onboard Cassini in 2001. Today, CDA science planning, operations, data analysis and evaluation, publications and outreach activities are in the focus of my activities. If not stated otherwise, all tests and data evaluations described in this work were executed by the author.

The success of Cassini-CDA with its advanced detection methods and discoveries lead to new ideas in dust sensor technology. Proposals in instrument development (Dust Telescope) were successful and I lead the design, manufacturing and laboratory tests of the new *Trajectory Sensor* and the biggest high-resolution ToF mass spectrometer of the world: our *Large Area Mass Analyser*. My laboratory tests showed the enormous potential of the new methods (sensitivity of <1 fC, mass resolution ≈ 200), and we defined them as Tools for *Dust Astronomy*³. The ESA proposal *Cosmic DUNE*⁴, a dust observatory using the spacecraft bus of Mars Express, was successful and this mission was investigated by ESA in a phase A study. Later, I worked in close cooperation with Eberhard Grün at the *DuneXpress* proposal and I lead the mission proposal *Sample Return of Interstellar Matter* in the framework of ESA's Cosmic Vision 2015-2025 program.

Furthermore, I am responsible for the Dust Accelerator Facility at the Max Planck Institute for Nuclear Physics in Heidelberg. International dust scientists are using this worldwide unique facility since many years. New ESA, NASA and JAXA projects are supported by myself by calibration and data analysis activities (BepiColombo, LADEE-LDEX).

³The former dust group leader, Eberhard Grün, received the Kuiper Prize in 2002 for his leadership in Dust Astronomy

⁴DUst Near Earth

Bibliography

All graphics and plots of this work were prepared by myself, if not stated otherwise. My main programming tool is IDL, enabling me, to work effectively with binary data as well as with object graphics. Major **publications** relevant for this work are (ref. journals):

Srama, R. et al., *The Cassini Cosmic Dust Analyzer*. Space Sci. Rev., 114(1-4):465–518, 2004

Srama, R. et al., *Laboratory detection of organic dust with the Cassini-CDA instrument*. In Horneck, G and LevasseurRegourd, AC and Rabin, BM and Slenzka, KB, editor, SPACE LIFE SCI., volume 33 of Adv. in Space Res., 1289–1293, 2004

Srama, R. et al., *Development of an advanced dust telescope*. Earth Moon and Planets, 95(1-4): 211–220, 2005

Srama, R. et al., *Performance of an advanced dust telescope*. In Danesy, D, editor, Proc. of the 4th Europ. Conf. on Space Debris, volume 587 of ESA SP, 171–176, 2005

Srama, R., *DUNE-eXpress - Dust astronomy with ConeXpress*. In Worms, JC and Anselmo, L, editor, Small Bodies in the Solar System; Space Debris, volume 38 of Adv. in Space Res., 2093–2101, 2006

Srama, R. et al., *In situ dust measurements in the inner Saturnian system*. Planet. and Space Sci., 54(9-10):967–987, 2006

Srama, R. et al., *Laboratory tests of the Large Area Mass Analyser*. In Workshop on Dust in Planetary Systems, volume 643 of ESA SP, 209–212, 2007

Srama, R. et al., *A trajectory sensor for sub-micron sized dust*. In Workshop on Dust in Planetary Systems, volume 643 of ESA SP, 213–217, 2007

Srama, R. and Siegfried Auer. *Low-charge detector for the monitoring of hyper-velocity micron-sized dust particles*. Meas. Sci. and Techn., 19(5), doi:10.1088/0957-0233/19/5/055203, 2008

Srama, R. et al., *Sample return of interstellar matter (SARIM)*. Experimental Astron., 23(1): 303–328, 2009

Srama, R. et al., *Mass spectrometry of hyper-velocity impacts of organic micrograins*. Rap. Comm. in Mass Spectrom., in press, 2009



The author in front of the large dust spectrometer LAMA in the dust accelerator laboratory.

Acknowledgements

The Cassini project is currently supported by the DLR grant 50 OH 0304, and the Dust Telescope was developed under the DLR grant 50 OO 0201. The author highly acknowledges the efficient and accurate work of the DLR group in Berlin (lead by Dr. Franz Lura), Gerrit Pahl and the MPI-K electronics group performed during the development and integration phase of the Cassini Dust Analyser.

This work would not have been accomplished without the never ending patience and support of my wife Iris – thank you so much! But there are many people who awaited the finish of this work and who supported me with their ideas, patience and inspirations or simply mitigated the work load.

Eberhard Grün supported me in many aspects for many years and it is just a pleasure to work with him over such a long time.

I want to thank Georg Moragas-Klostermeyer for his unbelievable hard effort to keep track of all the operation tasks of CDA – without him, the cosmic dust group would not have the data in our hands we are famous of today. We all use these data day by day and often not think about all the efforts standing behind this. Telecons, negotiations with the sequence leads and commanding takes a lot of time in a big international project like Cassini with its Distributed Operations system.

In this regard, I thank Gudrun Linkert for her reliable instrument monitoring and data processing - we could always count on her accurate work and she often was the first person discovering our instrument anomalies we had in the last years. Mou Roy and Marcia Burton at JPL provide an efficient interface to the Cassini project and they supported us in many ways mitigating especially the time difference between california and germany. Stefan Helfert is never to stop to improve our CDA flight software and his turn-around time in solving computer problems is outstanding.

Sascha Kempf is an inspiration in person – and he is fast. His countless ideas and his hard programming work for CDA ground data analysis, science planning and archiving is not to beat. I want to thank Uwe, Jessica, Stefan, Anna, Frank, Sean, Veerle and Peter which makes each day a pleasure to come to work.

Fortunately, we have a great support of our dust accelerator laboratory by Sebastian Bugiel, Günter Matt, Günter Baust, Gerhard Schäfer and Rainhard Hofacker. The laboratory is the second heart of our group enabling us to improve our instrumentation and to participate in international projects.

I am thankful to Hans-Peter Röser, René Laufer and Kathrin Schwalb who are supporting me in many ways to run and prepare our future projects.

Bibliography

Finally, I want to remember of Dietmar Linkert, our former instrument engineer, who was leading the electronics development of our Cassini CDA instrument. He passed away in 2009 much too early! His laboratory and management work made the Heidelberg dust group famous around the world, and he would be delighted to see, that his efforts were not useless and that new developments and challenges are waiting for us : *Dust Astronomy*.

A Appendix

A.1 Cassini-Huygens Mission Facts

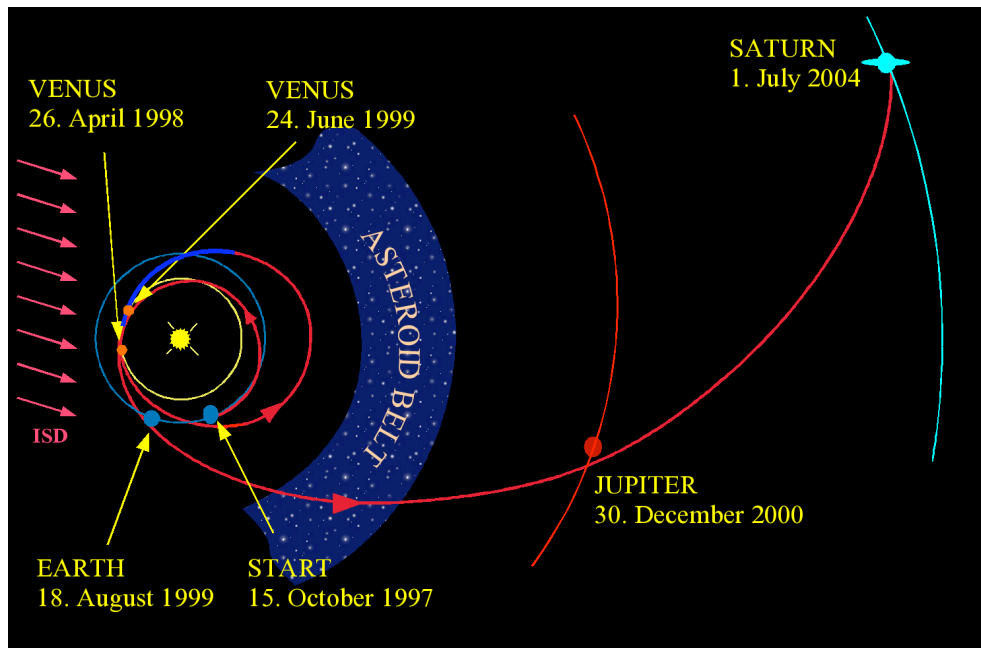


Figure A.1: Cassini interplanetary trajectory and interstellar dust direction.

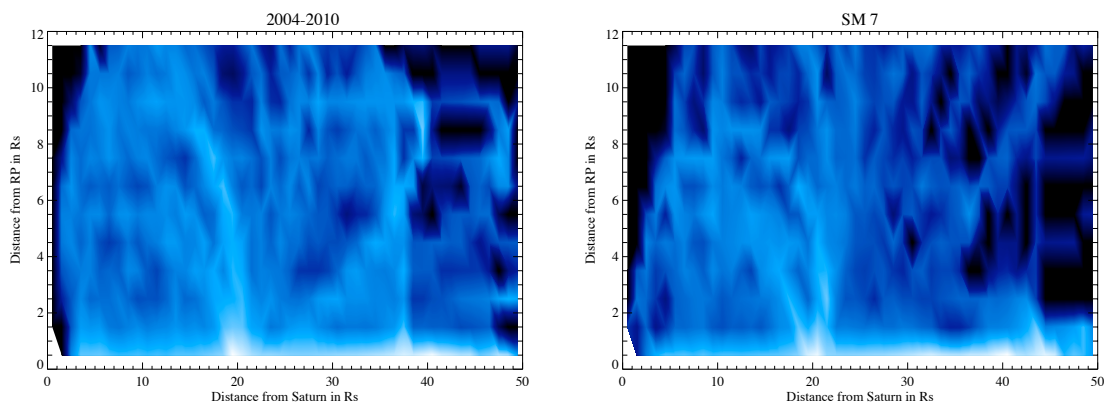


Figure A.2: Integrated Cassini dwell period (arb. units) in distance-altitude segments in the time frame 2004-182 to 2010-182 (Cassini prime tour + Extended mission, left plot), and in the time frame 2010-182 to 2017-180 (Cassini equinox mission, right plot). The numerous flybys at Titan lead to a high dwell time at 20 R_S distance in the ring plane.

A.1.1 CDA Pointing Statistics

For a global measurement of the saturnian dust environment with an in-situ instrument two requirements have to be met. First, the Cassini trajectory has to pass a wide range of distances and latitudes (compare Fig. A.2), and second, the dust instrument has to be able to point towards the dust RAM direction. How good was the CDA pointing in the Cassini tour? How much time the CDA boresight stayed within 30° of the dust RAM direction?

Here, the reconstructed CDA boresight profile in relation to the prograde circular dust RAM was investigated. Fig. A.3 shows the integrated time of CDA pointing towards the dust RAM direction. The parameters taken are distance from the ring plane in R_S (different coloured curves) and distance from Saturn. The prograde pointing of CDA is reaching almost 50% of the total Cassini dwell time in certain regions. In the ring plane (altitudes between 0 and $0.5 R_S$) the pointing coverage varied between 25% and 40%. These high values were only achieved by the optimised CDA articulation profile.

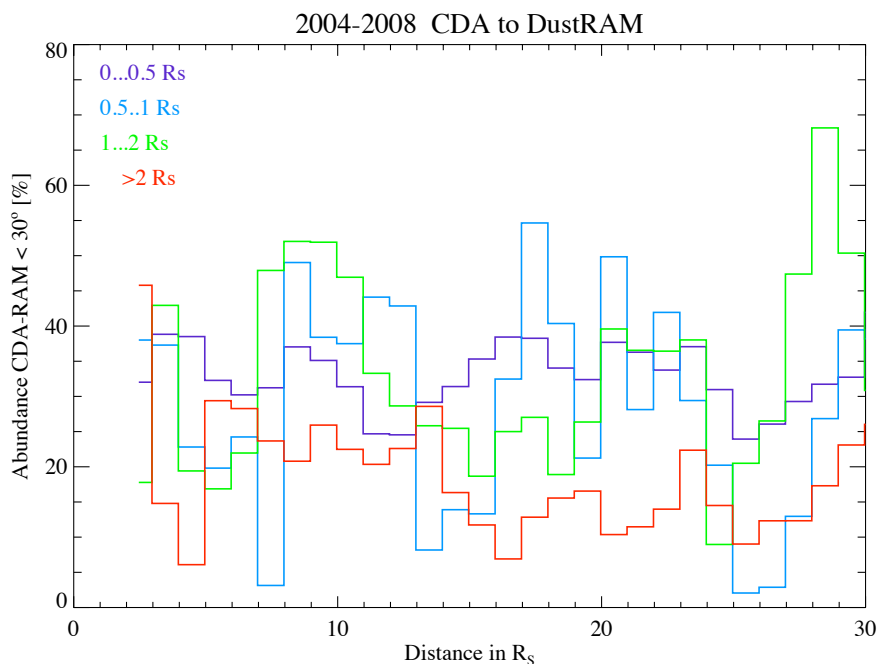


Figure A.3: CDA pointing statistics of the Cassini prime tour (2004-2008). The analysis is based on the reconstructed CDA pointing profile. High dust RAM coverage was achieved due to the optimised CDA articulation profile. Each curve shows the pointing coverage for limited distances from the ring plane.

A.1.2 Cassini Enceladus Flyby Geometry

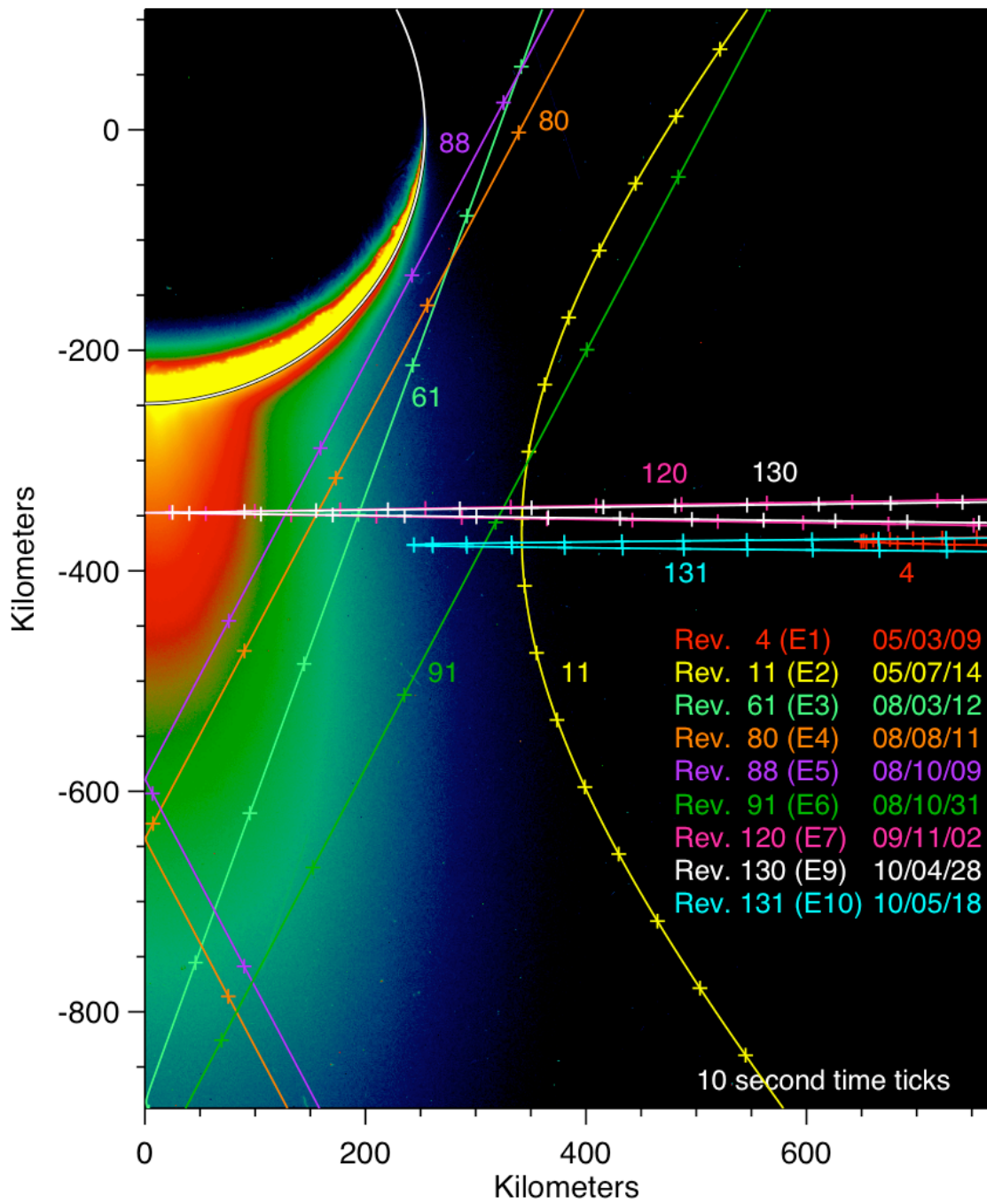


Figure A.4: Cassini trajectory in the moving Enceladus coordinate frame. (courtesy J. Spencer, SWRI, Boulder,USA)

A.2 Cosmic Dust Analyser Functional Diagram

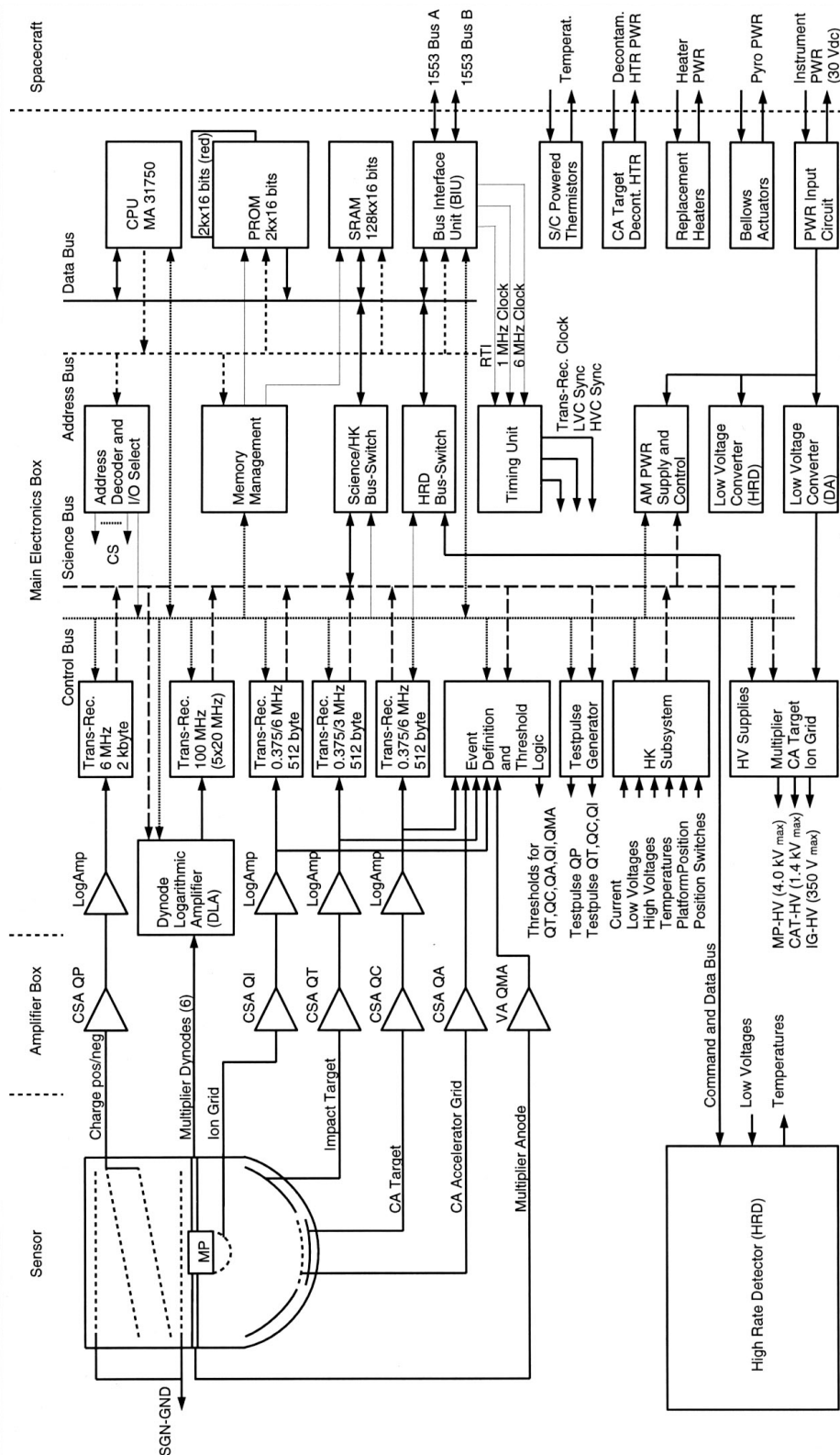


Figure A.5: CDA functional diagram (D. Linkert).

A.3 The Dust Accelerator Facility

The Dust Accelerator is a worldwide unique facility which allows the investigation of hyper-velocity dust impacts onto various materials.¹ The facility is designed to study the interaction of micro-grain impacts with target materials like planetary analogues, metals or interplanetary dust collector materials. The accelerator provides a laboratory platform for the study the physics of interplanetary dust impacts and the design and calibration of dust sensor instrumentation for space based applications (Fig. A.6).

Dust grain materials from nano to micron sizes are accelerated using a 2 MV Van-de-Graaff accelerator to velocities between 1 and 60 km s⁻¹ (compare Fig. 3.12). These velocities are relevant to the study the dust properties in planetary rings of the giant planets and impact ejecta processes on the surfaces of small bodies (asteroids, comets) as well as moons and planetary surfaces.



Figure A.6: 2 MV Van-de-Graaff dust accelerator. Left: Dust source and acceleration electrodes. Right: Accelerator tank operating at approximately 16 bar.

The accelerated micro-grains pass focussing and steering electrodes and their individual speed and charge is measured by sensitive beam detectors working with charge induction [Srama and Auer, 2008]. A special control hard- and software, the Particle Selection Unit, determines the grain speed and mass and selects individual dust grains on the basis of a speed and mass window given by the experimenter. A big thermal vacuum chamber with a diameter of 1.4 m allows for a simulation of the space environment (Fig. A.7). The accelerator can be operated in a single-shot mode and in a continuous mode. Dust materials include metal powders like iron or coated microspheres like glass, organic microspheres (polystyrene) or even minerals (pyroxen, anorthite) [Stübig et al., 2001, Hillier et al., 2009].

Studies at the dust accelerator are multi-disciplinary and are relevant in the field of planetary, physics, chemistry, astrophysics and astrobiology. Phenomena under study include

¹The accelerator is part of the EuroPlaNet Trans National Access program: <http://www.tna.europlanet-ri.eu/>

A Appendix

dust charging, dust magnetosphere interactions, dust impact flashes and the possibility of obtaining compositional measurements of impact plasma plumes. Such data has been shown to be of direct relevance to space missions like Galileo, Ulysses, Cassini, Rosetta, Stardust, New Horizon or BepiColombo. Future projects to the moon, to the inner Solar System (Solar Probe Plus), to the jovian system and to Saturn will carry dust instrumentation which has to be developed by applying micrometeoroid impact simulations in the laboratory.

The recent Stardust mission collected and returned samples of interplanetary and interstellar dust grains to Earth. Sample preparation and analysis requires the study and understanding of grain-collector material interaction during hyper-velocity impacts. Test and calibration of dust collectors and of in-situ dust detectors onboard interplanetary probes or Earth satellites is a major application of the facility. The laboratory generation and analysis of in-situ mass spectra of high-speed organic micro-grain impacts is essential for astrobiology studies and provide the basis for an understanding of the composition of interplanetary or interstellar micrometeoroids.

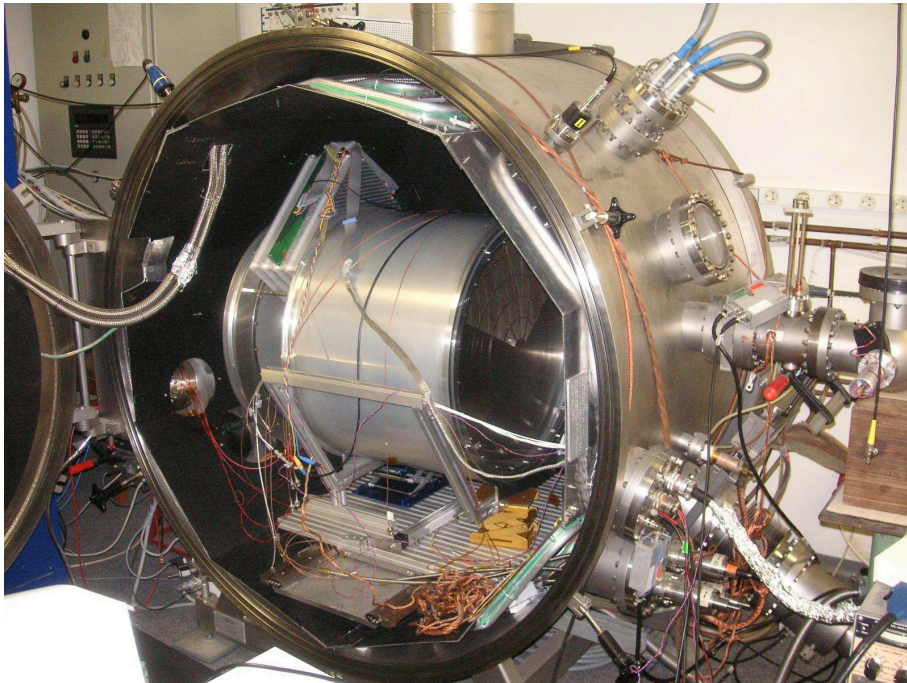


Figure A.7: Big vacuum chamber with the Dust Telescope for tests at the accelerator beam line.

A.4 Dust Analyser Calibration Tables

Table A.1: Charge to mass ratios for CAT impacts. The estimations for speeds $>100 \text{ km s}^{-1}$ show a reduced charge to mass ratio.

v [kms^{-1}]	QI/m C/kg	v km/s	QC/m C/kg
1.40	0.0182	1.15	0.0985348
1.73	0.0621	1.40	0.212548
2.03	0.143	1.64	0.623551
2.30	0.300	1.99	2.06874
2.83	0.60	2.41	5.04652
3.80	1.39	2.85	11.2257
4.6	2.49	3.46	24.9710
5.4	3.49	4.15	55.5467
6.7	8.25	5.27	109.260
8.4	25.8	6.56	184.286
9.3	38.4	8.10	422.735
11.3	67	9.78	940.4
13.2	124	11.5	1538
15.0	215	13.2	2092
17.1	311	15.5	3120
19.3	464	19.4	5103
21.0	832	22.7	7380
23.8	1586	25.9	17457
25.8	3318	29.6	45288
28.8	7848	32.0	91863
33.1	18565	35.2	231091
36.2	34339	39.7	546656
40.3	76385	43.7	1.075e+06
45.3	164771	48.6	1.989e+06
50.6	344662	55.2	4.424e+06
57.3	618206	64.2	7.695e+06
66.6	1.11e+06	97.0	3.927e+07
79.6	1.87e+06	136	16929
97.9	3.25e+06		
165	8346		

Table A.2: Charge to mass ratios for IIT impacts.

v [kms ⁻¹]	QI/m C/kg	v km/s	QT/m C/kg
1.09	0.032	1.065	0.070
1.26	0.076	1.205	0.130
1.48	0.175	1.389	0.264
1.73	0.358	1.56	0.535
2.02	0.661	1.75	0.901
2.3	1.194	2.01	1.70
2.6	1.905	2.30	3.49
2.9	3.355	2.59	6.26
3.3	5.223	2.89	10.2
3.7	7.743	3.21	15.3
4.2	12.36	3.55	22.8
4.8	16.6	3.86	31.9
5.5	22.3	4.25	46.2
6.1	26.5	4.81	64.8
7.0	34.7	5.2	77.9
7.9	44.4	5.8	93.7
9.2	51.5	6.5	116
10.9	64.2	7.4	140
12.7	70.9	8.5	173
14.8	88.4	9.9	215
16.5	128	11.1	258
18.4	209	12.7	320
20.0	368	14.6	410
21.6	649	16.0	630
23.2	1114	17.2	1031
24.7	2112	18.6	1850
26.8	3629	20.0	3421
28.4	6083	21.4	5596
30.6	10713	22.5	9152
33.2	20309	23.9	16929
35.6	31622	25.6	29445
38.8	46874	27.3	46702
42.3	66147	29.3	69654
45.8	88862	31.3	94732
49.7	116477	33.7	145701
54.7	156475	35.7	210726
61.6	195253	38.6	314289
68.8	237722	41.6	498483
77.5	296635	44.7	657419
87.3	352378	47.7	867031
97.9	418596	51.3	1.143e+06
168	11534	55.7	1.334e+06
		61.3	1.654e+06
		67.2	1.99e+06
		73.7	2.25e+06
		80.4	2.62e+06
		88.5	2.97e+06
		97.0	3.25e+06
		153	440789

Table A.3: Thresholds of the new classification scheme (2010) for the Chemical Analyser Target based on Eq. 3.37 and a grain density of 1200 kg m^{-3} .

Counter	QI [dn]	QI [C]	v in kms^{-1}	mass [kg]	diameter [μm]
A0	200	3,29E-012	6,0	2,40E-014	3,37
A0	200	3,29E-012	9,8	3,47E-015	1,77
A0	200	3,29E-012	12,5	1,33E-015	1,28
A0	200	3,29E-012	14,8	6,85E-016	1,03
A0	200	3,29E-012	16,2	4,80E-016	0,91
A1	170	1,66E-012	6	1,77E-014	3,04
A1	170	1,66E-012	9,8	2,61E-015	1,61
A1	170	1,66E-012	12,5	1,01E-015	1,17
A1	170	1,66E-012	14,8	5,25E-016	0,94
A1	170	1,66E-012	16,2	3,69E-016	0,84
A2	130	6,71E-013	6	1,18E-014	2,66
A2	130	6,71E-013	9,8	1,79E-015	1,42
A2	130	6,71E-013	12,5	7,05E-016	1,04
A2	130	6,71E-013	14,8	3,69E-016	0,84
A2	130	6,71E-013	16,2	2,61E-016	0,75
A3	100	3,31E-013	6	8,60E-015	2,39
A3	100	3,31E-013	9,8	1,34E-015	1,29
A3	100	3,31E-013	12,5	5,32E-016	0,95
A3	100	3,31E-013	14,8	2,80E-016	0,76
A3	100	3,31E-013	16,2	1,99E-016	0,68
A4	70	1,45E-013	6	5,95E-015	2,12
A4	70	1,45E-013	9,8	9,50E-016	1,15
A4	70	1,45E-013	12,5	3,82E-016	0,85
A4	70	1,45E-013	14,8	2,03E-016	0,69
A4	70	1,45E-013	16,2	1,45E-016	0,61
A5	45	5,82E-014	6	3,96E-015	1,85
A5	45	5,82E-014	9,8	6,50E-016	1,01
A5	45	5,82E-014	12,5	2,65E-016	0,75
A5	45	5,82E-014	14,8	1,42E-016	0,61
A5	45	5,82E-014	16,2	1,02E-016	0,55
A6	30	2,57E-014	6	2,75E-015	1,64
A6	30	2,57E-014	9,8	4,63E-016	0,9
A6	30	2,57E-014	12,5	1,91E-016	0,67
A6	30	2,57E-014	14,8	1,04E-016	0,55
A6	30	2,57E-014	16,2	7,46E-017	0,49
A7	20	1,03E-014	6	1,83E-015	1,43
A7	20	1,03E-014	9,8	3,17E-016	0,8
A7	20	1,03E-014	12,5	1,33E-016	0,6
A7	20	1,03E-014	14,8	7,25E-017	0,49
A7	20	1,03E-014	16,2	5,25E-017	0,44

Table A.4: Thresholds of the new classification scheme (2010) for the Impact Ionisation Target based on Eq. 3.28 and a grain density of 1200 kg m^{-3} .

Counter	QI [dn]	QI [C]	v in km s^{-1}	mass [kg]	diameter [μm]
I0	190	2,62E-012	6	1,32E-014	2,76
I0	190	2,62E-012	9,8	2,36E-015	1,55
I0	190	2,62E-012	12,5	1,01E-015	1,17
I0	190	2,62E-012	14,8	5,57E-016	0,96
I0	190	2,62E-012	16,2	4,06E-016	0,86
I1	160	1,32E-012	6	9,73E-015	2,49
I1	160	1,32E-012	9,8	1,80E-015	1,42
I1	160	1,32E-012	12,5	7,76E-016	1,07
I1	160	1,32E-012	14,8	4,34E-016	0,88
I1	160	1,32E-012	16,2	3,18E-016	0,8
I2	130	6,71E-013	6	7,22E-015	2,26
I2	130	6,71E-013	9,8	1,37E-015	1,3
I2	130	6,71E-013	12,5	6,01E-016	0,99
I2	130	6,71E-013	14,8	3,39E-016	0,81
I2	130	6,71E-013	16,2	2,50E-016	0,74
I3	100	3,31E-013	6	5,28E-015	2,03
I3	100	3,31E-013	9,8	1,03E-015	1,18
I3	100	3,31E-013	12,5	4,61E-016	0,9
I3	100	3,31E-013	14,8	2,63E-016	0,75
I3	100	3,31E-013	16,2	1,95E-016	0,68
I4	70	1,45E-013	6	3,67E-015	1,8
I4	70	1,45E-013	9,8	7,44E-016	1,06
I4	70	1,45E-013	12,5	3,37E-016	0,81
I4	70	1,45E-013	14,8	1,95E-016	0,68
I4	70	1,45E-013	16,2	1,45E-016	0,61
I5	45	5,82E-014	6	2,45E-015	1,57
I5	45	5,82E-014	9,8	5,17E-016	0,94
I5	45	5,82E-014	12,5	2,39E-016	0,72
I5	45	5,82E-014	14,8	1,40E-016	0,61
I5	45	5,82E-014	16,2	1,05E-016	0,55
I6	25	1,75E-014	6	1,44E-015	1,32
I6	25	1,75E-014	9,8	3,20E-016	0,8
I6	25	1,75E-014	12,5	1,52E-016	0,62
I6	25	1,75E-014	14,8	9,04E-017	0,52
I6	25	1,75E-014	16,2	6,85E-017	0,48
I7	14	3,04E-015	6	6,66E-016	1,02
I7	14	3,04E-015	9,8	1,59E-016	0,63
I7	14	3,04E-015	12,5	7,84E-017	0,5
I7	14	3,04E-015	14,8	4,79E-017	0,42
I7	14	3,04E-015	16,2	3,68E-017	0,39

A.5 Hyperplane Fitting of Impact Charges

The IDL² program listing below was extracted from the procedure *eva_fit3d.pro* of the program package *evalute.pro*. This program package was written by the author and reads the calibration data in order to generate plots and fits of various parameters (rise times, amplitudes, etc.) in a 2D or 3D style. The subroutine *eva_fit3d.pro* was developed to visualise and fit the dust speed v (x-axis), the charge yield Q (y-axis) and dust mass m (z-axis) with a hyperplane. The units are kms^{-1} (v), C (Q) and kg (m).

```
x1=ALOG10(x) & y1=ALOG10(y) & z1=ALOG10(z)

;limit the values and define the range of the fit:
a=WHERE(z1 GE -23 AND z1 LT -9 AND y1 GT -16 AND y1 LT -8,c)
x1=x1[a] & y1=y1[a] & z1=z1[a]
;x1,y1,z1 are all raw data points taken for the fit

;Average over small tiles (smooth), the output is x2,y2,z2
AVERAGE_3D_DATA,x1,y1,z1,x2,y2,z2,24

;prepare input format
fitinput = [TRANSPPOSE(x2),TRANSPPOSE(y2),TRANSPPOSE(z2)]

;use sfit routine of IDL: sfit: f(x,y)=SUM [kxj,i xi yi ]
;with [[k, y, y2], [x, xy, xy2], [x2, x2y, x2y2]].
;call with : result = SFIT(fitinput,deg,/irregular,kx=kx)
;If polynom degree=2 and keyword set of max_degree, then the result is: [k, y, y2, x, xy,
x2]
result = SFIT(fitinput,deg,/irregular,kx=kx,max_degree=maxdeg)

np=60 ;number of points for array field
;expand the QT charge range from 1e-11 to 1e-8 and for v to 400 km/s
MAKENXY, MIN(x1)-0.1, MAX(x1)+0.3,np, MIN(y1), MAX(y1)+3.0,np,xx,yy

t = FLTARR(np,np) ; Surface array.
;We should have: xx= FLTARR(np,np) & yy=FLTARR(np,np)
;Computation of surface plane with polynome_plane :
; FOR i=0,deg DO FOR j=0,deg DO t=t+kx[j,i]*xxi*yyj
t=POLYNOM_PLANE(kx,deg,xx,yy)

xs=MAKEN(MIN(x1), MAX(x1)+0.4, np)
ys=MAKEN(MIN(y1), MAX(y1)+3.0, np)

;Plot surface
SHADE_SURF,t,xs,ys, xrange=[0,0],yrange=[0,0], $
xcharsize=1.8, ycharsize=1.8, zcharsize=1.5, linestyle=2, /save
```

²Interactive Data Language

A Appendix

```
;Plot grid on top of surface
SURFACE,t,xs,ys, xrange=[0,0],yrange=[0,0], $
      xst=4, yst=4, zstyle=4, $ ;no axis linestyle=2, /NOERASE

;Plot data points
PLOTS,/t3d, x2,y2,z2, psym=4, col=250, thick=2

; Compute the projection of the original data points onto the surface
; zp=FLTARR(n_ELEMENTS(z2))
; Compute projected point onto surface
; FOR i=0,deg DO FOR j=0,deg DO zp = zp+kx[j,i]*x2^ i * y2^ j
zp=POLYNOM_PLANE(kx,deg,x2,y2)
;Display projected points on surface original points , projected onto surface:
PLOTS,/t3d,x2,y2,zp,psym=4,col=70,thick=2

;Draw lines between point and projected point
FOR i=0L,n_elements(x2)-1 DO BEGIN
      PLOTS, /t3d, [x2[i],x2[i]], [y2[i],y2[i]], [z2[i],zp[i]], color=80,thick=0.5
ENDFOR
```

The core function for the fit procedure is the routine *SFIT*, which has the arguments data and degree in the general call

```
result = sfit(fitinput,deg,/irregular,kx=kx,max_degree=maxdeg)
```

The data are a three-dimensional array of values to fit, and the degree specifies the highest exponent of the polynom (maximum degree of fit in one dimension). The keyword *irregular* allows a fit of unequal dimension sizes. The variable *kx* contains the array of coefficients for the polynomial function of *x* and *y*. More details can be found in the reference menu of the IDL programming language.

A.6 CDA Bench Checkout Equipment Software

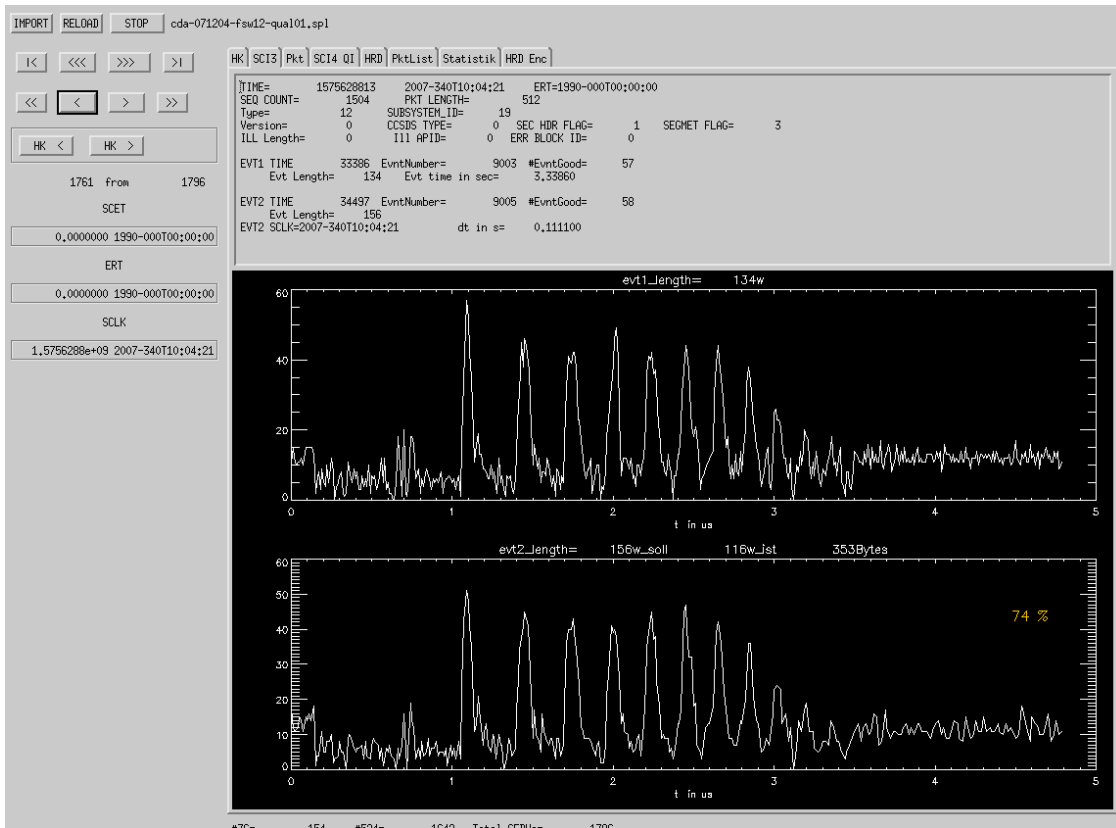


Figure A.8: CDA Bench Checkout Equipment software package BCE12 (2008). This package is used for the most recent version of the CDA flight software (version 12.2). The software was developed using the Interactive Data Language (IDL) and runs therefore on any operating system supporting IDL (Linux, MacOS, Sun, Windows). Due to the very distinct binary format and contents of the CDA data products of the flight software versions 10.x and 12.x, two different versions of the BCE program package were developed. In contrast, the program package JShow by Pentamino GmbH (not shown) is Java-based and capable to process both the data stream of flight software version 10.0 and of version 12.2.

A.7 High Rate Detector Sensitivity

The mass thresholds of the High Rate Detector are shown in Tab. A.5. The table is valid for iron particle impacts and the values were derived from Eq. 3.40. The four thresholds $m_1 \dots m_4$ are used to derive the mass distribution of impacting dust grains. The corresponding dust grain sizes are shown in Fig. 3.36. Mass thresholds for other materials like silicates (glass) would have to be derived by Eq. 3.40.

Table A.5: Mass thresholds in kg for iron dust impacts with different impact velocities. Values are given for the Low Range (LR) and the less sensitive range (High Range HR). Four different charge (mass) thresholds ($m_1 \dots m_4$) classify the impact events. The table refers to the small detector (top) and the big detector (bottom).

Detector2 : 6 μm foil (small detector, 10 cm^2)								
		v [km s^{-1}]						
		4	6	8	10	12	15	20
LR	m1	1.53E-14	5.99E-15	3.08E-15	1.84E-15	1.21E-15	7.22E-16	3.72E-16
LR	m2	8.62E-14	3.38E-14	1.74E-14	1.04E-14	6.83E-15	4.08E-15	2.10E-15
LR	m3	9.16E-13	3.59E-13	1.85E-13	1.11E-13	7.26E-14	4.34E-14	2.23E-14
LR	m4	6.46E-12	2.54E-12	1.31E-12	7.80E-13	5.12E-13	3.06E-13	1.58E-13
HR	m1	9.31E-14	3.65E-14	1.88E-14	1.12E-14	7.38E-15	4.41E-15	2.27E-15
HR	m2	5.27E-13	2.07E-13	1.06E-13	6.36E-14	4.18E-14	2.50E-14	1.29E-14
HR	m3	5.58E-12	2.19E-12	1.13E-12	6.74E-13	4.42E-13	2.64E-13	1.36E-13
HR	m4	3.91E-11	1.53E-11	7.90E-12	4.72E-12	3.10E-12	1.85E-12	9.53E-13
Detector 1 : 28 μm foil (big detector, 50 cm^2)								
		v [km s^{-1}]						
		4	6	8	10	12	15	20
LR	M1	8.93E-14	3.50E-14	1.80E-14	1.08E-14	7.08E-15	4.23E-15	2.18E-15
LR	M2	4.86E-13	1.91E-13	9.82E-14	5.87E-14	3.85E-14	2.30E-14	1.19E-14
LR	M3	5.16E-12	2.03E-12	1.04E-12	6.23E-13	4.09E-13	2.44E-13	1.26E-13
LR	M4	3.64E-11	1.43E-11	7.36E-12	4.40E-12	2.89E-12	1.73E-12	8.88E-13
HR	M1	4.66E-13	1.83E-13	9.42E-14	5.63E-14	3.70E-14	2.21E-14	1.14E-14
HR	M2	2.50E-12	9.82E-13	5.06E-13	3.02E-13	1.98E-13	1.19E-13	6.10E-14
HR	M3	2.69E-11	1.05E-11	5.43E-12	3.24E-12	2.13E-12	1.27E-12	6.55E-13
HR	M4	1.88E-10	7.39E-11	3.80E-11	2.27E-11	1.49E-11	8.92E-12	4.59E-12

A.8 High Rate Detector Noise

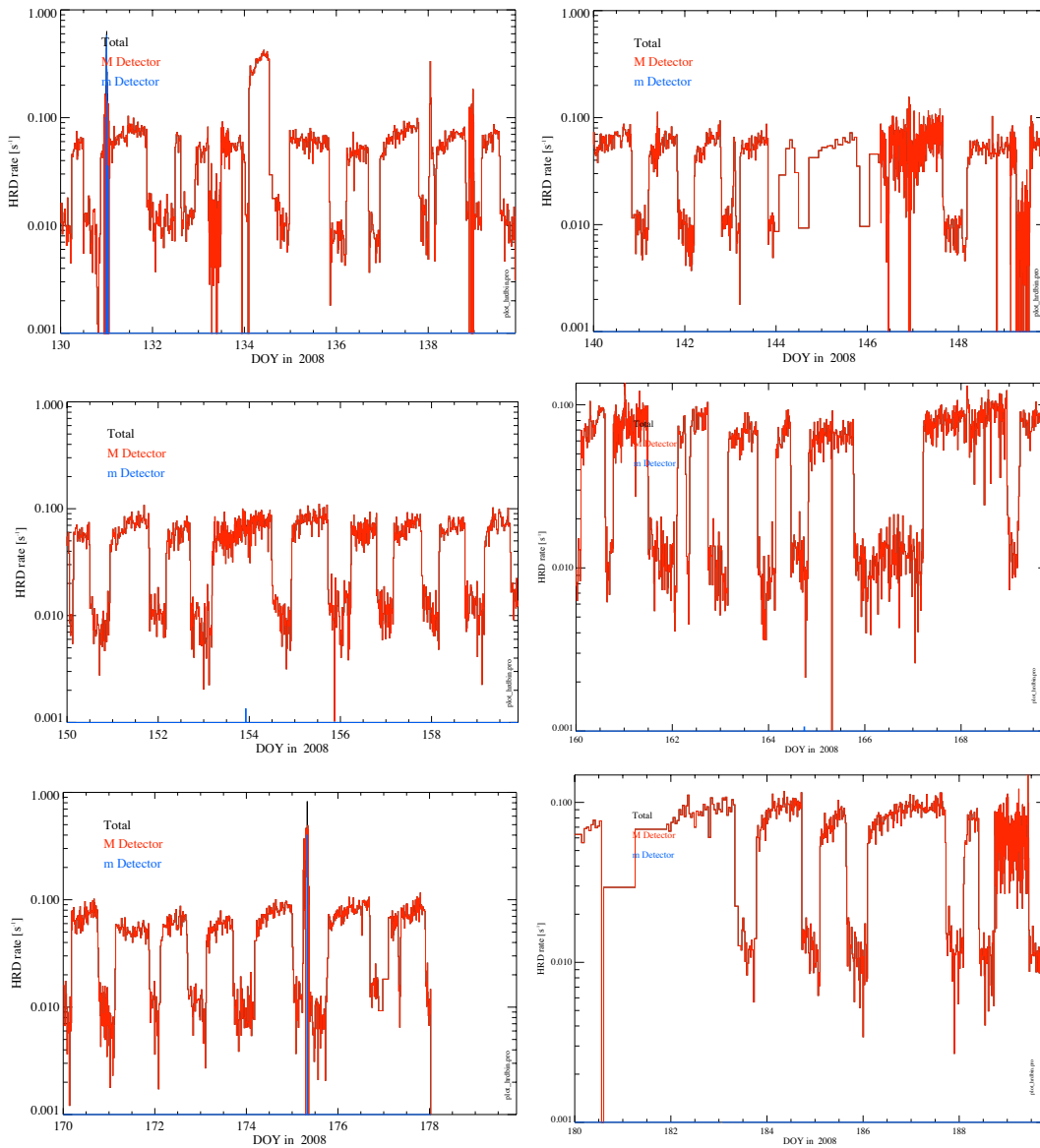


Figure A.9: Noise rate of the High Rate Detector in the year 2008 between DOY 130 and 190. Only the M1 channel of the 28 μm thick foil is affected by a characteristic pattern with two rate levels (around 0.01 s^{-1} and slightly below 0.1 s^{-1}). However, high event rates were measured during the ring plane crossings on day 131 and 175 which proofed the functionality of the sensors. The Cassini spacecraft moved on high-inclined orbits in this time frame (approx. 74°).

A.9 Measurements of Interstellar Dust

Interstellar dust entering our Solar System was already measured by in-situ interplanetary dust instruments aboard various spacecrafts. The interstellar stream was discovered by the dust detector of Ulysses [Grün et al., 1993] and it was later also seen by the dust instruments aboard Galileo [Baguhl et al., 1996], Cassini [Altobelli et al., 2003] and even Helios [Altobelli et al., 2006]. It was also shown, that the interstellar grains, which are deflected by the radiation pressure of the Sun, reach the inner Solar System and can be detected at 1 AU distance [Altobelli et al., 2005a]. Although the stream direction seems to be identical with the interstellar gas direction of 259° ecliptic longitude and 8° ecliptic latitude (J2000), local flux and directionality variations of the grains occur. The time variable Lorentz forces and radiation pressures (solar cycle) lead to a diffusion of the collimated beams. The grains have sizes between 0.01 and $1 \mu\text{m}$ with different optical properties and their interaction with the interplanetary magnetic field was described in Landgraf et al. [2003]. The forces lead to decreased dust densities behind the Sun, but only gradual effects should be observed in the upstream direction (Fig. A.10).

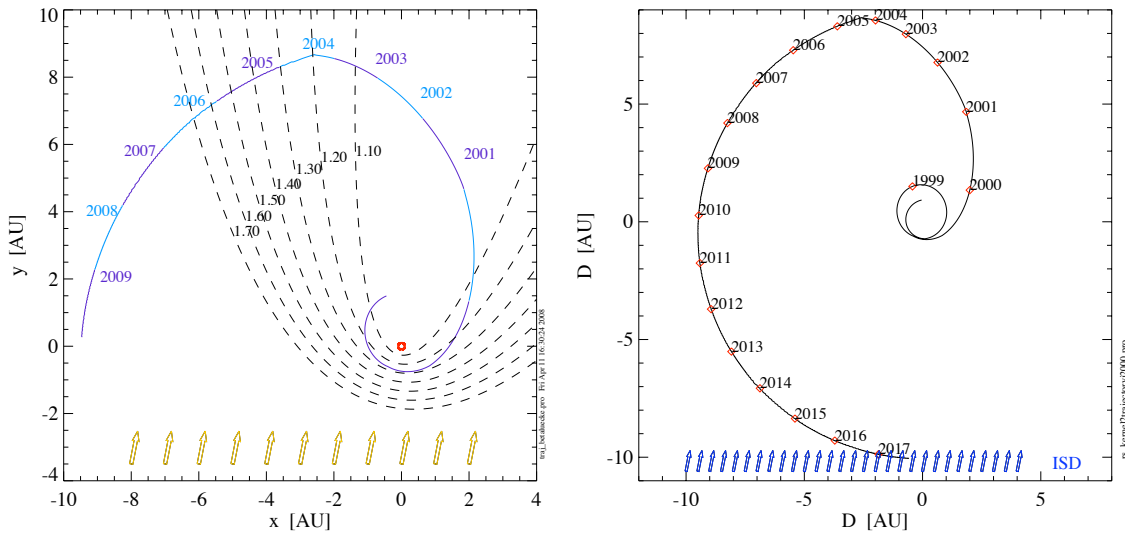


Figure A.10: Cassini trajectory and interstellar dust flux direction in an ecliptic J2000 coordinate system for the primary tour (left) and including the extended mission (right). The deflection cone of interstellar grains according to their β value (small black numbers in the left plot) is shown. The value β is defined as the ratio between solar radiation pressure and solar gravity. The region behind the Sun is depleted in interstellar grains. Dust particles with a $\beta=1$ pass the Solar System unaffected by radiation pressure and solar gravity. The effect of Lorentz forces is not shown.

What does this mean for interstellar dust measurements with Cassini? As shown in Fig. A.10, the Cassini trajectory was entering the region with diminished densities already in the year 2000. Additionally, the speed vectors of the interstellar grains and the Cassini spacecraft were almost parallel leading to low relative impact speeds and low fluxes. The situation im-

proved starting in 2005 and the highest dust densities and relative impact speeds are expected in 2008 to 2010, where Saturn moves against the interstellar flow direction. Fig. A.11 shows an overview of the relative impact velocities of interstellar grains aboard Cassini in the years 2005, 2006, 2007 and 2008. It can be seen, that the minimum speed is highest in 2008 leading also to the highest fluxes. This calculation considers a constant interstellar flux with no time variations and no gravitational focusing, and the flux and speed peaks are caused by the Cassini orbital velocities.

For a full picture of the interstellar fluxes along the Cassini trajectory, many facts would have to be considered (dust charge-to-mass ratios and optical properties, gravitational focusing of the Sun, Saturn and its moons, radiation pressure, Lorentz forces of the IPM and within Saturn's magnetosphere). Although this modelling is out of the scope of this work, the strong influence of gravitational focusing alone will be shown. Let's consider a collimated interstellar dust beam with velocities of 20 km s^{-1} , 30 km s^{-1} or 40 km s^{-1} as outlined in Fig. A.12. This figure shows schematically the focusing of a collimated beam behind Saturn. In the equatorial plane behind Saturn, strong deflection angles above 40° can occur for lower velocities at close distances.

Which deviation angles from the known interstellar direction of the dust will be observed by a spacecraft behind Saturn?

The ISD grains are described by hyperbolic orbits and the deflection angle θ_d (angle between the incoming and outgoing velocity vector) can be derived from formulas describing the conservation of energy E_{kin} and angular momentum L [Grant and Phillips, 2005]. The result is, that the deflection angle θ depends only on the semi-major axis a and the impact parameter b (Eq. A.1).

$$\tan\left(\frac{\theta}{2}\right) = \frac{a}{b} = \frac{G \cdot M_p}{h \cdot v^2} \quad (\text{A.1})$$

The semi major axis a is $a_{hyperbole} = \frac{\mu_p}{v^2}$ with the parameter $\mu_p = G \cdot M_p$ and depends on the planet mass M_p and the speed v .³ The speed of the dust grain v increases during approach and reaches a maximum at the pericentre $r = a \cdot (1 - e)$ of

$$v_{peri} = \sqrt{\frac{\mu_p}{a} \cdot \frac{1 + e}{1 - e}}.$$

We still need the eccentricity e which can be derived from the general hyperbola equation $b^2 = a^2(e^2 - 1)$. In order to calculate the deflection angle, we just need Eq. A.1. Interstellar grains with a speed $v = 26 \text{ km s}^{-1}$ and an impact parameter $b = 1.5 \cdot R_S$ have a deflection angle at Saturn of 64° . Particles with $b = 2.0 \cdot R_S$ and speeds of $v = 40 \text{ km s}^{-1}$ still have angles of $\theta = 22^\circ$. Even this simple example, taking only gravitational focusing into account, shows, that strong deviation angles from the known interstellar direction of 259° longitude and 8° latitude (upstream J2000 direction) can be observed. However, Cassini is only very short times

³Asymptotic velocity v (26 km s^{-1}), eccentricity e , $G = 6.67428 \cdot 10^{-11} \text{ m}^3 \text{ kg}^{-1} \text{ s}^{-2}$ and the planet mass $M_{saturn} = 5,685 \cdot 10^{26} \text{ kg}$.

A Appendix

close to the planet and to the focal plane which mitigates the effect. In summary, strong deviation angles of interstellar grains are possible, specifically within $20R_S$ of the planet in the downstream direction. Nevertheless, high impact speeds as given in Fig. A.11 shall occur, since Lorentz forces do not change the particle kinetic energy.

Quantitative considerations of the flux enhancements by gravitational focusing can be calculated [Jones and Poole, 2007], but their application is due to the many unknown factors difficult. In principle, enhancement factors of up to 200 are possible at distances of $4 R_S$ behind Saturn of interstellar grains with speeds of $v = 20 \text{ km s}^{-1}$ (V. Dikarev/M. Matney). At distances of $50 R_S$, this factor decreases down to the ideal values of 70.

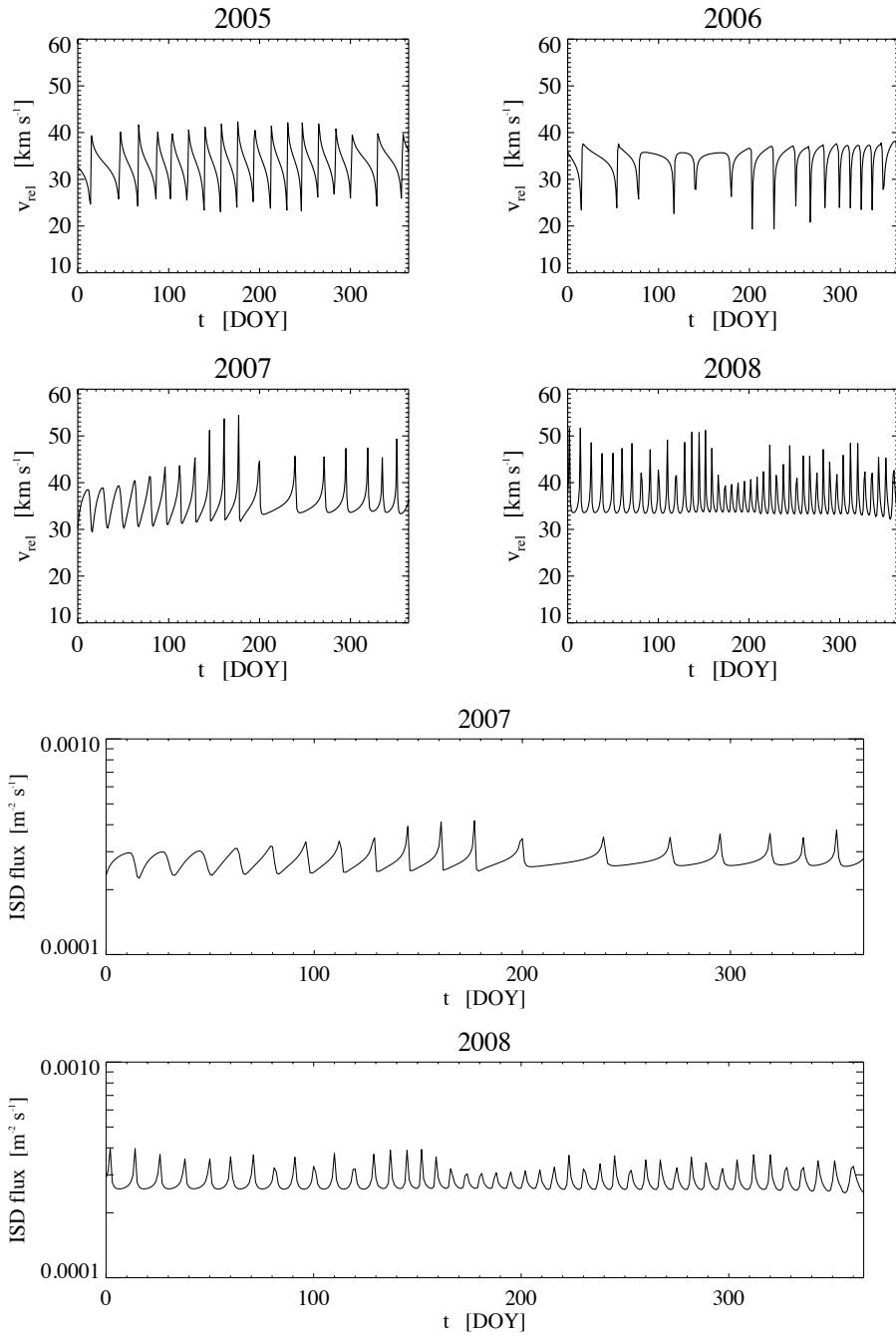


Figure A.11: Relative impact speeds and interstellar dust flux are modulated by Cassini's trajectory. A constant ISD flux and no Lorentz forces or gravitational focusing was assumed.

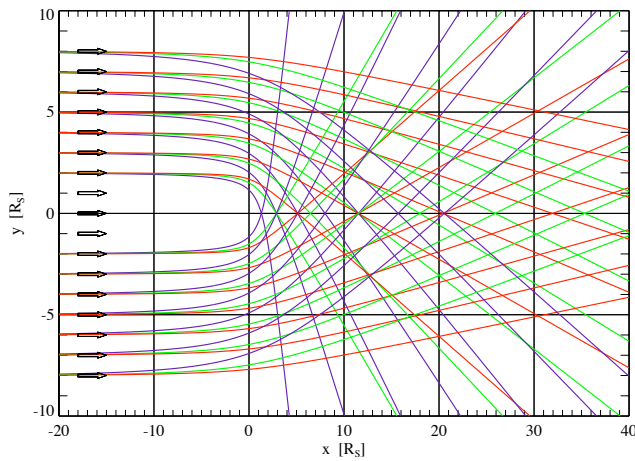


Figure A.12: Gravitational focusing of interstellar grains with 20 km s^{-1} , 30 km s^{-1} or 40 km s^{-1} behind Saturn (ideal case).

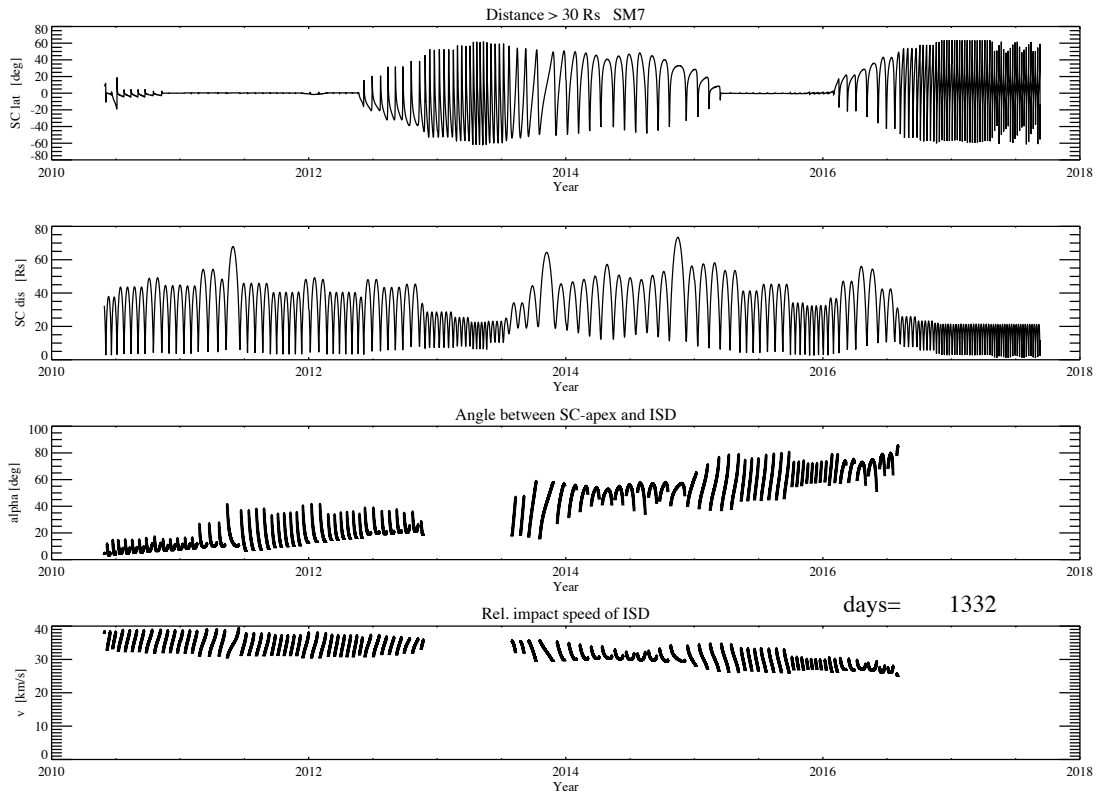


Figure A.13: Cassini tour SM-7 parameters in 2011 to 2017 (saturnian latitude and distance to Saturn) and the relative impact speed of interstellar grains at distances greater than $30 R_S$ (bottom). The relative impact speed is slightly decreasing due to the orbital motion of Saturn.

A.10 Acronyms

AU	Astronomical Unit
CA	Chemical Analyser
CAG	Chemical Analyser Grid
CAT	Chemical Analyser Target
CDA	Cosmic Dust Analyser
CME	coronal mass ejection
DA	Dust Analyser
DN	Digital number (units)
DT	Dust Telescope
EMB	Electronics main box
FWHM	full width half maximum
HRD	High Rate Detector
HGA	High Gain Antenna
IDP	interplanetary dust particle
IG	Ion grid
IID	Impact Ionisation Detector
IIT	Impact Ionisation Detector Target
IMF	interplanetary magnetic field
INMS	Ion and Neutral Mass Spectrometer
ISD	interstellar dust
ISS	Imaging Science Subsystem
LAMA	Large Area Mass Analyser
LIC	Local interstellar cloud
MP	Multiplier
PSU	Particle Selection Unit
SNR	signal-to-noise ratio
SOI	Saturn Orbit Insertion
TOF	time-of-flight
TS	Trajectory Sensor
QP	(CDA) charge sensor
UTC	Universal Time Coordinated